Hybrid Nanophotonic Elements and Sensing Devices based on Photonic Crystal Structures

DISSERTATION

zur Erlangung des akademischen Grades
doctor rerum naturalium
(Dr. rer. nat.)
im Fach Physik

eingereicht an der
Mathematisch-Naturwissenschaftlichen Fakultät I
Humboldt-Universität zu Berlin

von
Herrn Dipl.-Phys. Michael Barth
geboren am 14.05.1980 in Oelsnitz/V.

Präsident der Humboldt-Universität zu Berlin:
Prof. Dr. Dr. h. c. Christoph Markschies

Dekan der Mathematisch-Naturwissenschaftlichen Fakultät I:
Prof. Dr. Lutz-Helmut Schön

Gutachter:

1. Prof. Dr. Oliver Benson
2. Prof. Jelena Vučković, Ph.D.
3. Prof. Dr. Matthias Ballauff

Tag der mündlichen Prüfung: n.V.

Abstract

This thesis deals with the development and investigation of novel photonic crystal structures for applications in nanophotonics and optofluidics. Thereby, a first series of experiments focuses on the characterization and optimization of photonic crystal cavities in the visible wavelength range, demonstrating unprecedented cavity quality factors of up to 3400. These structures are subsequently employed as platforms for the creation of advanced hybrid nanophotonic elements by coupling external particles (such as diamond nanocrystals and metal nanoparticles) to the cavities in a well-controlled manner. For this purpose, a nanomanipulation method is developed, utilizing scanning probes for the deterministic positioning and assembly of particles on the photonic crystal structures. Various types of such hybrid elements are realized and investigated, including diamond-coupled cavities, plasmon-coupled cavities, and metal-diamond hybrid structures. These systems represent prototypes of fundamental nanophotonic/plasmonic building blocks for future integrated all-optical devices, providing control on the generation and coherent transfer of photons on the level of a single quantum emitter.

Apart from applications in nanophotonics different types of photonic crystal structures are also studied with regard to their performance as biochemical sensing elements. For the first time a thorough numerical analysis of the optical forces exerted on objects in the near-field of photonic crystal cavities is conducted, providing novel means to trap, detect, and investigate biological particles in integrated optofluidic devices. Furthermore, various types of photonic crystal fibers are studied with regard to their detection sensitivity in absorption and fluorescence measurements, revealing a clear superiority of selectively infiltrated hollow-core designs in comparison to solid-core fibers. For the first time the reliable detection of molecular concentrations down to 10^{-9} M is demonstrated, promising applications of such fiber-based sensors in analytical chemistry and medicine.

Keywords:
photonic crystal cavity, nanoparticle, nanomanipulation, optical force, photonic crystal fiber, optofluidic sensing

Zusammenfassung

Die vorliegende Forschungsarbeit widmet sich der Entwicklung und Untersuchung neuartiger photonischer Kristallstrukuren für Anwendungen in den Gebieten der Nanophotonik und Optofluidik. Dabei konzentriert sich eine erste Serie von Experimenten auf die Charakterisierung und Optimierung photonischer Kristallresonatoren im sichtbaren Spektralbereich, wobei bisher unerreichte Resonatorgüten von bis zu 3400 gezeigt werden können. Diese Strukturen werden anschließend als Plattformen zur Herstellung von hybriden nanophotonischen Bauelementen verwendet, indem externe Partikel (wie z.B. Diamant-Nanokristalle und Metall-Nanopartikel) in kontrollierter Art und Weise an die Resonatoren gekoppelt werden. Zu diesem Zweck wird eine Nanomanipulationsmethode entwickelt, welche Rastersonden zur gezielten Positionierung und Anordnung von Partikeln auf den photonischen Kristallstrukturen benutzt. Verschiedene Arten solcher Hybridelemente werden realisiert und untersucht, einschließlich Diamant-gekoppelter Resonatoren, Plasmon-gekoppelter Resonatoren und Metall-Diamant Hybridstrukturen. Diese Systeme repräsentieren Prototypen grundlegender nanophotonischer/plasmonischer Module für zukünftige integrierte optische Bauteile, welche Kontrolle über die Erzeugung und den kohärenten Transfer von Photonen auf dem Niveau eines einzelnen Quantenemitters ermöglichen.

Außer für Anwendungen auf dem Gebiet der Nanophotonik werden verschieden photonische Kristallstrukturen auch hinsichtlich ihres Leistungsvermögens als biochemische Sensorelemente erforscht. Zum ersten Mal wird eine umfassende numerische Analyse der optischen Kräfte auf Objekte im Nahfeld photonischer Kristallresonatoren durchgeführt, welche neue Möglichkeiten zum Einfang sowie zur Detektion und Untersuchung biologischer Partikel in integrierten optofluidischen Bauteilen bieten. Weiterhin werden unterschiedliche photonische Kristallfasern bezüglich ihrer Detektionssensitivität in Absorptions- und Fluoreszenzmessungen untersucht, wobei sich eine klare Überlegenheit von selektiv befüllten Hohlkern-Designs im Vergleich zu Festkern-Fasern offenbart. Zum ersten Mal kann die zuverlässige Detektion von molekularen Konzentrationen bis hinunter zu 10^{-9} M gezeigt werden, wodurch sich vielversprechende Anwendungen solcher Fasersensoren in der analytischen Chemie und Medizin abzeichnen.

Schlagwörter:
photonischer Kristallresonator, Nanopartikel, Nanomanipulation, optische Kraft, photonische Kristallfaser, optofluidische Sensorik

Contents

Abbreviations

abbreviation	explanation
a.u.	arbitrary units
AFM	atomic force microscope
APD	avalanche photodiode
CCD	charge-coupled device
CMOS	complementary metal-oxide semiconductor
LED	light-emitting diode
Eq./Eqs.	equation/equations
FDTD	finite-difference time-domain
FEM	finite element method
Fig./Figs.	figure/figures
FT	Fourier transformation
FWHM	full-width half-maximum
e.g.	*exempli gratia* (for example)
et al.	*et alii* (and others)
etc.	*et cetera* (and so forth)
i.e.	*id est* (that is)
NV	nitrogen-vacancy
ODMR	optically detected magnetic resonance
PML	perfectly matched layer
PMMA	polymethylmethacrylate
QED	quantum electrodynamics
Ref./Refs.	reference/references
RMS	root mean square
Sec./Secs.	section/sections
SERS	surface-enhanced Raman scattering
Tab./Tabs.	table/tables
TE	transverse electric
TM	transverse magnetic

Chapter 1

Introduction

There are only few research areas which have undergone such a rapid development in recent years as the field of nanotechnology. The urge to control matter and energy on ever smaller length scales is ubiquitous in modern science and bears great potentials for a vast range of applications, e.g., in material engineering, chemistry, medicine, electronics, and optics. With regard to the latter branch a novel field termed nano-optics or nanophotonics has evolved in the past two decades, dealing with the investigation and manipulation of light at the sub-wavelength scale, the study of fundamental interactions of light and matter on a nanoscopic level, and the development of novel optical materials.

One prominent example are photonic crystals [1, 2], which represent dielectric structures with an artificial periodicity on the order of a few hundred nanometers and allow light to be guided and stored in ultra-small volumes, only constrained by the diffraction limit. Furthermore, they provide the means to engineer the local optical mode structure perceived by light emitters, enabling the manipulation of the emission dynamics of the latter [3]. In this regard, especially planar photonic crystals and cavities (see Fig. 1.1a) have proven to be excellent candidates for a number of applications due to their relative ease of fabrication, compact design, and the possibility to be readily integrated into more complex structures. Thus, they represent key elements for the realization of future on-chip optoelectronic or all-optical devices, e.g., for quantum information processing [4, 5].

The scientific progress in the field of photonic crystals has been driven by technological advances of corresponding fabrication techniques (such as electron beam lithography) and analytical tools (such as atomic force and optical near-field microscopy). Only through the precise tailoring of material structures and properties on the nanometer scale has it become possible to control the flow of light in unprecedented ways. Therefore, it is of utmost importance to constantly explore novel fabrication and characterization strategies in order to enhance the functionality of

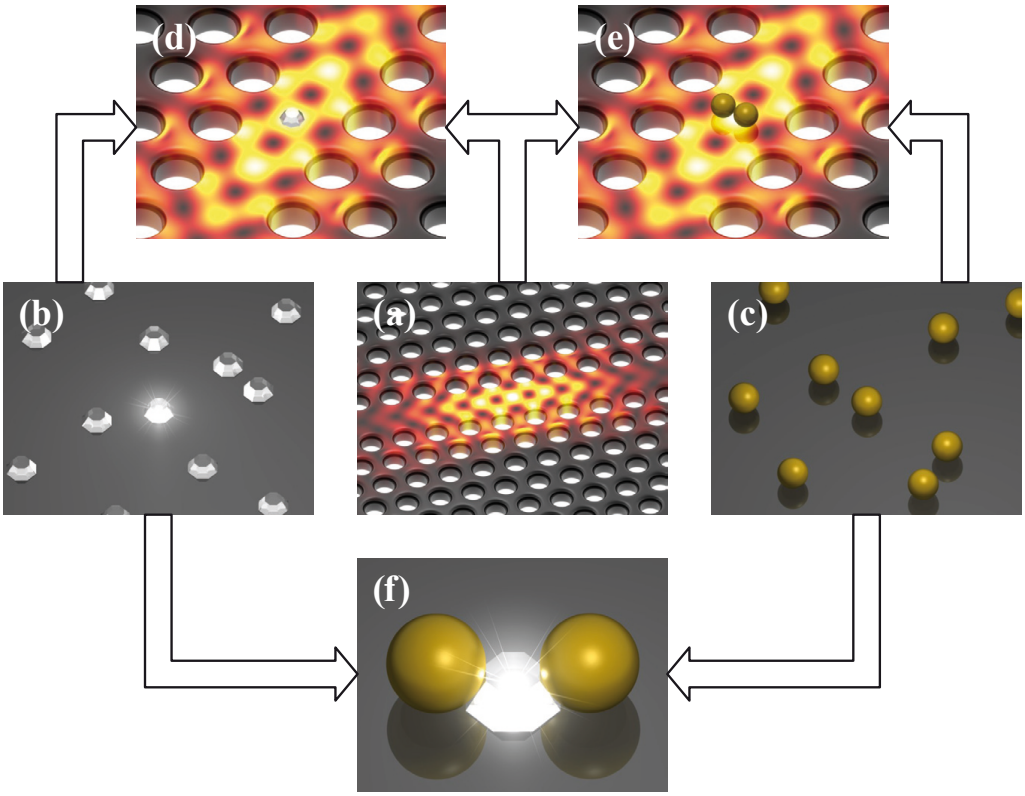

Figure 1.1: Illustration of the nanophotonic constituents employed in this thesis: **(a)** planar photonic crystal cavities, **(b)** diamond nanocrystals, and **(c)** metal nanoparticles. These are combined by means of nanomanipulation techniques to form hybrid nanophotonic elements: **(d)** diamond-loaded cavities, **(e)** plasmon-coupled cavities, and **(f)** plasmon-coupled diamond nanocrystals.

these fundamental nanophotonic building blocks and broaden their range of applications. For example, planar photonic crystals operating in the near-infrared are well established, but their counterparts in the visible wavelength range are much less advanced, mainly due to the lack of suitable material systems. Likewise, existing lithographic fabrication techniques are often limited to specific material combinations (such as III/V semiconductors), restricting the design flexibility and, hence, the achievable device performance. This is particularly crucial with regard to a tailored coupling of emitters to the optical modes of a photonic crystal structure, representing one of the key challenges on the way towards integrated photonic circuits.

The first two parts of this thesis are devoted to these problems, i.e., the development and investigation of planar photonic crystal cavities in the visible wavelength range and the exploration of novel techniques to facilitate a controlled coupling of arbitrary emitters (or other constituents) to them. For this purpose silicon nitride is employed as base material and a nanomanipulation method is used to deterministi-

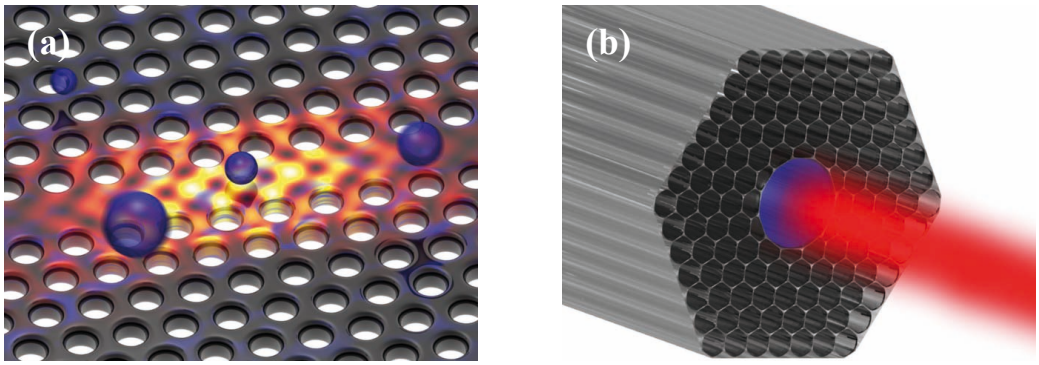

Figure 1.2: Illustration of two approaches for optofluidic sensing with photonic crystal structures: **(a)** optical trapping of particles in the near-field of planar photonic crystal cavities and **(b)** absorption/fluorescence detection with liquid-filled photonic crystal fibers.

cally assemble different kinds of nanoparticles on the cavities, thus enhancing their original functionality. Due to the combined nature of these systems they will be denoted as "hybrid" structures throughout this thesis. Thereby, two types of materials are of particular interest, namely diamond nanocrystals, which can contain various sorts of stable single photon emitters [6], and metal nanoparticles, which support extremely localized electromagnetic fields due to surface plasmon resonances [7]. In combination with photonic crystal cavities novel hybrid nanophotonic elements are created (see Fig. 1.1), whose optical properties are subsequently explored in experimental as well as theoretical studies.

The second major topic of this thesis deals with the application of photonic crystal structures in optofluidics, a research area which aims at the fusion of optics and microfluidics [8, 9]. Photonic crystals are ideally suited for this purpose due to their compact design and the ability to confine and guide light in microscopic dimensions. This offers unique possibilities to facilitate a controlled interaction between light and fluids in an integrated system. Here, two issues are of particular interest. In the third part of this thesis the question is addressed whether the enhanced electromagnetic field near planar photonic crystal cavities might be used to trap and manipulate small objects in a liquid environment via optical forces (see Fig. 1.2a). Such a scheme has barely been explored so far, but may provide novel means to detect and investigate biological entities such as cells, bacteria, or even macromolecules.

In the fourth part of this thesis a different type of photonic crystal structure is studied with regard to its optofluidic sensing performance, namely photonic crystal fibers [10, 11]. This special class of optical fibers exhibits a periodic arrangement of holes which can be employed as microfluidic channels and allow for an interaction of the guided light with infiltrated liquids along the whole length of the fiber (see Fig. 1.2b). Depending on the strength and character of this interaction such a sensing

scheme promises higher detection sensitivities than conventional devices relying on free-space optics, but a thorough investigation of the achievable detection limit is still lacking. Therefore, theoretical and experimental studies of different fiber designs are conducted in order to directly compare their performances as biochemical sensors and draw conclusions on the optimal sensing strategy.

It should be noted that all structures developed and studied within this thesis represent elementary building blocks for the realization of more complex photonic or optofluidic systems. By optimizing these fundamental elements and extending their capabilities the toolbox for creating future devices with novel functionalities is enlarged. It is the intention of the presented work to contribute to this ambitious goal. This said, the general scope and outline of this thesis is defined. More detailed introductions into the individual topics are provided in the corresponding chapters, which are organized as follows:

- In **Chapter 2** the fabrication, optimization, and optical characterization of photonic crystal cavities made from silicon nitride is reported. This chapter also provides the theoretical background knowledge for the understanding of photonic crystals in general.
- In **Chapter 3** the nanomanipulation method used for the controlled assembly of hybrid nanophotonic elements is introduced and three different systems are investigated, namely diamond-loaded cavities, plasmon-coupled cavities, and plasmon-coupled diamond nanocrystals.
- In **Chapter 4** a numerical analysis of the optical forces exerted on dielectric particles in the near-field of photonic crystal cavities is reported.
- In **Chapter 5** the optofluidic sensing performance of different types of photonic crystal fibers is investigated and directly compared.
- Finally, **Chapter 6** contains a short summary of this thesis as well as an outlook addressing open questions and future developments.

Chapter 2

Investigation and optimization of photonic crystal cavities in the visible

2.1 Introduction

In recent years planar photonic crystal cavities have received considerable attention as building blocks for novel light sources, including low-threshold nanolasers [12, 13] and efficient single photon sources [14, 15], but also as tools for studying quantum electrodynamic (QED) effects in general, such as Rabi-splitting [16, 17] and the Purcell enhancement of spontaneous emission [18, 19]. The key property, which makes photonic crystal cavities unique among other kinds of microcavities, is their extremely small mode volume, being typically on the order of the cubic wavelength. This extraordinarily tight confinement of light, combined with fairly high quality factors (10^3–10^6), provides an intense interaction of light and matter and makes photonic crystal cavities ideally suited for the realization of hybrid nanophotonic elements as proposed in this thesis.

Most of the research in this field has been concentrated on photonic crystals and corresponding emitters operating in the near infrared [20–25]. This is reasonable, since high refractive index materials (such as silicon or gallium arsenide) are readily available in this spectral region and the respective fabrication techniques are well developed. However, extending the wavelength range into the visible part of the spectrum is appealing for a number of applications, as it would allow, e.g., the combination with defect centers in diamond or other quantum emitters in the visible. Thereby, the main challenge lies in the choice of a suitable material, which has to be transparent in the corresponding wavelength range, while simultaneously featuring a sufficiently high refractive index to provide good optical confinement.

(Al,In,Ga)N-based material systems are one possibility, allowing the fabrication of devices emitting in the ultra-violet to green region [26–28]. Red laser emission from AlGaInP/GaInP photonic crystal membranes has also been demonstrated [29]. However, the fabrication of these III/V semiconductor devices is expensive and still technologically challenging, especially concerning freely suspended structures. Using organic materials is another possibility [30], being much more cost-effective and allowing an easy doping of the photonic crystal material with a large number of different emitters (such as dye molecules or colloidal quantum dots). However, they usually suffer from relatively small refractive indices.

Photonic crystal structures based on silicon nitride are an interesting alternative, combining a modest refractive index ($n \approx 2$) with cost-effectiveness and ease of fabrication due to its compatibility to standard CMOS (complementary metal-oxide semiconductor) technology. Pioneering studies by Makarova *et al.* [31] successfully demonstrated the potential of silicon nitride for the realization of nanophotonic building blocks in the yellow to red wavelength range. However, the cavity quality factors obtained in the cited work were limited to values of 200–300. Also in other material systems the best values achieved at that time were well below 1000. Thus, the basic question remains whether photonic crystal cavities with quality factors which are sufficiently high for the realization of pronounced cavity QED effects can be fabricated in the visible. The first part of this thesis is devoted to this question, presenting experimental as well as theoretical studies of silicon nitride photonic crystal cavities, specifically focusing on the optimization of the corresponding quality factors.

The chapter is organized as follows: In Sec. 2.2 the fundamentals of photonic crystals are introduced, providing the theoretical framework for this and also subsequent chapters. Experimental details of the fabrication and optical characterization of photonic crystal cavities are described in Sec. 2.3, accompanied by a brief outline of the employed computational methods. The discussion of the obtained results starts with the evaluation of L3-type photonic crystal cavities in Sec. 2.4, providing a detailed numerical as well as experimental analysis of the mode structure and corresponding quality factors. An optimization scheme for the cavity design is developed and tested by directly comparing experimental data and theoretical predictions, followed by a discussion of cavity QED effects in these structures. In Sec. 2.5 numerical and experimental results for double-heterostructure-type photonic crystal cavities are presented, demonstrating unprecedented quality factors (in the visible) larger than 3000. Furthermore, some issues concerning the mode polarization in the far-field are discussed. Finally, a short summary of this chapter as well as some concluding remarks are given in Sec. 2.6.

2.2 Theory of electromagnetism in photonic crystals

Photonic crystals constitute a special class of nanostructured materials, characterized by periodically alternating domains of dielectrics with different refractive indices [32]. Most importantly, the length scale of the periodicity (which can either be one-, two-, or three-dimensional) is typically on the order of the corresponding wavelength at which the material is supposed to operate, leading to the formation of a photonic band structure, in close analogy to the electronic band structure in atomic lattices. This section provides the theoretical background necessary for the understanding of photonic crystals in general (Sec. 2.2.1) and planar photonic crystal cavities in particular (Secs. 2.2.2 and 2.2.3). Apart from treating the basic optical properties of the latter, the main focus lies on topics of specific relevance for the experimental part of this chapter, namely the optimization of the cavity quality factor (Sec. 2.2.4) and the coupling of quantum emitters to the cavities (Sec. 2.2.5).

2.2.1 Fundamental optical properties of periodic dielectric media

Maxwell's equations and eigenvalue problem

The starting point for describing electromagnetic fields in an arbitrary photonic crystal structure are the macroscopic Maxwell equations [33]

$$\nabla \cdot \left[\varepsilon_0 \varepsilon(\boldsymbol{r}) \boldsymbol{E}(\boldsymbol{r},t)\right] = \rho \,, \tag{2.1}$$

$$\nabla \cdot \left[\mu_0 \mu(\boldsymbol{r}) \boldsymbol{H}(\boldsymbol{r},t)\right] = 0 \,, \tag{2.2}$$

$$\nabla \times \boldsymbol{E}(\boldsymbol{r},t) = -\mu_0 \mu(\boldsymbol{r}) \frac{\partial \boldsymbol{H}(\boldsymbol{r},t)}{\partial t} \,, \qquad \text{and} \tag{2.3}$$

$$\nabla \times \boldsymbol{H}(\boldsymbol{r},t) = \varepsilon_0 \varepsilon(\boldsymbol{r}) \frac{\partial \boldsymbol{E}(\boldsymbol{r},t)}{\partial t} + \boldsymbol{J} \,. \tag{2.4}$$

Here, $\boldsymbol{E}$ and $\boldsymbol{H}$ are the electric and magnetic field, ε_0 (ε) and μ_0 (μ) denote the vacuum (relative) dielectric permittivity and magnetic permeability, and ρ and $\boldsymbol{J}$ are the free charge and free current density, respectively. In the following, the analysis is restricted to purely dielectric media without any internal light sources such that $\rho = 0$ and $\boldsymbol{J} = 0$. Furthermore, as most dielectric materials exhibit a relative magnetic permeability close to unity, $\mu(\boldsymbol{r}) = 1$ is assumed for simplicity.

With these assumptions Eqs. (2.3) and (2.4) can be combined to yield the wave equations

$$\frac{1}{\varepsilon(\boldsymbol{r})} \nabla \times \left[\nabla \times \boldsymbol{E}(\boldsymbol{r},t)\right] = -\frac{1}{c^2} \frac{\partial^2 \boldsymbol{E}(\boldsymbol{r},t)}{\partial t^2} \qquad \text{and} \tag{2.5}$$

$$\nabla \times \left[\frac{1}{\varepsilon(\boldsymbol{r})} \nabla \times \boldsymbol{H}(\boldsymbol{r},t)\right] = -\frac{1}{c^2} \frac{\partial^2 \boldsymbol{H}(\boldsymbol{r},t)}{\partial t^2} \,, \tag{2.6}$$

where $c = 1/\sqrt{\varepsilon_0 \mu_0}$ denotes the vacuum speed of light. The time-dependence of the fields $\boldsymbol{E}$ and $\boldsymbol{H}$ can be separated from the spatial variation through expansion into a set of harmonic modes of the form $\boldsymbol{E}(\boldsymbol{r}, t) = \boldsymbol{E}(\boldsymbol{r}) \exp(-i\omega t)$ and $\boldsymbol{H}(\boldsymbol{r}, t) = \boldsymbol{H}(\boldsymbol{r}) \exp(-i\omega t)$, respectively, with ω being the frequency of the mode. This allows one to convert Eqs. (2.5) and (2.6) into respective eigenvalue problems

$$\frac{1}{\varepsilon(\boldsymbol{r})} \nabla \times \big[\nabla \times \boldsymbol{E}(\boldsymbol{r})\big] = \frac{\omega^2}{c^2} \boldsymbol{E}(\boldsymbol{r}) \qquad \text{and} \tag{2.7}$$

$$\nabla \times \left[\frac{1}{\varepsilon(\boldsymbol{r})} \nabla \times \boldsymbol{H}(\boldsymbol{r})\right] = \frac{\omega^2}{c^2} \boldsymbol{H}(\boldsymbol{r}) \,. \tag{2.8}$$

The eigenvectors $\boldsymbol{E}(\boldsymbol{r})$ and $\boldsymbol{H}(\boldsymbol{r})$ represent the spatial mode profiles of the harmonic eigenmodes (with frequency ω) of the considered photonic crystal structure. The latter is completely defined by the dielectric function $\varepsilon(\boldsymbol{r})$.

Photonic band structure

It is the fundamental property of any photonic crystal that the spatial variation of $\varepsilon(\boldsymbol{r})$ is periodic in at least one dimension such that $\varepsilon(\boldsymbol{r} + \boldsymbol{R}) = \varepsilon(\boldsymbol{r})$. Here, $\boldsymbol{R} = \sum_i m_i \boldsymbol{a}_i$ is an arbitrary lattice vector, written as a superposition of the primitive lattice vectors $\{\boldsymbol{a}_i\}$, with $\{m_i\}$ taking only integer values. This discrete translational symmetry allows one to apply Bloch's theorem, as known from solid-state physics [34], to the current problem. Consequently, the eigenvectors $\boldsymbol{E}(\boldsymbol{r})$ and $\boldsymbol{H}(\boldsymbol{r})$ can be expressed as plane waves (with wave vector $\boldsymbol{k}$) modulated by a periodic function:

$$\boldsymbol{E}_{\boldsymbol{k}n}(\boldsymbol{r}) = \boldsymbol{u}_{\boldsymbol{k}n}(\boldsymbol{r}) \mathrm{e}^{i\boldsymbol{k}\boldsymbol{r}} \,, \tag{2.9}$$

$$\boldsymbol{H}_{\boldsymbol{k}n}(\boldsymbol{r}) = \boldsymbol{v}_{\boldsymbol{k}n}(\boldsymbol{r}) \mathrm{e}^{i\boldsymbol{k}\boldsymbol{r}} \,. \tag{2.10}$$

Here, $\boldsymbol{u}_{\boldsymbol{k}n}$ and $\boldsymbol{v}_{\boldsymbol{k}n}$ satisfy the relations $\boldsymbol{u}_{\boldsymbol{k}n}(\boldsymbol{r} + \boldsymbol{R}) = \boldsymbol{u}_{\boldsymbol{k}n}(\boldsymbol{r})$ and $\boldsymbol{v}_{\boldsymbol{k}n}(\boldsymbol{r} + \boldsymbol{R}) = \boldsymbol{v}_{\boldsymbol{k}n}(\boldsymbol{r})$, respectively. The additional index n is introduced to distinguish the various discrete solutions of Eqs. (2.7) and (2.8) existing for each wave vector $\boldsymbol{k}$. Then, the corresponding eigenfrequencies $\omega_{\boldsymbol{k}n}$ form discrete bands $\omega_n(\boldsymbol{k})$, continuously varying with $\boldsymbol{k}$ (which has only the role of a free parameter) and labeled by n (the so-called band number) in order of increasing frequency. This is the physical origin of the photonic band structure, resulting from the periodicity of the dielectric medium. It can be understood as the optical analogue to the electronic band structure of solid-state materials, which stems from the modulation of the electronic wave function due to the periodic atomic potential.

The validity of Bloch's theorem in photonic crystal structures implies that the eigenmodes $\boldsymbol{E}_{\boldsymbol{k}n}(\boldsymbol{r})$ and $\boldsymbol{H}_{\boldsymbol{k}n}(\boldsymbol{r})$ are invariant under discrete translations of the wave vector $\boldsymbol{k}$ by a reciprocal lattice vector $\boldsymbol{G} = \sum_i m_i \boldsymbol{b}_i$. Here, $\{\boldsymbol{b}_i\}$ are the primitive

reciprocal lattice vectors defined by $\boldsymbol{a}_i \cdot \boldsymbol{b}_j = 2\pi\delta_{ij}$ and $\{m_i\}$ are again integer values. Then, $\omega_n(\boldsymbol{k}+\boldsymbol{G}) = \omega_n(\boldsymbol{k})$ is also valid and an eigenmode of arbitrary wave vector $\boldsymbol{k}$ can always be identified by a corresponding eigenmode within the first, irreducible Brillouin zone of the reciprocal lattice, spanned by $\{\boldsymbol{b}_i\}$. Consequently, it is sufficient to consider the photonic band structure only within this first Brillouin zone, as it contains the complete information on the optical mode structure of the photonic crystal.

Symmetry properties

Another important property of the photonic band structure results from the time-reversal symmetry of Maxwell's equations. Changing t to $-t$ is equivalent to taking the complex conjugate of the mode profiles $\boldsymbol{E}(\boldsymbol{r})$ and $\boldsymbol{H}(\boldsymbol{r})$. For example, inserting the eigenmodes (2.9) into Eq. (2.7) yields

$$\frac{1}{\varepsilon(\boldsymbol{r})}(\nabla + i\boldsymbol{k}) \times \Big[(\nabla + i\boldsymbol{k}) \times \boldsymbol{u}_{\boldsymbol{k}n}(\boldsymbol{r})\Big] = \frac{\omega_{\boldsymbol{k}n}^2}{c^2}\boldsymbol{u}_{\boldsymbol{k}n}(\boldsymbol{r}) \tag{2.11}$$

as well as its complex conjugate form

$$\frac{1}{\varepsilon(\boldsymbol{r})}(\nabla - i\boldsymbol{k}) \times \Big[(\nabla - i\boldsymbol{k}) \times \boldsymbol{u}_{\boldsymbol{k}n}^*(\boldsymbol{r})\Big] = \frac{\omega_{\boldsymbol{k}n}^2}{c^2}\boldsymbol{u}_{\boldsymbol{k}n}^*(\boldsymbol{r}) \; . \tag{2.12}$$

Here, $\varepsilon^*(\boldsymbol{r}) = \varepsilon(\boldsymbol{r})$ is assumed, which is true for a lossless dielectric material. As is obvious from Eqs. (2.11) and (2.12), $\boldsymbol{u}_{\boldsymbol{k}n}(\boldsymbol{r})$ and $\boldsymbol{u}_{\boldsymbol{k}n}^*(\boldsymbol{r})$ satisfy the same eigenvalue equation, but with reversed wave vector $\boldsymbol{k}$:

$$\boldsymbol{u}_{\boldsymbol{k}n}^*(\boldsymbol{r}) = \boldsymbol{u}_{-\boldsymbol{k}n}(\boldsymbol{r}) \; . \tag{2.13}$$

It follows that $\omega_{\boldsymbol{k}n} = \omega_{-\boldsymbol{k}n}$, which means that the photonic band structure possesses inversion symmetry with respect to $\boldsymbol{k}$ irrespective of the actual symmetry properties of the underlying photonic crystal structure.

Scaling properties

Finally, the scaling properties of periodic dielectric media shall briefly be discussed. For this purpose, the eigenvalue equation (2.7) is rewritten using the dimensionless variables $\boldsymbol{r}' = \boldsymbol{r}/a$ and $\omega' = a\omega/(2\pi c)$:

$$\frac{1}{\varepsilon(a\boldsymbol{r}')}\frac{1}{a}\nabla' \times \left[\frac{1}{a}\nabla' \times \boldsymbol{E}(a\boldsymbol{r}')\right] = \left(\frac{2\pi\omega'}{a}\right)^2 \boldsymbol{E}(a\boldsymbol{r}') \; . \tag{2.14}$$

Here, $\nabla' = a\nabla$ denotes the differentiation with respect to $\boldsymbol{r}'$. By defining new functions $\varepsilon'(\boldsymbol{r}') = \varepsilon(a\boldsymbol{r}')$ and $\boldsymbol{E}'(\boldsymbol{r}') = \boldsymbol{E}(a\boldsymbol{r}')$, Eq. (2.14) can be transformed into

the scale-invariant eigenvalue equation

$$\frac{1}{\varepsilon'(\boldsymbol{r}')}\nabla' \times [\nabla' \times \boldsymbol{E}'(\boldsymbol{r}')] = (2\pi\omega')^2 \boldsymbol{E}'(\boldsymbol{r}') \; . \tag{2.15}$$

An equivalent transformation can also be applied to Eq. (2.8). It follows that two photonic crystal structures which differ in their spatial dimensions only by a constant factor share similar eigenfunctions and eigenfrequencies, convertible by scaling with the same factor. Consequently, the optical properties of a periodic dielectric medium are independent of the absolute length scale (when using normalized units) and solutions obtained for one particular system can easily be adopted to corresponding structures of different sizes by simple rescaling.

2.2.2 Optical properties of planar photonic crystals

While the optical properties discussed so far are inherent to all periodic dielectric media, the specific characteristics of planar photonic crystals shall now be discussed. They constitute a special class of photonic crystals which are periodic in two dimensions (x and y) and have a finite extent (without any periodicity) in the third dimension (z). The most prominent example is a thin dielectric slab (of thickness t) perforated with a regular pattern of holes, as is schematically shown in Fig. 2.1b. Although various periodic arrangements of holes are possible, only the hexagonal lattice structure (see Fig. 2.1a) is considered here. It is composed of a triangular unit cell and characterized by the lattice constant a, the hole radius r, and the dielectric constant ε of the slab material (assuming that the surrounding material is air). To understand the band structure and the associated optical properties of such a photonic crystal slab, it is instructive to consider the corresponding two-dimensional structure (with infinite extend in z direction) and then return to the true three-dimensional system, as is done in the following.

Two-dimensional photonic crystals

One of the main characteristics of a two-dimensional system is that it has always mirror symmetry along the third dimension (namely the z axis) with respect to any point z. This has immediate consequences for the types of modes which can exist in the structure. In general, these can be categorized into even and odd modes [32]. The former obey the relations $\boldsymbol{E}_{\boldsymbol{k}n}(x,y,z) = -\boldsymbol{E}_{\boldsymbol{k}n}(x,y,-z)$ and $\boldsymbol{H}_{\boldsymbol{k}n}(x,y,z) = \boldsymbol{H}_{\boldsymbol{k}n}(x,y,-z)$, while for the latter $\boldsymbol{E}_{\boldsymbol{k}n}(x,y,z) = \boldsymbol{E}_{\boldsymbol{k}n}(x,y,-z)$ and $\boldsymbol{H}_{\boldsymbol{k}n}(x,y,z) = -\boldsymbol{H}_{\boldsymbol{k}n}(x,y,-z)$ is valid. This is true as long as the wave vector $\boldsymbol{k}$ is restricted to the x-y plane, which is fulfilled for any genuine two-dimensional system. From these symmetry properties it follows that even modes can only have non-zero field components E_x, E_y, and H_z, while odd modes are restricted to non-zero components

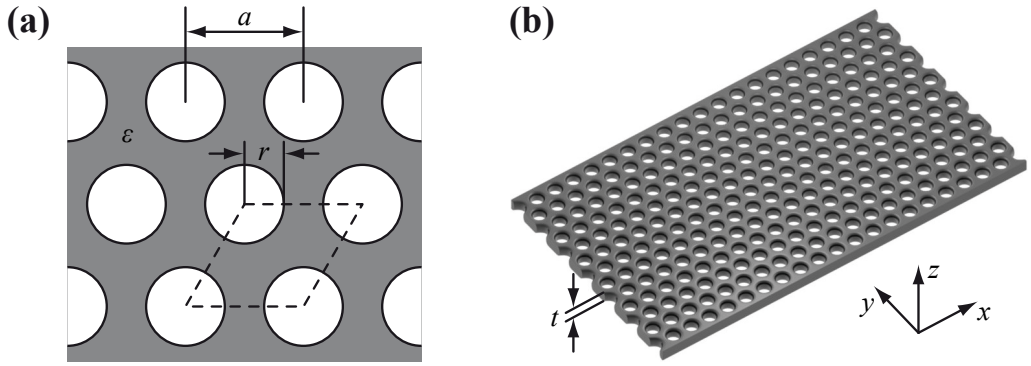

Figure 2.1: **(a)** Two-dimensional hexagonal photonic crystal lattice of holes (with radius r and lattice constant a) in a dielectric substrate (with dielectric constant ε). The dashed lines indicate the corresponding unit cell. **(b)** Illustration of a hexagonal photonic crystal slab of thickness t.

H_x, H_y, and E_z. Consequently, two classes of (decoupled) mode polarizations can be distinguished: transverse electric (TE) modes, for which the electric field is confined within the x-y plane, and transverse magnetic (TM) modes, for which the magnetic field is confined within the x-y plane.

In Fig. 2.2a the calculated band structure of a specific two-dimensional photonic crystal (with realistic material parameters) is shown, displaying both mode polarizations. As can be seen, the bands formed by TE and TM modes are quite different. Most strikingly, a photonic band gap (indicated in orange) exists for TE polarization, while there is no such gap for TM polarization. Therefore, any application exploiting the band gap effect is restricted to TE polarized light only. This is a consequence of the relatively low refractive index $n = 2.01$ assumed for the dielectric material, which corresponds to silicon nitride. For high-index materials (such as silicon or gallium arsenide), a complete photonic band gap can exist for both polarizations. In general, increasing the ratio r/a leads to a shift of the entire photonic band structure (including the band gap) towards higher frequencies, as the modes are forced to have a higher fraction of their field intensity located inside the air-filled holes. At the same time, the width of the band gap increases. However, too large values of r/a are unfavorable for the mode properties of three-dimensional photonic crystal slabs due to higher radiation losses, as is discussed below.

Photonic crystal slabs

When considering the true three-dimensional slab structure, the wave vector $\boldsymbol{k}$ is no longer confined to the x-y plane, but can have a finite component k_z. In this case, the so-called projected band structure $\omega_n(\boldsymbol{k}_\parallel)$ is usually used to illustrate the optical properties of the system [32], as is shown in Fig. 2.2b. Here, $\boldsymbol{k}_\parallel = (k_x, k_y)$ is the in-plane component of the wave vector $\boldsymbol{k}$, which is a conserved quantity due to

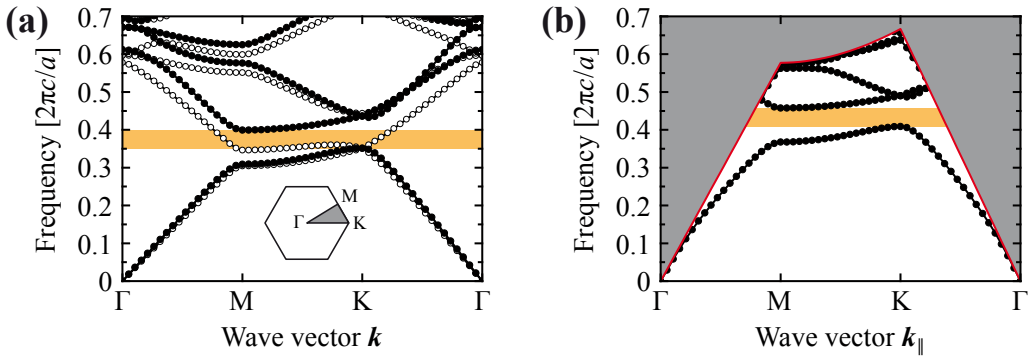

Figure 2.2: **(a)** Calculated band structure of the two-dimensional hexagonal photonic crystal shown in Fig. 2.1a with a hole radius $r = 0.3a$ and a dielectric constant $\varepsilon = 4.04$. The filled/open circles represent TE/TM modes. The orange bar indicates the band gap for TE polarization and the inset displays the Brillouin zone and corresponding symmetry points in k-space. **(b)** Calculated projected band structure of the photonic crystal slab shown in Fig. 2.1b with a thickness $t = 0.74a$ and all other parameters as in (a). Only TE-like modes are shown for clarity. The red line represents the light line, above which a continuum of extended states exists (gray shaded area). Details of the computational method are provided in Sec. 2.3.3.

the translational symmetry of the system. The projected band structure is divided into two distinct regions, separated by the light line $\omega = c|\boldsymbol{k}_{\parallel}|$. For all frequencies above the light line, extended states exist which can propagate in air and are thus not confined to the photonic crystal slab. As the wave vector component k_z of these extended states can take arbitrary values, they form a continuum (the so-called light cone) for each value of $\boldsymbol{k}_{\parallel}$.

Below the light line there still exist discrete bands, composed of modes which are confined and guided within the slab due to total internal reflection and which decay exponentially along z into the surrounding air. Strictly speaking, only at the center of the slab (at $z = 0$) these modes can be regarded as purely TE or TM polarized, because this is the only symmetry plane in z direction. However, as the mode polarization is nearly maintained at some distance away from $z = 0$ due to the continuity of the electromagnetic fields (at least for thin dielectric slabs with $t < \lambda/2$), the different guided modes are usually classified as TE-like and TM-like, respectively [32]. Like in the two-dimensional case, a photonic band gap only exists for TE-like modes, as is indicated in the band structure shown in Fig. 2.2b. The width of this gap depends on the slab thickness t. For very thin slabs the modes are only weakly guided due to the small vertical effective refractive index contrast and the gap becomes extremely narrow. For very thick slabs higher order modes start to populate the gap, thus reducing its width. Consequently, depending on the application, an optimal slab thickness exists, which typically lies in the range $0.5a < t < a$ [35].

It should be noted that the TE photonic band gap in Fig. 2.2b is incomplete, meaning that it solely refers to the guided modes and not to the extended states in the light cone. This has important consequences (in terms of radiation losses) for the confinement of localized defect modes, which are treated in the subsequent sections. It should further be noted that the discussed optical properties only apply to photonic crystal slabs with mirror symmetry in z direction. If this symmetry is broken, e.g., due to the presence of a solid substrate, the classification into TE-like and TM-like modes is no longer valid (meaning that both types of modes start to couple to each other [35]) and the photonic band gap in Fig. 2.2b may vanish.

2.2.3 Defect modes in planar photonic crystals

Due to the strictly periodic arrangement of holes, the photonic crystal slabs considered so far exhibited perfect translational symmetry in the x-y plane, leading to the formation of a photonic band gap. Within the frequency range of this gap, no (guided) modes can exist. However, if the symmetry is broken by the introduction of a defect into the otherwise periodic structure, localized defect modes may occur inside the band gap [36, 37], which are spatially confined to the area of the defect and which decay exponentially into the surrounding (periodic) photonic crystal lattice. Strictly speaking, these defect modes are not created inside the band gap (as the total number of optical states has to be preserved [38]), but are rather formed by modes which are either pulled down (donor-type modes) or pushed up (acceptor-type modes) from the upper or lower bands, respectively, depending on whether the effective dielectric constant is locally increased or decreased due to the defect [39].

Many different types of lattice distortions exist which can be used to generate defect modes. For example, individual holes may be increased or decreased in size [40, 41], shifted with respect to neighboring holes [13], or may be omitted at all [12, 42]. If this modification is restricted to a small region of the photonic crystal slab, one usually refers to it as a point defect or photonic crystal cavity. By consecutively combining a large number of these point defects, a so-called line defect or photonic crystal waveguide is created, along which light can be steered through the photonic crystal structure. In the following, the optical properties of three particular kinds of defects are investigated in more detail, namely the so-called L3 cavity, the W1 waveguide, and the double-heterostructure cavity.

Point defect: L3 cavity

The basic L3 cavity [43] is created by removing three consecutive holes in a line from the periodic hexagonal lattice, as is shown in Fig. 2.3a. Due to the local increase of the dielectric constant at the site of the defect, bulk modes from the

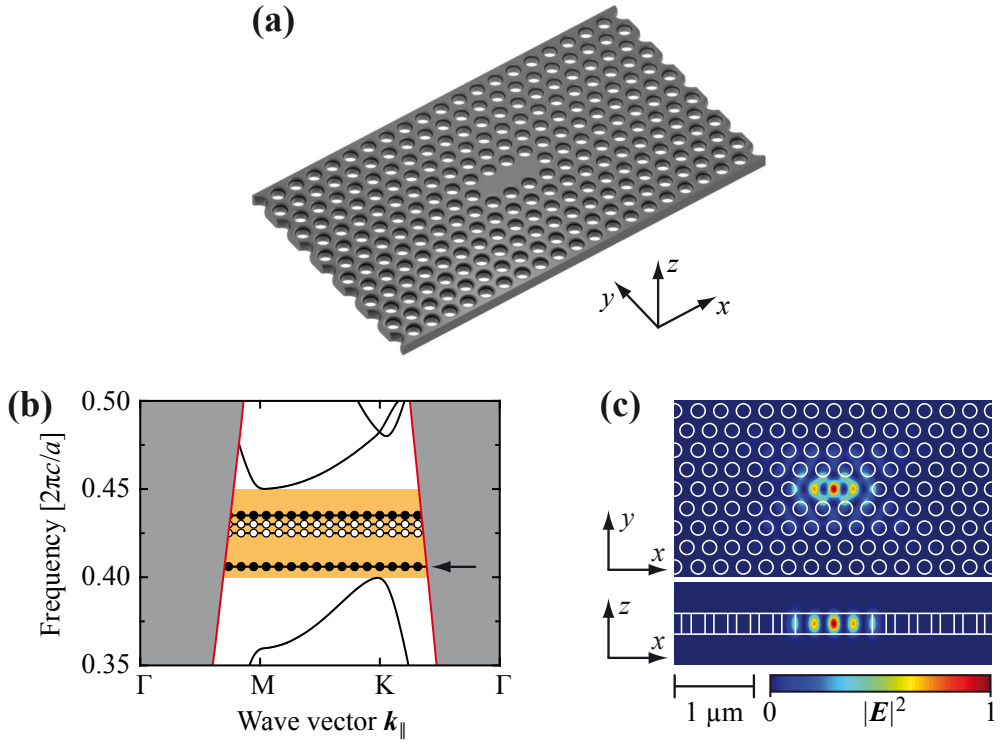

Figure 2.3: **(a)** Illustration of a photonic crystal slab hosting an L3 cavity, created by omitting three consecutive holes in a line. **(b)** Zoom into the projected band structure of the L3 cavity shown in (a). The thickness of the photonic crystal slab is $t = 0.93a$ and all other parameters are the same as in Fig. 2.2b. Only TE-like modes are shown for clarity. Black curves represent bulk modes, filled/open circles denote odd/even defect modes (with respect to the y direction) within the band gap (orange), and the red lines indicate the light line with a continuum of extended states above (gray shaded area). **(c)** Calculated electric field intensity distribution $|\boldsymbol{E}|^2$ of the fundamental L3 cavity mode, indicated by an arrow in (b). Displayed are cross sections through the central x-y and x-z planes of the cavity.

upper band are lowered in frequency and pulled down into the band gap, where they form localized defect modes. As can be seen from the projected band structure in Fig. 2.3b, these defect modes appear as flat bands with vanishing group velocity. This is a consequence of the spatial localization of the mode energy in the area of the lattice defect. Within the x-y plane the mode is confined due to the band gap of the surrounding bulk photonic crystal, while the confinement in z direction is provided by total internal reflection. Therefore, a standing wave is formed, which decays exponentially in all three dimensions. As an example, the mode profile of the fundamental L3 cavity mode (i.e., the mode with lowest frequency) is displayed in Fig. 2.3c.

The major difference between defect modes and bulk modes (of the undisturbed photonic crystal lattice) is that for a defect structure the translational symmetry is completely broken and hence the wave vector $\boldsymbol{k}$ is no longer conserved [32]. Consequently, the cavity modes can couple to extended states of the same frequency ω in

the light cone, which means that the mode energy leaks out of the cavity through radiative loss. The rate κ at which this loss occurs depends on the overlap (in k-space) of the wave vector distribution of the cavity mode and that of the extended states [44]. This ultimately determines the time scale $\tau = 1/\kappa$ on which light can be trapped inside the cavity, usually expressed as the cavity quality factor $Q = \omega/\kappa$. A detailed discussion of the quality factor and strategies to optimize it are provided in Sec. 2.2.4.

Analogues to bulk modes, the various defect modes can be classified according to their symmetry properties. In the particular example of Fig. 2.3b all observed cavity modes are TE-like, as no band gap exists for TM polarization. Furthermore, the modes can be distinguished as odd or even with respect to the x-z mirror plane, indicated by filled or open circles in Fig. 2.3b, respectively. A complete analysis of the mode profiles and symmetry properties of the different L3 cavity modes is given in conjunction with the experimental investigation in Sec. 2.4.

Line defect: W1 waveguide

The W1 photonic crystal waveguide [45] is created by removing an entire line of holes from the periodic hexagonal lattice, as is shown in Fig. 2.4a. Similar to the case of the L3 cavity, bulk modes from the upper band are pulled down into the band gap due to the local increase of the dielectric constant, forming defect modes. Again, these modes are confined in the y and z direction by the photonic band gap effect and total internal reflection, respectively. Contrary to cavity modes, however, there is a translational symmetry in x direction which allows the waveguide modes to propagate freely along the line defect. Consequently, they are not standing waves anymore but traveling ones and thus exhibit dispersion, as can be seen from the projected band structure $\omega(k_x)$ in Fig. 2.4b.

Furthermore, the translational symmetry in x direction imposes that the wave vector component k_x is a conserved quantity [32]. This means that waveguide modes are intrinsically lossless and can, in principle, be guided indefinitely as long as the waveguide exhibits no bends or other distortions which lift the translational symmetry. However, this is only true for a system with mirror symmetry in z direction, for which TE-like and TM-like modes are decoupled. The presence of a substrate, e.g, would induce coupling between both polarizations and thus destroy the lossless guiding of the waveguide modes, since there is no band gap for TM polarization.

A deeper analysis of the band structure in Fig. 2.4b reveals that actually two different kinds of waveguide modes exist [46]: those which lie completely below the light cone as well as below the continuum of bulk modes (indicated as darker and lighter gray shaded areas in Fig. 2.4b, respectively) and those which have frequencies within the band gap. The former are entirely guided by total internal reflection and

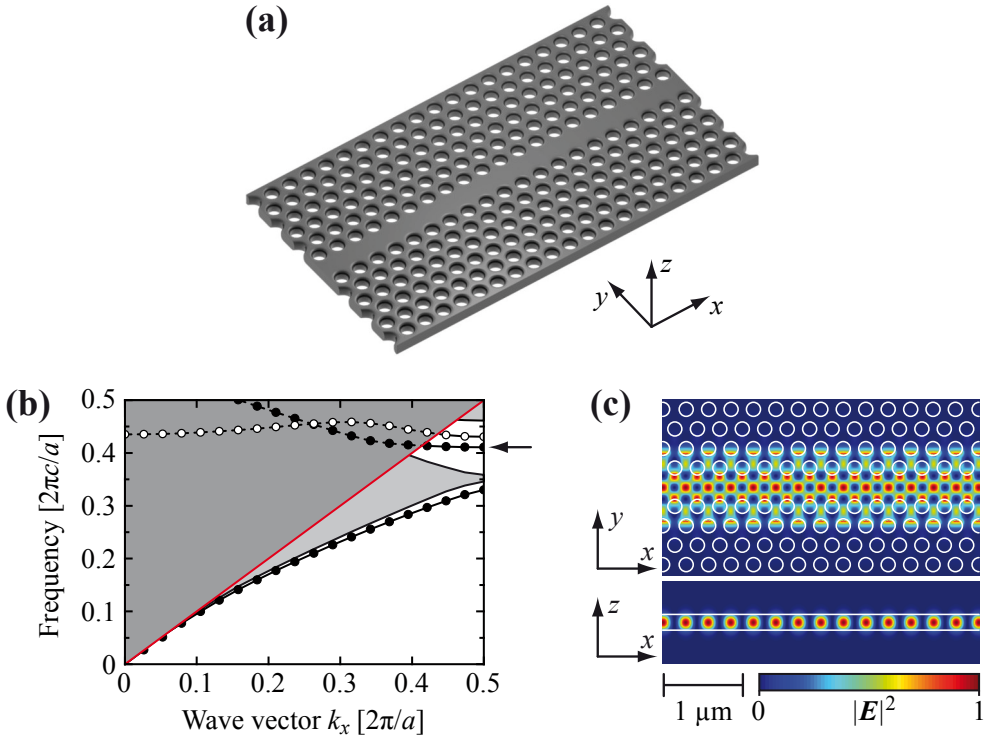

Figure 2.4: **(a)** Illustration of a photonic crystal slab hosting a W1 waveguide, created by omitting a complete line of holes. **(b)** Calculated projected band structure of the W1 waveguide shown in (a). All lattice parameters are the same as in Fig. 2.2b. Only TE-like modes are shown for clarity. Lighter gray shaded areas represent a continuum of bulk modes, filled/open circles denote odd/even waveguide modes (with respect to the y direction), and the red line indicates the light line with a continuum of extended states above (darker gray shaded area). **(c)** Calculated electric field intensity distribution $|\boldsymbol{E}|^2$ of the fundamental gap-guided W1 waveguide mode, indicated by an arrow in (b). Displayed are cross sections through the central x-y and x-z planes of the waveguide.

therefore termed index-guided modes. The latter are denoted as gap-guided modes and rely on a combination of photonic band gap effect (in the lateral direction) and total internal reflection (in the vertical direction) as described above. As an example, the mode profile of the fundamental gap-guided mode is displayed in Fig. 2.4c.

In addition to the distinct guiding mechanisms, index- and gap-guided modes also differ in their behavior at the edge of the Brillouin zone. While index-guided modes always have a finite group velocity $v_x = \mathrm{d}\omega/\mathrm{d}k_x$, the dispersion relation becomes flat at $k_x = \pi/a$ for gap-guided modes (see Fig. 2.4b) and thus v_x tends to zero [47]. This so-called slow light effect considerably increases the interaction of the waveguide mode with the surrounding material, which can be exploited, e.g., to enhance nonlinear effects [48] or to boost the coupling to incorporated (quantum) emitters [49]. However, in any practical application the achievable reduction of the group velocity is inherently limited by fabrication disorder [50].

Modulated line defect: double-heterostructure cavity

After having introduced the basic concepts and optical properties of point and line defects, a third type of defect structure shall now be discussed, which represents a combination of both. This so-called modulated line defect consists of a waveguide whose geometry is locally distorted to form an optical potential well. In other words, the optical properties of a certain section of the waveguide are altered such that it supports optical modes which are not allowed to propagate in the adjacent waveguide sections. Consequently, localized cavity modes are formed in addition to the propagating waveguide modes.

Many different ways to realize such an optical potential well exist, e.g., by shifting adjacent holes [51, 52], altering the hole radii [53], infiltrating the holes with liquids or other materials [54–56], or locally changing the refractive index of the photonic

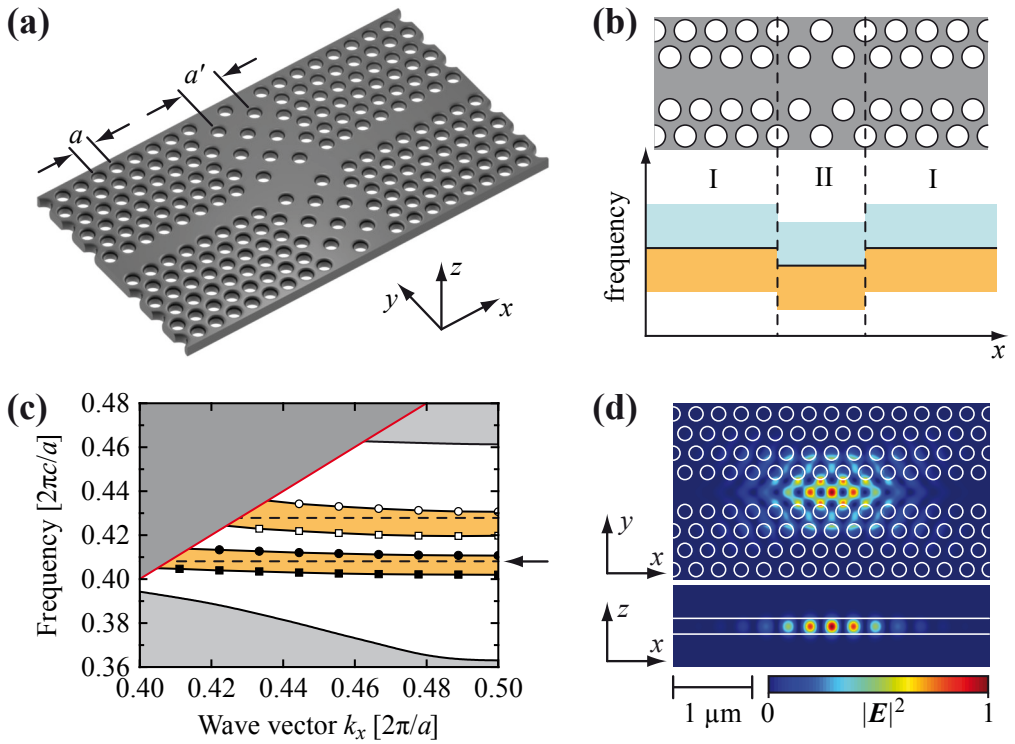

Figure 2.5: **(a)** Illustration of a double-heterostructure cavity, created by locally modulating a W1 waveguide. **(b)** Schematic representation of the optical potential well formed by the double-heterostructure. **(c)** Zoom into the projected band structure of a W1 waveguide. All lattice parameters and plot details are the same as in Fig. 2.4b, except that in addition to the guided modes of a waveguide with lattice constant a (circles) those of a waveguide with lattice constant $a' = 1.037a$ are also displayed (squares). The frequency gap between these modes in lattice sections I and II, respectively, is indicated in orange and the spectral position of the resulting cavity modes is marked by dashed lines. **(d)** Calculated electric field intensity distribution $|\boldsymbol{E}|^2$ of the fundamental double-heterostructure cavity mode, indicated by an arrow in (c). Displayed are cross sections through the central x-y and x-z planes of the cavity.

crystal slab itself [57]. Here, a specific type of modulated line defect is investigated, namely the so-called double-heterostructure cavity [58]. As illustrated in Fig. 2.5a, it consists of a W1 waveguide whose lattice constant a is increased to $a' > a$ over two lattice periods in x direction. In y direction a is retained to ensure lattice matching of the different waveguide sections. The increase of the lattice constant induces a shift of the entire photonic band structure (including the waveguide modes) to lower frequencies [59], as is schematically shown in Fig. 2.5b. There, the solid black curve represents the fundamental gap-guided waveguide mode (see also Fig. 2.4b), which divides the band structure into two regions: the transmission band at higher frequencies (indicated in light blue), where guided modes exist, and the so-called mode gap at lower frequencies (indicated in orange), where no transmission through the waveguide is possible [60]. Consequently, the frequency of the fundamental mode in lattice section II (with lattice constant a') lies within the mode gap region of lattice section I (with lattice constant a), where it is not allowed to propagate. Hence, an optical potential well is formed.

For a more quantitative analysis a zoom into the projected band structure of Fig. 2.4b is shown in Fig. 2.5c, displaying the two gap-guided waveguide modes as they exist in the unmodified section I. In addition, the corresponding modes for a waveguide with a modified lattice constant $a' = 1.037a$ are depicted, as they would exist in section II if the latter was infinitely long. However, due to the small spatial extend of the potential well, discrete cavity modes (indicated by dashed lines in Fig. 2.5c) with frequencies between those of the pure section I and section II waveguide modes are formed. Thereby, the separation in frequency to the corresponding section I mode increases with increasing ratio a'/a.

The mode profile of the fundamental cavity mode is displayed in Fig. 2.5d. It is spatially confined by three different mechanisms: total internal reflection in z direction, the photonic band gap effect in y direction, and the mode gap effect in x direction. The latter causes the cavity mode to decay exponentially into the adjacent waveguide sections I with very short decay lengths on the order of the lattice constant [61]. Strictly speaking, there is only a complete mode gap below the fundamental waveguide mode, where no other guided modes exist. However, cavity resonances can occur near all stationary points in the band structure (such as the second order mode shown in Fig. 2.5c) where no modes with similar wave vector components (and matching frequency) are available [62]. A complete analysis of the various resonances occurring in this system is given in conjunction with the experimental investigation in Sec. 2.5.

As a concluding remark it should be mentioned that the main advantage of modulated line defects compared to simple point defects lies in the much higher quality factor Q achievable in these systems. For example, values of $\approx 10^6$ have

been reported for double-heterostructure cavities made from silicon [52, 58], while corresponding L3 cavities in the same material system were limited to quality factors $Q \approx 10^5$ [63]. The physical reasons for these differences and ways to exploit them for optimization purposes are discussed next.

2.2.4 Optimization strategies for photonic crystal cavities

It was already pointed out in Sec. 2.2.3 that the spatial localization of cavity modes in photonic crystal slabs leads to optical losses through coupling to radiation modes in the light cone. This is an inevitable consequence of the two-dimensional nature of planar photonic crystals and could, in principle, be lifted by using a full three-dimensional photonic crystal structure with an omnidirectional band gap. However, the latter imposes extremely challenging demands on fabrication and handling methods [64–66], being the reason why most practical implementations so far mainly rely on planar systems. As a result the exploration of techniques to optimize the cavity design and to reduce radiation losses has been subject of intense research in recent years [43, 44, 63, 67–70]. In the following, after introducing the relevant cavity parameters which have to be considered in any optimization, the most important design rules (known to date) are reviewed.

Relevant cavity parameters

When optimizing the optical properties of a photonic crystal cavity, various parameters and figures of merit have to be taken into account, depending on the specific application. The most important one is the quality factor Q, which is a measure for the optical losses of the cavity and can be expressed in different (equivalent) ways:

$$Q = \frac{\omega_\mathrm{c} U}{P} = \frac{\omega_\mathrm{c}}{\kappa} = \frac{\omega_\mathrm{c}}{\Delta\omega} \,. \tag{2.16}$$

Here, ω_c is the frequency of a particular cavity mode and U is the electromagnetic energy stored in this mode, defined as

$$U = \frac{1}{2} \int\limits_V \mathrm{d}\boldsymbol{r} \left[\varepsilon_0 \varepsilon(\boldsymbol{r}) \left|\boldsymbol{E}(\boldsymbol{r})\right|^2 + \mu_0 \mu(\boldsymbol{r}) \left|\boldsymbol{H}(\boldsymbol{r})\right|^2 \right] . \tag{2.17}$$

P denotes the corresponding loss power, i.e., the amount of energy leaking from the cavity per cycle $T = 2\pi/\omega_\mathrm{c}$. This energy loss leads to a decaying field intensity

$$I(t) = I_0 \mathrm{e}^{-\kappa t} \,, \tag{2.18}$$

with κ being the loss rate. The shape of the cavity resonance in frequency space is then determined by the Fourier transformation of the time-varying cavity field,

yielding a Lorentzian spectral intensity distribution

$$I(\omega) = I_0 \frac{\kappa/2}{(\omega - \omega_\mathrm{c})^2 + (\kappa/2)^2} = I_0 \frac{\Delta\omega/2}{(\omega - \omega_\mathrm{c})^2 + (\Delta\omega/2)^2} \ . \tag{2.19}$$

Thus, κ is equivalent to the FWHM (full-width half-maximum) value $\Delta\omega$ of the resonance peak, justifying the last expression on the right hand side of Eq. (2.16).

For planar photonic crystals the loss power P can be divided into two contributions, namely in-plane losses $P_\parallel$, occurring due to the coupling to guided modes in the slab, and out-of-plane losses $P_\perp$, caused by coupling to radiative modes within the light cone. Consequently, $P = P_\parallel + P_\perp$ and from Eq. (2.16) it follows that the quality factor Q can also be decomposed into contributions $Q_\parallel$ and $Q_\perp$, related by

$$\frac{1}{Q} = \frac{1}{Q_\parallel} + \frac{1}{Q_\perp} \ . \tag{2.20}$$

The in-plane component $Q_\parallel$ is mainly a function of the number N of hole layers surrounding the cavity and can, in principle, be made arbitrarily large by adding more layers, since $Q_\parallel$ increases exponentially with N. Therefore, its contribution in Eq. (2.20) vanishes and $Q \approx Q_\perp$ is predominantly determined by out-of-plane losses, which is in deed the case in most practical applications. Then, in order to maximize Q and minimize cavity losses, the main task lies in reducing the coupling to radiative free-space modes [44], as is discussed below.

The second important cavity parameter is the effective mode volume V_eff, which is a measure for the spread of the mode energy U in space or, correspondingly, for the localization of light within the area of the cavity. For dielectric cavities it is usually defined as the integral of the electric field intensity over the entire relevant volume, normalized to the field maximum:

$$V_\mathrm{eff} = \frac{\int_V \mathrm{d}\boldsymbol{r}\, \varepsilon(\boldsymbol{r}) \left|\boldsymbol{E}(\boldsymbol{r})\right|^2}{\max\left\{\varepsilon(\boldsymbol{r}) \left|\boldsymbol{E}(\boldsymbol{r})\right|^2\right\}} \ . \tag{2.21}$$

V_eff is often expressed in units of the cubic wavelength $(\lambda/n)^3$, where n is the refractive index of the cavity material. Due to the diffraction limit the field localization in a dielectric cavity is inherently limited to values $V_\mathrm{eff} \approx 0.25\ (\lambda/\mathrm{n})^3$ [71]. However, much smaller effective mode volumes can be obtained in metallic cavities [72], although the definition in Eq. (2.21) may become inappropriate in these cases and care has to be taken when interpreting the corresponding results. This issue becomes relevant for plasmonic-photonic hybrid cavities and is discussed in more detail in Sec. 3.6.

Q and V_{eff} are the key parameters for a large number of applications, as they represent the spectral and spatial confinement of the electromagnetic energy density. For an efficient emitter-cavity coupling (see Sec. 2.2.5), one either desires to maximize the ratio Q/V_{eff} (in the weak coupling regime) [18] or $Q/\sqrt{V_{\text{eff}}}$ (in the strong coupling regime) [16], while for nonlinear optical effects Q^2/V_{eff} is the relevant figure of merit [73]. Consequently, both quantities, Q and V_{eff}, should always be taken into account simultaneously when optimizing a particular cavity design.

Fourier space analysis of cavity loss

Contrary to other types of optical microcavities (such as microspheres, -toroids, or -pillars [74]), the effective mode volume of most photonic crystal cavity designs is inherently very small (on the order of the cubic wavelength) and therefore offers only limited scope for optimization. On the other hand, there is much room for improvement with regard to the cavity loss (and thus Q) by reducing the out-of-plane coupling to radiative modes in the light cone, as stated above. To do so, one requires knowledge on the distribution of wave vectors $\boldsymbol{k}$ which contribute to a specific cavity mode [44]. Within this distribution all wave vectors with a parallel component $|\boldsymbol{k}_{\parallel}| \leq 2\pi/\lambda$ (i.e., lying inside the light cone) can couple to radiative modes because the conservation law for $|\boldsymbol{k}_{\parallel}|$ is fulfilled at the interface between the photonic crystal slab and the surrounding air. Here, λ is the free-space wavelength of the cavity mode. In contrast, if $|\boldsymbol{k}_{\parallel}| > 2\pi/\lambda$, the conservation law does no longer hold at the interface and the light becomes confined to the slab due to total internal reflection.

The wave vector distribution $\tilde{f}(\boldsymbol{k})$ can be obtained by applying a spatial Fourier transformation

$$\mathcal{F}(f) = \tilde{f}(\boldsymbol{k}) = \int \mathrm{d}\boldsymbol{r}\, f(\boldsymbol{r}) \mathrm{e}^{i\boldsymbol{k}\boldsymbol{r}} \tag{2.22}$$

to the field distribution $f(\boldsymbol{r})$. This is exemplified in Fig. 2.6 for three model functions, representing cavity modes with an effective mode index $n_{\text{eff}} = 2$ and a resonance wavelength $\lambda_{\text{c}} = \lambda/n_{\text{eff}}$. These model functions illustrate some of the general tendencies concerning cavity losses. If the spatial extend of the mode profile is rather broad (Fig. 2.6a), the corresponding wave vector distribution (Fig. 2.6d) is relatively narrow and vanishes inside the region of the light cone, i.e., no coupling to radiative modes can occur. By squeezing the cavity mode into smaller volumes (Fig. 2.6b), the k_x distribution (Fig. 2.6e) broadens due to the stronger spatial confinement and some overlap with the light cone arises. Consequently, a reduction of the mode volume is usually accompanied by an increase of out-of-plane losses, unless compensated by other mechanisms (discussed below).

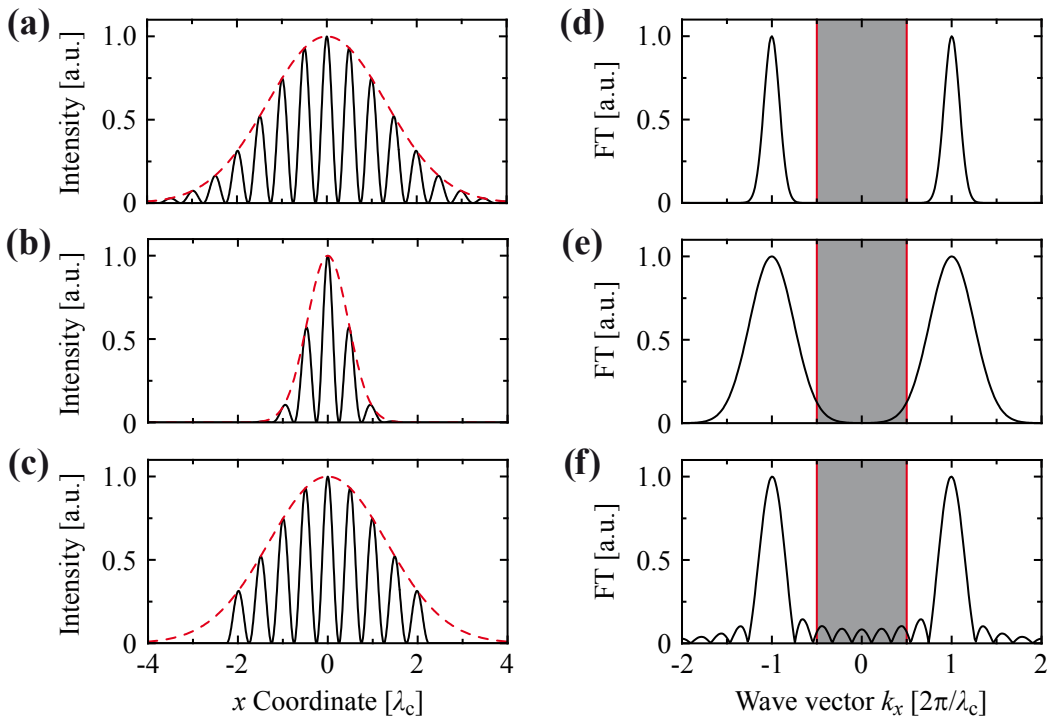

Figure 2.6: **(a–c)** Spatial intensity distribution (black curves) of various localized optical modes with wavelength $\lambda_c = \lambda/2$ and Gaussian envelopes (dashed red curves), having either a broad (a) or narrow (b) extend in space. In (c) the otherwise Gaussian mode profile is truncated at both sides. **(d–f)** Fourier transformation (FT) of the respective mode profiles in (a–c). The gray shaded areas (enclosed by red lines) represent the light cone $k_x \leq 2\pi/\lambda$, in which coupling to radiative free-space modes is allowed.

However, a large mode volume does not necessarily imply low losses. If the Gaussian mode profile in Fig. 2.6a is disturbed by truncating it at both sides (Fig. 2.6c), the resulting wave vector distribution (Fig. 2.6f) exhibits multiple side lobes within the light cone, considerably increasing the coupling to radiative modes. From a mathematical point of view this is a consequence of the abrupt change in the spatial function, which requires a large number of additional k_x components in the Fourier series to accurately model the mode profile. Therefore, a smooth decay of the cavity mode into the surrounding structure is desired to minimize out-of-plane losses [43, 63]. A Gaussian envelope function is particularly appealing for this purpose, as it again translates into a well-localized Gaussian wave vector distribution.

Optimization strategies

Based on the insight gained from the Fourier analysis, the strategy for optimizing the cavity design is straightforward. Obviously, the spatial mode profile has to be engineered such that the fraction of wave vectors lying within the leaky region of the associated k-space distribution is minimized. This can be achieved by modifying the

local dielectric environment of the defect, e.g, by shifting adjacent holes or changing their size, thereby shaping the field pattern. The impact of this spatial modification on the wave vector distribution is manifold, as already became apparent from the discussion of Fig. 2.6. In the following, the mechanisms for optimizing the quality factor Q shall be investigated in more detail for the practical example of the L3 cavity design (see Sec. 2.2.3).

In order to perform a quantitative analysis of the radiative cavity loss, the field profile directly above the surface of the photonic crystal slab has to be calculated (Fig. 2.7a), from which the corresponding wave vector distribution is found via a two-dimensional spatial Fourier integral over a sufficiently large area A around the cavity:

$$\mathcal{F}_2(f) = \tilde{f}(k_x, k_y) = \iint\limits_A \mathrm{d}x\,\mathrm{d}y\, f(x,y)\mathrm{e}^{i(k_x x + k_y y)} \; . \tag{2.23}$$

In principle, all information on the far-field radiation pattern (and thus on the loss power P) is contained in the Fourier transformation of the near-field components E_x, E_y, H_x, and H_y. However, it can be shown [70] that the evaluation of the fields E_z and H_z gives equivalent results, yielding an expression for P of the form

$$\begin{aligned} P &\propto \iint\limits_{|\boldsymbol{k}_\parallel|\leq|\boldsymbol{k}|} \mathrm{d}k_x\,\mathrm{d}k_y\, \frac{k_z}{|\boldsymbol{k}_\parallel|^2}\left[\varepsilon_0\left|\mathcal{F}_2(E_z)\right|^2 + \mu_0\left|\mathcal{F}_2(H_z)\right|^2\right] \\ &= \iint\limits_{|\boldsymbol{k}_\parallel|\leq|\boldsymbol{k}|} \mathrm{d}k_x\,\mathrm{d}k_y\, \frac{k_z}{|\boldsymbol{k}_\parallel|^2} K^2(k_x, k_y) \; . \end{aligned} \tag{2.24}$$

Here, $|\boldsymbol{k}_\parallel|^2 = k_x^2 + k_y^2$ and $|\boldsymbol{k}| = 2\pi/\lambda$. The calculated Fourier spectrum $K(k_x, k_y)$ for the unmodified L3 cavity is shown in Fig. 2.7e. The main $|\boldsymbol{k}_\parallel|$ contribution is localized near the edges of the Brillouin zone, but there is also a considerable amplitude inside the light cone. To reduce this fraction of leaky $|\boldsymbol{k}_\parallel|$ components, different mechanisms can be exploited.

Delocalization Omitting more holes from the defect or shifting adjacent holes outwards increases the spatial extend of the cavity mode, thus reducing the spread of the $|\boldsymbol{k}_\parallel|$ distribution and the overlap with the light cone (see Fig. 2.6). However, this is always accompanied by a corresponding increase of the mode volume V_{eff} and care has to be taken not to decrease the appropriate figure of merit, e.g, Q/V_{eff}. In fact, the L3 cavity design already represents a suitable tradeoff between Q and V_{eff}, because the increase in the mode volume from a simple one-hole defect to a three-hole defect structure is modest compared to the large improvement in the quality factor.

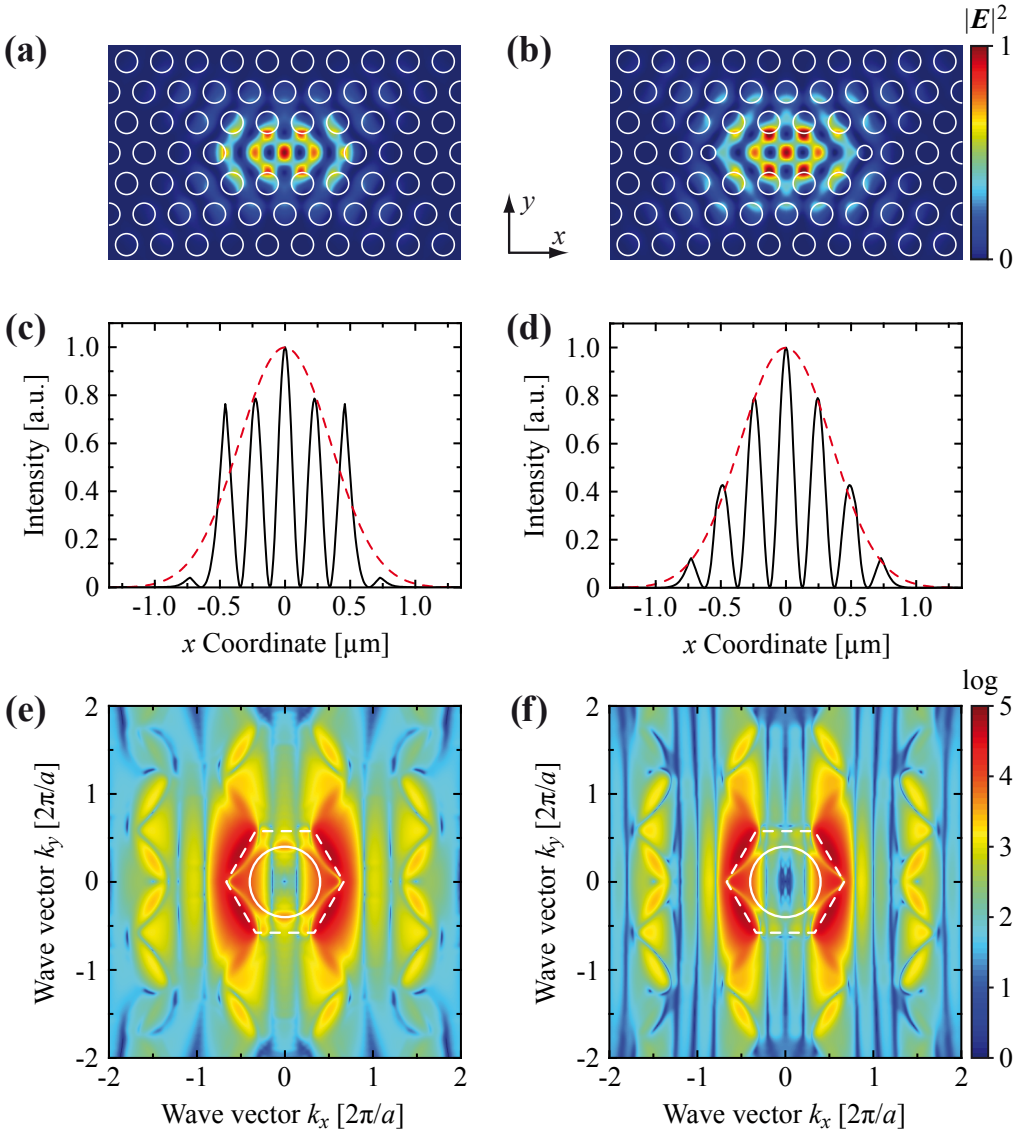

Figure 2.7: **(a,b)** Calculated electric field intensity distributions $|\boldsymbol{E}|^2$ (above the surface of the photonic crystal slab) of the fundamental cavity mode of an unmodified (a) and optimized (b) L3 cavity, respectively. The lattice parameters are $a = 270$ nm, $t = 0.93a$, and $r = 0.3a$. **(c,d)** Corresponding plots of the intensity profiles (black) along the central x axis. The dashed red curves represent an idealized Gaussian envelope function. **(e,f)** Two-dimensional spatial Fourier spectra $K(k_x, k_y)$ obtained from the mode profiles shown in (a) and (b), respectively. The solid white circles indicate the light cone, while the dashed white lines represent the irreducible Brillouin zone. Note the logarithmic color scale.

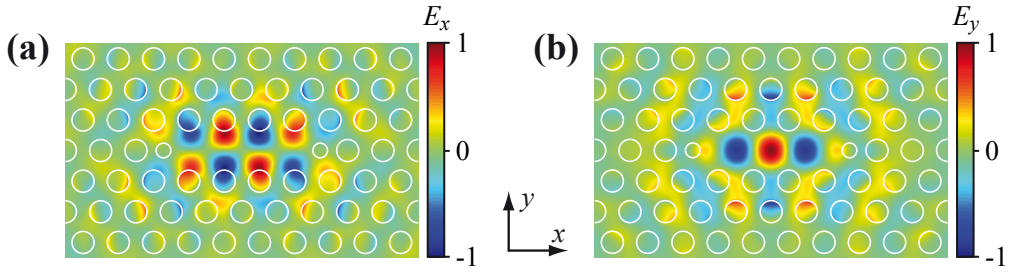

Figure 2.8: Calculated electric field components **(a)** E_x and **(b)** E_y of the fundamental (optimized) L3 cavity mode as shown in Fig. 2.7b.

Gentle confinement A much more efficient way of increasing Q is by engineering the spatial mode profile such that it resembles a Gaussian envelope function (see Fig. 2.6). As can be seen from Fig. 2.7c, there is a strong mismatch between this (idealized) Gaussian envelope and the actual intensity pattern of the fundamental L3 cavity mode. A considerable improvement is readily achieved by reducing the radius of the two outer holes and shifting them outwards (Fig. 2.7b), leading to a much smoother, Gaussian-like decay of the mode into the surrounding structure (Fig. 2.7d). In the corresponding Fourier spectrum (Fig. 2.7f) a strong suppression of leaky $|\boldsymbol{k}_{\parallel}|$ components inside the light cone is observed, which is mostly attributed to the smoother envelope function and only marginally to the slightly increased mode volume. This gentle mode confinement is the main reason why double-heterostructure cavities can exhibit much higher quality factors then corresponding L3 cavities (see Sec. 2.2.3), as the complete absence of holes along the waveguide leads to a very smooth decay of the field intensity in x direction and thus to a strong reduction of radiation losses.

Cancelation Another mechanism which can cause a suppression of cavity losses and has not been discussed yet is the effect of cancelation in the far-field [67]. Whenever certain components of the light radiated from the cavity have opposite phase, they interfere destructively in the far-field and, therefore, do not contribute to the loss power P. In Fourier space this is equivalent to an elimination of the corresponding wave vectors within the light cone. Such a cancelation occurs if the spatial mode profile meets certain symmetry criteria [44], as is the case, e.g., for the E_x component of the fundamental L3 cavity mode (Fig. 2.8a). Although the spatial distribution of E_x is not smooth in y direction (which should induce strong radiation losses), the overall contribution of this field component to the loss power P is very small. The reason is that the corresponding fields above and below the central x axis have opposite phase and thus cancel each other in the far-field to a large extend. In contrast, the respective E_y component (Fig. 2.8b) does not exhibit such symmetry properties and is therefore the main source for radiation losses in this type of cavity.

As becomes apparent from these considerations, the total quality factor of a particular cavity design is determined by a large number of factors and depends sensitively on the exact cavity geometry. Slight changes in the defect structure can significantly alter the radiation loss due to one or several of the mechanisms described above, requiring a careful theoretical analysis of the modal properties to determine the optimal design strategy. The concept of gentle confinement, e.g., plays the dominant role in the optimization of the L3 cavity design in Sec. 2.4.2, while the cancelation effect becomes important in the discussion of particle-loaded cavities in Sec. 3.5.2.

2.2.5 Quantum electrodynamics in photonic crystal cavities

So far, the discussion of photonic crystal cavities primarily focused on their intrinsic optical properties, i.e., without regarding any interaction with light emitters or other types of (external) materials. This shall now be supplemented by considering the interplay between such emitters and the electromagnetic field in an optical cavity in the framework of quantum electrodynamics (QED). A review of the foundations of QED, which goes beyond the scope of this thesis, can, e.g., be found in Refs. [75, 76].

In the following, the electromagnetic field is treated in its quantized form and the emitters are modeled as atom-like systems with discrete energy levels. For simplicity, the basic principles of the resulting light-matter interaction are investigated for the case of a single quantum emitter coupled to a single cavity mode. This so-called Jaynes-Cummings model [77] allows for the deduction of important parameters of the coupled emitter-cavity system and their values necessary for certain applications. Furthermore, the analysis serves as a foundation for the interpretation of the experimental results in Sec. 2.4.

Interaction of a single quantum emitter with a single cavity mode

As a starting point the cavity mode is assumed to be in the (vacuum) ground state with energy $\hbar\omega_\mathrm{c}/2$. Then, an integration of the cavity field $\boldsymbol{E}_\mathrm{c}(\boldsymbol{r})$ over the entire quantization volume V has to satisfy

$$\int\limits_V \mathrm{d}\boldsymbol{r}\, \varepsilon_0\varepsilon(\boldsymbol{r})\big|\boldsymbol{E}_\mathrm{c}(\boldsymbol{r})\big|^2 = \frac{\hbar\omega_\mathrm{c}}{2}\ . \tag{2.25}$$

Using the definition of the effective mode volume V_eff in Eq. (2.21), this can be rewritten as

$$\varepsilon_0\varepsilon(\boldsymbol{r}_\mathrm{m})\big|\boldsymbol{E}_\mathrm{c}(\boldsymbol{r}_\mathrm{m})\big|^2 V_\mathrm{eff} = \frac{\hbar\omega_\mathrm{c}}{2}\ , \tag{2.26}$$

where $\boldsymbol{r}_\mathrm{m}$ denotes the point of maximum $\varepsilon(\boldsymbol{r})\big|\boldsymbol{E}_\mathrm{c}(\boldsymbol{r})\big|^2$. Consequently, the peak amplitude of the vacuum cavity field is given by [75]

$$\big|\boldsymbol{E}_\mathrm{c}(\boldsymbol{r}_\mathrm{m})\big| = \sqrt{\frac{\hbar\omega_\mathrm{c}}{2\varepsilon_0\varepsilon(\boldsymbol{r}_\mathrm{m})V_\mathrm{eff}}}\,, \tag{2.27}$$

which is related to the field amplitude at an arbitrary position $\boldsymbol{r}$,

$$\big|\boldsymbol{E}_\mathrm{c}(\boldsymbol{r})\big| = \sqrt{\frac{\xi(\boldsymbol{r})\hbar\omega_\mathrm{c}}{2\varepsilon_0\varepsilon(\boldsymbol{r})V_\mathrm{eff}}}\,, \tag{2.28}$$

via the ratio $\xi(\boldsymbol{r})$ of the respective electric field energy densities:

$$\xi(\boldsymbol{r}) = \frac{\varepsilon(\boldsymbol{r})\big|\boldsymbol{E}_\mathrm{c}(\boldsymbol{r})\big|^2}{\varepsilon(\boldsymbol{r}_\mathrm{m})\big|\boldsymbol{E}_\mathrm{c}(\boldsymbol{r}_\mathrm{m})\big|^2}\,. \tag{2.29}$$

Next, the coupling of a single two-level quantum emitter (at position $\boldsymbol{r}$) to the cavity mode is considered. The emitter is assumed to be initially in its excited state $|e\rangle$ from which it can decay into the ground state $|g\rangle$ via spontaneous emission of a photon of energy $\hbar\omega$. The corresponding transition dipole moment is given by $\boldsymbol{\mu} = q\langle e|\boldsymbol{d}|g\rangle$, with q being the unit charge and $\boldsymbol{d}$ denoting the coordinate operator. The coupled emitter-cavity system can be described by the Jaynes-Cummings Hamiltonian [77]

$$H = H_\mathrm{em} + H_\mathrm{cav} + H_\mathrm{int}\,, \tag{2.30}$$

where

$$H_\mathrm{em} = \hbar\omega\hat{\sigma}_+\hat{\sigma}_- \qquad \text{and} \qquad H_\mathrm{cav} = \hbar\omega_\mathrm{c}\left(\hat{a}^\dagger\hat{a} + \frac{1}{2}\right) \tag{2.31}$$

are the Hamiltonians of the emitter (in free space) and of the cavity (without emitter), respectively. $\hat{\sigma}_+ = |e\rangle\langle g|$ and $\hat{\sigma}_- = |g\rangle\langle e|$ are the raising and lowering operators of the emitter, while $\hat{a}^\dagger$ and $\hat{a}$ denote the photon creation and annihilation operators of the cavity field, respectively. The third term in Eq. (2.30) describes the interaction between the emitter and the cavity and (in the dipole and rotating wave approximation [75]) is given by

$$\begin{aligned} H_\mathrm{int} &= -i\boldsymbol{\mu}\cdot\boldsymbol{E}_\mathrm{c}(\boldsymbol{r})\,\left(\hat{\sigma}_+\hat{a} - \hat{a}^\dagger\hat{\sigma}_-\right) \\ &= -i\sqrt{\frac{\xi(\boldsymbol{r})\hbar\omega_\mathrm{c}|\boldsymbol{\mu}|^2}{2\varepsilon_0\varepsilon(\boldsymbol{r})V_\mathrm{eff}}}\,\left|\hat{\boldsymbol{\mu}}\cdot\hat{\boldsymbol{E}}_\mathrm{c}(\boldsymbol{r})\right|\,\left(\hat{\sigma}_+\hat{a} - \hat{a}^\dagger\hat{\sigma}_-\right)\,. \end{aligned} \tag{2.32}$$

Here, $\hat{\boldsymbol{\mu}}$ and $\hat{\boldsymbol{E}}_\mathrm{c}(\boldsymbol{r})$ denote the unit vectors of the transition dipole moment and of the cavity field, respectively. Note that if multiple optical modes are involved in the consideration, the expressions for H_cav and H_int have to be converted into a sum over all possible modes. By defining the coupling parameter

$$g(\boldsymbol{r}) = \frac{|\boldsymbol{\mu}|}{\hbar}\sqrt{\frac{\xi(\boldsymbol{r})\hbar\omega_\mathrm{c}}{2\varepsilon_0\varepsilon(\boldsymbol{r})V_\mathrm{eff}}}\,\left|\hat{\boldsymbol{\mu}}\cdot\hat{\boldsymbol{E}}_\mathrm{c}(\boldsymbol{r})\right| , \tag{2.33}$$

Eq. (2.32) takes the simple form

$$H_\mathrm{int} = -i\hbar g(\boldsymbol{r})\left(\hat{\sigma}_+\hat{a} - \hat{a}^\dagger\hat{\sigma}_-\right) . \tag{2.34}$$

In the same way as the Hamiltonian in Eq. (2.30) can be separated into three distinct contributions, the energy flow in the coupled emitter-cavity system can be described in terms of three rates (see Fig. 2.9a), namely the dipole excitation decay rate γ of the emitter, the field intensity decay rate κ of the cavity, and the emitter-cavity coupling rate $g(\boldsymbol{r})$ defined in Eq. (2.33). γ comprises all decay channels of the excitation energy other than coupling to the cavity mode, including emission into free-space modes as well as non-radiative processes. κ characterizes the losses of the cavity mode and is inherently linked to the quality factor Q of the cavity via Eq. (2.16). Depending on the ratio of the rates γ, κ, and $g(\boldsymbol{r})$, two major regimes can be distinguished in which the emitter is either said to be weakly or strongly coupled to the cavity mode [78], as is discussed in more detail in the following.

Weak coupling regime

If the coupling rate $g(\boldsymbol{r})$ is small compared to γ and/or κ, the system is said to be in the weak coupling regime. Typically, $g(\boldsymbol{r}) < \gamma \ll \kappa$. In this case, no coherent interaction between the emitter and the cavity field takes place, as the excitation energy is either directly dissipated (via γ) or, once transferred to the cavity mode, is lost to radiation modes (via κ). Therefore, the probability for repopulating the excited state $|e\rangle$ of the emitter is very low, leading to an irreversible exponential decay (see Fig. 2.9b). According to the Weisskopf-Wigner approximation [79], the spontaneous emission rate $\Gamma_\mathrm{c}(\boldsymbol{r},\omega)$ into the cavity mode can then be calculated from Fermi's golden rule [80]

$$\Gamma_\mathrm{c}(\boldsymbol{r},\omega) = \frac{2\pi}{\hbar}\left|\langle g|H_\mathrm{int}|e\rangle\right|^2\rho(\omega) = \frac{2\pi}{\hbar}\left|\boldsymbol{\mu}\cdot\boldsymbol{E}_\mathrm{c}(\boldsymbol{r})\right|^2\rho(\omega) , \tag{2.35}$$

where $\rho(\omega)$ is the corresponding density of optical states at the location of the emitter.

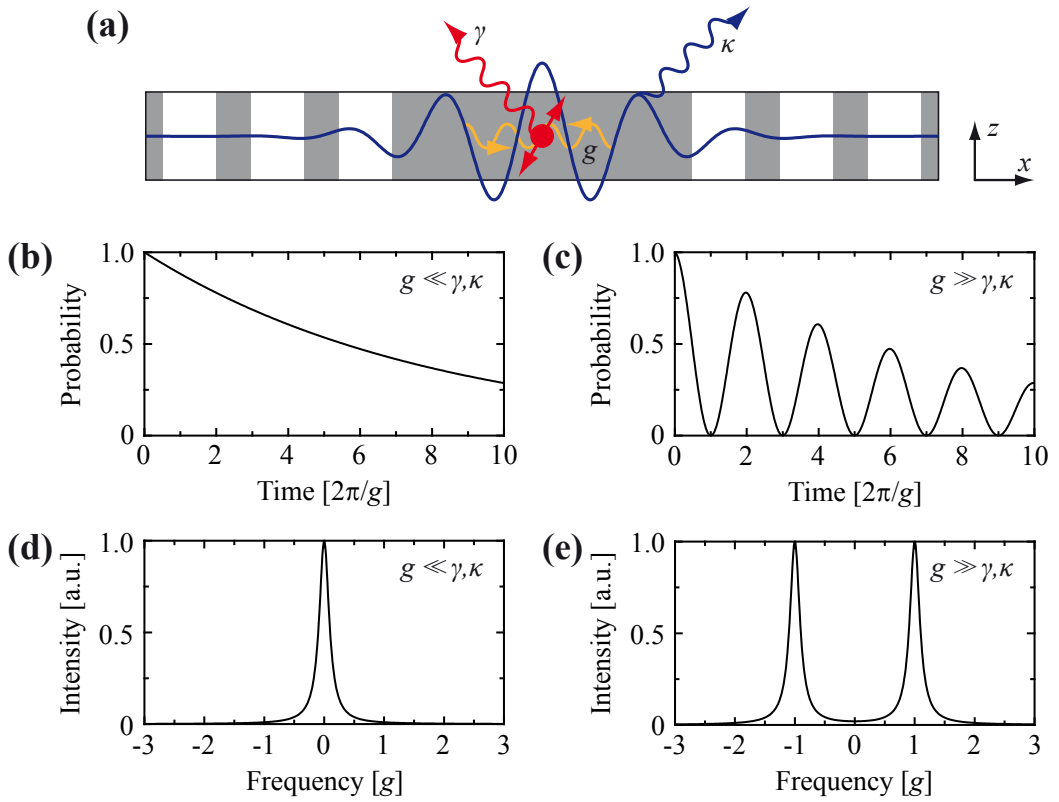

Figure 2.9: **(a)** Schematic illustration of the coupling between a dipole emitter (red) and a single cavity mode (blue) in a photonic crystal slab. The system is described by three rates, the dipole decay rate γ (red), the cavity decay rate κ (blue), and the emitter-cavity coupling rate g (orange). **(b,c)** Exemplary probability functions for the emitter to be in the excited state $|e\rangle$ in the case of weak (b) and strong coupling (c), respectively. **(d,e)** Exemplary cavity spectra for the case of weak (d) and strong coupling (e), respectively, assuming zero detuning between the emitter and the cavity (i.e., $\omega = \omega_c$).

In the case of a Lorentzian cavity spectrum [Eq. (2.19)], $\rho(\omega)$ takes the form

$$\rho(\omega) = \frac{1}{\pi\hbar} \frac{\Delta\omega/2}{(\omega - \omega_c)^2 + (\Delta\omega/2)^2} , \tag{2.36}$$

yielding the expression

$$\Gamma_c(\boldsymbol{r}, \omega) = \frac{2|\boldsymbol{\mu}|^2 Q}{\varepsilon_0 n^2(\boldsymbol{r}) \hbar V_{\text{eff}}} \frac{\xi(\boldsymbol{r}) \left|\hat{\boldsymbol{\mu}} \cdot \hat{\boldsymbol{E}}_c(\boldsymbol{r})\right|^2}{1 + 4Q^2(\omega/\omega_c - 1)^2} . \tag{2.37}$$

Here, Eqs. (2.16), (2.28), (2.29), and (2.35) were used as well as the relation $\varepsilon(\boldsymbol{r}) = n^2(\boldsymbol{r})$. The first factor on the right hand side of Eq. (2.37) represents the maximum emission rate for the ideal case of an emitter with transition frequency $\omega = \omega_c$, location $\boldsymbol{r} = \boldsymbol{r}_m$, and dipole moment orientation parallel to the corresponding electric field polarization $\hat{\boldsymbol{E}}_c(\boldsymbol{r})$. The second factor accounts for any spectral or spatial mismatch between the emitter and the cavity field.

It should be noted that the intrinsic bandwidth of the emitter is assumed to be much narrower than the width $\Delta\omega$ of the cavity resonance. However, if the emission bandwidth is comparable to or even broader than $\Delta\omega$, the Lorentzian mode density in Eq. (2.36) has to be convoluted with the respective emitter spectrum [81]. When multiple emitters with random locations and orientations are considered, $\xi(\boldsymbol{r})$ has to be substituted by the corresponding spatial average $\langle\xi(\boldsymbol{r})\rangle$ in Eq. (2.37) and the directional factor becomes $\langle|\hat{\boldsymbol{\mu}}\cdot\hat{\boldsymbol{E}}_\mathrm{c}(\boldsymbol{r})|^2\rangle \approx 1/3$ [81].

Fermi's golden rule can also be applied for the calculation of the spontaneous emission rate $\Gamma_0(\omega)$ in a homogeneous medium with refractive index n, for which the density of optical states is $\rho(\omega) = nV\omega^2/(\pi^2c^3)$, yielding [75]

$$\Gamma_0(\omega) = \frac{n|\boldsymbol{\mu}|^2\omega^3}{3\pi\varepsilon_0\hbar c^3}\,. \tag{2.38}$$

By normalizing $\Gamma_\mathrm{c}(\boldsymbol{r},\omega)$ to the respective rate in a homogeneous medium with $n = n(\boldsymbol{r})$, the so-called cavity Purcell factor [82]

$$F_\mathrm{c} = \frac{\Gamma_\mathrm{c}(\boldsymbol{r},\omega)}{\Gamma_0(\omega)} = \frac{6\pi c^3 Q}{n^3\omega^3 V_\mathrm{eff}}\,\frac{\xi(\boldsymbol{r})|\hat{\boldsymbol{\mu}}\cdot\hat{\boldsymbol{E}}_\mathrm{c}(\boldsymbol{r})|^2}{1+4Q^2(\omega/\omega_\mathrm{c}-1)^2} \tag{2.39}$$

is obtained, which is often also expressed as a function of the corresponding wavelength $\lambda = 2\pi c/\omega$:

$$F_\mathrm{c} = \frac{\Gamma_\mathrm{c}(\boldsymbol{r},\lambda)}{\Gamma_0(\lambda)} = \frac{3\lambda^3 Q}{4\pi^2 n^3 V_\mathrm{eff}}\,\frac{\xi(\boldsymbol{r})|\hat{\boldsymbol{\mu}}\cdot\hat{\boldsymbol{E}}_\mathrm{c}(\boldsymbol{r})|^2}{1+4Q^2(\lambda/\lambda_\mathrm{c}-1)^2}\,. \tag{2.40}$$

As the total decay rate of the emitter is given by $\Gamma = \Gamma_\mathrm{c} + \gamma$ [18], a Purcell factor $F_\mathrm{c} > 1$ means that the spontaneous emission is dominated by the corresponding rate Γ_c into the cavity mode. The accompanied emission enhancement scales with Q/V_eff, again highlighting the role of large quality factors and small mode volumes. In the case of a very large Purcell factor $F_\mathrm{c} \gg 1$, almost the entire excitation energy is converted into photons in the cavity mode and the spontaneous emission coupling factor [78]

$$\beta = \frac{\Gamma_\mathrm{c}}{\Gamma_\mathrm{c}+\gamma} = \frac{\Gamma_\mathrm{c}/\Gamma_0}{\Gamma_\mathrm{c}/\Gamma_0+\gamma/\Gamma_0} \approx \frac{F_\mathrm{c}}{F_\mathrm{c}+1} \tag{2.41}$$

reaches values close to unity. This, however, is only true as long as $g(\boldsymbol{r}) < \gamma, \kappa$. Beyond this condition the spontaneous emission process becomes reversible, i.e., there is a non-vanishing probability that the excited state $|e\rangle$ is repopulated, marking the onset of strong coupling.

Strong coupling regime

If the coupling rate $g(\boldsymbol{r})$ is larger than both, γ and κ, the time scale on which the emitter interacts coherently with the cavity field is shorter than that of any energy dissipating process. Instead of an irreversible decay of the excited state $|e\rangle$ of the emitter (as in the weak coupling regime), an oscillatory behavior arises due to a partial repopulation of $|e\rangle$, i.e., the excitation energy is transferred back and forth between the emitter and the cavity field (see Fig. 2.9c). Then, the emitter and the cavity can no longer be described separately by individual quantum states, but form a set of common eigenstates (so-called dressed states) [83]. In this case, the perturbative approach used above to derive the properties of the system in the weak coupling regime is not valid anymore. Instead, the master equation for the density matrix of the emitter-cavity system has to be solved [84], yielding an expression for the frequencies $\Omega_\pm$ and the corresponding linewidths $\Gamma_\pm$ of the common eigenstates of the form [17]

$$\Omega_\pm - \frac{i}{2}\Gamma_\pm = \frac{1}{2}(\omega_\mathrm{c} + \omega) - \frac{i}{4}(\gamma + \kappa) \pm \sqrt{g^2(\boldsymbol{r}) + \frac{1}{4}\left[(\omega_\mathrm{c} - \omega) - \frac{i}{2}(\gamma - \kappa)\right]^2} \,. \tag{2.42}$$

At zero detuning ($\omega = \omega_\mathrm{c}$) this simplifies to

$$\Omega_\pm - \frac{i}{2}\Gamma_\pm = \omega_\mathrm{c} - \frac{i}{4}(\gamma + \kappa) \pm \sqrt{g^2(\boldsymbol{r}) - \frac{1}{16}(\gamma - \kappa)^2} \,. \tag{2.43}$$

From Eq. (2.43) it follows that for $g(\boldsymbol{r}) > |\gamma - \kappa|/4$ the spectrum of the system consists of a doublet of lines (see Fig. 2.9e) instead of a single line as in the weak coupling case $g(\boldsymbol{r}) \leq |\gamma - \kappa|/4$ (see Fig. 2.9d). This so-called Rabi splitting is characteristic for the strong coupling regime and corresponds to an anti-crossing behavior of the individual lines of the emitter and the cavity, respectively, when tuned relative to each other in frequency [16, 17]. For $g(\boldsymbol{r}) \gg \gamma, \kappa$ the line splitting $\Omega = \Omega_+ - \Omega_-$ is approximately $2g(\boldsymbol{r})$, the same rate at which the energy oscillates between the emitter and the cavity field.

It is interesting to note that in the weak coupling regime, where $g(\boldsymbol{r}) < \gamma \ll \kappa$, the linewidths $\Gamma_\pm$ in Eq. (2.43) take the form [84]

$$\Gamma_+ = \kappa \qquad \text{and} \qquad \Gamma_- = \frac{4g^2(\boldsymbol{r})}{\kappa} + \gamma = \Gamma_\mathrm{c} + \gamma = \Gamma \,. \tag{2.44}$$

Thus, the same results as in the perturbative approach are retrieved for the cavity decay rate κ and the modified emission rate Γ of the emitter, respectively.

Application of cavity QED effects

The coupled emitter-cavity system studied above is of utmost importance for a large number of applications, as it represents a fundamental building block for nanophotonic devices: a single quantum emitter whose emission properties are tailored through interaction with a single cavity mode. Photonic crystal cavities are particularly suited for this purpose, since they exhibit by far the smallest mode volume among various types of microcavities [74]. This is favorable for achieving large Purcell factors $F_\mathrm{c} \propto Q/V_\mathrm{eff}$ as well as for the realization of the strong coupling condition $g(\boldsymbol{r}) \gg \gamma, \kappa$, since $g(\boldsymbol{r})/\gamma \propto 1/\sqrt{V_\mathrm{eff}}$ and $g(\boldsymbol{r})/\kappa \propto Q/\sqrt{V_\mathrm{eff}}$. The best choice for values of $g(\boldsymbol{r})$, γ, and κ strongly depends on the specific application and whether operation in the weak or strong coupling regime is desired. In the following, a brief overview of the most common fields of application and the corresponding emitter-cavity parameters is given.

Single photon sources The ability to create single photons on demand is essential, e.g., for the implementation of various schemes for quantum cryptography [85, 86], linear-optical quantum computation [5], and quantum teleportation [87]. Key requirements are a high photon flux, which necessitates high emission rates as well as good extraction and collection efficiencies for the emitted photons, a low multi-photon probability, and, for some applications, a high degree of quantum indistinguishability [88], i.e., a good spatial, spectral, and temporal overlap of the photon wave functions.

The Purcell enhancement effect in a photonic crystal cavity can help to boost the emission rate Γ of a single quantum emitter [18, 89] and to channel the emitted photons to the desired target location with high efficiency, e.g., through coupling of the cavity to an integrated waveguide [90]. A large value of F_c also improves the photon indistinguishability [14, 15] by shortening the emission lifetime $\tau = 1/\Gamma$, thus reducing the impact of any dephasing processes resulting from interactions of the emitter with its environment. In order to suppress the probability for retrieving more than one photon per excitation pulse, $\Gamma \ll \kappa$ should be satisfied, ensuring that there is only one photon at a time in the cavity. Furthermore, a coherent interaction between the emitter and the cavity field is often undesired as it may induce a jitter in the arrival times of the photons. Consequently, the weak coupling regime is ideal for implementing cavity-enhanced single photon sources, although corresponding systems operating in the strong coupling regime have also been demonstrated [91].

Low-threshold lasers The Purcell effect can also be exploited to decrease the lasing threshold [92] in photonic crystal cavities, leading to a smoother onset of the lasing activity at considerably lower powers [13, 93] than would be possible in large-

scale devices. The key mechanism is the enhancement of the spontaneous emission rate Γ_c into one particular cavity mode, while emission into all other (non-lasing) modes is efficiently suppressed, partly due to the presence of the photonic band gap. According to Eq. (2.41), extremely high coupling factors β can be achieved in this way [94, 95], resulting in almost threshold-less lasing activity.

Quantum information processing While the previous examples relied on operation in the weak coupling regime, many applications in quantum information processing [4, 96] require strong coupling conditions $g(\boldsymbol{r}) \gg \gamma, \kappa$. For example, in a quantum network single photons need not only to be generated (as described above), but have also to perform logic operations (through interaction in a quantum phase gate [97]) and need to be detected (through quantum non-demolition measurements [98]). These processes require a highly non-linear interaction between coincident photons, which can be facilitated by the Rabi splitting effect in the strong coupling regime. If (on average) one photon is present in the coupled emitter-cavity system, two eigenstates exist with frequencies given by Eq. (2.43), but there is no state at the frequency of the bare emitter anymore (so-called photon blockade [99]). Consequently, the reflection properties of a photonic crystal cavity can be controlled by the number of photons in the cavity [100], which allows the realization of controlled phase gates and photon number measurements [101].

2.3 Experimental and computational methods

This section contains a detailed description of the experimental techniques employed for the fabrication (Sec. 2.3.1) and optical characterization (Sec. 2.3.2) of the photonic crystal cavities. Furthermore, it provides a brief introduction into the computational methods used for calculating photonic band structures and cavity mode properties, namely the plane wave expansion method (Sec. 2.3.3) and finite-difference time-domain simulations (Sec. 2.3.4).

2.3.1 Fabrication of photonic crystal cavities

All photonic crystal cavities investigated throughout this thesis were fabricated by collaborators at the Application Center for Microengineering, Helmholtz-Centre Berlin for Materials and Energy (formerly BESSY GmbH), using electron beam lithography and reactive ion etching. Stoichiometrical silicon nitride (Si_3N_4) was chosen as the prime material system for this purpose due to its transparency in a wide spectral window in the visible (down to ≈ 550 nm), the modest refractive index of $n \approx 2$ [102], which is sufficiently high to produce a pronounced photonic band gap effect, and the relative ease of fabrication compatible with standard CMOS

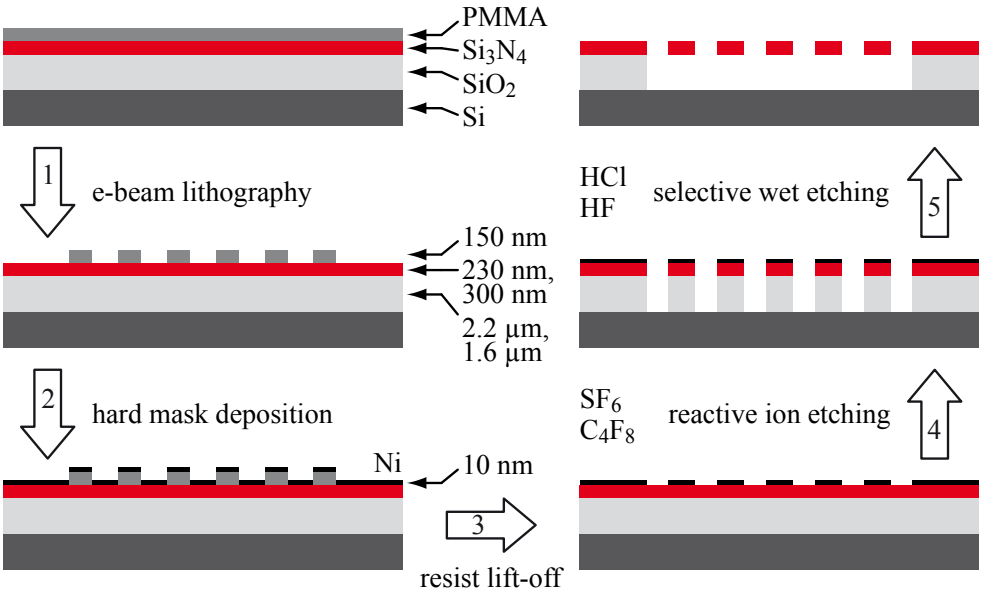

Figure 2.10: Scheme of the fabrication process for Si_3N_4 photonic crystal membrane structures. Details of each fabrication step are provided in the text.

(complementary metal-oxide semiconductor) technology. A scheme of the complete fabrication process is shown in Fig. 2.10 and a short description of each process step is provided in the following. A more detailed discussion can be found in Ref. [103].

As a starting material silicon (Si) wafers with a thin Si_3N_4 film grown by low pressure chemical vapor deposition (Si-Mat) were used. The Si_3N_4 layer had a thickness of either 230 nm or 300 nm, with a 2.2 µm or 1.6 µm thick layer of thermally oxidized silicon dioxide (SiO_2) underneath, respectively. As resist material a 150 nm thick film of polymethylmethacrylate (PMMA) was deposited on the wafer using a spin-coating technique and subsequent drying in a vacuum oven. The patterning of the resist (step 1 in Fig. 2.10) occurred by means of a 30 kV electron beam in a LEO 1560 scanning electron microscope equipped with a Nanomaker lithography toolkit (Interface Company). After developing the exposed resist for 10 s in AR 600-50 (Allresist), the sample was rinsed in isopropyl alcohol and deionized water, resulting in a corresponding negative PMMA pattern of the desired photonic crystal structure. This pattern was then inverted by depositing a 10–20 nm thick nickel (Ni) layer on top of the wafer by thermal evaporation (step 2) and subsequent dissolution of the PMMA using N,N-dimethylformamid (lift-off process, step 3), resulting in a corresponding Ni mask.

The transfer of the pattern into the underlying layers of the wafer occurred by means of reactive ion etching, performed in a Plasmalab 80 Plus etcher (Oxford Instruments). As reactive agents sulphur hexafluoride (SF_6) and octafluor cyclobutan (C_4F_8) were employed, with the etching process (step 4) working as follows.

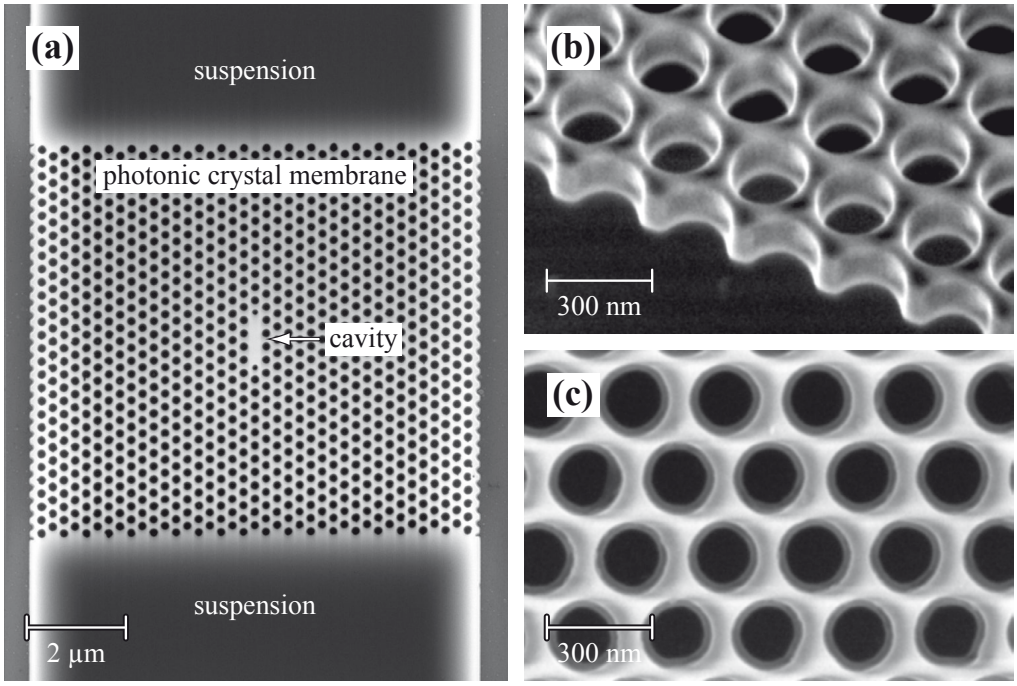

Figure 2.11: Scanning electron microscope images of some of the fabricated samples. **(a)** Top view of a photonic crystal membrane structure (with $a = 270$ nm, $r = 0.34a$, and $t = 1a$) including an L3 cavity and suspensions at both sides. **(b)** Tilted view, showing the edge of the photonic crystal membrane. **(c)** Close-up view of the membrane holes revealing the slightly tilted side walls, appearing as dark gray rings in the image.

Both gases are dissociated in an inductively coupled plasma to provide free fluorine radicals, which chemically etch the Si_3N_4 as well as the SiO_2, while simultaneously reacting with fluorocarbons from the decomposed C_4F_8 to form a thin passivation layer of CF_2, preventing further etching. By using an additional radio frequency directional plasma, which accelerates the positively charged ions towards to sample surface, this passivation layer can selectively be removed on all horizontal surfaces, enabling preferential vertical etching of the holey structure. Thereby, the ratio of the CF_2 formation and removal rates determines the quality of the etching process, ideally resulting in perfectly vertical side walls of the photonic crystal holes under equilibrium conditions. These conditions can be adjusted by changing the gas composition and pressure as well as the power density of the plasma and were subject to constant optimization during the course of this thesis.

After the reactive ion etching the remaining Ni mask was removed using a 10% solution of hydrochloric acid (HCl). Finally, the SiO_2 was selectively etched by a 50% solution of hydrofluoric acid (HF) (step 5) such that the oxide completely dissolved beneath the photonic crystal structure but still supported the adjacent suspensions. This resulted in freely suspended photonic crystal membranes with a sufficiently large layer of air underneath to ensure vertical symmetry.

An image of one of the fabricated samples is shown in Fig. 2.11a, exhibiting a lattice constant $a = 270$ nm, which was kept constant throughout this thesis. A detailed investigation before and after the final wet etching step revealed that not only the SiO_2, but also the Si_3N_4 was partly removed by the HF. This resulted in a reduction of the thickness t of the Si_3N_4 layer by ≈ 30 nm (as deduced, e.g., from Fig. 2.11b), leading to corresponding values $t \approx 200\,\text{nm} = 0.74a$ and $t \approx 270\,\text{nm} = 1a$ for the different types of wafers, respectively. Likewise, the hole diameter increased by $\approx$ 5–30 nm (depending on the initial size of the holes), restricting the smallest possible hole radius which could reliably be fabricated to $r \approx 50\,\text{nm} = 0.18a$. From a statistical analysis the typical deviation of the hole radius from its mean value was found to be ≈ 5 nm, including slight irregularities in the circular shape of the holes. Furthermore, during an early stage of the optimization process, a tilt of the side walls of up to 7° occurred in most of the samples, as can be seen, e.g., in Fig. 2.11c. This tilt resulted from an imbalance of the etching and passivation rates as discussed above and could almost completely be diminished in later samples by improving the corresponding etching recipe.

2.3.2 Optical spectroscopy on photonic crystal cavities

The optical properties of the fabricated samples were investigated under ambient conditions at room temperature by means of fluorescence spectroscopy. Thereby, either a thin layer of dye molecules (nile red, Invitrogen) or the intrinsic luminescence of the silicon nitride layer itself [104] served as emission source for the optical characterization. In both cases the samples were initially cleaned in a 50:50 mixture of H_2O_2 and H_2SO_4 and subsequently rinsed in deionized water. The deposition of the dye layer occurred by spin-coating a solution of nile red in ethanol (concentration $\approx 10^6$ M) on the entire wafer. A home-built microscopy setup was then used to locally excite and collect the fluorescence from the sample. A scheme of this setup is shown in Fig. 2.12 and a detailed description is provided in the following.

For continuous wave (cw) excitation either a Beam-Lok 2080 Ar^+ laser (emission wavelength $\lambda = 514$ nm, Spectra Physics) or a Verdi V-10 frequency-doubled Nd:YAG laser ($\lambda = 532$ nm, Coherent) was employed. In both cases the laser beam was sent through a single-mode fiber to achieve a clean mode profile. The polarization direction of the excitation light could be controlled by polarizers and a $\lambda/2$ waveplate. A 100×/0.9 NA microscope objective (Nikon) was employed to focus the laser beam onto a diffraction-limited spot on the sample surface and to collect the resulting fluorescence emission. Thereby, the lateral position of the laser focus could be adjusted with an accuracy of ≈ 50 nm by means of a beam steering unit, consisting of two identical lenses which could be shifted relative to each other via linear actuators. Typical excitation powers at the entrance of the microscope ob-

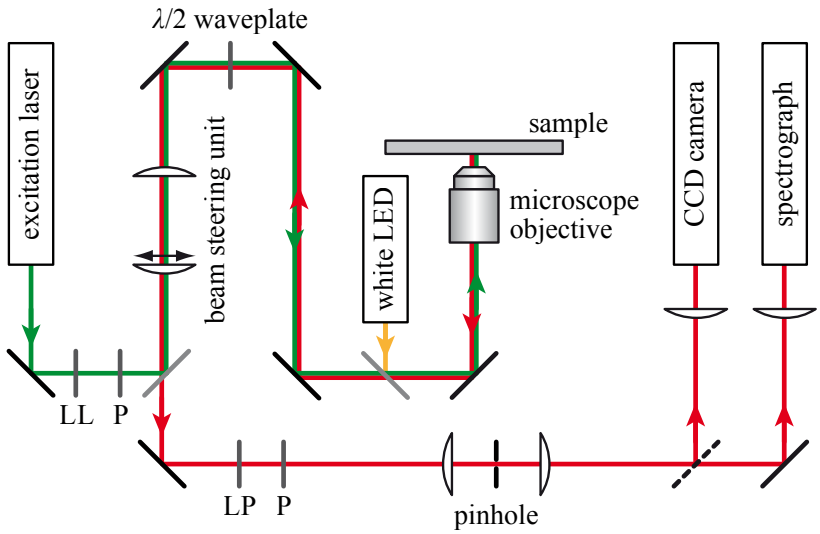

Figure 2.12: Schematic illustration of the experimental setup for fluorescence spectroscopy on planar samples. The abbreviations are defined as follows: LL – laser line filter, LP – long-pass filter, P – polarizer, LED – light-emitting diode, CCD – charge-coupled device.

jective were ≈ 1 µW in the case of dye-coated samples and ≈ 100 µW in the case of bare photonic crystal structures. In addition to the laser beam, white light from an LED could be coupled into the excitation path for imaging purposes via a 8:92 pellicle beam splitter.

The separation of the fluorescence from the excitation light occurred by means of a 10:90 beam sampler and a 550 nm long-pass filter. The emission and/or the reflected white light from the sample could then be directed onto different detector systems, the first one being a CCD camera (ORCA, Hamamatsu) which was usually employed to image the sample and to position the laser focus with respect to the corresponding structure of interest. After proper alignment and insertion of a 100 µm pinhole for spatial filtering, the fluorescence light could be sent through a spectrograph (SpectraPro 500i, Princeton Instruments) and subsequently be monitored by a CCD camera (SPEC-10, Roper Scientific). In this way, fluorescence spectra from the samples were recorded, using typical integration times of 10–20 s.

2.3.3 Plane wave expansion method

Throughout this thesis the experimental studies were always accompanied by numerical simulations of the corresponding photonic crystal structures. Three different computational methods were employed for this purpose, depending on the type of problem which had to be solved. Here, the general principles and fields of application of the so-called plane wave expansion method are briefly discussed. The other two methods, namely finite-difference time-domain and finite element simulations, are treated in Secs. 2.3.4 and 5.3.3, respectively.

General principles

The plane wave expansion method is a tool to numerically solve the Maxwell eigenvalue equation (2.8) for a periodic dielectric structure. As described in Sec. 2.2.1, the corresponding eigenvectors can be expressed as Bloch functions $\boldsymbol{H}_{\boldsymbol{k}n}(\boldsymbol{r}) = \boldsymbol{v}_{\boldsymbol{k}n}(\boldsymbol{r})\mathrm{e}^{i\boldsymbol{k}\boldsymbol{r}}$ and Eq. (2.8) takes the form

$$(\nabla + i\boldsymbol{k}) \times \left[\frac{1}{\varepsilon(\boldsymbol{r})}(\nabla + i\boldsymbol{k}) \times \boldsymbol{v}_{\boldsymbol{k}n}(\boldsymbol{r})\right] = \frac{\omega_{\boldsymbol{k}n}^2}{c^2}\boldsymbol{v}_{\boldsymbol{k}n}(\boldsymbol{r}) \; . \tag{2.45}$$

The basic idea is now to expand the fields $\boldsymbol{v}_{\boldsymbol{k}n}(\boldsymbol{r})$ as well as the reciprocal dielectric constant $1/\varepsilon(\boldsymbol{r})$ into a discrete set of plane waves,

$$\boldsymbol{v}_{\boldsymbol{k}n}(\boldsymbol{r}) = \sum_{\boldsymbol{G}} \tilde{\boldsymbol{v}}_{\boldsymbol{k}n}(\boldsymbol{G})\mathrm{e}^{i\boldsymbol{G}\boldsymbol{r}} \qquad \text{and} \tag{2.46}$$

$$\frac{1}{\varepsilon(\boldsymbol{r})} = \sum_{\boldsymbol{G}} \frac{1}{\tilde{\varepsilon}(\boldsymbol{G})}\mathrm{e}^{i\boldsymbol{G}\boldsymbol{r}} \; . \tag{2.47}$$

Here, $\tilde{\boldsymbol{v}}_{\boldsymbol{k}n}(\boldsymbol{G})$ and $1/\tilde{\varepsilon}(\boldsymbol{G})$ are the respective Fourier coefficients and the sum extends over all reciprocal lattice vectors $\boldsymbol{G}$. Substituting Eqs. (2.46) and (2.47) into Eq. (2.45) yields a set of linear eigenvalue equations

$$\sum_{\boldsymbol{G}'} \frac{1}{\tilde{\varepsilon}(\boldsymbol{G}-\boldsymbol{G}')}(\boldsymbol{k}+\boldsymbol{G}) \times \left[(\boldsymbol{k}+\boldsymbol{G}') \times \tilde{\boldsymbol{v}}_{\boldsymbol{k}n}(\boldsymbol{G}')\right] = -\frac{\omega_{\boldsymbol{k}n}^2}{c^2}\tilde{\boldsymbol{v}}_{\boldsymbol{k}n}(\boldsymbol{G}) \; , \tag{2.48}$$

from which the coefficients $\tilde{\boldsymbol{v}}_{\boldsymbol{k}n}(\boldsymbol{G})$ can be determined by choosing a suitable set of vectors $\boldsymbol{G}$ and applying iterative solvers. Details and subtleties of this computation can, e.g., be found in Ref. [105].

Application to photonic crystal structures

As the plane wave expansion method works in the frequency domain, it directly yields the eigenfrequencies $\omega_{\boldsymbol{k}n}$ and corresponding eigenvectors $\boldsymbol{H}_{\boldsymbol{k}n}(\boldsymbol{r})$ for a given wave vector $\boldsymbol{k}$ and is thus favorable for the calculation of photonic band structures and eigenmodes of periodic systems. In this thesis the free software package MIT Photonic Bands was employed for this purpose, with the general computation procedure working as follows. First, an appropriate unit cell of the structure is defined and periodic boundary conditions are applied, i.e., the field values on opposing sides of the unit cell (with length $|\boldsymbol{L}|$) are set such that they only differ by a phase factor $\mathrm{e}^{\pm i\boldsymbol{k}\boldsymbol{L}}$. The modeled geometry $\varepsilon(\boldsymbol{r})$ is then discretized (with typically 16 mesh cells per lattice constant a) and used as input parameter for the calculation as described above. Thereby, the convergence of the calculation can be improved by interpolating the dielectric constant in each mesh cell, as is discussed in more detail in Sec. 2.3.4.

When the considered photonic crystal structure contains defects or is not periodic in one or more directions, the described method for calculating the band structure can still be applied, provided that a sufficiently large supercell is chosen as the fundamental building block. For example, a single planar photonic crystal slab was modeled as an artificial periodic arrangement of many slabs, typically separated by air gaps of thickness $6a$. This approach is valid as long as the distance between the individual slabs is large enough such that their mutual interaction can be neglected. Then, the artificial periodicity does not alter the calculated band structure significantly. It should be noted, however, that the eigenmodes obtained in such an infinite system are inherently lossless and the supercell approach could therefore not be applied to analyze quantities like radiation losses and quality factors of defect modes. Furthermore, the employed plane wave algorithm did not allow the incorporation of material absorption or dispersion in the computational model. Therefore, the finite-difference time-domain method had to be used to treat these kinds of problems, as is discussed next.

2.3.4 Finite-difference time-domain simulations

The finite-difference time-domain (FDTD) method is a powerful algorithm for numerically solving time-dependent electromagnetic problems in arbitrary geometries, including media with complex and dispersive dielectric functions. For the numerical simulations presented in this thesis, the software package FDTD Solutions (Lumerical) was employed, the basic calculation principles of which are introduced in the following.

General principles

The key element of the FDTD method is the Yee algorithm [106], which enables the calculation of the temporal evolution of the electric and magnetic fields $\boldsymbol{E}(\boldsymbol{r},t)$ and $\boldsymbol{H}(\boldsymbol{r},t)$, respectively. For this purpose, Maxwell's curl equations (2.3) and (2.4) have to be transformed from differentials into finite differences, both in the time domain

$$\frac{\partial F(x,t)}{\partial t} \longrightarrow \lim_{\Delta\tau\to 0} \frac{F\left(x,t+\frac{\Delta\tau}{2}\right) - F\left(x,t-\frac{\Delta\tau}{2}\right)}{\Delta\tau} \tag{2.49}$$

as well as in the space domain

$$\frac{\partial F(x,t)}{\partial x} \longrightarrow \lim_{\Delta s\to 0} \frac{F\left(x+\frac{\Delta s}{2},t\right) - F\left(x-\frac{\Delta s}{2},t\right)}{\Delta s}\,, \tag{2.50}$$

where Δt and Δs correspond to the mesh size of the temporal and spatial grid, respectively. Applying these transformations to Maxwell's curl equations results in

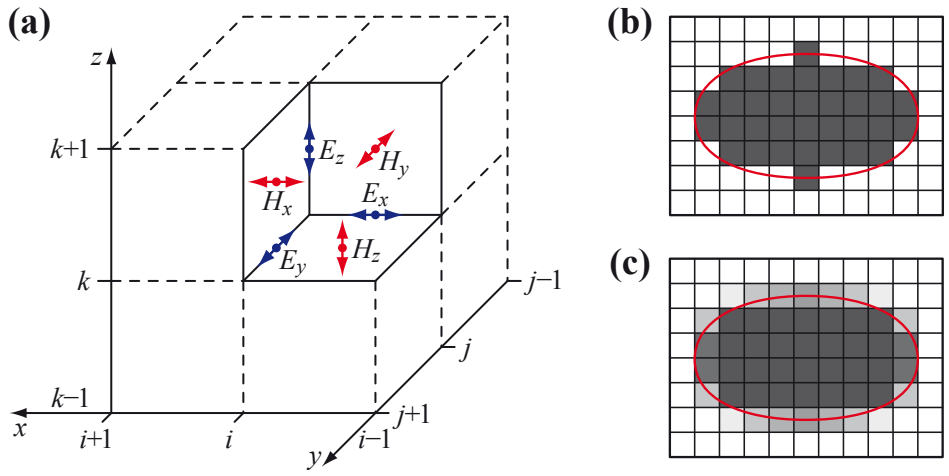

Figure 2.13: **(a)** Schematic representation of the three-dimensional Yee-cell and the corresponding spatial definition of the different field components. **(b,c)** Illustration of the meshing procedure for an elliptical object (red) without spatial averaging (b) and with spatial averaging applied (c). The different shadings of gray indicate the refractive index value appointed to each grid cell.

expressions of the form

$$E_x\Big|^{m+\frac{1}{2}}_{i+\frac{1}{2},j,k} = E_x\Big|^{m-\frac{1}{2}}_{i+\frac{1}{2},j,k} + c_0\frac{\Delta\tau}{\Delta s}\varepsilon^{-1}\Big|_{i+\frac{1}{2},j,k}\left[\left(H_z\Big|^{m}_{i+\frac{1}{2},j+\frac{1}{2},k} - H_z\Big|^{m}_{i+\frac{1}{2},j-\frac{1}{2},k}\right) - \left(H_y\Big|^{m}_{i+\frac{1}{2},j,k+\frac{1}{2}} - H_y\Big|^{m}_{i+\frac{1}{2},j,k-\frac{1}{2}}\right)\right] \quad \text{and} \tag{2.51}$$

$$H_x\Big|^{m+1}_{i,j+\frac{1}{2},k+\frac{1}{2}} = H_x\Big|^{m}_{i,j+\frac{1}{2},k+\frac{1}{2}} - c_0\frac{\Delta\tau}{\Delta s}\left[\left(E_z\Big|^{m+\frac{1}{2}}_{i,j,k+\frac{1}{2}} - E_z\Big|^{m+\frac{1}{2}}_{i,j-1,k+\frac{1}{2}}\right) - \left(E_y\Big|^{m+\frac{1}{2}}_{i,j+\frac{1}{2},k} - E_y\Big|^{m+\frac{1}{2}}_{i,j+\frac{1}{2},k-1}\right)\right] \tag{2.52}$$

as well as according formulations for the y and z components of $\boldsymbol{E}(\boldsymbol{r},t)$ and $\boldsymbol{H}(\boldsymbol{r},t)$, respectively. Here, the lower indices $\{i,j,k\}$ denote the coordinates in space, while the upper index m denotes the step in time. As is obvious from Eqs. (2.51) and (2.52), the field components of $\boldsymbol{E}$ and $\boldsymbol{H}$ are defined at different points on the spatial grid, the so-called Yee-cell (see Fig. 2.13a). Thereby, the corresponding dielectric constant ε is centered at the same point in space as the components of the electric field $\boldsymbol{E}$, resulting in three distinct grids $\{\varepsilon_x,\varepsilon_y,\varepsilon_z\}$ with different spatial offsets.

The actual geometry $\varepsilon(\boldsymbol{r})$ of the simulated structure can be discretized to these grids in two different ways, which are illustrated schematically (for an elliptical object of dielectric constant ε_2 in an environment with ε_1) in Figs. 2.13b and 2.13c, respectively. The so-called staircase method (Fig. 2.13b) either assigns values ε_1 or ε_2 to each grid cell, depending on which material occupies the majority of the cell.

This approach can be refined by applying a spatial averaging procedure (Fig. 2.13c), which scales the dielectric constant according to the fractions of ε_1 and ε_2 in each cell, resulting in a smoother transition at the surface of the object. Usually, this considerably improves the convergence properties of the calculation. However, if metal objects (exhibiting negative $\mathrm{Re}\{\varepsilon\}$ and non-zero $\mathrm{Im}\{\varepsilon\}$) are involved in the simulation, the averaging procedure can lead to artificial surface properties and should thus be avoided.

Apart from their location at different spatial positions, the fields $\boldsymbol{E}$ and $\boldsymbol{H}$ are also defined at different points in time. As seen from Eqs. (2.51) and (2.52), $\boldsymbol{E}(t + \Delta\tau/2)$ is calculated from $\boldsymbol{H}(t)$, $\boldsymbol{H}(t + \Delta\tau)$ is calculated from $\boldsymbol{E}(t + \Delta\tau/2)$, and so forth. To ensure the stability of this so-called leap frog algorithm (in a three-dimensional simulation), $\Delta\tau$ and Δs should satisfy the relation $\Delta\tau/\Delta s < 1/(\sqrt{3}c)$ and Δs should be smaller than $\approx 1/10$ of the wavelength in the medium of highest refractive index [107, 108]. For periodic structures (such as photonic crystals) Δs should further be an integer fraction of the lattice constant a in each dimension to avoid artificial distortions of the periodicity due to the spatial discretization.

Application to photonic crystal structures

The FDTD method provides a direct solution of the electromagnetic field in the time and space domain. By applying Fourier transformations corresponding solutions in the frequency and wave vector domain can be obtained as well, enabling, e.g., the calculation of photonic band structures. However, compared to the plane wave expansion method (see Sec. 2.3.3), the FDTD algorithm is much less efficient and reliable in this regard and was therefore not employed for this purpose. Its strength lies in the solution of problems involving finite photonic crystal structures (rather than infinite periodic ones), which may contain lattice defects, in/out-coupling elements, etc. In this case, periodic boundary conditions cannot be applied anymore. Instead, open boundaries are required which do not reflect outgoing field energy back into the simulation region or, at least, strongly suppress reflections.

One of the most efficient and widely used approaches to tackle this open boundary problem is the so-called perfectly matched layer (PML) scheme. Its basic idea relies on the introduction of artificial material layers with increasing conductivity at the outer regions of the computational domain such that the electromagnetic energy of an impinging wave is gradually absorbed while traveling through these layers. At the same time, the wave is perfectly transmitted from one layer to the next, avoiding the reflection of energy back into the inner simulation region. To achieve these material properties for waves of all directions, anisotropic tensors $\boldsymbol{\varepsilon} = \varepsilon\mathbf{S}$ and $\boldsymbol{\mu} = \mu\mathbf{S}$ are introduced for the dielectric and paramagnetic constant, respectively,

such that they fulfill the relations

$$\nabla \times \boldsymbol{H}(\boldsymbol{r},t) = -i\omega\varepsilon\mathbf{S}\cdot\boldsymbol{E}(\boldsymbol{r},t) \qquad \text{and} \tag{2.53}$$

$$\nabla \times \boldsymbol{E}(\boldsymbol{r},t) = i\omega\mu\mathbf{S}\cdot\boldsymbol{H}(\boldsymbol{r},t)\ , \tag{2.54}$$

with the tensor $\mathbf{S}$ being defined as

$$\mathbf{S} = \begin{bmatrix} \frac{s_y s_z}{s_x} & 0 & 0 \\ 0 & \frac{s_x s_z}{s_y} & 0 \\ 0 & 0 & \frac{s_x s_y}{s_z} \end{bmatrix}\ , \qquad s_i = \kappa_i + i\frac{\sigma_i}{\omega}\ . \tag{2.55}$$

Here, ω is the frequency of the wave, σ is the material conductivity, and κ is an additional absorption parameter. Through proper choice of σ and κ the energy impinging on the PML region can strongly be absorbed while keeping numerical reflection errors to a minimum.

Having established a computational domain with open boundaries, various properties of finite photonic crystal systems can be investigated, such as the quality factor of defect modes, the transmission through a waveguide, or the in/out-coupling of light into the structure. This requires the choice of a suitable radiation source and the subsequent calculation of the time evolution of the electromagnetic field. For example, when performing a defect mode analysis, a narrow-band pulse from a dipole source was usually injected into the system. Thereby, care has to be taken regarding the position and orientation of the dipole with respect to the defect mode of interest in order to provide an efficient and probably selective excitation. From the recorded time series the energy stored inside the defect can be extracted and the corresponding quality factor Q, defined as the relative amount of energy lost per cycle $T = 2\pi/\omega$ (see Sec. 2.2.4), can be calculated via

$$Q = \frac{2\pi}{\ln\left[\left|\boldsymbol{E}(t)\right|^2/\left|\boldsymbol{E}(t+T)\right|^2\right]}\ . \tag{2.56}$$

Apart from the quality factor and the near-field distribution of a defect mode, sometimes the far-field radiation pattern is of interest (see, e.g., Sec. 2.5.2). The latter can be calculated by monitoring the local fields in a plane directly above the photonic crystal structure and applying a spatial Fourier transformation. In this way, the corresponding distribution of wave vectors in k-space is obtain, which can subsequently be used to project the mode profile into the far-field. This approach is valid as long as the field intensity vanishes at the edges of the monitor plane, which is usually fulfilled for a well-localized defect mode.

2.4 Investigation and optimization of L3 cavities

In the course of this thesis the first attempt to realize photonic crystal cavities in the visible with high quality factors Q relied on the well-known L3 cavity design as introduced in Sec. 2.2.3. This choice was led by the fact that the L3 geometry is one of the most extensively studied types of photonic crystal cavities, with rich knowledge available from corresponding implementations in the near infrared [43, 63]. It supports a spectrally well separated fundamental mode, whose quality factor has been optimized to values $> 5 \times 10^4$ in experiments with silicon-based photonic crystals by adjusting the surrounding holes of the cavity [63] (see also Sec. 2.2.4). Therefore, the L3 design seems a promising candidate for realizing high-Q cavities in the visible, while keeping the mode volume on the order of the cubic wavelength. In the following, numerical as well as experimental results concerning the mode structure (Sec. 2.4.1) and design optimization (Sec. 2.4.2) of L3 cavities made from silicon nitride are presented, accompanied by a discussion of cavity QED effects observed in these structures (Sec. 2.4.3).

2.4.1 Mode analysis

Numerical simulations

First, the general mode structure of the unmodified L3 geometry (i.e., without adjustment of the adjacent holes) is studied, serving as a starting point for the subsequent optimization of the cavity design. Corresponding FDTD simulations (see Sec. 2.3.4) were performed for a photonic crystal structure with a lattice constant $a = 270$ nm, slab thickness $t = 1a$, and hole radius $r = 0.3a$. For the silicon nitride membrane a refractive index $n = 2.01$ was assumed, according to the specification (at 632 nm) of the manufacturer. The dimension of the entire simulated structure was $28a \times 14\sqrt{3}a \times 6a$ in the x, y, and z direction, respectively, with a mesh size of $a/20 \times \sqrt{3}a/34 \times a/27$. The applied lateral dimensions coincide with those of

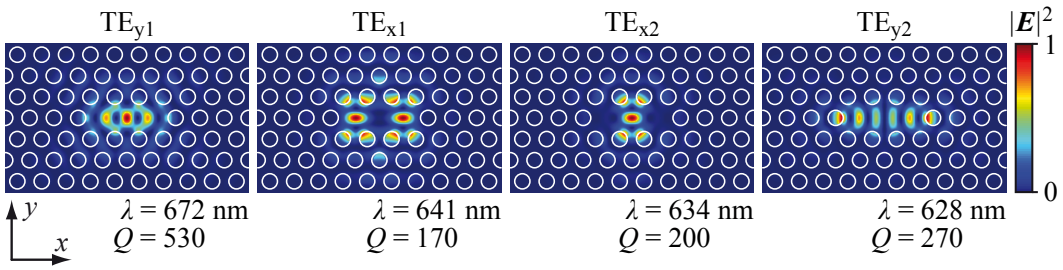

Figure 2.14: Calculated electric field intensity distributions $|\boldsymbol{E}|^2$, resonance wavelengths λ, and quality factors Q of all four modes of an L3 cavity. The lattice parameters are $a = 270$ nm, $t = 1a$, and $r = 0.3a$. The modes are denoted as TE$_x$ or TE$_y$ according to the corresponding field polarization on the central x axis.

the fabricated structures and should not be chosen considerably smaller than that, since lateral losses are much more significant in such a low-index system due to the weaker optical confinement compared to high-index photonic crystals.

Four different L3 cavity modes could be identified, which are all TE-like in character and coincide with the defect states found in corresponding band structure calculations (see Fig. 2.3b). A fifth mode of higher frequency, as reported for gallium arsenide L3 cavities [109], could not be found in the simulations, probably because it lies outside the spectral window of the photonic band gap, which is much narrower in low-index materials. The intensity profiles $|\boldsymbol{E}|^2$ of the different modes are depicted in Fig. 2.14, being denoted as $\mathrm{TE_x}$ or $\mathrm{TE_y}$ according to the field polarization on the central x axis. The resonance wavelengths λ and quality factors Q [deduced via Eq. (2.56)] are also displayed, showing that the fundamental mode $\mathrm{TE_{y1}}$ exhibits the highest quality factor $Q = 530$. Note that all modes shift to shorter wavelengths as the hole radius r increases, because a larger part of the cavity field has to reside in air, effectively increasing the mode energy. This is accompanied by a reduction of the quality factor due to larger out-of-plane losses.

Experimental results

For the experimental implementation a variety of photonic crystal structures with different hole radii r was fabricated using the method described in Sec. 2.3.1. Thereby, the lattice constant $a = 270\,\mathrm{nm}$ was always the same, while the membrane thickness varied, taking either values $t = 1a$ or $t = 0.74a$, depending on which type of wafer was used. Images of a typical L3 cavity are shown in Fig. 2.15, revealing the slightly conical shape of the membrane holes already discussed in Sec. 2.3.1. The samples were investigated by means of fluorescence spectroscopy as described in Sec. 2.3.2.

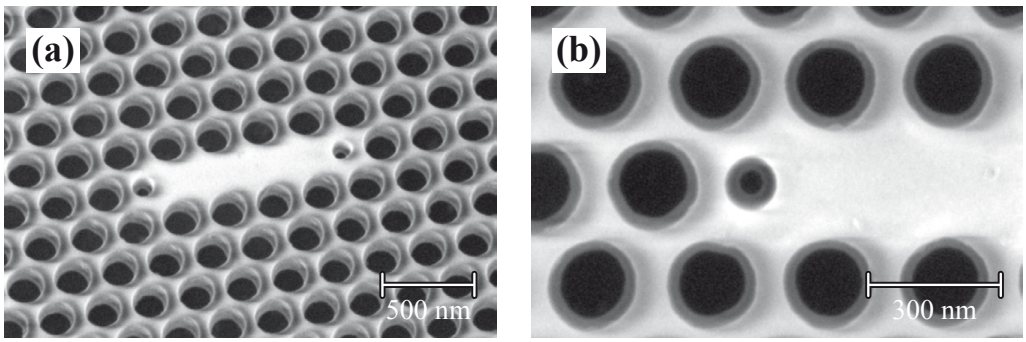

Figure 2.15: **(a)** Scanning electron microscope image of one of the fabricated (modified) L3 cavities. **(b)** Close-up view of the membrane holes, revealing their slightly conical shape, which gets more pronounced with decreasing hole radius.

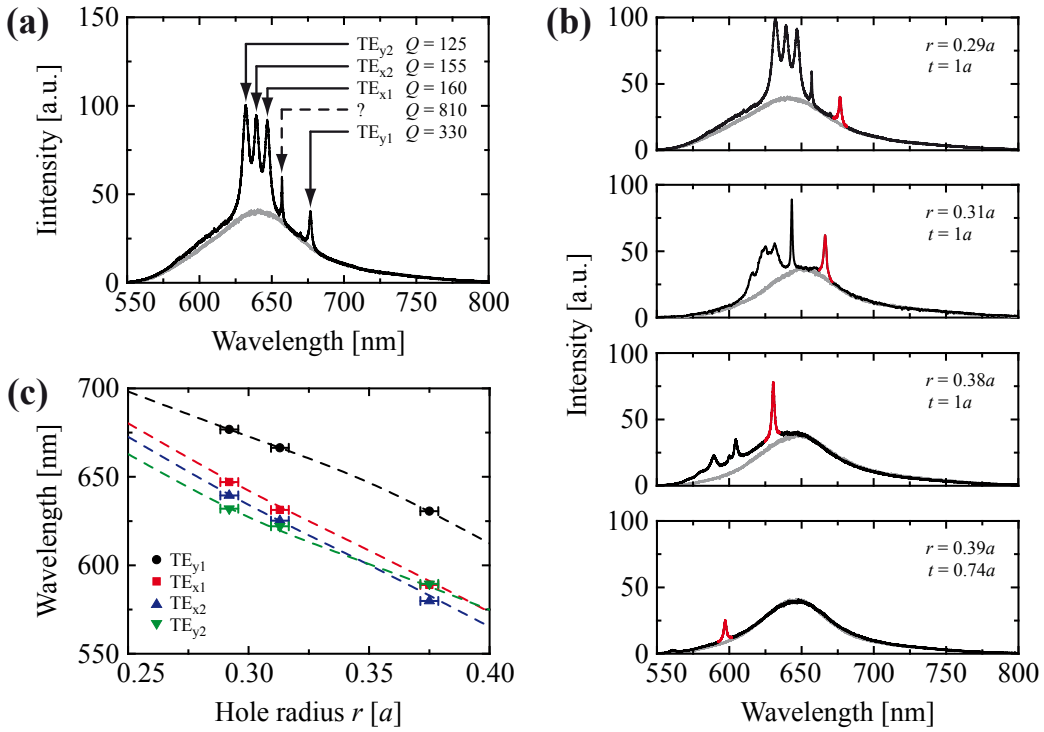

Figure 2.16: **(a)** Fluorescence spectrum (black) from an unmodified L3 cavity coated with nile red. The resonance peaks were identified by comparison with corresponding numerical simulations. The lattice parameters are $a = 270$ nm, $t = 1a$, and $r = 0.29a$. The gray curve represents a (scaled) reference spectrum recorded from a spot next to the cavity. **(b)** Series of fluorescence (black) and corresponding reference spectra (gray) from samples with different values of r and t, demonstrating the shift of the resonance wavelength. For clarity, the fundamental cavity mode TE_{y1} is highlighted in red. **(c)** Comparison of the measured peak wavelengths (symbols) with the calculated behavior (dashed curves) for the first three spectra shown in (b).

A selected fluorescence spectrum from a dye-coated (unmodified) L3 cavity is shown in Fig. 2.16a, accompanied by a reference spectrum recorded from a spot next to the cavity (but still on the photonic crystal membrane). A strong spectral modification is observed in form of several resonance peaks, indicating the coupling of the dye molecules to the individual cavity modes. As the molecules were distributed randomly on the photonic crystal surface, not all of them couple efficiently to the cavity field and thus a large unaltered background emission remains.

Four of the resonance peaks can readily be identified and assigned to the corresponding modes obtained from the FDTD simulations (see Fig. 2.14). The respective quality factors Q have been determined by a Lorentzian fit and are also displayed in Fig. 2.16a. As expected, the experimental Q values are always smaller than the calculated ones, mainly due to fabrication imperfections discussed later. One additional peak is observed in some of the spectra (indicated by a dashed arrow in Fig. 2.16a), which is not predicted by the simulations. It occurs only in thicker samples with

$t = 1a$ and its far-field emission is clearly polarized in y direction. Remarkably, this unidentified resonance typically exhibits a quality factor $Q \approx 800$, exceeding that of all other modes of the unmodified L3 cavity design. All attempts to reproduce this mode in the numerical simulations failed, even if the conical shape of the holes was taken into account, and therefore its origin remains unclear. However, as its quality factor seems to be largely insensitive to the optimization procedure discussed below, the unidentified resonance is not considered in the further analysis.

A number of fluorescence spectra for different lattice parameters r and t is shown in Fig. 2.16b, demonstrating the shift of the resonance peaks to smaller wavelengths as r increases and t decreases. While the fundamental cavity mode $\mathrm{TE_{y1}}$ is always clearly separated, the other modes start to overlap and even cross each other. This is in accordance with the theoretically expected behavior, as can be seen from the comparison of the experimental peak positions (obtained from multi-Lorentzian fits) with the calculated ones in Fig. 2.16c. It should be noted that the indicated values of r in Fig. 2.16 (and all subsequent figures) represent averaged radii, as the holes of the fabricated structures were in fact conical. However, simulations with conical holes indicate that the resulting mode structure can well be described by such an effective hole radius, an assumption which is supported by the excellent agreement between the experimental and theoretical data shown in Fig. 2.16c.

2.4.2 Optimization of the quality factor

Numerical simulations

Next, the optimization of the cavity design by modifying the adjacent hole geometry is discussed. Although successfully applied in high-index systems [43, 63], the applicability of this procedure to low-index materials (such as silicon nitride) has to be justified. For this reason, a thorough numerical analysis using FDTD simulations was carried out prior to the experiments. Thereby, the investigation exclusively focused on the fundamental cavity mode $\mathrm{TE_{y1}}$, exhibiting the most promising spectral properties.

Three different parameters of the cavity geometry were modified in order to achieve a more gentle confinement of the modal field and thus a reduction of radiation losses, as described in Sec. 2.2.4. These modifications are summarized in Fig. 2.17a. First, the radius r' of the left and right boundary holes was reduced and second, the holes were shifted outwards by a distance s, similar to the approach in Ref. [110]. The impact on the quality factor of the fundamental cavity mode can be seen in Fig. 2.17c. For example, a nearly five-fold enhancement occurs for $r' = 0.2a$ and $s = 0.2a$. Further decrease of r' or increase of s does not improve the quality factor significantly. Besides, too small hole radii or too large shifts can be problematic

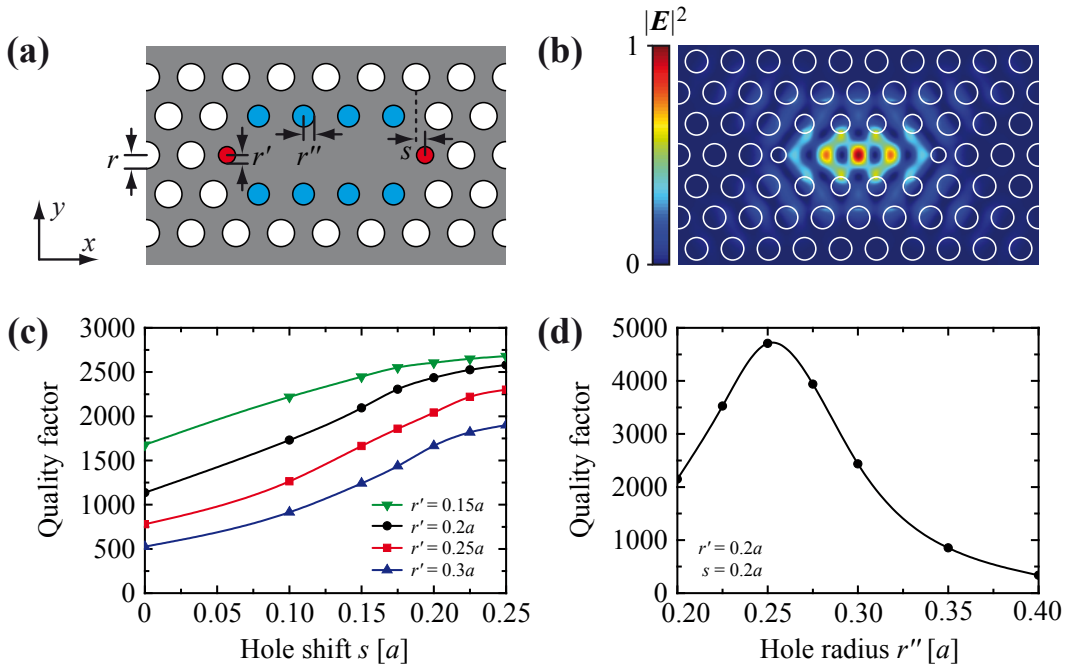

Figure 2.17: **(a)** Schematic representation of the optimized L3 cavity design. The radius of the surrounding holes is reduced to r' (left and right holes, red) and r'' (upper and lower holes, cyan), respectively. Additionally, the left and right holes are displaced outwards by a distance s. **(b)** Calculated electric field intensity distribution $|\boldsymbol{E}|^2$ of the optimized fundamental cavity mode TE_{y1}. **(c)** Calculated quality factors Q for various values of r' and s with fixed $t = 1a$ and $r = r'' = 0.3a$. **(d)** Calculated quality factors Q for various values of r'' with fixed $r' = 0.2a$ and $s = 0.2a$ and all other parameters as in (c).

from an experimental point of view, since a reliable and reproducible fabrication becomes more challenging. Therefore, the values $r' = 0.2a$ and $s = 0.2a$ were chosen as suitable parameters and kept constant during further optimization steps. Shifting the neighbor and next-neighbor holes to the left and right of the cavity (as has been done, e.g., in Ref. [63]) did not lead to any significant improvement. Instead, as a third modification, the radius r'' of the upper and lower boundary holes of the cavity was altered. The impact on the quality factor is shown in Fig. 2.17d. Obviously, an additional boost of Q by more than a factor of two can be achieved by slightly reducing r'' to $0.25a$, leading to a maximum quality factor $Q = 4700$. This nearly nine-fold enhancement (compared to the unmodified L3 design) is much higher than a corresponding factor of ≈ 2 reported in a similar study [111], where only the shift s was used as optimization parameter.

The intensity profile of the optimized geometry is displayed in Fig. 2.17b. The corresponding mode volume V_{eff} can be calculated via Eq. (2.21), yielding a value $V_{\mathrm{eff}} = 1.32\,(\lambda/n)^3$. According to Eq. (2.40), this results in a maximum Purcell factor $F_{\mathrm{c}} \approx 270$ for an emitter which is spectrally and spatially aligned with respect to the intensity maximum $\left|\boldsymbol{E}(\boldsymbol{r}_{\mathrm{m}})\right|^2$ of the cavity mode. Here, $\boldsymbol{r}_{\mathrm{m}}$ is located at the center of

the cavity. In the case of external emitters which are placed on top of the photonic crystal slab, the ratio $\xi(\boldsymbol{r})$ [see Eq. (2.29)] reaches only values of ≈ 0.2 at best, reducing the possible Purcell factor to $F_\mathrm{c} \approx 50$. Furthermore, the experimentally observed Purcell enhancement is usually only a fraction of the predicted one, as spectral and spatial misalignments can significantly reduce the coupling between the emitters and the cavity mode. Nonetheless, the numerical results are encouraging and suggest that cavity QED effects investigated in high-index photonic crystals (see Sec. 2.2.5) might also be observable in such a low-index system. This is discussed in more detail in Sec. 2.4.3.

Experimental results

To test the theoretical predictions a variety of L3 cavities with different geometrical parameters (see Fig. 2.17a) was fabricated. The results from measurements on a series of samples with varying hole radius r' and shift s are shown in Fig. 2.18a. As expected, the quality factor in general improves with decreasing r' and increasing s, reaching values of up to ≈ 800. In other structures of a similar type even values $Q = 960$ were measured. In accordance with the numerical analysis a further boost can be achieved by reducing the hole radius r'', as is seen from measurements on another series of cavities in Fig. 2.18b, demonstrating a maximum quality factor $Q = 1460$. The corresponding fluorescence spectrum of this optimized cavity is shown in Fig. 2.19a.

To compare the experimentally determined dependence of Q on the design parameters with the theoretically expected behavior, the measured quality factor can be decomposed into two components, namely Q_ideal of the idealized, simulated structure and Q_loss, comprising all additional losses due to fabrication imperfections, absorption, etc. In analogy to Eq. (2.20), Q_loss can then be deduced from the calculated and measured values using the relation $1/Q_\mathrm{loss} = 1/Q - 1/Q_\mathrm{ideal}$, yielding $Q_\mathrm{loss} \approx 1000$. Assuming that this value is independent of the specific design parameters r', r'', and s, the theoretical predictions in Figs. 2.17c and 2.17d were scaled accordingly and the corrected estimations for Q are displayed in Figs. 2.18a and 2.18b, respectively, showing reasonable agreement with the experimental data.

The main contribution to Q_loss in these measurements is certainly the conical shape of the membrane holes (see Fig. 2.15b), as can be deduced from corresponding simulations of structures with tilted hole walls. For example, a tilt of 5° (relative to the vertical direction) induces a drop of the theoretical quality factor from $Q = 4700$ to $Q = 1950$. The reason for this is found in the vertical asymmetry, which leads to a coupling of the confined TE-like modes to propagating TM-like modes [112, 113], effectively increasing losses in the horizontal direction. After a careful optimization of the etching process (see Sec. 2.3.1), the conicity of the membrane

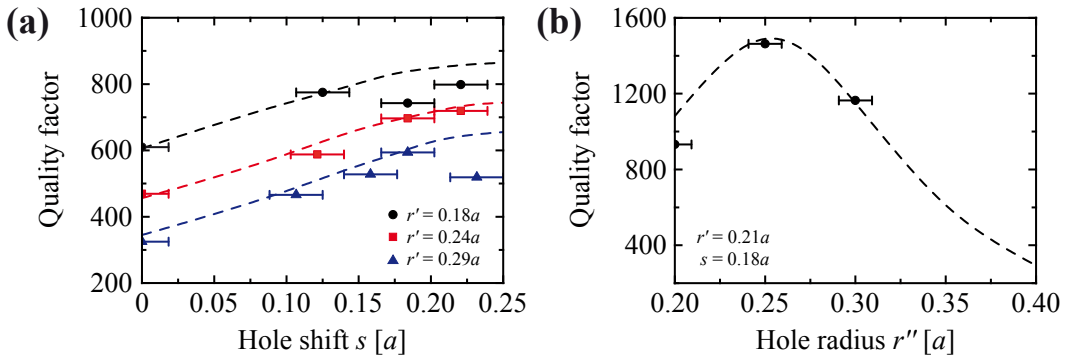

Figure 2.18: **(a)** Measured quality factors Q (symbols) of the fundamental cavity mode TE_{y1} of a series of optimized L3 cavities with different values of r' and s. The other parameters $a = 270$ nm, $t = 1a$, and $r = r'' = 0.29a$ are fixed. The dashed curves represent the corresponding theoretical predictions. **(b)** Measured quality factors Q (symbols) of another series of optimized L3 cavities with different values of r''. The other parameters $a = 270$ nm, $t = 0.74a$, $r = 0.3a$, $r' = 0.21a$, and $s = 0.18a$ are fixed. Again, the dashed curve represents the corresponding theoretical prediction. The error bars in (a) and (b) indicate the uncertainties in the determination of s and r'' from scanning electron microscope images.

holes could strongly be reduced to tilts $< 1°$. Measurements on corresponding samples revealed a further improvement of the cavity quality factor to values of up to ≈ 2200 (see Fig. 2.19b). Note that these later measurements were performed on thinner membranes with $t = 0.74a$, for which numerical simulations predict $Q = 3800$ (instead of $Q = 4700$).

The remaining discrepancy $Q_{\text{loss}} \approx 5000$ between the experimentally and theoretically obtained quality factors is partly attributed to distortions of the circular shape and position of the holes. This may also explain the rich modal structure observable in the spectra of optimized cavities as displayed, e.g., in Figs. 2.19a and 2.19b. Usually, much more resonance peaks occur than predicted by corresponding calculations, which might be a consequence of slight asymmetries in the fabricated sample geometry. From simulations based on scanning electron microscope images of some of the cavities and comparison to the respective idealized structures (with perfectly circular holes), a value $Q_{\text{loss}} \approx 10000$ is deduced for this type of losses.

Additionally, surface roughness may play an important role. Although measurements with an atomic force microscope yielded an RMS (root mean spare) value of only ≈ 0.4 nm at the top of the photonic crystal membranes, the roughness of the hole walls (which is not directly accessible to measurements) might be considerably larger [114, 115]. Apart from these structural imperfections, absorption caused by the silicon nitride itself might also be a source for further losses. The influence of the dye molecules, however, seems to be negligible, since measurements on the samples before and after coating with nile red showed no noticeable change in the corresponding cavity quality factor.

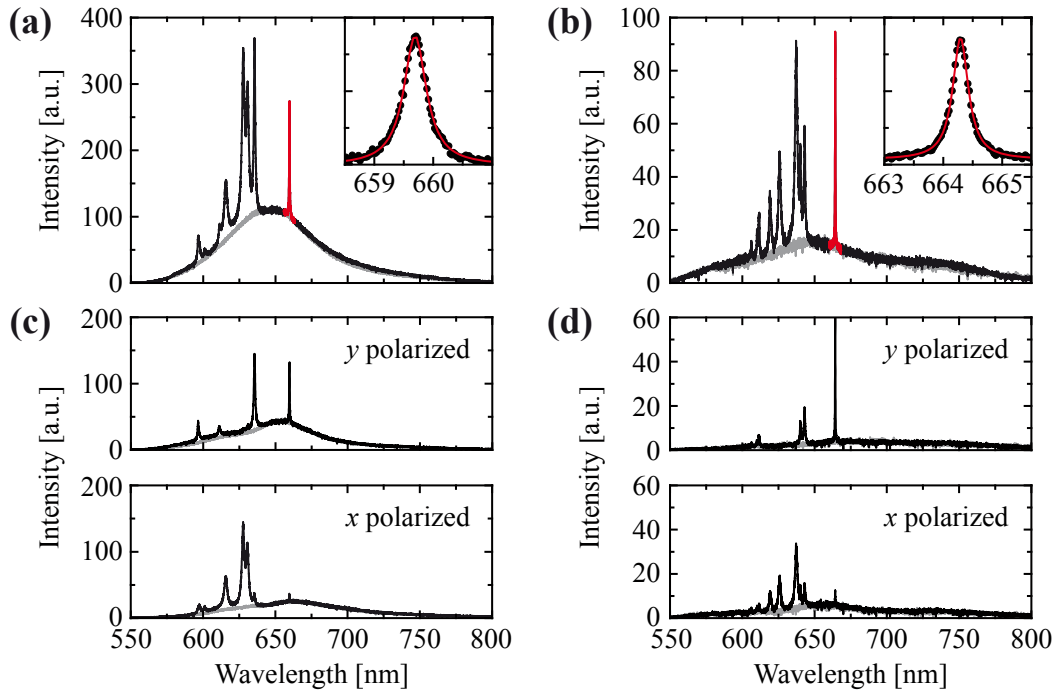

Figure 2.19: **(a)** Fluorescence spectrum from an optimized L3 cavity coated with nile red (black) and a corresponding reference spectrum (gray). The lattice parameters are $a =$ 270 nm, $t = 0.74a$, $r = 0.3a$, $r' = 0.21a$, $r'' = 0.25a$, and $s = 0.18a$. The fundamental cavity mode TE_{y1} is highlighted in red and a respective Lorentzian fit (red) to the experimental data (black) is shown in the inset, yielding a quality factor $Q = 1460$. **(b)** Corresponding spectra from a similar cavity as in (a), but without dye coating and with reduced conicity of the membrane holes. The obtained quality factor is $Q = 2080$. **(c,d)** Spectra from the same cavities as in (a) and (b), respectively, but recorded with polarization filtering.

The various emission peaks recorded from unmodified as well as optimized L3 cavities all showed a pronounced far-field polarization, with the modes TE_x and TE_y being polarized in x and y direction, respectively. This is illustrated for two spectra in Figs. 2.19c and 2.19d, respectively. The detected polarization always coincides with the symmetry properties of the respective cavity mode (at least for those peaks which could clearly be identified), which is a consequence of the destructive interference of certain field components in the far-field [116]. Note that this cancelation effect is the same as the one already discussed in conjunction with optimization strategies in Sec. 2.2.4.

2.4.3 Observation of cavity QED effects

Finally, having fabricated and tested photonic crystal cavities with promisingly high quality factors, the suitability of these structures for the observation of cavity QED effects shall be discussed. The presence of such effects is already indicated by the occurrence of resonance peaks in the spectra, which result from an enhanced emission

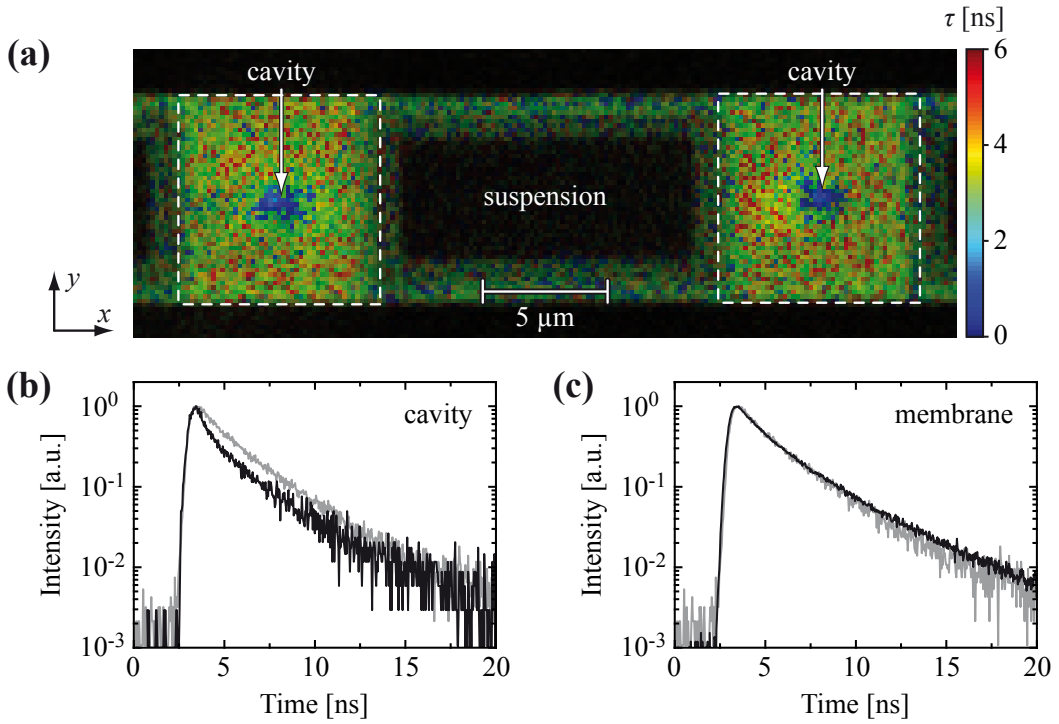

Figure 2.20: **(a)** Fluorescence lifetime image of two adjacent (optimized) L3 cavity structures coated with nile red. The brightness of the colors represents the intensity of the respective fluorescence signal at each point. The dashed lines indicate the boundaries of the photonic crystal membranes and the cavities are clearly visible as areas of reduced (average) lifetime. **(b,c)** Fluorescence time traces (black) from one of the photonic crystal structures shown in (a). The signal was either integrated over a small area around the cavity itself (b) or over the entire surrounding membrane structure, excluding the cavity (c). A corresponding reference curve (gray) from an unpatterned region is shown for comparison.

probability of the dye molecules into the cavity modes due to an increased density of optical states at the corresponding wavelengths. A fraction of the photons stored inside the cavity is then scattered into the far-field and collected by the microscope objective, leading to the characteristic emission peaks. However, the height of these peaks mainly depends on the respective collection efficiency and is not necessarily linked to the actual coupling strength between the emitters and the cavity. To gain insight into these processes, a direct analysis of the emission decay rate is necessary.

Following the above estimation of the Purcell factor F_c and using the best experimental quality factors $Q \approx 2000$ as well as a rough guess of the mode volume $V_{\text{eff}} \approx 1.5\,(\lambda/n)^3$, this yields a maximum value $F_c \approx 100$ or, if dye molecules at the photonic crystal surface are considered, $F_c \approx 20$. In the actual experiment not just one individual emitter is coupled to the cavity, but a whole ensemble of dye molecules, distributed on its surface. Assuming a uniform dye layer with randomly oriented molecules and an effective excitation/detection spot diameter of ≈ 500 nm FWHM, a spatially averaged Purcell factor $\langle F_c \rangle \approx 0.015 F_c \approx 0.3$ is calculated for

the fundamental cavity mode. Consequently, the averaged emission rate into the cavity mode is small compared to that into free space and one would not expect to see a significant influence on the radiative lifetime in such an ensemble measurement. However, due to their broad emission band, the dye molecules couple to multiple cavity modes simultaneously, effectively increasing the observable Purcell enhancement.

To study the changes in the emission decay rate of the molecules experimentally, the samples were investigated using a fluorescence lifetime imaging system (PicoQuant), courtesy of Dr. Y. Rakovich, Trinity College, Dublin (Ireland). The setup essentially consisted of a confocal laser scanning microscope, equipped with a 50×/0.5 NA objective and a 480 nm picosecond-pulsed diode laser, capable of performing a real-time analysis of the fluorescence time traces recorded at each spot of the scanning area. An example of a corresponding image is shown in Fig. 2.20a, displaying the average fluorescence lifetime of nile red molecules on two adjacent photonic crystal cavity structures. Obviously, there seems to be a decrease in the lifetime in the regions close to the cavities. A more detailed analysis of the time trace recorded from one of these cavities (Fig. 2.20b) confirms this observation, clearly showing an increase in the decay rate in comparison to a reference measurement on an unpatterned region of the sample. This accelerated decay is apparently linked to the enhanced emission into the cavity modes. Contrary to this, the time trace from the surrounding photonic crystal membrane (Fig. 2.20c) is nearly unaffected, exhibiting even a slight decrease of the decay rate, which may be attributed to the reduced density of optical states due to the photonic band gap.

However, a true quantitative analysis in terms of the Purcell factor is not possible, since the recorded time traces in Figs. 2.20b and 2.20c are highly multi-exponential, being composed of contributions from a huge ensemble of molecules. To draw conclusions on the achievable coupling strength between an emitter and the various cavity modes, experiments with single, precisely located emitters would be necessary. Ways towards the realization of such experiments by using nanomanipulation techniques are pursued in Chapter 3.

2.5 Investigation of double-heterostructure cavities

As demonstrated in the previous section, the optimization of the L3 design enabled the fabrication of photonic crystal cavities with quality factors $Q \approx 2000$ in the visible. However, the corresponding theoretical limit is only twice as large ($Q \approx 4000$), leaving not much room for further improvement regarding this specific geometry. From high-index photonic crystal structures it is well known that modulated waveguide cavities [52, 58] (see Sec. 2.2.3) can exhibit much higher quality factors due to

the gentler confinement of the cavity field (see Sec. 2.2.4). Therefore, it is appealing to implement such a modulated waveguide structure in the silicon nitride photonic crystals studied here in order to further improve the performance of cavities operating in the visible wavelength range. For this purpose, the double-heterostructure design (as described in Sec. 2.2.3) was chosen, because it is the most easiest to fabricate, involving only a slight local change in the lattice constant a. In the following, the results of numerical as well as experimental investigations on these cavities are presented, again focusing on the mode structure and corresponding quality factors (Sec. 2.5.1). Furthermore, the polarization properties of the far-field radiation are studied (Sec. 2.5.2), exhibiting significant differences compared to those of the L3 cavity design.

2.5.1 Mode analysis

Numerical simulations

The particular cavity geometry under investigation consisted of a W1 waveguide (see Sec. 2.2.3) in a photonic crystal membrane of thickness $t = 0.74a$, whose lattice constant $a = 270$ nm was enlarged to $a' = 280$ nm $= 1.037a$ over two lattice periods along the direction of the waveguide to create an optical potential well (see Fig. 2.5). An image of such a structure is shown in Fig. 2.21a, although the change between

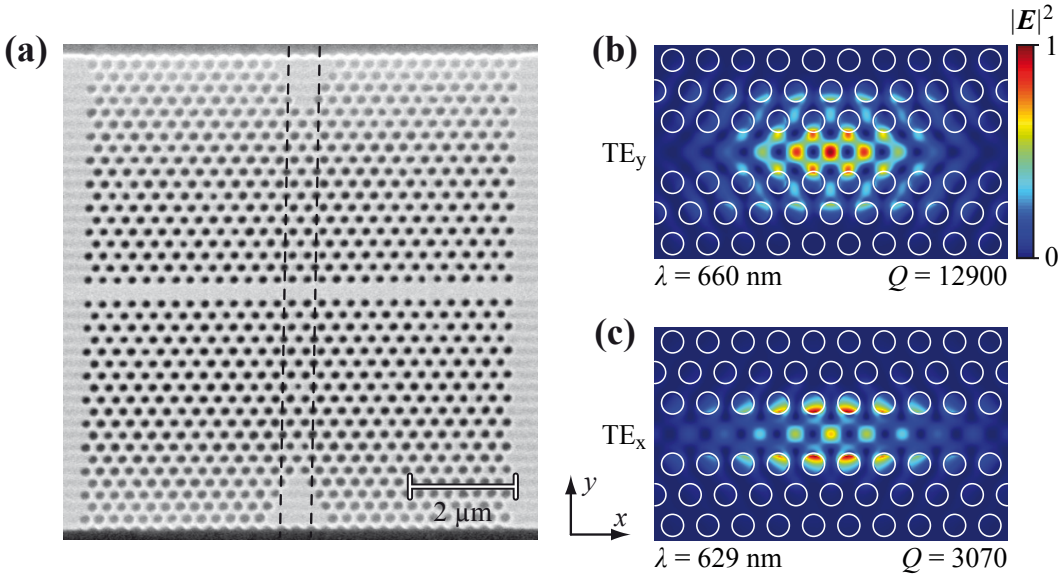

Figure 2.21: **(a)** Scanning electron microscope image of one of the fabricated double-heterostructure cavities. The dashed lines indicate the region of increased lattice constant a'. **(b,c)** Calculated electric field intensity distributions $|\boldsymbol{E}|^2$, resonance wavelengths λ, and quality factors Q of the cavity modes TE_y (b) and TE_x (c), respectively. The lattice parameters are $a = 270$ nm, $a' = 280$ nm, $t = 0.74a$, and $r = 0.3a$. The modes are denoted according to the corresponding field polarization on the central x axis.

a and a' is too small to be seen. Corresponding FDTD simulations were performed for a double-heterostructure cavity with a hole radius $r = 0.3a$. Thereby, the size of the computational domain and the mesh resolution were identical to those used in the studies of L3 cavities (see Sec. 2.4.1).

Two different cavity modes could be identified, originating from the odd and even TE waveguide mode near $k_x = \pi/a$ in the Brillouin zone (see Fig. 2.5c). They are denoted as $\mathrm{TE_y}$ and $\mathrm{TE_x}$, respectively, according to their field polarization along the central waveguide axis. The corresponding intensity profiles $|\boldsymbol{E}|^2$, resonance wavelengths λ, and quality factors Q are displayed in Figs. 2.21b and 2.21c, respectively. Obviously, much higher quality factors (compared to L3 cavities) can readily be achieved without any complicated design optimization, reaching theoretical values $Q > 10000$. At the same time, the mode volume V_{eff} increases only slightly to values of $1.62\,(\lambda/n)^3$ and $1.67\,(\lambda/n)^3$ for the modes $\mathrm{TE_y}$ and $\mathrm{TE_x}$, respectively, making double-heterostructure cavities superior to their L3 counterparts in terms of the achievable Purcell factor $F_{\mathrm{c}} \propto Q/V_{\mathrm{eff}}$ [see Eq. (2.40)].

Experimental results

Again, spectroscopic measurements were employed for the experimental investigation of the cavity modes and respective quality factors. This time, the intrinsic fluorescence of the silicon nitride was directly monitored, making an additional coating with dye molecules obsolete and leaving the photonic crystal structures clean for subsequent experiments (see Chapter 3). A selected fluorescence spectrum from a cavity with a hole radius $r = 0.28a$ is shown in Fig. 2.22a. Two narrow resonance peaks occur at 668 nm and 640 nm, which can clearly be assigned to the modes $\mathrm{TE_y}$ and $\mathrm{TE_x}$, respectively, by comparison to numerical simulations. The corresponding experimental quality factors were determined as $Q = 3400$ and $Q = 1600$, respectively. The much broader peak at 627 nm originates from the stationary point of the even waveguide mode (see Fig. 2.4b) near $k_x = 0$ in the Brillouin zone [117]. As this point lies deep within the leaky region above the light cone, the corresponding mode suffers from heavy radiation losses, leading to a very low quality factor.

To test the reproducibility of the experimental results, a series of 20 identically fabricated cavities was evaluated and the obtained quality factors Q and resonance wavelengths λ are summed up in Fig. 2.22b. In the case of the $\mathrm{TE_y}$ mode, the quality factors vary between 2200 and 3400 in all samples, which represents a clear improvement compared to the previous results obtained from L3 cavities. Even the $\mathrm{TE_x}$ mode exhibits values $Q > 1000$ in most of the samples, although in this case three structures did not show a corresponding resonance at all and had to be omitted from the analysis. Together with the larger standard deviation ΔQ of the quality factor (see Fig. 2.22b), this hints at a much higher sensitivity of the $\mathrm{TE_x}$

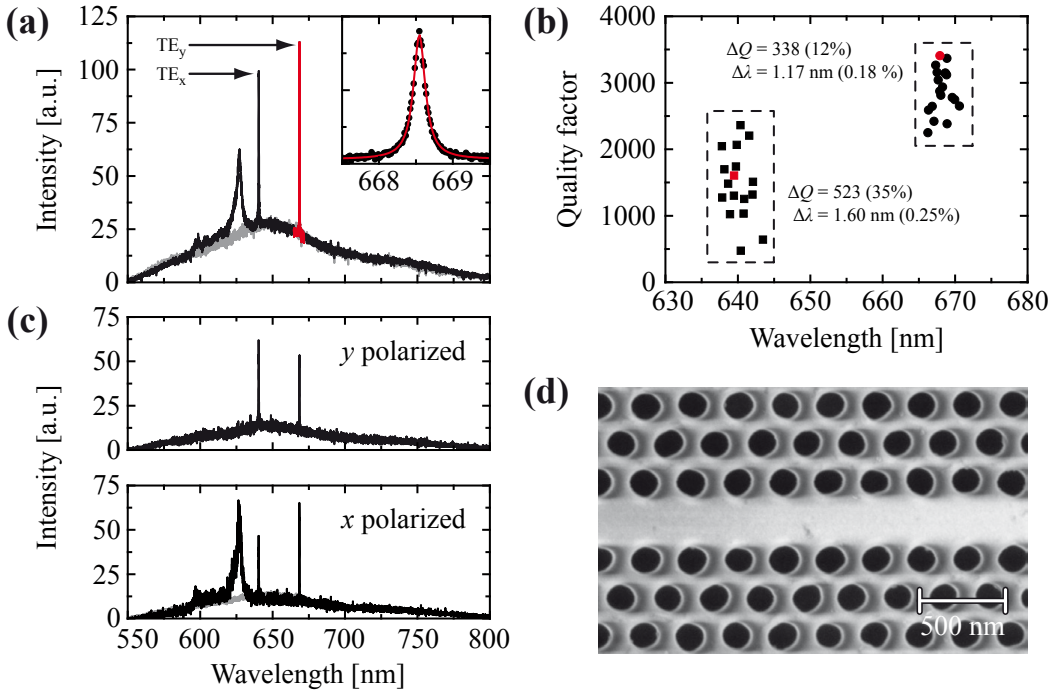

Figure 2.22: **(a)** Spectrum of the intrinsic silicon nitride fluorescence from a double-heterostructure cavity (black) and a corresponding reference spectrum (gray). The lattice parameters are $a = 270$ nm, $a' = 280$ nm, $t = 0.74a$, and $r = 0.28a$. The fundamental cavity mode TE_y is highlighted in red and a respective Lorentzian fit (red) to the experimental data (black) is shown in the inset, yielding a quality factor $Q = 3400$. **(b)** Quality factors Q for the modes TE_y (circles) and TE_x (squares), measured from a series of 20 identically fabricated cavities and plotted versus the corresponding resonance wavelength λ. The respective standard deviations ΔQ and $\Delta\lambda$ are also displayed. The red data points indicate the values derived from the spectrum shown in (a). **(c)** Spectra from the same cavity as in (a), but recorded with polarization filtering. The spectra were corrected for the polarization-dependent response of the spectrograph. **(d)** Scanning electron microscope image of one of the cavities, showing no noticeable tilt of the hole walls, but some distortions in the circularity of the holes.

mode to structural imperfections compared to the TE_y mode. The same holds for the respective standard deviation $\Delta\lambda$ of the resonance wavelength. In other samples with larger hole radii r the observed quality factors were lower on average, which is in accordance with corresponding numerical calculations, predicting decreasing Q and λ with increasing r.

At the time of these studies the experimental quality factors $Q \approx 3000$ represented the highest ever obtained for photonic crystal cavities in the visible. However, there is still a large discrepancy to the theoretical prediction $Q > 10000$. Contrary to earlier experiments with L3 cavities, the conical shape of the membrane holes should only play a minor role, as it was already strongly reduced in these samples (see Fig. 2.22d). Instead, deviations in the circularity and position of the holes seem now to be the limiting factor. This was confirmed by performing FDTD simula-

tions based on scanning electron microscope images of the cavities, thus taking into account any lateral irregularities in the photonic crystal structure. Quality factors $Q \approx 5500$ and $Q \approx 2500$ were deduced for the modes TE_y and TE_x, respectively, being in much better agreement with the experimental findings. This is also consistent with the contribution $Q_{loss} \approx 10000$ for this type of fabrication imperfection obtained in the corresponding analysis of L3 cavities (see Sec. 2.4.2). Consequently, a substantial improvement of the fabrication precision is necessary before a further increase of the quality factor can be achieved [118]. With this in mind, no additional optimization of the double-heterostructure design (although certainly possible [119]) was performed in the course of this thesis, as a significant impact on the experimental results is not expected.

2.5.2 Polarization properties

Finally, a surprising feature concerning the emission from the double-heterostructure cavities shall be discussed, namely the lack of a pronounced far-field polarization of the two cavity modes. This becomes obvious from the polarization-resolved spectra in Fig. 2.22c. While the broad resonance peak of the leaky mode is clearly polarized in x direction, the modes TE_y and TE_x seem to be almost unpolarized, in strong contrast to corresponding observations on L3 cavities (see Figs. 2.19c and 2.19d) as well as other studies of double-heterostructure cavities [117].

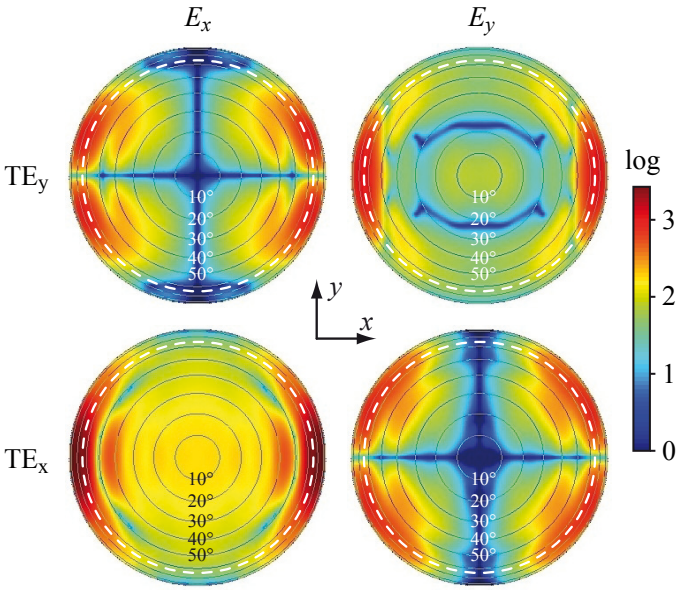

Figure 2.23: Calculated electric field distributions $|E_x|$ and $|E_y|$ of the double-heterostructure cavity modes TE_y and TE_x, projected to the far-field and displayed in an angular plot. The lattice parameters of the cavity are the same as in Fig. 2.21. The dashed white circles indicate the emission cone collected by the microscope objective used in the experiment. Note the logarithmic color scale.

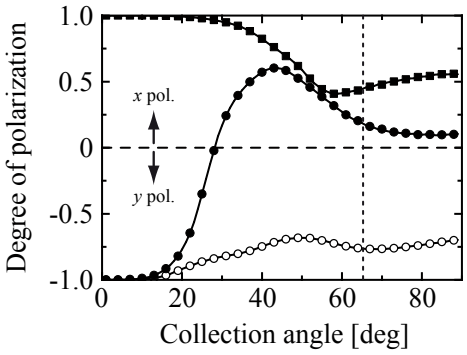

Figure 2.24: Degree of polarization D as a function of the collection angle θ for the modes TE_y (circles) and TE_x (squares) of a double-heterostructure cavity. The lattice parameters are the same as in Fig. 2.23. Positive and negative values correspond to a preferential polarization in x and y direction, respectively. The analogues results for the TE_{y1} mode of an (unmodified) L3 cavity with identical lattice parameters (open circles) are shown for comparison. The dotted vertical line indicates the collection angle of the microscope objective used in the experiment.

In order to understand this behavior the far-field radiation pattern for the individual cavity modes was deduced from corresponding FDTD simulations by monitoring the near-field in a plane directly above the photonic crystal slab and applying a spatial Fourier transformation (see Sec. 2.3.4). Note that an additional rotation of the field vectors had to be performed to account for the beam collimation through the microscope objective, which changes the polarization direction of the detected light. The results of these calculations are depicted in Fig. 2.23. As expected from the symmetry of the near-field distribution, the field components E_x and E_y of the modes TE_y and TE_x cancel in the far-field, respectively, but only for directions nearly perpendicular to the plane of the photonic crystal slab [116].

If arbitrary directions are considered, the resulting degree of polarization D which is observed on the detector strongly depends on the employed collection optics, i.e., the numerical aperture of the microscope objective. This can be seen in Fig. 2.24, where

$$D = \frac{|E_x|^2 - |E_y|^2}{|E_x|^2 + |E_y|^2} \tag{2.57}$$

is integrated over the respective collection cone with half-opening angle θ. Obviously, the detected emission exhibits a pronounced polarization for small collection angles $\theta < 20°$, which easily explains the results from cryogenic measurements in Ref. [117], where an objective with a small numerical aperture NA = 0.4 was used. For high-NA objectives, however, the polarization can completely vanish or even change its direction. This is particularly fulfilled for the microscope objective employed here, which provides a collection angle $\theta = 65°$ and explains the observations in Fig. 2.22c.

It should be noted that the exact degree of polarization measured experimentally varied between different samples, which suggests a strong sensitivity to structural imperfections.

The complicated polarization behavior of the emission from double-heterostructure cavities is fundamentally different from that of L3 cavities. As seen from the corresponding data in Fig. 2.24, a high degree of polarization is maintained in the case of the TE_{y1} mode (see Fig. 2.14) even for large collection angles θ. This example illustrates that also cavity modes with apparently similar near-field profiles can exhibit quite distinct far-field properties and underlines the necessity of a thorough theoretical investigation when interpreting such experimental results.

2.6 Summary and conclusions

In this chapter the fabrication, optimization, and optical characterization of photonic crystal cavities made from silicon nitride was reported. It could be shown that these structures are capable of operating in a large part of the visible spectrum due to the wide transparency window down to wavelengths of 550 nm. The combination of a well-developed fabrication technique and a careful optimization of the cavity design allowed the realization of cavities with quality factors exceeding 1000, a regime previously unachieved in the visible. In particular, a maximum quality factor of 3400 was demonstrated for cavities of the double-heterostructure type. An analysis of the various optical loss mechanisms revealed that this value is not fundamentally limited by the cavity design or material properties, but is a consequence of remaining fabrication imperfections.

Note that part of these findings have already been published in Barth *et al.* 2007a, 2008a (see List of Own Publications).

Meanwhile, silicon nitride photonic crystal structures have also been employed in other studies, e.g., for the realization of nanowire-based light sources [120] or plasmonic sensing devices [121], proving the versatility of this material system as a tool for the manipulation of visible light. However, its usefulness for cavity QED applications, especially those requiring high Purcell factors [122], has still to be proven. Currently, no evident approach is available how to further boost the quality factor in view of the high sensitivity of this low-index material to inevitable fabrication imperfections. Only a material with a higher refractive index may enable photonic crystal cavities in the visible with optical properties truly comparable to those of their counterparts in the near infrared.

Diamond has been investigated for this purpose [123, 124], but the fabrication of corresponding structures is extremely challenging [125, 126]. Recently, gallium phosphide has emerged as a promising candidate [127], exhibiting refractive indices

$n = 3.25$–3.45 in the wavelength range 550–700 nm [128]. Indeed, quality factors of up to 11000 have already been demonstrated with this material [129] and a corresponding implementation using the double-heterostructure design investigated here is subject of forthcoming studies. If the fabrication process proves to be reliable, gallium phosphide may supersede silicon nitride as the prime material for applications in the visible. Either way, the toolbox for creating nanophotonic devices will become larger.

Chapter 3

Assembly and investigation of hybrid nanophotonic elements

3.1 Introduction

The photonic crystal cavities studied in the previous chapter represent a versatile platform for the creation of nanophotonic devices in the visible, as they (in principle) provide control on the generation, manipulation, and transfer of photons when integrated into more complex structures. In this regard, the most challenging issue is the deterministic coupling of suitable quantum emitters to the cavities, especially if the corresponding application requires operation on a single photon level. Then, a specific emitter has not only to be spectrally and spatially aligned with respect to the cavity field, but also the coupling of other emitters has to be prevented in order to suppress unwanted background emission. Therefore, a simple coating technique, which randomly distributes dye molecules or colloidal quantum dots on the photonic crystal sample [22, 24, 25], is not suitable for most practical implementations, as was already discussed in Sec. 2.4.3. Likewise, individual self-assembled quantum dots, which are the most common type of emitters used in conjunction with III/V semiconductor devices [14, 18, 21, 23], cannot directly be incorporated into the material system employed here (i.e., silicon nitride). Consequently, alternative ways to obtain a certain degree of control and selectivity on the coupling of external emitters to the photonic crystal cavities have to be explored.

A promising approach to tackle this problem is the application of a nanoassembly method which exploits the manipulation capabilities of an atomic force microscope (or other scanning probe techniques) to deterministically place and arrange individual nanoparticles on the photonic crystal structures. Any material (or combination of materials) can be used for this purpose, provided that it is available in the form of nanoscopic particles. The latter might contain a single or multiple emitters, or

may enhance the functionality of the underlying photonic crystal platform in other ways, thus allowing the creation of a multitude of hybrid nanophotonic elements for various applications .

The second part of this thesis is devoted to the exploration of this powerful concept, which has not been studied in the context of photonic crystal devices yet. Thereby, two types of materials are of particular interest, namely diamond nanocrystals and metal nanoparticles. Diamond nanocrystals can contain various types of fluorescent defect centers [6], among which the nitrogen-vacancy center is the most prominent one. It represents a solid-state quantum emitter with unique optical properties and may therefore be used to study and exploit cavity QED effects in the visible. On the other hand, metal nanoparticles support plasmon resonances, which can lead to extremely localized and enhanced electromagnetic fields [7]. In conjunction with photonic crystal structures a novel type of plasmonic-photonic hybrid cavity might be created, presumably combining some of the benefits of both worlds, plasmonics and photonics. Ultimately, a combination of all three constituents (i.e., photonic crystal cavities, diamond nanocrystals, and metal nanoparticles) can be envisaged, enabling the simultaneous control of the emission properties of quantum emitters via plasmonic and photonic QED effects. Although this final goal could not be achieved within the course of this thesis, various stages towards its realization are presented in this chapter.

The chapter is organized as follows: In Sec. 3.2 the fundamental optical properties of nitrogen-vacancy defect centers in diamond are introduced, followed by an overview on the basics of plasmon excitations in metal nanoparticles in Sec. 3.3. Experimental details of the nanomanipulation and particle deposition method are provided in Sec. 3.4, accompanied by a brief description of the optical setup used to investigate the assembled hybrid structures. The first systems to be discussed in Sec. 3.5 are dielectric nanoparticles coupled to L3 and double-heterostructure photonic crystal cavities. The impact of the particles on the cavity properties are studied theoretically as well as experimentally. In particular, the deterministic coupling of a single diamond nanocrystal to a cavity mode is demonstrated for the first time. The experimental realization of a novel plasmonic-photonic hybrid cavity is then presented in Sec. 3.6. Various configurations involving gold nanospheres and nanorods are investigated, revealing a pronounced coupling between the plasmonic resonances and the different cavity modes, which depends sensitively on the respective field polarizations. A first step towards the combination of both approaches is reported in Sec. 3.7, where the plasmonic enhancement of the single photon emission from nitrogen-vacancy defect centers in diamond nanocrystals is demonstrated. Finally, a short summary of this chapter as well as some concluding remarks are given in Sec. 3.8.

3.2 Optical properties of defect centers in diamond

Diamond is one of the most outstanding and versatile materials on earth owing to its exceptional physical characteristics. This not only includes the extreme hardness and thermal conductivity, but also remarkable optical properties. Diamond possesses a relatively high refractive index $n = 2.42$ (at a wavelength of 600 nm) and a very large electronic band gap of 5.5 eV [130], resulting in a wide transparency window down to a wavelength of 225 nm. Impurity atoms can form defect centers in the otherwise rigid diamond lattice, more then 100 of which are known to be luminescent [6]. It is these defect centers which make diamond (and diamond nanocrystals in particular) appealing for the present purpose, as they represent photostable emitters in the visible wavelength range, operating even at room temperature. The most prominent among them is the nitrogen-vacancy (NV) defect center, which has been extensively studied on a single center level [6, 131] and shows great promise as a candidate for room temperature quantum information processing [132] owing to its outstanding optical and spin properties. In the following, an overview on these properties is given in general terms (Sec. 3.2.1) as well as with regard to the single photon character of the NV emission (Sec. 3.2.2). Furthermore, the peculiarities related to diamond nanocrystals in comparison to bulk diamond are discussed (Sec. 3.2.3).

3.2.1 Nitrogen-vacancy defect centers

The NV defect center is formed in the diamond lattice by one missing carbon atom (the vacancy) and an adjacent substitutional nitrogen atom as depicted in Fig. 3.1a. It can occur in two different charge configuration, either neutral (NV^0) or negatively charged (NV^-) with the additional electron presumably provided by excess nitrogen atoms in the vicinity of the NV center [133]. In nitrogen-rich type Ib diamond the NV^- state is usually the dominant one. Its electronic structure is still not fully understood and subject to intense experimental and theoretical research [134–140]. A common model of the energy level scheme is shown in Fig. 3.1b, summarizing some of the knowledge corroborated by experimental investigations.

The NV^- center has a triplet ground state ^3A with an energetic splitting of 2.88 GHz between the spin sublevels $^3A_{m=0}$ and $^3A_{m=\pm1}$ due to spin-spin interactions [141, 142]. The excited state ^3E is also a triplet, split by spin-spin as well as spin-orbit coupling [136, 139]. The transition $^3A \leftrightarrow {}^3E$ gives rise to a pronounced zero phonon absorption/emission line at 637 nm [143], which is flanked by phonon sidebands resulting from transitions into higher vibronic levels of the states ^3E and ^3A, respectively. The fraction of light emitted into the zero phonon line (relative to the entire emission intensity) is $\approx 5\%$ (see Fig. 3.2a). The radiative lifetime of the excited state ^3E is found to be ≈ 12 ns in bulk diamond [144].

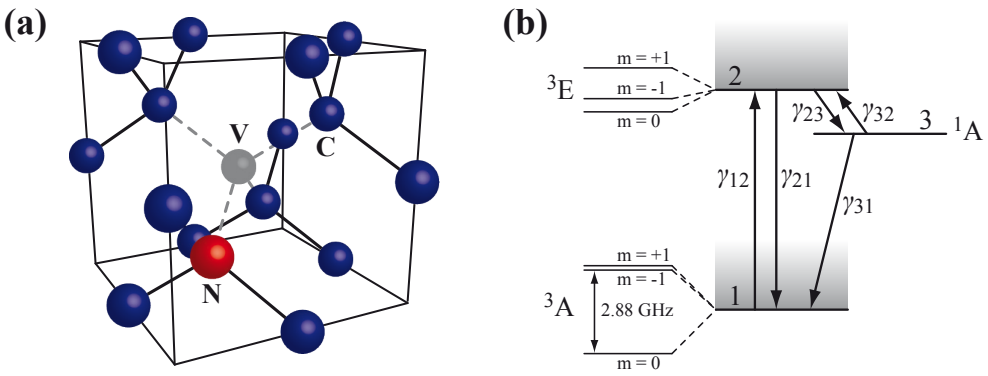

Figure 3.1: **(a)** Schematic representation of the atomic structure of the nitrogen-vacancy (NV) defect center, consisting of one missing carbon atom (vacancy V) and an adjacent substitutional nitrogen atom (N). **(b)** Energy level scheme of the NV^- center. ^3A and ^3E denote the triplet ground (1) and excited state (2), respectively, and ^1A is a metastable singlet state (3). The corresponding transition rates γ_{ij} between these states are indicated as arrows. The gray shaded areas represent the vibronic level structure of the states ^3A and ^3E, respectively.

In addition to the triplet ground and excited state, experimental evidence strongly suggests the existence of a metastable singlet state ^1A, which lies energetically between ^3A and ^3E [145]. The presence of this metastable state has important consequences for the spin as well as fluorescence properties of the NV^- center, since there is a finite probability for an intersystem crossing $^3E \rightarrow {}^1A$. The corresponding transition rate γ_{23} (see Fig. 3.1b) strongly depends on the spin sublevel in which the excited state ^3E is prepared. For the spin states $^3E_{m=\pm1}$ a value $\gamma_{23} \approx 0.65\gamma_{21}$ is found [146], while for the spin state $^3E_{m=0}$ the corresponding transition probability γ_{23} is at least three orders of magnitude smaller [147]. On the other hand, the state ^1A preferentially decays to the spin sublevel $^3A_{m=0}$ of the triplet ground state [136]. Consequently, the repeated optical excitation of the NV^- center predominantly populates the spin state $^3A_{m=0}$ and thus leads to a strong, optically induced spin polarization [148, 149]. Thereby, the spin dephasing time can reach values as long as 1.8 ms at room temperature in high-purity type IIa diamond [150], currently limited by the interaction with paramagnetic impurities (such as ^{13}C atoms) and, ultimately, by the spin-lattice relaxation time, which is on the order of 10^2–10^4 s.

The dependence of the intersystem crossing rate γ_{23} on the spin sublevel of ^3E not only allows for an optical initialization, but also for an optical read-out of the spin state of the NV^- center [147]. As long as the system is in the spin state $m = 0$, repeated absorption-emission cycles (under resonant excitation) are mostly spin-conserving [151] and give rise to a specific fluorescence intensity $I_{m=0}$. Once a spin-flip into one of the states $m = \pm1$ occurs, the probability for a transition to the metastable (non-fluorescent) state ^1A increases significantly, resulting in dark periods and thus in a reduced fluorescence intensity $I_{m\pm1} < I_{m=0}$. It is this change

in the fluorescence signal which allows the detection of the spin state, e.g., in ODMR (optically detected magnetic resonance) experiments [131]. These outstanding spin properties, i.e., the extremely long spin memory in combination with the possibility for an optical initialization and read-out of the spin state, are the foundation which makes NV^- centers promising candidates for quantum information processing at room temperature [152–156].

It should be mentioned that the fluorescence properties change drastically with decreasing temperature, especially regarding the duration of the dark intervals, which depends on the depopulation rates γ_{31} and γ_{32} (see Fig. 3.1b). At room temperature a thermally driven transition to the triplet state ^{3}E with a rate $\gamma_{32} \approx \gamma_{23}/4$ [146] provides an efficient mechanism for fluorescence recovery, while at cryogenic temperatures γ_{32} tends to zero and the dark time is mainly determined by γ_{31}, which is approximately three orders of magnitude smaller than γ_{23} [145]. Consequently, the detected fluorescence intensity drops dramatically with decreasing temperature if the system is excited resonantly, requiring the application of an additional laser of higher frequency to depopulate the metastable state ^{1}A (so-called deshelving technique) [157]. Only then a sufficiently large photon flux can also be achieved at low temperatures to allow the detection of a single NV center.

3.2.2 Single photon emission from defect centers

As was already pointed out in Sec. 2.2.5, efficient and stable single photon sources are a key requirement for quantum communication and quantum information processing. The basic operation principle relies on the fact that a single quantum system cannot emit more than one photon at a time [158], since it has to be re-excited after each emission event. Possible implementations of solid-state single photon sources involve organic molecules [159, 160], self-assembled semiconductor quantum dots [161, 162], or colloidal semiconductor nanocrystals [163]. These systems, however, suffer either from a finite lifetime due to photobleaching (in the case of molecules and colloidal quantum dots) or from the necessity to be operated at cryogenic temperatures (in the case of self-assembled quantum dots). Defect centers in diamond provide both, long-term photostability and room temperature operation [146, 164], and are therefore prime candidates for the implementation of quantum communication protocols [85, 165]. It should be noted that, apart from NV centers [146, 166], various other types of defect centers in diamond have also been demonstrated to be efficient single photon sources, including nickel-nitrogen (NE8) [167, 168] and silicon-vacancy (SiV) centers [169].

A typical room temperature fluorescence spectrum from a single NV center in a diamond nanocrystal is shown in Fig. 3.2a, exhibiting two zero phonon lines at 575 nm and 637 nm, respectively, flanked by pronounced phonon sidebands. While

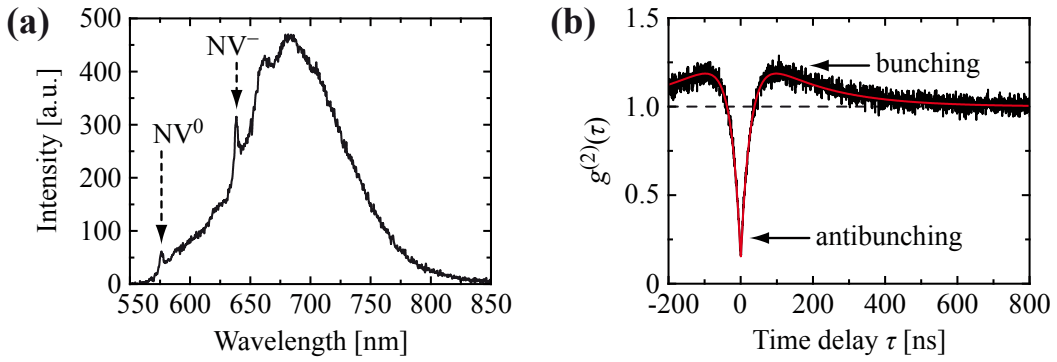

Figure 3.2: **(a)** Typical fluorescence spectrum of a single NV defect center in a diamond nanocrystal, recorded at room temperature. Two zero phonon lines are visible, associated with the neutral (NV^0) and negatively charged (NV^-) state of the center. **(b)** Measured autocorrelation function $g^{(2)}(\tau)$ (black) of the same NV center as in (a). Details of the experimental methods are provided in Sec. 3.4.2. The red curve represents a fit to the experimental data [using Eq. (3.5)] and the dashed black line indicates the asymptotic behavior for $\tau \to \infty$, marking the transition from the photon antibunching ($g^{(2)}(\tau) < 1$) to the photon bunching regime ($g^{(2)}(\tau) > 1$).

the 637 nm line is characteristic for the NV^- state, the 575 nm line can be attributed to the neutral NV^0 state of the defect center [133]. The occurrence of both zero phonon transitions is the result of a continuous conversion process $NV^- \leftrightarrow NV^0$, probably induced by a charge transfer from/to nearby electron donors [170, 171].

The assumption that the spectral features in Fig. 3.2a stem from a single NV center can be proven by recording the second-order autocorrelation function

$$g^{(2)}(\tau) = \frac{\langle : I(t)I(t+\tau) : \rangle}{\langle I(t) \rangle^2} , \tag{3.1}$$

which describes the degree of correlation between photons emitted at different times t as a function of the temporal separation τ. Here, $I(t) = \boldsymbol{E}(t) \cdot \boldsymbol{E}^*(t)$ denotes the emission intensity and $\langle : \ldots : \rangle$ represents the temporal mean in normal order. For laser light, which exhibits a Poissonian photon statistics, $g^{(2)}(\tau) = 1$ for all values of τ. Thermal light sources show an increased probability of emitting multiple photons at the same time (so-called photon bunching) [172], manifested in an increased autocorrelation function $g^{(2)}(0) = 2$ at zero time delay. On the other hand, single quantum emitters cannot emit more than one photon at a time (so-called photon antibunching) [158], resulting in a depleted autocorrelation value $g^{(2)}(0) = 0$. The measured autocorrelation function of the NV center (Fig. 3.2b) exhibits both, antibunching as well as bunching behavior, which is typical for a three-level system involving intersystem crossing to a metastable state [173]. To decide whether a single NV center contributes to the detected signal, the value $g^{(2)}(\tau = 0)$ is of particular interest, which scales with the number N of independent quantum emitters

as $g^{(2)}(0) = 1 - 1/N$. Therefore, a value $g^{(2)}(0) < 0.5$ unambiguously proves the single photon character of the emission, as is clearly the case for the measurement presented in Fig. 3.2b.

An analytic expression for the $g^{(2)}(\tau)$ function of a single NV center can be obtained from the rate equations

$$\frac{\partial \varrho_1(t)}{\partial t} = -\gamma_{12}\varrho_1(t) + \gamma_{21}\varrho_2(t) + \gamma_{31}\varrho_3(t) \,, \tag{3.2}$$

$$\frac{\partial \varrho_2(t)}{\partial t} = \gamma_{12}\varrho_1(t) - (\gamma_{21} + \gamma_{23})\varrho_2(t) + \gamma_{32}\varrho_3(t) \,, \qquad \text{and} \tag{3.3}$$

$$\frac{\partial \varrho_3(t)}{\partial t} = \gamma_{23}\varrho_2(t) - (\gamma_{31} + \gamma_{32})\varrho_3(t) \tag{3.4}$$

for the population $\varrho_i(t)$ of the various energy levels shown in Fig. 3.1b. Assuming the initial conditions to be $\varrho_1 = 1$, $\varrho_2 = 0$, and $\varrho_3 = 0$, a solution for the population $\varrho_2(t)$ of the excited state ^{3}E can be obtained, which is directly proportional to the photon emission probability. The second-order autocorrelation function is then given by

$$g^{(2)}(\tau) = \frac{\varrho_2(\tau)}{\varrho_2(\tau \to \infty)} = 1 + C\mathrm{e}^{-\Gamma_2\tau} - (C+1)\mathrm{e}^{-\Gamma_3\tau} \,, \tag{3.5}$$

with the coefficients and decay times being defined as

$$C = \frac{\Gamma_3(\gamma_{31} + \gamma_{32} - \Gamma_2)}{(\gamma_{31} + \gamma_{32})(\Gamma_2 - \Gamma_3)} \qquad \text{and} \tag{3.6}$$

$$\Gamma_{2,3} = \frac{1}{2}\Big(A \pm \sqrt{A^2 - 4B}\Big) \,, \tag{3.7}$$

where

$$A = \gamma_{12} + \gamma_{21} + \gamma_{23} + \gamma_{31} + \gamma_{32} \qquad \text{and} \tag{3.8}$$

$$B = \gamma_{12}(\gamma_{23} + \gamma_{31} + \gamma_{32}) + \gamma_{21}(\gamma_{31} + \gamma_{32}) + \gamma_{23}\gamma_{31} \,. \tag{3.9}$$

Equation (3.5) can be used to fit the experimental data (see Fig. 3.2b), providing some insight into the interplay of the various transition rates γ_{ij}. This is discussed in more detail in Sec. 3.7.2, where the plasmon-enhanced emission from individual NV centers is investigated. From the steady-state population $\varrho_2(t \to \infty)$ one can also obtain the maximum emission rate Γ_{em} under saturation (i.e., $\gamma_{12} \to \infty$), which is given by

$$\Gamma_{\mathrm{em}}(\gamma_{12} \to \infty) = \gamma_{21}\varrho_2(t, \gamma_{12} \to \infty) = \frac{\gamma_{21}}{1 + \gamma_{23}/(\gamma_{31} + \gamma_{32})} \,. \tag{3.10}$$

Compared to a pure two-level system (where $\gamma_{23} = 0$), this emission rate is limited by the dwell time of the NV center in the (dark) metastable state ^{1}A.

3.2.3 Diamond nanocrystals versus bulk diamond

So far, no clear distinction was made between defect centers which are hosted in diamond nanocrystals and bulk diamond films, respectively. In solid-state systems, however, the optical properties of emitters usually depend on the structure and quality of the surrounding material. This is particularly true for defect centers in diamond, as measurements on diamond nanocrystals have revealed clear deviations of the optical properties of individual NV centers from their counterparts in bulk films. First and foremost, the modified dielectric environment leads to a change of the spontaneous emission rate γ_{21}, which depends on the average refractive index in the surrounding of the (sub-wavelength) nanocrystal [see Eq. (2.38)] and affects the excited state lifetime $\tau_2 = \phi/\gamma_{21}$ (with $\phi \approx 0.7$ [6] denoting the fluorescence quantum yield). For example, an increase of τ_2 from the bulk value of 12 ns to values of ≈ 25 ns has been reported for nanocrystals on a silica surface [174].

Apart from changes in the radiative lifetime, also shifts in the spectral position of the zero phonon transition have been observed in diamond nanocrystals, exhibiting a distribution of ≈ 5 nm around the bulk emission wavelength of 637 nm [157, 175]. This inhomogeneous broadening is attributed to local strain in the nanocrystals, leading to modifications of the energetic position of the excited state ^{3}E and thus to shifts in the transition frequency [136]. Furthermore, the spectral width of individual zero phonon lines is usually found to be much broader (up to several orders of magnitude) than the lifetime-limited value of 12 MHz, not only in diamond nanocrystals [175, 176], but also in bulk material [151, 157]. This effect is mainly attributed to the photoionization of nitrogen impurities (which are abundant in type Ib diamond) in the vicinity of the NV center. The resulting charge fluctuations lead to jumps of the transition frequency, observable as spectral diffusion and, when averaged, as linewidth broadening in excitation measurements.

Nitrogen impurities are also the limiting factor for the spin coherence time in type Ib diamond (≈ 10 µs [176]), which is so far the only available material for diamond nanocrystals. In fact, it has been demonstrated that in nitrogen-depleted type IIa diamond films the linewidth can reach almost lifetime-limited values of 13 MHz [177, 178], and that spin coherence times of up to 1.8 ms [150] are possible, as discussed in Sec. 3.2.1. The question whether these beneficial properties can be transferred to type IIa diamond nanocrystals remains the subject of future studies.

3.3 Optical properties of metal nanoparticles

Metal particles with sizes much smaller than the wavelength of light exhibit optical properties which are quite different from those of the corresponding bulk materials, especially regarding their scattering and absorption characteristics. The latter

are responsible, e.g., for the bright colors in stained glass windows and have been of interest for centuries [179]. The peculiar nanoparticle properties originate from the interplay between light and collective electron oscillations at the surface of the metal, so-called surface plasmon polaritons. It is these polaritons which have attracted considerable attention in recent years due to their ability to concentrate and guide light in sub-wavelength structures [7], being the foundation for the entire research area of plasmonics [180, 181]. In the following, the basic optical properties of surface plasmon polaritons in general (Sec. 3.3.1) and those in metal nanoparticles (Sec. 3.3.2) are discussed, focusing on the effects of field localization and enhancement as well as on the related phenomenon of spontaneous emission modification near metal structures (Sec. 3.3.3).

3.3.1 Surface plasmon polaritons

Plasmons are collective oscillations of the electron gas in a metal. At the interface to a dielectric material, these oscillations lead to fluctuations in the surface charge density of the metal, giving rise to electromagnetic waves in the dielectric. This coupled plasmonic-photonic excitation is termed surface plasmon polariton or, as in the following, simply surface plasmon. It can occur in a traveling form (propagating, e.g, on a planar surface or along a metal wire) or in a stationary form (localized, e.g., at a metal nanoparticle or in a plasmonic cavity). Although only metal nanoparticles are employed in the experimental part of this chapter, it is instructive to consider at first the basic optical properties of surface plasmons at a planar interface before advancing to the more complicated case of metal nanoparticles.

As a starting point an interface (in the x-y plane) between two media (with dielectric functions ε_1 and ε_2, respectively) shall be considered, upon which a p-polarized plane wave is impinging (in the x-z plane). Then, the following relations can be deduced from momentum conservation and continuity requirements [180, 182]:

$$\varepsilon_i |\boldsymbol{k}|^2 = k_x^2 + k_{z,i}^2 \qquad (i = 1, 2) \qquad \text{and} \tag{3.11}$$

$$\varepsilon_2 k_{z,1} = \varepsilon_1 k_{z,2} \; . \tag{3.12}$$

Here, k_x and $k_{z,i}$ are the respective wave vector components in the two media. Combining Eqs. (3.11) and (3.12) yields the dispersion relations

$$k_x^2 = \frac{\varepsilon_1 \varepsilon_2}{\varepsilon_1 + \varepsilon_2} |\boldsymbol{k}|^2 \qquad \text{and} \tag{3.13}$$

$$k_{z,i}^2 = \frac{\varepsilon_i^2}{\varepsilon_1 + \varepsilon_2} |\boldsymbol{k}|^2 \qquad (i = 1, 2) \; . \tag{3.14}$$

In order to obtain waves which are bound to the surface (as is the case for surface plasmons), $k_{z,1}$ and $k_{z,2}$ in Eq. (3.14) have to be purely imaginary. Under the assumption that the imaginary parts ε_i'' of the dielectric functions $\varepsilon_i = \varepsilon_i' + i\varepsilon_i''$ are much smaller than the corresponding real parts ε_i', this condition can only be fulfilled if $\varepsilon_1 + \varepsilon_2 < 0$. On the other hand, k_x in Eq. (3.13) has to be real for surface plasmons propagating along the interface, leading to the additional requirement $\varepsilon_1\varepsilon_2 < 0$. Consequently, one of the materials must exhibit a negative dielectric function with an absolute value exceeding that of the other (positive) dielectric material in order to allow the existence of surface plasmons. Note that no such solution is possible if s-polarized waves are considered, as no surface charge oscillations occur in this case.

In the optical wavelength range the above-mentioned conditions are fulfilled for interfaces between dielectrics and metals (particularly noble metals such as silver or gold), the latter typically exhibiting large negative ε_2' and small ε_2'' (see Appendix A). Using the Drude model for a free electron gas [183], the dielectric function of the metal is given by

$$\varepsilon_{\mathrm{D}}(\omega) = 1 - \frac{\omega_{\mathrm{p}}^2}{\omega^2 + i\kappa\omega} \,, \tag{3.15}$$

where $\omega_{\mathrm{p}} = \sqrt{\rho_{\mathrm{e}} e^2/(m_{\mathrm{e}}\varepsilon_0)}$ is the bulk plasma frequency, with e, ρ_{e}, and m_{e} being the elementary charge, volume density, and mass of the electrons, respectively. κ is a damping factor which accounts for electron-electron and electron-phonon scattering. In the case of gold, Eq. (3.15) reproduces the general trend of the experimentally obtained dielectric function for wavelengths above 600 nm (see Appendix A), while at shorter wavelengths the simple Drude model is no longer valid as interband transitions in the metal become significant.

As an example, the electric field (intensity) distribution for a surface plasmon at a gold-air interface is shown in Fig. 3.3a, assuming a wavelength $\lambda = 633$ nm. The decay length of the electric field $|\boldsymbol{E}|$ is approximately $\lambda/2 \approx 300$ nm in air and is on the order of the skin depth $\lambda/(4\pi\sqrt{\varepsilon_2}) \approx 20$ nm in the gold film. Due to the large jump of $|\varepsilon_i'|$ at the interface, the electric field is strongly enhanced directly above the gold surface. This field enhancement is one of the key properties which makes surface plasmons attractive for a number of applications, including surface-enhanced Raman scattering [184, 185], fluorescence enhancement [186–188], and biochemical sensing [189]. It becomes even more pronounced in the case of metal nanoparticles, as is discussed below.

Another important property of surface plasmons is related to the dispersion relation $\omega(k_x)$, which can be derived from Eq. (3.13) and is plotted in Fig. 3.3b, assuming a Drude-type dielectric function $\varepsilon_{\mathrm{D}}(\omega)$ as given by Eq. (3.15). Although becoming inaccurate at higher frequencies, it qualitatively illustrates the fact that

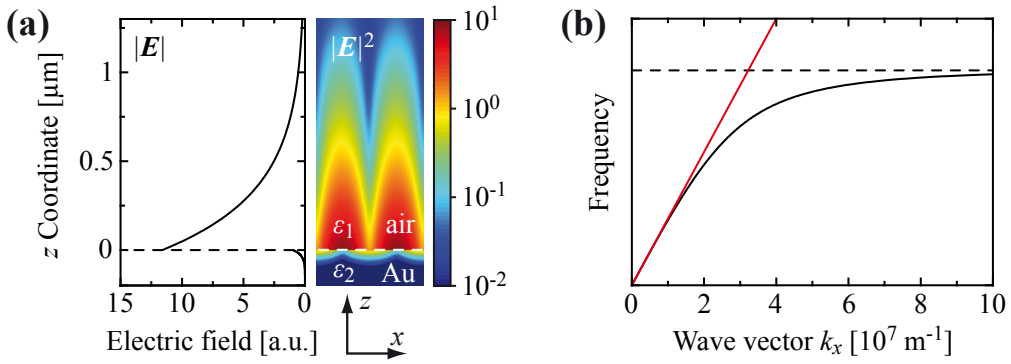

Figure 3.3: **(a)** Calculated electric field (intensity) distribution of a standing surface plasmon wave at the interface between a gold film and air. The exponential decay of $|\boldsymbol{E}|$ (left) is derived from Eq. (3.14), while the intensity pattern $|\boldsymbol{E}|^2$ (right) results from numerical simulations. The dielectric function for gold at 633 nm is assumed as $\varepsilon_2 = -11.6 + 1.2i$. **(b)** Dispersion relation $\omega(k_x)$ (black) for a surface plasmon at the gold-air interface according to Eq. (3.13), using a Drude-type dielectric function $\varepsilon_\mathrm{D}(\omega)$ [Eq. (3.15)]. The solid red line represents the light line $\omega = c|\boldsymbol{k}|$ and the dashed black line marks the frequency at which $\varepsilon_2(\omega) = -\varepsilon_1$.

the plasmon dispersion curve always lies below the light line $\omega = c|\boldsymbol{k}|$. Consequently, surface plasmons (on a planar interface) cannot be excited by light propagating in free space and, in turn, cannot radiate into free-space modes due to the momentum mismatch. Coupling between surface plasmons and radiation modes can be facilitated, e.g., through corrugations on the metal surface (which break the translational symmetry) or by using evanescent coupling schemes (such as frustrated total internal reflection or near-field sources) [180, 182].

3.3.2 Plasmon excitation in metal nanoparticles

Contrary to planar interfaces, where the wave vector component k_x is conserved, surface plasmons in metal nanoparticles can directly be excited by an incident plane wave. The external driving field $\boldsymbol{E}_0$ induces a displacement of the electrons with respect to the positively charged metal lattice, leading to charge accumulations at the surface of the particles and hence to large electromagnetic fields in the immediate surrounding. This is shown for a number of different nanoparticle configurations and excitation polarizations in Fig. 3.4.

In the case of a metal sphere [with $\varepsilon_2(\omega)$] in a dielectric medium (with ε_1), the corresponding field distribution in the quasi-static approximation [180, 182] is given by

$$\boldsymbol{E}_1(\boldsymbol{r}) = \boldsymbol{E}_0 + \alpha_0(\omega)\frac{3(\hat{\boldsymbol{x}}\cdot\hat{\boldsymbol{r}})\hat{\boldsymbol{r}} - \hat{\boldsymbol{x}}}{4\pi\varepsilon_0\varepsilon_1|\boldsymbol{r}|^3}|\boldsymbol{E}_0| \qquad \text{and} \tag{3.16}$$

$$\boldsymbol{E}_2(\boldsymbol{r}) = \frac{3\varepsilon_1}{\varepsilon_2(\omega) + 2\varepsilon_1}\boldsymbol{E}_0\ . \tag{3.17}$$

Here, $\boldsymbol{E}_1(\boldsymbol{r})$ and $\boldsymbol{E}_2(\boldsymbol{r})$ are the fields in the dielectric and in the metal, respectively. The driving plane wave $\boldsymbol{E}_0$ is polarized in x direction, with $\hat{\boldsymbol{x}}$ denoting the corresponding unit vector. The second term on the right hand side of Eq. (3.16) is identical to the field of an induced dipole moment $\boldsymbol{\mu}_1 = \alpha_0(\omega)\boldsymbol{E}_0$ at the center ($\boldsymbol{r} = 0$) of the sphere [33], with the polarizability $\alpha_0(\omega)$ being defined as

$$\alpha_0(\omega) = 4\pi\varepsilon_0\varepsilon_1 R^3 \frac{\varepsilon_2(\omega) - \varepsilon_1}{\varepsilon_2(\omega) + 2\varepsilon_1} \,. \tag{3.18}$$

According to Eqs. (3.16) and (3.18), the magnitude of the dipole field $\boldsymbol{E}_1(\boldsymbol{r})$ reaches a maximum for $\varepsilon_2'(\omega) \approx -2\varepsilon_1'$, a behavior which is denoted as surface plasmon resonance (see Fig. 3.4h). It is this resonance which dominates the extinction spectra of metal nanoparticles, with the scattering and absorption cross sections being given by [180, 182]

$$\sigma_{\text{scat}} = \frac{|\boldsymbol{k}|^4}{6\pi\varepsilon_0}\big|\alpha_0(\omega)\big|^2 \qquad \text{and} \tag{3.19}$$

$$\sigma_{\text{abs}} = \frac{|\boldsymbol{k}|}{\varepsilon_0\sqrt{\varepsilon_1}}\text{Im}\{\alpha_0(\omega)\} \,, \tag{3.20}$$

respectively. From Eqs. (3.19) and (3.20) it follows that $\sigma_{\text{scat}} \propto R^6$ and $\sigma_{\text{abs}} \propto R^3$, which means that absorption is the primary loss mechanism in small metal particles, while scattering becomes dominant with increasing particle size.

Based on the above-mentioned condition $\varepsilon_2'(\omega) \approx -2\varepsilon_1'$, it could be suspected that the resonance frequency is independent of the particle radius R. However, for radii $R < 20$ nm electron scattering at the particle surface becomes a significant contribution to the damping factor κ in Eq. (3.15), inducing a size dependence $\kappa \propto 1/R$, which leads to a red-shift and a broadening of the plasmon resonance [190]. On the other hand, for radii $R > 20$ nm the quasi-static dipole approximation becomes inaccurate as also higher multipole excitations contribute to the induced electromagnetic field and retardation effects have to be taken into account [191]. Then, with R increasing beyond the skin depth of the metal, the homogeneous polarization field inside the particle [as predicted by Eq. (3.17)] is squeezed towards the surface, resulting in an incomplete polarization.

To some extend these effects can be included in the dipole approximation by replacing the polarizability $\alpha_0(\omega)$ by the generalized expression [192]

$$\alpha(\omega) = \alpha_0(\omega)\left[1 - \frac{|\boldsymbol{k}|^2}{4\pi\varepsilon_0 R}\alpha_0(\omega) - i\frac{\sqrt{\varepsilon_1}|\boldsymbol{k}|^3}{6\pi\varepsilon_0}\alpha_0(\omega)\right]^{-1} \,. \tag{3.21}$$

Here, the second term on the right hand side of Eq. (3.21) accounts for depolarization, while the third, so-called radiation reaction term describes the radiative

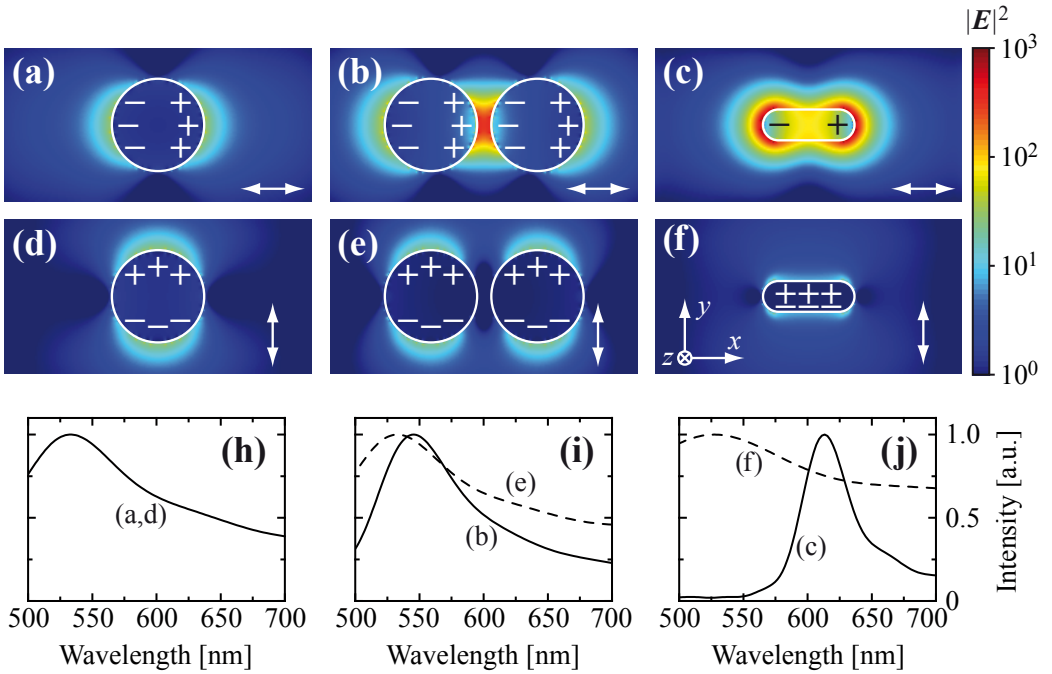

Figure 3.4: Calculated electric field intensity distributions $|\boldsymbol{E}|^2$ of various gold nanoparticles (in air) upon excitation with a plane wave (propagating in z direction). **(a,d)** A single 60 nm gold sphere. **(b,e)** A pair of 60 nm gold spheres with a 10 nm gap in between. **(c,f)** A single gold rod 20 nm in diameter and 60 nm in length. The incident wave is either polarized in x direction (a–c) or in y direction (d–f). The intensity pattern is always plotted at the peak wavelength of the respective plasmon resonance. The charge distribution inside the gold nanoparticles is also depicted schematically for each configuration. **(h–j)** Normalized resonance spectra of the configurations shown in (a–f) as indicated at each curve.

damping of the plasmon excitation. The net effect of both corrections is a red-shift and a broadening of the (dipole) plasmon resonance with increasing radius R of the particle.

If the spherical nanoparticle is elongated in a particular direction (see Figs. 3.4c and 3.4f), the plasmon resonance splits into two distinct bands (see Fig. 3.4j), corresponding to electron oscillations along the minor axes (transverse plasmon resonance) and along the major axis (longitudinal plasmon resonance), respectively [190, 191]. The peak wavelength of the transverse plasmon resonance (Fig. 3.4f) of such a nanorod resembles that of the spherical particle and is practically insensitive to the aspect ratio $r = R_1/R_2$, where R_1 and R_2 denote the length and width of the nanorod, respectively. The peak wavelength of the longitudinal plasmon resonance (Fig. 3.4c) shifts to the red with increasing aspect ratio r, which can intuitively be understood from the larger separation of the surface charges at both ends of the rod and the corresponding reduction in electromagnetic energy. As seen in Fig. 3.4c, this is typically accompanied by a very strong field enhancement, resulting from the large charge accumulations at the ends of the rod (so-called lightning rod effect) [193] and

the reduced impact of absorption damping (caused by interband transitions in the metal) at longer wavelengths [194]. The latter effect also leads to a narrowing of the plasmon resonance (see Fig. 3.4j).

If two metal nanoparticles are brought into close proximity of each other (see Figs. 3.4b and 3.4e), the individual plasmon excitations start to couple via the evanescent electromagnetic field [195, 196]. Again, two distinct plasmon resonances occur (see Fig. 3.4i), corresponding to electron oscillations perpendicular and parallel to the dimer axis (i.e., the axis connecting both particles), respectively. In the case of perpendicular excitation (Fig. 3.4e), the field configuration as well as the resonance wavelength largely resemble those of the individual particles, since only a slightly repulsive interaction occurs. In the case of parallel excitation (Fig. 3.4b), the interaction is attractive, resulting in a red-shift of the respective resonance wavelength and a very pronounced field enhancement in the gap between the particles. For example, extremely high local enhancement factors on the order of 10^5 have been predicted for very small particle separations $\Delta x \approx 2$ nm [193].

It has been found experimentally that both effects, the resonance shift as well as the field enhancement, follow a scaling law of the form $\exp(-s/L)$, where $s = \Delta x/(2R)$ is the gap size normalized to the particle diameter (or another characteristic length in the case of non-spherical particles) and $L \approx 0.2$ is a universal decay constant, taking similar values for a variety of metals and particle shapes [197]. Note that if the gap size is reduced to values below $\Delta x \approx 1$ nm, conductive coupling sets in, resulting in an abrupt renormalization of the plasmon resonance towards shorter wavelengths [198].

Finally, it should be emphasized that not only the size and shape of the metal nanoparticle determines the spectral position of the plasmon resonance, but also the dielectric surrounding. As is seen from the resonance condition $\varepsilon_2'(\omega) \approx -2\varepsilon_1'$ and Eq. (3.15), an increase in the local dielectric constant ε_1 leads to a red-shift of the resonance wavelength, being the foundation for a variety of sensing applications utilizing metal nanoparticles [189].

3.3.3 Fluorescence enhancement near metal nanoparticles

As was already mentioned above, the strong field enhancement near metal nanoparticles can be exploited to influence the emission properties of molecules or other quantum emitters [186–188]. In analogy to the emitter-cavity coupling discussed in Sec. 2.2.5, the surface plasmon mode couples to the transition dipole moment of the emitter, thus altering the decay dynamics of the latter. However, in comparison to cavity modes (which typically exhibit very narrow spectral linewidths), the plasmon resonance is broad-band and usually affects the excitation as well as the emission process. In this sense, the metal nanoparticle can be viewed as a transceiver for

the emitter, converting far-field radiation (via the surface plasmon resonance) into a strongly localized near-field and *vice versa*. This analogy has inspired the term nanoantennas [199] for such devices.

In detail, the presence of the metal nanoparticle influences the excitation rate γ_{exc} as well as the radiative rate γ_{rad} of the emitter (through the localized surface plasmon field), but also induces an additional non-radiative decay channel caused by absorption losses in the metal (characterized by the rate γ_{abs}) [200]. The apparent enhancement of the total emission rate Γ_{em} (below saturation) in comparison to the corresponding rate $\Gamma_{\mathrm{em},0}$ without metal particle is then given by [201]

$$\frac{\Gamma_{\mathrm{em}}}{\Gamma_{\mathrm{em},0}} = \frac{\gamma_{\mathrm{exc}}}{\gamma_{\mathrm{exc},0}} \frac{\phi}{\phi_0} = \frac{\gamma_{\mathrm{exc}}}{\gamma_{\mathrm{exc},0}} \frac{\gamma_{\mathrm{rad}}}{\gamma_{\mathrm{rad},0}} \frac{\gamma_{\mathrm{rad},0} + \gamma_{\mathrm{nr},0}}{\gamma_{\mathrm{rad}} + \gamma_{\mathrm{nr}} + \gamma_{\mathrm{abs}}} , \tag{3.22}$$

where $\phi = \gamma_{\mathrm{rad}}/(\gamma_{\mathrm{rad}} + \gamma_{\mathrm{nr}} + \gamma_{\mathrm{abs}})$ and $\phi_0 = \gamma_{\mathrm{rad},0}/(\gamma_{\mathrm{rad},0} + \gamma_{\mathrm{nr},0})$ denote the fluorescence quantum yield of the emitter with and without metal particle, respectively. γ_{nr} and $\gamma_{\mathrm{nr},0}$ represent the corresponding intrinsic non-radiative decay channels, for which $\gamma_{\mathrm{nr}} = \gamma_{\mathrm{nr},0}$ is assumed in the following. Then, the quantum yield ϕ can be rewritten in terms of the individual rate enhancements as

$$\phi = \frac{\gamma_{\mathrm{rad}}/\gamma_{\mathrm{rad},0}}{\gamma_{\mathrm{rad}}/\gamma_{\mathrm{rad},0} + \gamma_{\mathrm{abs}}/\gamma_{\mathrm{rad},0} + (1-\phi_0)/\phi_0} . \tag{3.23}$$

In general, the different rates depend on a multitude of factors, such as the size and shape of the nanoparticle, the position and orientation of the dipole moment of the emitter relative to the nanoparticle, and the dielectric environment. In order to get an intuitive understanding of the underlying physics, it is instructive to consider a simple model system, i.e., a gold nanosphere of radius R and a dipole emitter located at a distance Δx from the sphere surface (see inset in Fig. 3.5a), both being excited by a plane wave $\boldsymbol{E}_0$ polarized in x direction. Below saturation the excitation rate γ_{exc} is proportional to $\left|\boldsymbol{\mu}_0 \cdot \boldsymbol{E}(\boldsymbol{r}_0)\right|^2$, with $\boldsymbol{\mu}_0$ and $\boldsymbol{r}_0$ denoting the transition dipole moment and the position of the emitter, respectively, and $\boldsymbol{E}(\boldsymbol{r}_0)$ representing the excitation field. In the dipole approximation, $\boldsymbol{E}(\boldsymbol{r}_0) = \boldsymbol{E}_0$ for the case without nanoparticle, while in the presence of the particle $\boldsymbol{E}(\boldsymbol{r}_0) = \boldsymbol{E}_1(\boldsymbol{r}_0)$ as given by Eq. (3.16). In the ideal situation of an emitter located on and oriented along the central x axis (where coupling to the surface plasmon is most efficient), the enhancement of the excitation rate takes the form

$$\frac{\gamma_{\mathrm{exc}}}{\gamma_{\mathrm{exc},0}} = \frac{\left|\boldsymbol{\mu}_0 \cdot \boldsymbol{E}_1(\boldsymbol{r}_0)\right|^2}{\left|\boldsymbol{\mu}_0 \cdot \boldsymbol{E}_0\right|^2} = \left| 1 + \frac{2R^3}{(R+\Delta x)^3} \frac{\varepsilon_2(\omega_{\mathrm{exc}}) - \varepsilon_1}{\varepsilon_2(\omega_{\mathrm{exc}}) + 2\varepsilon_1} \right|^2 , \tag{3.24}$$

which is plotted in Fig. 3.5a for a 60 nm gold sphere and an excitation wavelength $\lambda_{\mathrm{exc}} = 532$ nm.

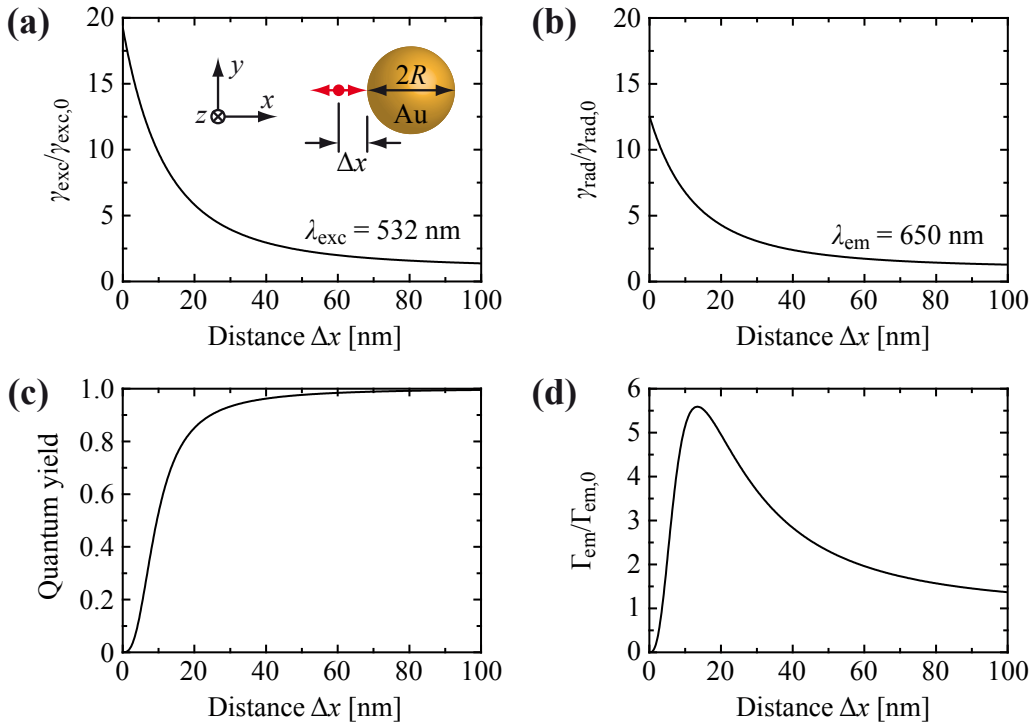

Figure 3.5: Calculated emission properties of a single dipole emitter located at a distance Δx from a 60 nm gold sphere [see inset in (a)]. **(a)** Enhancement of the excitation rate γ_{exc} (at a wavelength $\lambda_{exc} = 532$ nm) according to Eq. (3.24). For the dielectric function of gold a value $\varepsilon_2 = -4.7 + 2.4i$ is assumed. **(b)** Enhancement of the radiative rate γ_{rad} (at a wavelength $\lambda_{em} = 650$ nm) according to Eq. (3.26). For the dielectric function of gold a value $\varepsilon_2 = -13 + 1.05i$ is assumed. **(c)** Fluorescence quantum yield ϕ according to Eq. (3.23), assuming $\phi_0 = 1$. **(d)** Enhancement of the total emission rate Γ_{em} according to Eq. (3.22).

While the external field $\boldsymbol{E}_0$ is the driving force for excitation processes, the dipole moment $\boldsymbol{\mu}_0$ itself constitutes the source when considering emission from the coupled emitter-particle system. According to Fermi's golden rule [see Eq. (2.35)], the radiative rate $\gamma_{rad,0}$ (without metal particle) is proportional to $|\boldsymbol{\mu}_0|^2$. The corresponding dipole field $\boldsymbol{E}_{\boldsymbol{\mu}_0}(\boldsymbol{r})$ induces a secondary dipole moment

$$\boldsymbol{\mu}_1(\boldsymbol{r}) = \alpha_0(\omega)\boldsymbol{E}_{\boldsymbol{\mu}_0}(\boldsymbol{r}) = \alpha_0(\omega)\frac{3(\boldsymbol{\mu}_0 \cdot \hat{\boldsymbol{r}}_{r_0})\hat{\boldsymbol{r}}_{r_0} - \boldsymbol{\mu}_0}{4\pi\varepsilon_0\varepsilon_1|\boldsymbol{r} - \boldsymbol{r}_0|^3} \tag{3.25}$$

in the gold sphere, where $\hat{\boldsymbol{r}}_{r_0}$ denotes the unit vector pointing along the direction defined by $\boldsymbol{r} - \boldsymbol{r}_0$. This induced dipole moment also contributes to the far-field emission such that $\gamma_{rad} \propto \left|\boldsymbol{\mu}_0 + \boldsymbol{\mu}_1(\boldsymbol{r})\right|^2$ [201], yielding an enhancement of the radiative rate

$$\frac{\gamma_{rad}}{\gamma_{rad,0}} = \frac{\left|\boldsymbol{\mu}_0 + \boldsymbol{\mu}_1(\boldsymbol{r})\right|^2}{|\boldsymbol{\mu}_0|^2} = \left|1 + \frac{2R^3}{(R+\Delta x)^3}\frac{\varepsilon_2(\omega_{em}) - \varepsilon_1}{\varepsilon_2(\omega_{em}) + 2\varepsilon_1}\right|^2 . \tag{3.26}$$

Again, the emitter was assumed to be located on and oriented along the central x axis. Apparently, Eq. (3.26) has the same functional form as Eq. (3.24) and is plotted in Fig. 3.5b for an emission wavelength $\lambda_{\mathrm{em}} = 650$ nm.

An expression for the absorption rate γ_{abs} can be obtained by analyzing the power P_{abs} dissipated inside the metal, which is given by [187]

$$P_{\mathrm{abs}} = \frac{\varepsilon_0 \varepsilon_2'' \omega_{\mathrm{em}}}{2} \int\limits_V \mathrm{d}\boldsymbol{r} \left|\boldsymbol{E}(\boldsymbol{r})\right|^2 . \tag{3.27}$$

Here, $\boldsymbol{E}(\boldsymbol{r})$ is the electric field distribution inside the metal and the integration runs over the entire volume V of the metal structure. For a spherical particle in the dipole approximation, $\boldsymbol{E}(\boldsymbol{r}) = \boldsymbol{E}_2$ as given by Eq. (3.17) (but with $\boldsymbol{E}_0$ being substituted by $\boldsymbol{E}_{\boldsymbol{\mu}_0}$), resulting in an expression $P_{\mathrm{abs}} \propto \mathrm{Im}\{\alpha_0(\omega_{\mathrm{em}})\}/|\Delta x|^6$ [202]. However, this approach is only valid for distances $\Delta x > R$, while at short separations $\Delta x \ll R$ (where dissipative processes become significant) the emitter effectively interacts with a plane metal surface. Then, the integration of the dipole field $\boldsymbol{E}_{\boldsymbol{\mu}_0}(\boldsymbol{r})$ has to be performed over the metal half space, yielding the relative absorption rate [201]

$$\frac{\gamma_{\mathrm{abs}}}{\gamma_{\mathrm{rad},0}} = \frac{P_{\mathrm{abs}}}{P_{\mathrm{rad},0}} = \frac{3c^3}{8\sqrt{\varepsilon_1}\omega_{\mathrm{em}}^3} \mathrm{Im}\left\{\frac{\varepsilon_2(\omega_{\mathrm{em}}) - \varepsilon_1}{\varepsilon_2(\omega_{\mathrm{em}}) + \varepsilon_1}\right\} \frac{1}{|\Delta x|^3} , \tag{3.28}$$

where the total radiation power in a homogeneous medium is given by $P_{\mathrm{rad},0} = \sqrt{\varepsilon_1}|\boldsymbol{\mu}_0|^2\omega_{\mathrm{em}}^4/(12\pi\varepsilon_0 c^3)$.

With Eqs. (3.24), (3.26), and (3.28) at hand, the quantum yield ϕ [Eq. (3.23)] and the emission rate enhancement $\Gamma_{\mathrm{em}}/\Gamma_{\mathrm{em},0}$ [Eq. (3.22)] can be calculated. The corresponding functions (using $\lambda_{\mathrm{exc}} = 532$ nm, $\lambda_{\mathrm{em}} = 650$ nm, and $\phi_0 = 1$) are plotted in Figs. 3.5c and 3.5d, respectively. Note that although the underlying analysis is very simple, the results in Fig. 3.5 agree astonishingly well with rigorous numerical simulations of a similar system [201]. Obviously, fluorescence quenching dominates at very short distances $\Delta x < 10$ nm, while a considerable net enhancement of the emission rate Γ_{em} occurs for separations $\Delta x \approx 10$–20 nm.

As the spectral maxima of γ_{abs} and $\gamma_{\mathrm{exc/rad}}$ are determined by $\varepsilon_2'(\omega) \approx -\varepsilon_1'$ and $\varepsilon_2'(\omega) \approx -2\varepsilon_1'$, respectively, the emission rate Γ_{em} peaks at a wavelength which is red-shifted relative to the plasmon resonance of the nanoparticle [203, 204]. With growing ε_1 the peak of the plasmon resonance and, accordingly, that of the emission enhancement shifts to longer wavelengths and increases in strength due to a reduction of absorption losses in the metal [205]. Other particle shapes (such as nanorods) and/or multi-particle configurations (such as dimer structures) support much larger electromagnetic fields and, consequently, enable much higher emission enhancement factors on the order of 10^3 [206].

Finally, it should be mentioned that not only the various transition rates of an emitter can be altered in the presence of a metal nanoparticle, but also the angular emission pattern. This effect occurs if the nanoparticle exhibits a preferential dipole moment orientation (as is the case, e.g., for nanorods) which does not coincide with that of the emitter. Then, the total angular emission is a mixture of both dipole contributions, with that of the metal particle being the dominant one for wavelengths near the plasmon resonance. Consequently, nanoantennas can be employed to reversibly control the angular emission of a single emitter [207, 208]. However, for spherical particles as the one treated above, such an effect does not occur since the induced dipole moment $\boldsymbol{\mu}_1$ is always oriented in the same direction as $\boldsymbol{\mu}_0$.

3.4 Experimental methods

Although the main details of the fabrication of photonic crystal cavities and their optical characterization were already provided in Secs. 2.3.1 and 2.3.2, the combination with diamond or metal nanoparticles required the development of a versatile assembly technique, which is introduced in the following (Sec. 3.4.1). Furthermore, a modified spectroscopic setup was employed for some of the experiments presented in this chapter, being capable of performing photon correlation measurements as well as simultaneous assembly steps. This setup is described in Sec. 3.4.2.

3.4.1 Manipulation of nanoparticles using scanning probes

The realization of hybrid nanophotonic elements as proposed in this thesis requires a method to assemble the individual constituents (namely photonic crystal cavities and diamond or metal nanoparticles) in a well-controlled manner. For this purpose, the possibility of depositing and moving individual particles on the photonic crystal surface by means of scanning probes was explored. Compared to lithographic or self-assembly methods, such a technique offers the advantage that the constituents are not fixed and can, in principle, be rearranged at any time after the assembly to study different configurations of one and the same system.

After impressive experiments showing the manipulation of single atoms with a scanning tunneling microscope [209], the first demonstration of the controlled positioning of nanometer-sized objects on a surface was performed by applying an atomic force microscope (AFM) [210]. Since these pioneering studies several groups have used AFM manipulation to create artificial structures from individual nanoparticles, e.g., to improve surface enhanced Raman spectroscopy [211] or to engineer surface plasmon resonances [212, 213]. However, the capability of this technique to realize hybrid nanophotonic elements has not been explored so far and is therefore one of the main subjects of this thesis. In the following, after introducing the basic

principles of atomic force microscopy, the general approach as well as peculiarities of the particle manipulation with an AFM are discussed. Furthermore, a method is described which allows the local deposition of small particle reservoirs near the photonic crystal structures prior to the AFM manipulation.

Principles of atomic force microscopy

Atomic force microscopy [214] utilizes the local mechanical interaction of a sharp tip with the surface of a sample to gain information on the topography or other physical properties of the latter. For this purpose, the tip is mounted on a cantilever, which deflects towards or away from the surface depending on whether the force between the tip and the sample is attractive or repulsive, respectively. By scanning the tip over the sample surface and detecting the change in the deflection of the cantilever, an image of the corresponding surface area is obtained. This operation principle is schematically depicted in Fig. 3.6a. Usually, the deflection is measured by means of a laser beam being reflected from the back of the cantilever, thus translating the microscopic bending into a macroscopic change of the beam path. By detecting the position of the laser beam with a quadrant photodiode, the optical information can then be converted into an electrical signal.

For a deeper understanding of the operation principles of an AFM, one has to consider the forces arising between the tip and the sample surface. If both are uncharged, the interaction is always attractive at larger separations due to van der

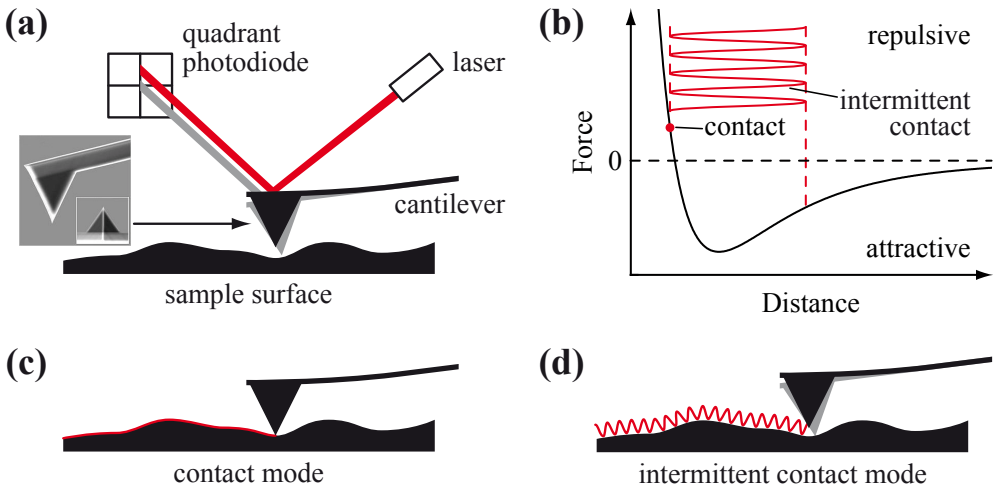

Figure 3.6: **(a)** Schematic illustration of the operation principle of an AFM, demonstrating the optical read-out of the cantilever deflection. The inset shows a scanning electron microscope image of the employed AFM tip. **(b)** Qualitative distance dependence of the force between the tip and the sample (solid black curve) derived from the Lennard-Jones potential [Eq. (3.29)]. The corresponding operational regimes for contact mode and intermittent contact mode are indicated in red. **(c,d)** Schematic illustration of contact mode and intermittent contact mode operation, respectively.

Waals and capillary forces (under ambient conditions) and becomes repulsive at shorter distances due to the Pauli principle as soon as the electron orbitals start to overlap. This behavior is usually approximated by the Lennard-Jones potential [215]

$$V(x) = 4\epsilon\left[\left(\frac{\sigma}{x}\right)^{12} - \left(\frac{\sigma}{x}\right)^{6}\right] \tag{3.29}$$

of two interacting (neutral) particles, where x is their mutual separation, ϵ is the depth of the potential well, and σ is the point where $V(x) = 0$. The corresponding force $F(x) = -\nabla V(x)$ is plotted in Fig. 3.6b and is proportional to the deflection of the cantilever. By applying a feedback system while scanning the sample, the height of the cantilever above the surface can be adjusted such that the deflection (and thus the force) is kept constant at a specific value. If this value lies within the repulsive part of the force diagram (see Fig. 3.6b), the tip always stays in direct "physical" contact with the sample (so-called contact mode imaging, Fig. 3.6c).

Another possibility is to use a vibrating cantilever and to measure the amplitude of the oscillation instead of the static deflection. In this case, the tip periodically oscillates between the attractive and repulsive force regime (see Fig. 3.6b) and has direct contact to the surface only within a small time interval during each period (so-called intermittent contact or tapping mode imaging, Fig. 3.6d). Apart from the amplitude, which maps the topography of the sample, this mode of operation also provides a phase signal (of the cantilever movement relative to the driving oscillation), which allows the extraction of additional information on the characteristics of the surface. For example, the damping of the cantilever oscillation (and thus the phase shift) varies for different materials and, therefore, phase imaging is often able to identify regions of distinct chemical composition even on a topographically flat surface. Other modes of operation (such as non-contact imaging) are also possible, but not relevant for the experiments performed within the scope of this thesis, where the focus lies on the active manipulation of particles on the surface of the samples.

Particle manipulation with an atomic force microscope

The manipulation capability of an AFM arises from the repulsive forces acting when the tip is in direct contact with the surface. If these forces (in the lateral direction) exceed the frictional or adhesive forces occurring between the surface and an object, the latter can be dragged by the tip while scanning an area. Exploiting this effect in a controlled manner is the basis for the deterministic manipulation of nanoparticles as required for the proposed assembly of hybrid structures. However, prior to the manipulation the corresponding sample area has to be imaged without influencing

the position of the particles, which can be facilitated by operating the AFM in intermittent contact mode, where the lateral forces are much smaller. Therefore, the general approach is a two-step process. First, a specific sample area is imaged in intermittent contact mode and the particles of interest are identified. Second, the AFM is switched into contact mode and the tip is moved along a line crossing the location of the target particle, presumably moving the latter into the desired direction. The resulting formation is then evaluated through intermittent contact imaging and the whole procedure is repeated until the desired configuration is reached.

For the experiments in this thesis a NanoWizard AFM (JPK) was employed, providing the possibility to define arbitrary paths along which the tip can be moved in contact mode. As shown in the inset in Fig. 3.6a, Si cantilevers of the type Arrow-NC (Nanoworld) were used, which are favorable due to the location of the tip at the outermost edge of the cantilever, allowing an easy positioning on the area of interest when viewed from above. The tip radius is specified as < 10 nm and the cantilever design is optimized for intermittent contact mode operation (force constant 42 N/m, resonance frequency 285 kHz). However, it also proved to work in contact mode as long as the contact force was kept small, i.e., close to the minimum needed to reliably move particles on the surface.

First manipulation attempts were made with polystyrene beads (40 nm in diameter, Invitrogen) as well as diamond nanocrystals (20–100 nm in size, Mikrodiamant). An example is shown in Fig. 3.7. Thereby, typical ranges over which the particles could be moved in a single step turned out to be at best a few hundred nanometers (often even less than 100 nm) for arbitrary directions, as the particles slipped to the side of the tip after a short distance. However, there usually existed one particular direction in which movements over several micrometers could easily be achieved and which always coincided with the orientation of the cantilever. This effect is attributed to the specific shape of the tip, being a triangular pyramid with one broad and two narrower side faces. Obviously, the broader face enabled long-range movements due to the larger interaction area between the particle and the tip, an assumption which is also supported by the fact that manipulation usually became easier as the tip grew blunter in the course of operation. Consequently, if particle movements over long distances were required, the sample had to be aligned properly with respect to the cantilever or, alternatively, very blunt tips had to be used.

Apart from just dragging the particle on the surface, there is also a certain chance that it gets attached to the tip during manipulation, as happened in the case of particle A in Fig. 3.7. This effect occurs if the adhesion force [210]

$$F_{\mathrm{pt}} = 4\pi\zeta \frac{R_{\mathrm{p}} R_{\mathrm{t}}}{R_{\mathrm{p}} + R_{\mathrm{t}}} \tag{3.30}$$

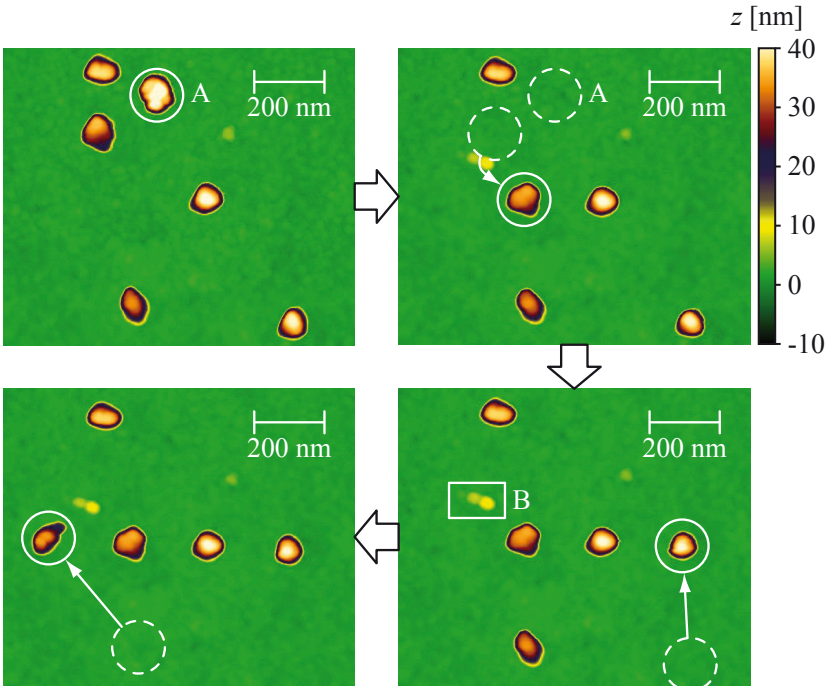

Figure 3.7: Series of AFM images demonstrating the manipulation of diamond nanocrystals spin-coated on a glass coverslip. The surface appears slightly grainy due to a thin layer of polyvinyl alcohol necessary to prevent aggregation of the nanocrystals. The individual particle movements are indicated by white circles. The nanocrystal denoted as A got attached to the tip and was deposited outside the scan area. The object denoted as B appeared during the manipulation of one of the particles.

between the particle and the tip overcomes the corresponding force $F_{\mathrm{ps}} = 4\pi\zeta R_{\mathrm{p}}$ between the particle and the surface. Here, R_{p} and R_{t} are the radius of the particle and of the tip, respectively, and ζ is the interfacial energy, which is assumed to be approximately equal for the particle-tip and particle-surface interaction. Obviously, the probability that the particle sticks to the tip increases with increasing R_{t}, a fact which was also observed experimentally as the tips grew blunter during manipulation. In some cases the stuck particle could again be deposited on the surface by applying a higher contact force while moving the tip, but this procedure was not reliable enough to allow a controlled pick-and-place of particles as demonstrated by other groups using special metal-coated tips [216].

Other peculiarities of the manipulation procedure involve the sudden appearance of objects on the surface, as can be seen in Fig. 3.7 (note the object denoted as B). They might be fragments from the particles or from the tip, which loosen due to the forces arising during manipulation. This was one of the main problems when moving soft particles such as polystyrene beads, which could easily be torn apart and were therefore only employed for test purposes in an early stage of the experiments. A much more severe effect concerns the dragging of particles even in intermittent

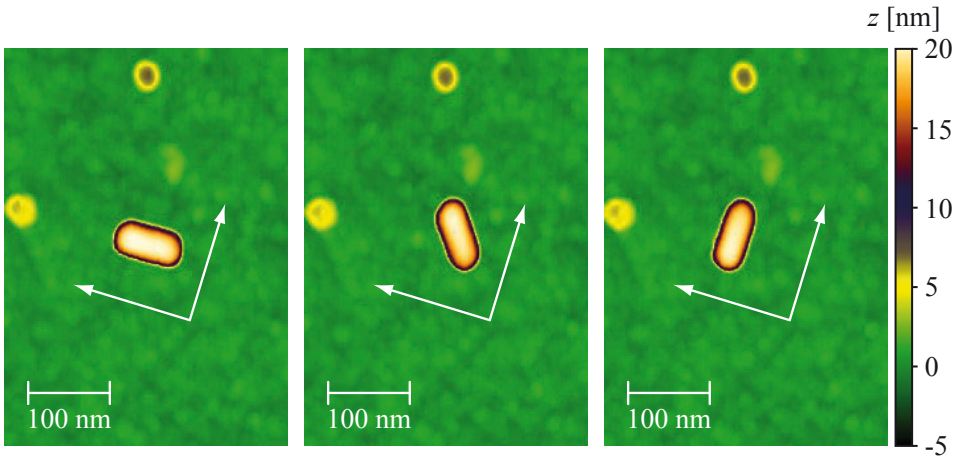

Figure 3.8: Series of AFM images demonstrating the rotation of a single gold nanorod (20 nm in diameter, 80 nm in length) spin-coated on a glass coverslip. The surface appears slightly grainy due to a thin layer of cetrimonium bromide being a remnant from the nanorod synthesis. The coordinate axes serve as a guide to the eye.

contact mode. Although the lateral forces should be very small in this case, it was sometimes observed (especially after longer periods of manipulation) that particles were pushed by the tip when imaging an area. Such a behavior usually made a controlled positioning impossible and could only be prevented by replacing the cantilever with a fresh one. The origin of this effect is unknown, but seems to be related to the degradation of the tip.

The accuracy with which particles can be positioned on the surface and relative to each other is mainly limited by the spatial resolution of the AFM, which, in turn, is determined by the radius R_t of the tip. In the experiments presented here, this accuracy was ≈ 10 nm at best when fresh tips were employed. In this case, it was not only possible to move particles, but also to rotate them in a controlled manner, as is demonstrated in Fig. 3.8 for a sample of gold nanorods (provided by the group of Prof. Dr. C. Sönnichsen, University of Mainz, see Appendix B). This ability is essential for the creation of plasmonic-photonic hybrid cavities as discussed in Sec. 3.6, where metal nanoparticles have precisely to be aligned with respect to the polarization of the cavity field.

Deposition of nanoparticles on photonic crystal structures

Although the manipulation capabilities described above are sufficient to precisely position and assemble nanoparticles on a surface, these particles have to be deposited near the desired location in the first place. In early experiments with polystyrene beads a simple spin-coating technique was used for this purpose, distributing the beads uniformly on the entire sample. In the case of photonic crystal structures, this method has the severe drawback that particles unavoidably get trapped inside

the holes, where they cannot be accessed by the AFM tip, thus influencing the optical properties of the structure in an uncontrolled manner. This is discussed in more detail in Sec. 3.5.1. Consequently, ways had to be explored which allow the deterministic deposition of particles at a predefined location on the sample prior to the AFM manipulation.

Ideally, one would like to pick up an individual particle somewhere (e.g., from a spin-coated glass coverslip) and place it directly at the desired position (e.g., on the photonic crystal cavity). As was already mentioned above, such a controlled pick-and-place could not be achieved in the course of this thesis, mainly for two reasons. First, the probability for depositing a particle once it got attached to the tip was very small for the employed Si cantilevers ($\approx 20\%$ success probability). In several of these rare successful events the particle disengaged from the tip already during imaging in intermittent contact mode, hinting at a very small adhesive force. Second, the cantilever could only roughly be positioned near the photonic crystal structure by means of an optical microscope, such that the final location for deposition had to be found through AFM imaging itself. Consequently, if a particle was picked up from a different sample, the chance for loosing it during this initial scanning procedure was very high. Therefore, in all corresponding attempts the particle was either lost before reaching the actual photonic crystal structure or was still attached to the tip (discernible from characteristic imaging artifacts), but could not be disengaged from the latter. Recent experiments with platinum-coated tips yielded much more promising results, enabling a pick-and-place of individual particles with relatively high success probability. However, corresponding cantilevers were not employed during the course of this thesis.

As an alternative a modified version of the so-called "dip-pen" nanolithography technique [217] was developed, which is capable of directly transferring assemblies of molecules [218] or nanometric particles [219] from a solution to the desired location on the sample surface. In the present case a tapered silica fiber (produced by a heating and drawing process) as shown in Fig. 3.9a was employed as "pen". Thereby, the radius of the fiber tip had to be small enough to provide sufficient accuracy in positioning, while the whole device needed to be robust such that the fiber would not break upon contact with the surface. A suitable value for the tip radius turned out to be $\approx$ 1–2 µm. The whole deposition and manipulation procedure is schematically illustrated in Fig. 3.9b and works as follows.

First, the tapered fiber is dipped into a solution of particles and the solvent is allowed to evaporate such that a sufficient number of particles gets attached to the tip. In a second step the fiber is brought into contact with the area next to the photonic crystal structure using a mechanical translation stage (positioning accuracy ≈ 0.5 µm, Thorlabs) and a boom-stand optical microscope (110× magni-

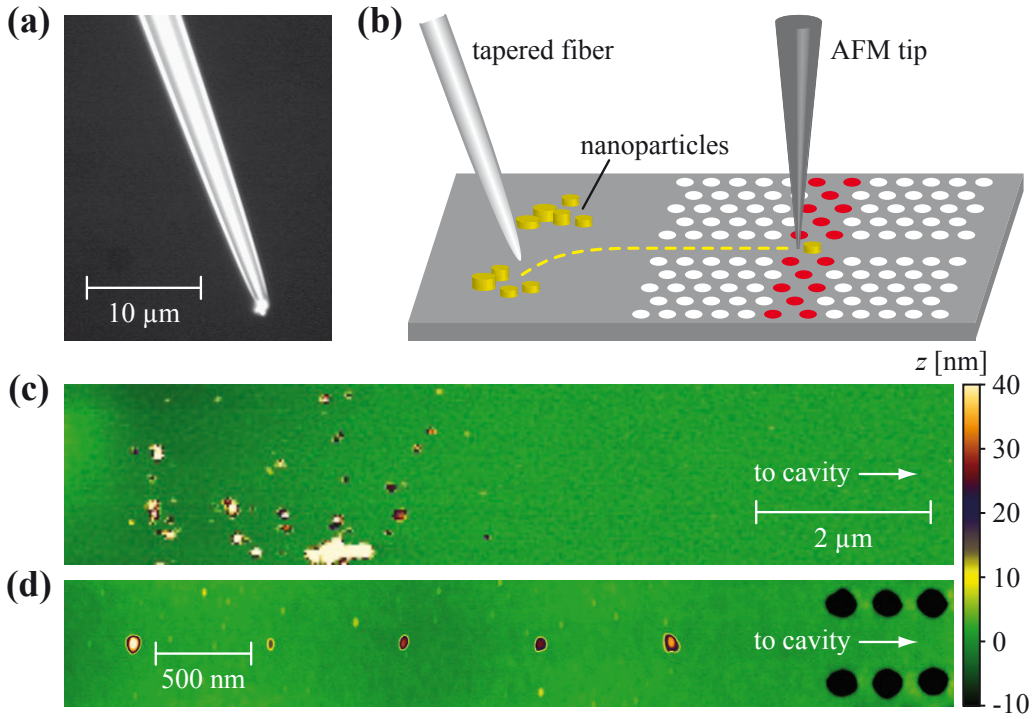

Figure 3.9: **(a)** Optical microscope image of a tapered fiber employed for dip-pen particle deposition. Note the small aggregation of polystyrene beads (≈ 1 µm in diameter) visible at the tip of the fiber. **(b)** Schematic illustration of the deposition and manipulation procedure used for delivering individual nanoparticles to the double-heterostructure photonic crystal cavities. **(c)** AFM image of the area next to the photonic crystal field, where small aggregates of diamond nanocrystals were deposited via the dip-pen technique. **(d)** AFM image of five selected diamond nanocrystals, which were maneuvered from the reservoirs shown in (c) to the entrance of the photonic crystal structure.

fication, Olympus). By gently moving the fiber tip on the sample surface, some of the particles are rubbed off and form small aggregates (see Fig. 3.9c), which serve as local reservoirs for the subsequent AFM manipulation step (see Fig. 3.9d). The dip-pen method is only applicable if the particles can easily be maneuvered from the deposition area to the photonic crystal cavity, which is, e.g., not fulfilled for an L3 cavity design with multiple layers of adjacent holes to be crossed. Therefore, this technique was exclusively employed in conjunction with double-heterostructure photonic crystal cavities (see Sec. 2.2.3), providing a convenient pathway between the cavity region and the outside area via the waveguide structure.

3.4.2 Optical spectroscopy and photon correlation measurements on hybrid structures

The optical properties of the hybrid structures were investigated by means of two different spectroscopic setups, depending on the specific type of samples used in the experiments. For opaque samples the same setup as described in Sec. 2.3.2 was

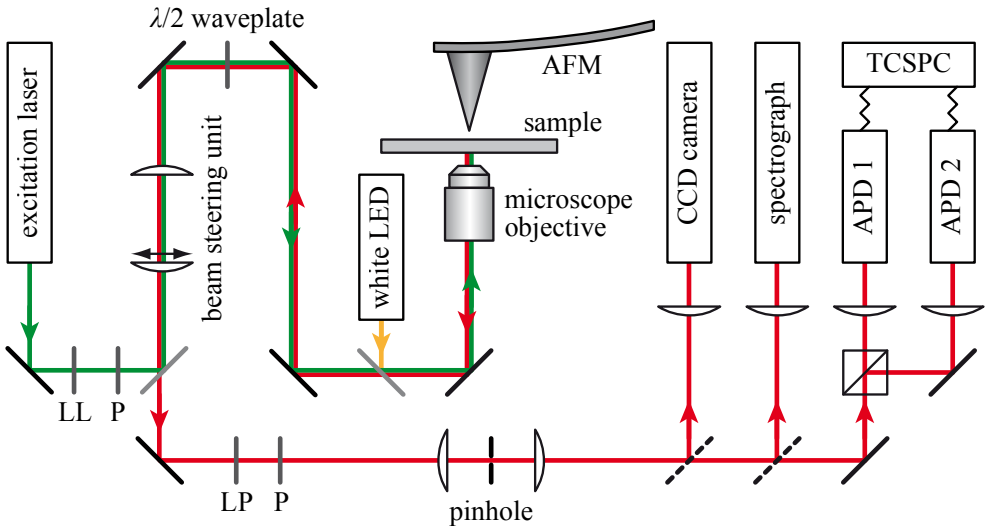

Figure 3.10: Schematic illustration of the experimental setup for fluorescence and photon correlation measurements on planar samples. The abbreviations are defined as follows: LL – laser line filter, LP – long-pass filter, P – polarizer, LED – light-emitting diode, AFM – atomic force microscope, CCD – charge-coupled device, APD – avalanche photodiode, TCSPC – time-correlated single photon counting.

employed. This particularly applies to all experiments involving photonic crystal cavities (see Secs. 3.5 and 3.6), since the underlying silicon wafers only allowed an optical access from the top side. In this case, no simultaneous manipulation and optical characterization was possible, resulting in very time-consuming realignment procedures as the samples had to be transferred back and forth between the AFM and the microscope stage, respectively.

For transparent samples (such as glass coverslips, see Sec. 3.7) a combination of AFM manipulation (from the top side) and optical investigation (from the bottom side) could be facilitated. For this purpose, a setup similar to the one described in Sec. 2.3.2 was employed, but with the additional capability of mounting the AFM on top of the sample stage, as is schematically shown in Fig. 3.10. Instead of an air objective, a 60×/1.4 NA oil immersion objective (Olympus) was used. In addition to the continuous wave excitation with an Ar^+ or Nd:YAG laser, pulsed excitation could be performed with a frequency-doubled, picosecond-pulsed amplified diode laser (emission wavelength $\lambda = 531$ nm, pulse width < 100 ps, repetition rate 10 kHz–40 MHz, PicoQuant).

Apart from CCD imaging and spectroscopic measurements, the light collected from the sample could be analyzed in a Hanbury-Brown and Twiss correlator [172], consisting of a 50:50 beam splitter cube and two avalanche photodiodes (APDs, PerkinElmer), which allowed the detection of single photon events in each beam path. A time-correlated single photon counting system (TimeHarp, PicoQuant)

was then employed to monitor the difference in the photon arrival times between both APDs, from which the second-order autocorrelation function $g^{(2)}(\tau)$ [Eq. (3.1)] could be deduced. Under pulsed excitation this system could also be used to record fluorescence lifetime traces by detecting the signal from only one APD in relation to the corresponding trigger signal from the excitation laser.

3.5 Nanoparticle-loaded photonic crystal cavities

With the nanomanipulation method introduced in Sec. 3.4.1, all ingredients for the realization of the proposed hybrid photonic crystal cavities are at hand. A particularly appealing application of this technique is the controlled assembly of fluorescent nanoparticles on top of the cavities, allowing the deterministic coupling of one or multiple quantum emitters to the various cavity modes. So far, such a deterministic coupling has only been achieved in III/V semiconductor systems by fabricating the entire photonic crystal structure around a preselected, self-assembled quantum dot, chosen from a random distribution [19, 220]. Although this approach proved to be very effective [17, 221], it is practically limited to a single emitter and a single cavity only [222]. An extension to a system incorporating multiple emitters and/or cavities requires a scalable fabrication technique, capable of providing quantum dots in a well-defined pattern [223]. Although feasible, these site-controlled quantum dots do currently not exhibit the desired optical properties in terms of spectral linewidth and single photon characteristics. Such restrictions do not apply to the proposed nanoassembly method, which can be used to couple all sorts of different emitters to the photonic crystal cavities, as long as they are available in the form of nanoscopic particles. In the following, two experiments demonstrating the feasibility of this approach are presented, starting with dye-doped polystyrene beads (Sec. 3.5.1) and continuing with diamond nanocrystals (Sec. 3.5.2) as emitters. In both cases the optical properties of the assembled systems are investigated by means of numerical simulations and spectroscopic measurements.

3.5.1 Coupling of polystyrene beads to photonic crystal cavities

Numerical simulations

As the deposition of nanoscopic particles alters the local dielectric environment, the optical properties of a particle-loaded cavity presumably differ from those of a bare structure. To study the impact of this modification, a number of FDTD simulations was performed prior to the experimental studies, using an optimized L3 cavity design (see Sec. 2.4.2) with an intrinsic quality factor $Q_0 = 3800$ as a test platform. A spherical particle was placed on top of the cavity center (see inset in

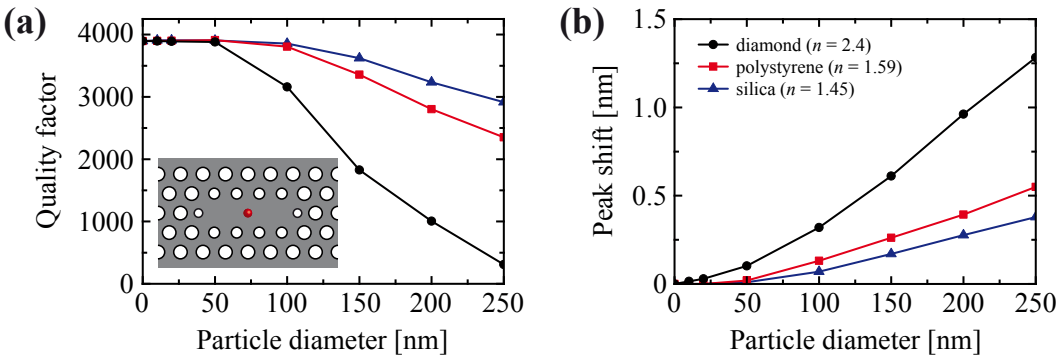

Figure 3.11: **(a)** Calculated quality factors Q of the fundamental mode TE_{y1} of an optimized L3 cavity (see inset) loaded with a spherical dielectric particle of varying size on top of its center. The lattice parameters (as defined in Sec. 2.4.2) are $a = 270$ nm, $t = 0.74a$, $r = 0.3a$, $r' = 0.2a$, $r'' = 0.25a$, and $s = 0.2a$. **(b)** Corresponding shifts $\delta\lambda$ of the resonance wavelength relative to the mode of the bare cavity. The calculations were performed for three different particle materials (i.e., silica, polystyrene, and diamond) with refractive indices as indicated in the legend.

Fig. 3.11a) and the resulting quality factor Q as well as the shift $\delta\lambda$ of the resonance wavelength was monitored as a function of the diameter d and refractive index n of the particle. Three different materials were studied, namely silica ($n = 1.45$), polystyrene ($n = 1.59$), and diamond ($n = 2.4$). The results are summarized in Fig. 3.11. As expected, the quality factor decreases with increasing diameter and refractive index of the particle (Fig. 3.11a), since the latter acts as a local scatterer, leading to additional radiation losses. Likewise, the resonance wavelength shifts to the red (Fig. 3.11b), because a growing fraction of the field intensity is located inside the higher dielectric material of the particle. For diameters $d < 50$ nm, however, the impact on the quality factor Q is negligible and the resonance shift $\delta\lambda$ stays well below the linewidth $\Delta\lambda = 0.17$ nm of the cavity resonance, even for diamond particles. A more comprehensive theoretical study, including also variations of the particle position, is presented in Sec. 3.5.2.

Experimental results

For a first experimental demonstration a sample containing L3 cavities was spin-coated with a dilute concentration of dye-doped polystyrene beads (40 nm in diameter, Invitrogen) such that the surface of the photonic crystal structure was covered with a sparse distribution of particles. An AFM image of one of these cavities directly after the coating procedure is shown in Fig. 3.12a (top). In order to exclusively couple a single particle to the cavity mode, a particular bead was selected and placed at the cavity center (where the fundamental mode TE_{y1} has its electric field maximum, see Fig. 2.14), while all other beads were moved aside. The final

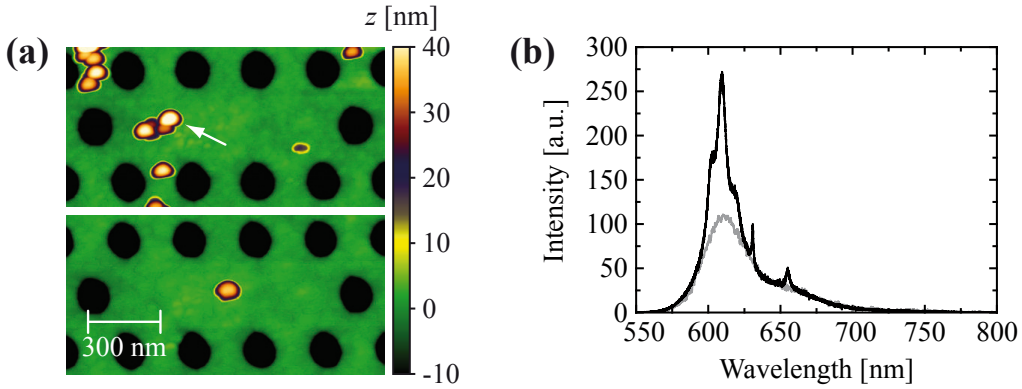

Figure 3.12: **(a)** AFM images of polystyrene beads (40 nm in diameter) distributed on top of an (unmodified) L3 cavity. The lattice parameters are $a = 270$ nm, $t = 1a$, and $r = 0.34a$. The upper/lower image shows the particle distribution before/after the AFM manipulation. Note that the shape of the polystyrene beads appears slightly distorted due to a degradation of the AFM tip. The arrow in the upper image marks the particle which was subsequently placed at the center of the cavity. **(b)** Fluorescence spectrum (black) from the particle-loaded cavity shown in (a). The gray curve represents a (scaled) reference spectrum from beads on an unpatterned region of the sample.

configuration is also displayed in Fig. 3.12a (bottom), proving the feasibility of a controlled particle manipulation on a photonic crystal structure.

The occurrence of pronounced resonance peaks in the corresponding fluorescence spectrum (see Fig. 3.12b) indicates the coupling of the dye emission to the various cavity modes. However, repeated measurements on the same cavity with different particle locations did not show any significant variation in the spectral shape, even if the polystyrene bead was entirely removed. Therefore, the dominant fraction of the collected emission intensity seems to originate from sources other than the selected particle, most likely from beads which got trapped inside the membrane holes during the coating procedure. These particles are not accessible to AFM manipulation and can alter the optical properties of the cavity in an uncontrolled way, including the generation of parasitic background emission as observed here. Consequently, this simple spin-coating technique turned out to be unsuitable for the present purpose and a more deterministic deposition method had to be developed (see Sec. 3.4.1), which was employed in all subsequent experiments.

3.5.2 Coupling of diamond nanocrystals to photonic crystal cavities

With regard to a controlled particle deposition, L3 cavities are rather impractical, since they are completely surrounded by membrane holes, making a direct particle transport from a sample region outside the photonic crystal area extremely difficult. Double-heterostructure cavities provide an elegant solution to this problem, because the particles can easily be moved in and out of the cavity via the integrated

waveguide. In combination with the "dip-pen" deposition method introduced in Sec. 3.4.1, this allowed the repetition of the experiment described above with only one polystyrene bead in the entire photonic crystal structure. However, corresponding fluorescence measurements were hindered by the rapid photobleaching of the dye-doped bead, making an investigation of the site-selective emitter-cavity coupling impossible. Consequently, more photostable emitters have to be employed for this type of experiment.

NV defect centers in diamond (see Sec. 3.2) are promising candidates, providing single photon emission at room temperature without any bleaching or blinking. Enhancing these beneficial optical properties through coupling to a cavity mode has been subject of numerous theoretical and experimental studies. In principle, an appropriate cavity can directly be realized in diamond [123, 124], but first experimental demonstrations [125, 126] suffered from large absorption and scattering losses owing to the polycrystallinity of the employed diamond material. Corresponding implementations with single-crystalline diamond [224] are very challenging and have not been realized yet. The use of diamond nanocrystals containing NV centers is an appealing alternative, as they can be coupled to all types of (non-diamond) cavities. First realizations with microsphere [225] and microdisk resonators [226] already exist, although the degree of control on the particle-cavity coupling was quite limited in these studies. A true deterministic coupling to photonic crystal cavities, as is targeted here, has not been demonstrated so far.

Numerical simulations

Again, a numerical analysis was conducted prior to the experiment, using a double-heterostructure cavity (see Sec. 2.5.1) with an intrinsic quality factor $Q_0 = 7700$ as a foundation. Instead of spheres, the diamond nanocrystals were modeled as cuboids of height h and lateral dimensions $2h$, which is a better representation of their true shape. In order to allow more general conclusions, the calculated quality factor Q of the particle-loaded cavity was decomposed into contributions Q_0 and Q_{dia}, associated with the intrinsic losses of the bare cavity and additional scattering losses induced by the diamond cuboid, respectively. In analogy to Eq. (2.20), these quantities are linked through the relation $1/Q = 1/Q_0 + 1/Q_{\mathrm{dia}}$. The resulting values of Q_{dia} for a particle of varying height h, placed on top of the cavity center (see inset in Fig. 3.13c), as well as the corresponding resonance shifts $\delta\lambda$ are displayed in Figs. 3.13a and 3.13c, respectively. Obviously, diamond nanocrystals with sizes of ≈ 20 nm support quality factors $> 10^5$, making them suitable candidates even for cavity QED experiments involving much higher intrinsic values Q_0. These findings are consistent with recent theoretical studies of a different photonic crystal cavity design [122].

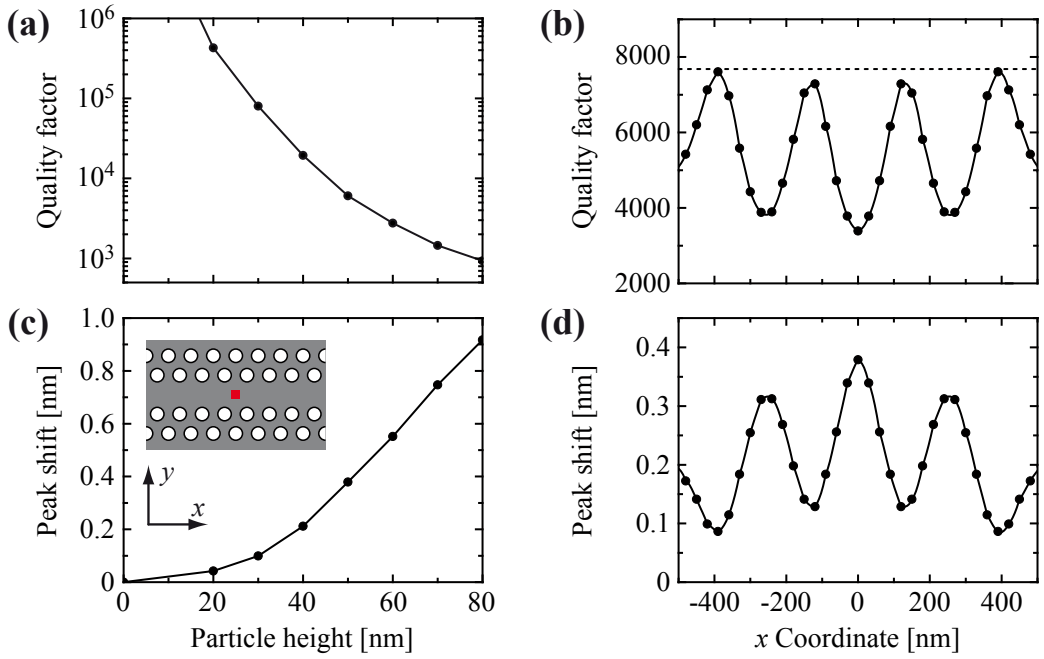

Figure 3.13: **(a)** Calculated quality factors Q_{dia}, associated with scattering losses induced by a diamond cuboid (of height h and width $2h$) placed on top of the center of a double-heterostructure cavity [see inset in (c)]. The lattice parameters are $a = 270$ nm, $t = 0.74a$, and $r = 0.32a$. **(b)** Corresponding total quality factors Q of the fundamental cavity mode $\mathrm{TE_y}$ as a function of the position of the diamond particle (of height $h = 50$ nm) on the central x axis. The dotted line indicates the value $Q_0 = 7700$ of the bare cavity. **(c,d)** Corresponding resonance shifts $\delta\lambda$ for the configurations shown in (a) and (b), respectively.

Further insight into the mutual interaction between the particle and the cavity mode can be gained by varying the position of the diamond nanocrystal on the cavity surface. For this purpose, a number of calculations with a cuboid of fixed height $h = 50$ nm, placed at different locations on the central x axis, was performed. The obtained quality factors Q and corresponding resonance shifts $\delta\lambda$ are displayed in Figs. 3.13b and 3.13d, respectively. Both, Q and $\delta\lambda$, follow the general trend of the electric field intensity $|\boldsymbol{E}|^2$ (see Fig. 2.21), exhibiting their largest/smallest deviations from the values of the bare cavity at the respective intensity maxima/minima. Ideally, the shift in the resonance wavelength should tend to zero at the field nodes. However, the relatively large size of the diamond nanocrystal leads to a spatial averaging effect and thus to a non-vanishing contribution to $\delta\lambda$. Contrary to this, the quality factor Q nearly resumes the value Q_0 of the bare cavity at the intensity minima, despite the spatial averaging.

This peculiar behavior is analogues to the findings of previous studies investigating the influence of an AFM tip on the optical properties of a photonic crystal cavity [227, 228]. It arises from the different ways in which the quality factor and the resonance wavelength respond to the presence of a local scatterer. While $\delta\lambda$ is

directly proportional to $|\boldsymbol{E}|^2$ at the position of the scatterer, Q does not only depend on the local near-field, but is also determined by far-field interference effects, as was already discussed in conjunction with the cancelation effect in Sec. 2.2.4. Similar to the L3 cavity mode $\mathrm{TE}_{\mathrm{y1}}$ shown in Fig. 2.8, the E_y field component of the double-heterostructure cavity mode TE_{y} has opposite signs at opposing sides of a field node on the central x axis. Consequently, when placed symmetrically at such a field node, the light scattered by a diamond nanocrystal mostly interferes destructively in the far-field and the original quality factor Q_0 is nearly maintained, even if the resonance wavelength is significantly detuned.

This offers interesting possibilities to use the controlled placement of dielectric nanoparticles to tune the cavity resonance without affecting the quality factor too much. Contrary to corresponding experiments with AFM tips [228], the tuning effect would be permanent (but still adjustable) and could be independently applied to several nearby cavities at the same time. An elegant variant of this technique was recently demonstrated by Seo *et al.* [229], who used the controlled deposition of carbonaceous nanodots to tune photonic crystal cavities.

Experimental results

To test the theoretical predictions a small reservoir of diamond nanocrystals (with sizes of 20–100 nm, Mikrodiamant) was deposited near a double-heterostructure cavity (with an intrinsic quality factor $Q_0 = 3200$) using the method described in Sec. 3.4.1. A relatively large particle (55 nm in height, 50–100 nm in width) was selected and moved into the cavity to achieve a noticeable impact on the optical properties of the latter. Note that this particular diamond nanocrystal did not contain any defect centers, which were present in only $\approx 1\%$ of all investigated particles. AFM images of some of the realized configurations are shown in Fig. 3.14a. Care was taken to keep the orientation of the nanocrystal (discernible from its asymmetric shape) constant in all configurations to ensure consistency between the individual measurements. The corresponding quality factors Q and resonance shifts $\delta\lambda$ of the particle-loaded cavity were determined from the recorded spectra of the intrinsic silicon nitride fluorescence and are displayed in Figs. 3.14c and 3.14d, respectively.

For a quantitative comparison between the experimental and theoretical results, the simulations presented in Fig. 3.13 were repeated for a more realistic cavity and particle geometry, which was directly deduced from the AFM images. The corresponding calculated electric field intensity distribution $|\boldsymbol{E}|^2$ of the fundamental cavity mode TE_{y} is displayed in Fig. 3.14b, clearly showing an asymmetry in the mode profile due to fabrication imperfections (note the slightly irregular shape of the holes). The calculated quality factors Q were scaled such that the predicted intrinsic value $Q_0 = 4800$ matches the respective experimental value $Q_0 = 3200$,

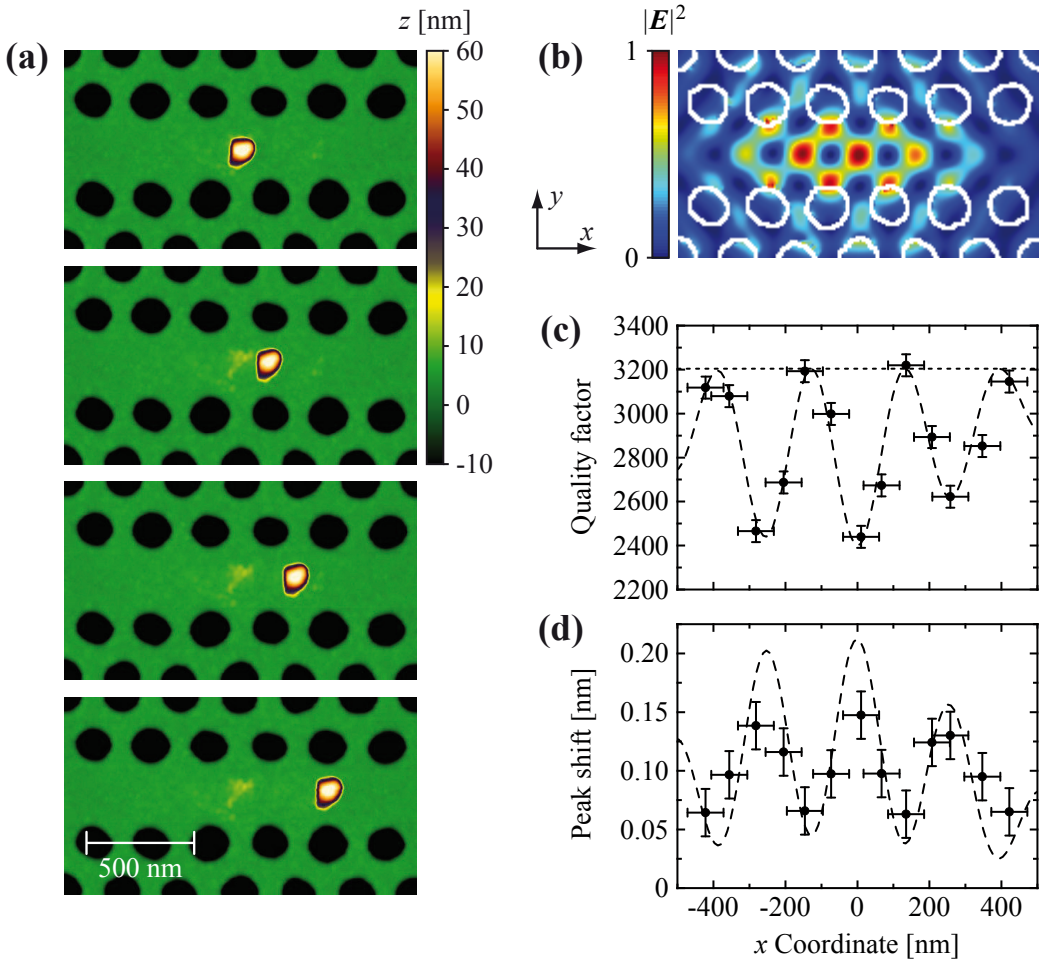

Figure 3.14: **(a)** AFM images of a diamond nanocrystal (55 nm in height) placed at different positions on top of a double-heterostructure cavity. The lattice parameters are $a = 270$ nm, $t = 0.74a$, and $r = 0.32a$. **(b)** Calculated electric field intensity distribution $|\boldsymbol{E}|^2$ of the fundamental mode of the cavity geometry shown in (a). **(c,d)** Measured quality factors Q (c) and resonance shifts $\delta\lambda$ (d) of the diamond-loaded cavity as a function of the particle position on the central x axis. The dashed curves represent the corresponding theoretical predictions when fabrication imperfections are taken into account. The dotted line in (c) indicates the value $Q_0 = 3200$ of the bare cavity. The error bars for x mark the lateral extend of the diamond nanocrystal.

which is justified because not all imperfections (such as surface roughness) can be accounted for in the simulations. These refined theoretical results are also displayed in Fig. 3.14c, showing excellent agreement with the experimental data. Even the asymmetric mode profile is correctly reproduced. With regard to the resonance shift $\delta\lambda$ (Fig. 3.14d), the theoretical prediction slightly overestimates the magnitude of the wavelength change found experimentally. This might be due to the irregular shape of the diamond nanocrystal and the resulting non-perfect contact with the photonic crystal surface. However, the general trend in the experiment agrees well with the simulated data.

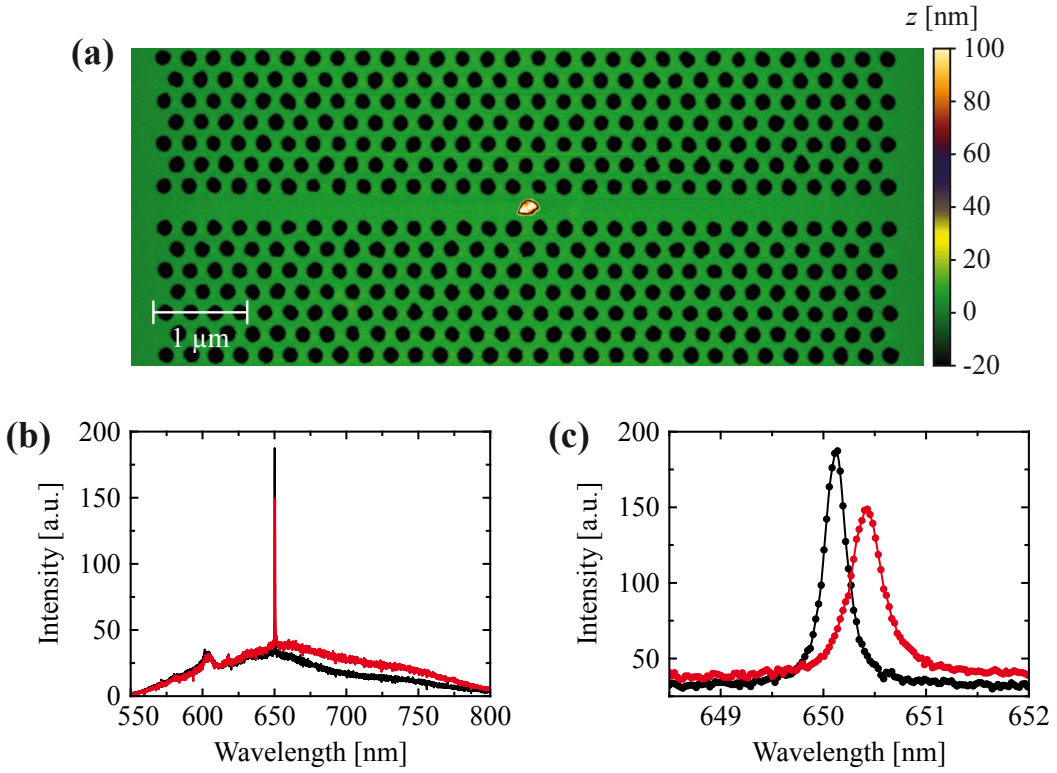

Figure 3.15: **(a)** AFM image of a different diamond nanocrystal (100 nm in height) on top of the same cavity as the one displayed in Fig. 3.14a. **(b)** Fluorescence spectrum (red) from the diamond-loaded cavity shown in (a). A corresponding spectrum of the bare cavity (black) is also displayed for comparison. **(c)** Zoom into the resonance peak of the diamond-loaded (red) and bare cavity (black), respectively.

Having successfully demonstrated the precise control of the mutual particle-cavity interaction, the next step would be the coupling of a single NV center to the cavity mode. As was already stated above, only $\approx 1\%$ of the employed diamond nanocrystals actually contained NV centers, making a search among the deposited particles extremely cumbersome. However, a promising candidate (with a rather large size of ≈ 100 nm) could be found and was moved into the same cavity as the one used in the previous experiment (see Fig. 3.15a). Unfortunately, the optical powers needed to excite the NV emission are comparable to those generating a substantial fluorescence from the silicon nitride membrane. Therefore, only a small fraction of the total collected intensity actually originates from the diamond nanocrystal, as is seen from a comparison with the bare cavity spectrum (under identical excitation conditions) shown in Fig. 3.15b. Due to this large background signal photon correlation measurements become meaningless and thus no definite conclusion is possible whether the detected particle emission stems from a single NV center. Also, an analysis of the resonance peak (Fig. 3.15c) provides no indication of a coupling between the NV center and the cavity mode, since the observed spectral broadening

and red-shift is simply due to the presence of the diamond nanocrystal as discussed above. Further attempts to realize such a coupled emitter-cavity system failed for the same reason, i.e., the strong background fluorescence from the silicon nitride, preventing a conclusive investigation of cavity QED effects.

Various approaches can be envisaged to circumvent this problem, first of all the use of a different material system for the fabrication of the photonic crystal cavities. As was already discussed in Sec. 2.6, gallium phosphide would be appealing, not only because of its high refractive index, but also due to its much weaker intrinsic emission. Corresponding implementations are in progress, but could not be completed during the course of this thesis. An entirely different approach relies on a much more selective excitation of the NV emission in order to efficiently suppress the background fluorescence from the silicon nitride. Such a selective excitation may be facilitated by exploiting the localized and enhanced electromagnetic field near metal nanoparticles (see Sec. 3.3). A corresponding combined plasmonic-photonic cavity system has not been realized so far and would also be of high interest from a fundamental point of view, as is discussed in the next section.

3.6 Plasmonic-photonic hybrid cavities

Due to their ability to concentrate electromagnetic energy in volumes much smaller than the corresponding wavelength, surface plasmons provide a very strong interaction between light and matter [230, 231], potentially enhancing the excitation as well as emission rate of nearby emitters (see Sec. 3.3.3). It seems appealing to combine this enhancement, which is broad-band in character, with the spectrally narrow resonances of an appropriate cavity design. Various types of such plasmonic cavities have already been realized [232–236], exhibiting mode volumes V_{eff} down to $(100\ \text{nm})^3$ [233]. However, the achieved quality factors Q were always limited to values < 100. The reason is found in the rather large amount of metal which interacts with the confined light, leading to significant ohmic losses. Hybrid cavity structures employing a dielectric or semiconducting fundament are a possible solution to this problem, as was recently demonstrated for silica microdisks coated with a thin metal layer [237]. Quality factors $Q \approx 1000$ were achieved, although on the expense of a larger mode volume $V_{\text{eff}} \approx (2.5\ \mu\text{m})^3$. Even in this case, however, the dielectric core was still completely covered with metal.

The nanomanipulation technique introduced in Sec. 3.4.1 provides the means for creating a novel type of plasmonic hybrid structure by depositing individual metal nanoparticles on the dielectric backbone of a photonic crystal cavity. While the nanoparticles lead to strongly localized electromagnetic fields, the optical feedback is exclusively provided by the surrounding (dielectric) photonic crystal lattice,

potentially reducing ohmic losses to a minimum. Such a device combines the characteristics of both, plasmonic and photonic elements, and may therefore be termed plasmonic-photonic hybrid cavity. As a similar structure has not been studied so far, its true potential is yet unexplored. In the following, two experimental realizations are presented, using either gold nanorods (Sec. 3.6.1) or antenna structures assembled from individual gold nanospheres (Sec. 3.6.2) as the metal constituents. In both cases the optical properties of these cavity systems are investigated by means of numerical simulations and spectroscopic measurements.

3.6.1 Coupling of gold nanorods to photonic crystal cavities

Numerical simulations

The first system to be studied is a single gold nanorod (20 nm in diameter, 50 nm in length) placed upon the center of a double-heterostructure cavity with a hole radius $r = 0.28a$ and an intrinsic (theoretical) quality factor $Q_0 = 9100$. As discussed in Sec. 3.3.2, such a nanorod supports two plasmon resonances along its longitudinal and transverse axis, respectively, whereby the longitudinal resonance is usually much more pronounced (see Fig. 3.4). Due to this anisotropy two different configurations were investigated, with the nanorod being either oriented in y direction (i.e., perpendicular to the waveguide axis, see Fig. 3.16a) or in x direction (i.e., parallel to the waveguide axis, see Fig. 3.16b).

Corresponding FDTD simulations of these structures were performed using geometrical parameters closely resembling those of the experimentally studied system. Compared to previous calculations involving only dielectric materials, a much denser computational grid had to be used to accurately reproduce the plasmonic effects near the surface of the metal. Therefore, the general mesh size of $a/20 \times \sqrt{3}a/34 \times a/27$ converged to $(2\ \mathrm{nm})^3$ in the vicinity of the gold nanorod and no mesh averaging was applied (see Sec. 2.3.4). While the refractive index $n = 2.01$ of the silicon nitride was assumed to be wavelength-independent, the material dispersion of gold was fully taken into account employing the data shown in Appendix A.

For both configurations the calculated electric field intensity distributions $|\boldsymbol{E}|^2$ of the fundamental cavity mode $\mathrm{TE_y}$ are displayed in Figs. 3.16c and 3.16d, respectively. Apparently, the cavity field efficiently couples to the plasmon resonance of the nanorod if the latter is oriented parallel to the corresponding field polarization (Fig. 3.16c). As a consequence, the intensity maximum shifts from the center of the photonic crystal slab to its surface and the quality factor decreases to $Q = 4350$. Contrary to this, a much weaker coupling effect is observed if the nanorod is oriented perpendicular to the field polarization (Fig. 3.16d), leading only to a marginal reduction of the quality factor. The same behavior occurs for the $\mathrm{TE_x}$ mode, but

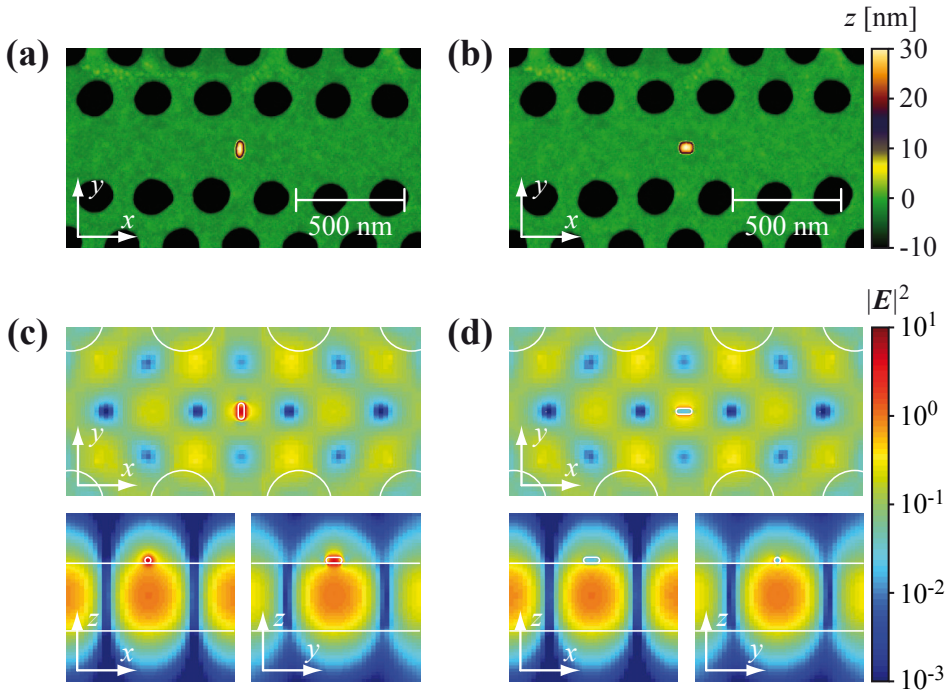

Figure 3.16: (a,b) AFM images of a gold nanorod (20 nm in diameter, 50 nm in length) placed on top of a double-heterostructure cavity in different orientations. The lattice parameters are $a = 270$ nm, $t = 0.74a$, and $r = 0.28a$. The nanorod appears in a slightly different aspect ratio in both images due to the convolution with the shape of the AFM tip. **(c,d)** Corresponding calculated electric field intensity distributions $|\boldsymbol{E}|^2$ of the fundamental mode $\mathrm{TE_y}$ for the configurations shown in (a) and (b), respectively. Each panel displays x-y, x-z, and y-z cross sections through the center of the gold nanorod. The logarithmic color scale is always normalized to the respective $|\boldsymbol{E}|^2$ value at the center of the photonic crystal slab.

with interchanged orientations of the nanorod (see Tab. 3.1), since the respective field polarization is perpendicular to that of the $\mathrm{TE_y}$ mode. This opens interesting possibilities to tailor the light-matter coupling, e.g., by creating a system which can be efficiently excited at the wavelength of the plasmon-coupled mode (with lower Q, but high plasmonic field enhancement) and emits at the wavelength of the unaffected mode (with high Q), or *vice versa*.

Such a system provides an ideal platform, e.g, to generate and harvest single photons with high efficiency, as the interaction of the emitter with the excitation field is strongly increased [238], while a narrow-band emission channel exists to collect and distribute the generated photons. A similar scheme may also be employed to solve the background problem discussed in conjunction with the NV emission in Sec. 3.5.2. Note that, in general, the shift of the intensity maximum to the surface of the photonic crystal slab is advantageous for all applications where external emitters (or other types of external materials) have to be coupled to the cavity mode, as the evanescent interaction is strongly increased in this way.

Experimental results

To experimentally test the predicted polarization-selective coupling, chemically synthesized gold nanorods (provided by the group of Prof. Dr. C. Sönnichsen, University of Mainz) were employed. Details of the synthesis and their optical properties are provided in Appendix B. A particular nanorod was selected and placed on top of the double-heterostructure cavity, the latter exhibiting resonance wavelengths of 640 nm (TE_x mode) and 668 nm (TE_y mode). The assembled configurations (see Figs. 3.16a and 3.16b) were subsequently investigated by monitoring the intrinsic fluorescence of the silicon nitride. The corresponding resonance spectra for both cavity modes are displayed in Fig. 3.17.

Clearly, a strong impact on the width and shape of the resonance peak can be observed for those cases in which the nanorod is oriented parallel to the respective mode polarization (Figs. 3.17d and 3.17e). Thereby, the asymmetric lineshape results from interference effects of light scattered or radiated directly from the nanorod and light reaching the detector on other pathways. This effect is analogues to the Fano resonances observed in atomic systems [239] and is discussed in more detail

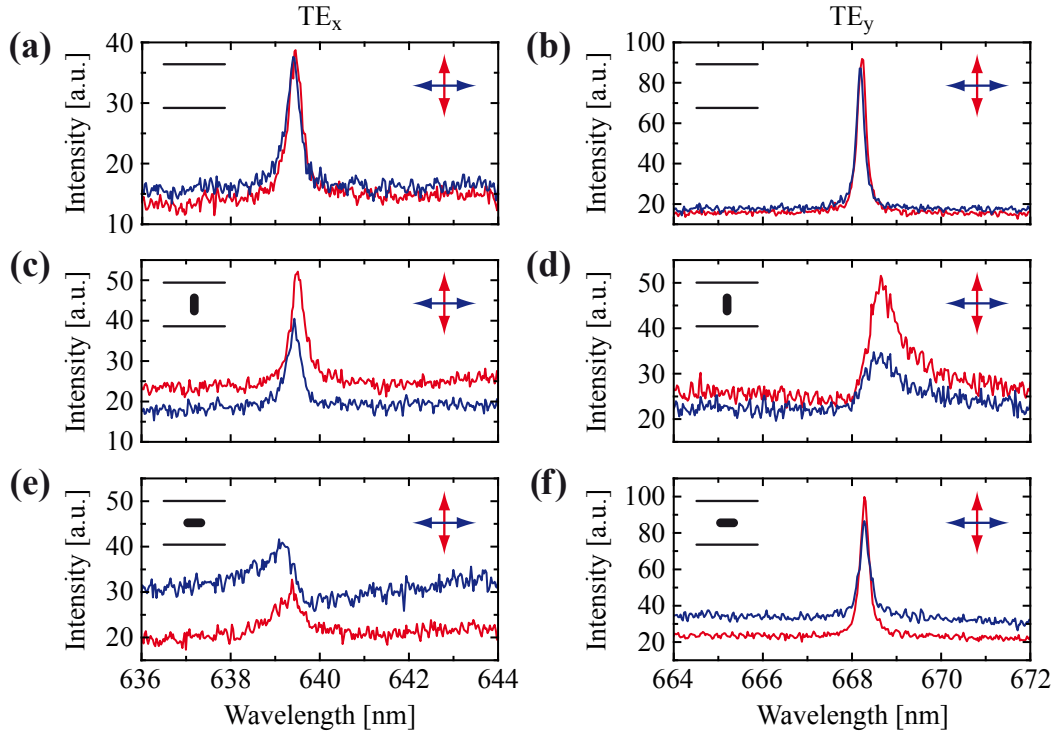

Figure 3.17: **(a,b)** Resonance peaks of the modes TE_x (a) and TE_y (b) for the bare double-heterostructure cavity (without nanorod). **(c,d)** Resonance peaks of the modes TE_x (c) and TE_y (d) for the configuration shown in Fig. 3.16a (see inset). **(e,f)** Resonance peaks of the modes TE_x (e) and TE_y (f) for the configuration shown in Fig. 3.16b (see inset). In each plot blue and red curves refer to excitation polarizations in x and y direction, i.e., parallel and perpendicular to the waveguide axis, respectively.

	$Q_{\mathrm{exp}}(\mathrm{TE_x})$	$Q_{\mathrm{theo}}(\mathrm{TE_x})$	$Q_{\mathrm{exp}}(\mathrm{TE_y})$	$Q_{\mathrm{theo}}(\mathrm{TE_y})$
	3060 ± 50	9110	1860 ± 30	3150
	890 ± 80	4350	1840 ± 30	3130
	3010 ± 50	8880	870 ± 80	2730

Table 3.1: Experimentally and theoretically obtained quality factors Q_{exp} and Q_{theo}, respectively, of the modes $\mathrm{TE_x}$ and $\mathrm{TE_y}$. The configurations (from top to bottom line) are: bare cavity without gold nanorod, nanorod oriented perpendicular to the waveguide axis, and nanorod oriented parallel to the waveguide axis.

in Sec. 3.6.2. For those cases in which the nanorod is oriented perpendicular to the respective mode polarization (Figs. 3.17c and 3.17f), the spectral lineshape is nearly unaffected, indicating a very weak coupling between the cavity field and the plasmonic resonance, in accordance with the theoretically predicted behavior. Note that the observed fluorescence intensity is largest if the excitation polarization matches the orientation of the nanorod, which is attributed to the plasmonic enhancement of the intrinsic gold emission [240].

For a quantitative analysis the quality factors Q were determined from the resonance spectra in Fig. 3.17 by fitting either a Lorentzian or a Fano-type function [see Eq. (3.32)] to the experimental data. The corresponding values for the different configurations are summarized and compared to the calculations in Tab. 3.1. The predicted diametrical behavior of the two cavity modes is clearly visible, which means that the nanorod couples either to the $\mathrm{TE_x}$ or $\mathrm{TE_y}$ mode, depending on its orientation. The associated reduction of the quality factor (with respect to the bare cavity) is considerably larger than expected from the calculations. This discrepancy might be related to surface roughness, not only of the gold nanorod, but also of the underlying silicon nitride membrane, effectively increasing radiative losses of the excited particle plasmon. Nonetheless, the observed quality factors $Q \approx 900$ are still much higher than in most other plasmonic cavities investigated so far and the extreme orientation/polarization sensitivity illustrates the potential of this hybrid system to tailor the mutual coupling between plasmonic and photonic resonances.

3.6.2 Coupling of gold nanospheres to photonic crystal cavities

Numerical simulations

Next, a more complex metal structure is considered, namely a plasmonic nanoantenna consisting of two gold nanospheres (60 nm in diameter) placed upon the center of a double-heterostructure cavity with a hole radius $r = 0.34a$ and an intrinsic (the-

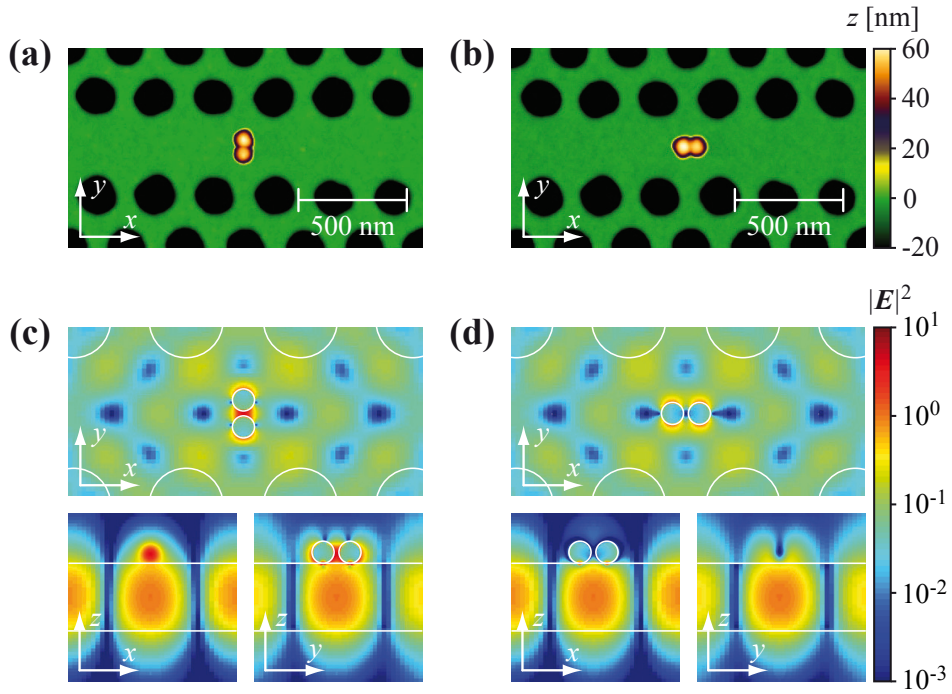

Figure 3.18: (a,b) AFM images of two gold nanospheres (60 nm in diameter) placed on top of a double-heterostructure cavity in different alignment directions. The lattice parameters are $a = 270$ nm, $t = 0.74a$, and $r = 0.34a$. The width of the gap between the spheres is determined as (15 ± 5) nm (a) and (5 ± 5) nm (b), respectively. **(c,d)** Corresponding calculated electric field intensity distributions $|\boldsymbol{E}|^2$ of the fundamental mode $\mathrm{TE_y}$ for the configurations shown in (a) and (b), respectively. Each panel displays x-y, x-z, and y-z cross sections through the center of the gold dimer. The gap between the two nanospheres has a width of 20 nm in the simulations. The logarithmic color scale is always normalized to the respective $|\boldsymbol{E}|^2$ value at the center of the photonic crystal slab.

oretical) quality factor $Q_0 = 4300$. The nanoantenna is either aligned in y direction (i.e., perpendicular to the waveguide axis, see Fig. 3.18a) or in x direction (i.e., parallel to the waveguide axis, see Fig. 3.18b). The corresponding calculated electric field intensity distributions $|\boldsymbol{E}|^2$ of the fundamental cavity mode $\mathrm{TE_y}$ are displayed in Figs. 3.18c and 3.18d, respectively. Again, an efficient coupling between the cavity field and the plasmon excitation of the nanoantenna only occurs for alignment directions parallel to the corresponding field polarization (Fig. 3.18c). In this case, a pronounced "hot spot" is created in the gap between the nanospheres, which increases in strength with decreasing separation Δx (see Sec. 3.3.2). In the example shown in Fig. 3.18c, a moderate separation $\Delta x = 20$ nm was chosen, allowing other materials (such as diamond nanocrystals) to be inserted into the gap. The calculated $|\boldsymbol{E}|^2$ value at the center $\boldsymbol{r}_0$ between the spheres is still 22 times higher than that of the bare photonic crystal cavity (at the same point), potentially enhancing the interaction of the cavity field with a quantum emitter. At the same time, the calculated quality factor decreases only moderately to $Q = 2600$.

To further quantify this enhancement effect the corresponding cavity Purcell factor F_c for a dipole emitter located at $\boldsymbol{r}_0$ and oriented along the y direction can be determined using Eq. (2.40). Thereby, the mode volume V_eff is defined as

$$V_\mathrm{eff} = \frac{\int_V \mathrm{d}\boldsymbol{r}\, \epsilon(\boldsymbol{r}) \left|\boldsymbol{E}(\boldsymbol{r})\right|^2}{\epsilon(\boldsymbol{r}_0) \left|\boldsymbol{E}(\boldsymbol{r}_0)\right|^2} \,, \tag{3.31}$$

with $\epsilon(\boldsymbol{r})$ being either identical to the dielectric constant $\varepsilon(\boldsymbol{r})$ of the dielectric material or given by $\epsilon(\boldsymbol{r}) = \mathrm{Re}\Big\{\mathrm{d}\big[\omega\varepsilon(\boldsymbol{r},\omega)\big]/\mathrm{d}\omega\Big\}$ [33] for the metal constituents. Note that Eq. (3.31) differs from the usual definition of the mode volume in Eq. (2.21), where $\max\Big\{\varepsilon(\boldsymbol{r})\left|\boldsymbol{E}(\boldsymbol{r})\right|^2\Big\}$ appears in the denominator instead of $\epsilon(\boldsymbol{r}_0)\left|\boldsymbol{E}(\boldsymbol{r}_0)\right|^2$. This, however, would result in unrealistically small values of V_eff due to the extremely high local field intensities occurring at certain points near the metal surface. Consequently, the fixed reference point $\boldsymbol{r}_0$ is used here for all calculations, in this way automatically accounting for a reduced coupling strength if the emitter is not located at the field maximum of the cavity mode. For the configuration shown in Fig. 3.18c, a reduction of V_eff by a factor of 32 compared to the bare photonic crystal cavity is deduced (see Tab. 3.2). Together with the corresponding change in the quality factor, this still yields a ≈ 20 times net enhancement of the Purcell factor.

Experimental results

To experimentally probe the optical properties of the nanoantenna-cavity system, two gold nanospheres (BBInternational) were assembled on top of the double-heterostructure cavity (with resonance wavelengths of 604 nm and 638 nm) as displayed in Figs. 3.18a and 3.18b. Spectroscopic measurements on these configurations reveal a substantial contribution of the plasmon-enhanced emission from the gold nanoantenna to the collected fluorescence signal, as becomes apparent from the spectra in Fig. 3.19. For a single gold nanosphere this emission is weak compared to the background fluorescence from the silicon nitride. However, if two nanospheres are brought together and excited along their alignment axis, a strong increase occurs due to the hot spot formation discussed above, accompanied by a red-shift of the plasmon resonance (see Sec. 3.3.2). In this case, the gold emission (which is linearly polarized along the alignment axis of the nanospheres) dominates over that from the silicon nitride and the nanoantenna can be treated as a point-like light source.

This allows one to study the coherent interaction between the plasmon excitation of the nanoantenna and the cavity mode, manifested in the asymmetric, Fano-like lineshape observed in the resonance spectra (see Fig. 3.20). Fano resonances result from an interference of the two possible pathways on which a photon emitted by the source (i.e., the nanoantenna) can reach the detector, namely directly through

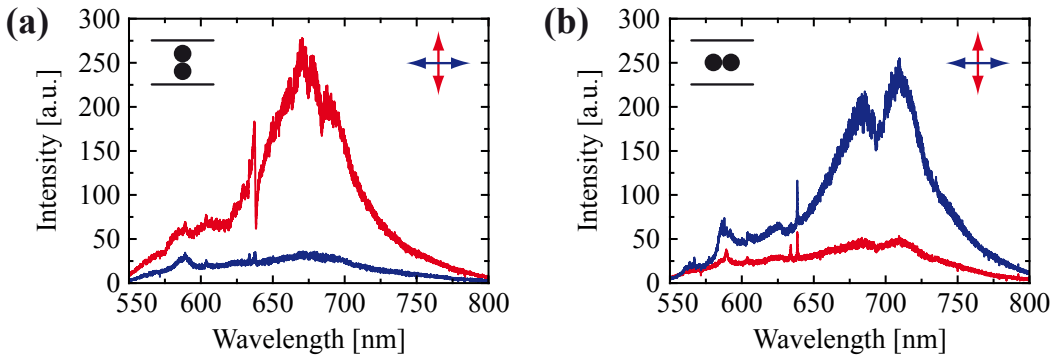

Figure 3.19: (a,b) Fluorescence spectra from the configurations shown in Figs. 3.18a (a) and 3.18b (b) (see insets), respectively. In each plot blue and red curves refer to excitation polarizations in x and y direction, i.e., parallel and perpendicular to the waveguide axis, respectively.

emission into a continuum of extended free-space modes or resonantly through emission into the cavity mode and subsequent out-coupling to free-space modes. Note that a pronounced Fano effect is only produced when the polarization of the source and that of the radiation from the cavity mode coincide, as can be seen from the polarization-resolved spectra in Figs. 3.20d and 3.20e.

For a quantitative analysis of the resonance spectra, a model by Barclay *et al.* [226] is adopted, according to which the spectral lineshape of a point-like emitter coupled to a cavity mode can be described by a function of the form

$$S(\lambda) = A\left|1 + \frac{\xi\sqrt{F_{\mathrm{ph}}}\exp(-i\Delta\Phi)}{1 + 2iQ(1-\lambda_{\mathrm{c}}/\lambda)}\right|^2 . \tag{3.32}$$

Here, λ_{c} is the central wavelength of the cavity mode, $\xi = \xi_{\mathrm{c}}/\xi_{\mathrm{d}}$ is the ratio of the collection efficiencies for radiation from the cavity and for direct emission from the nanoantenna, respectively, $\Delta\Phi = \Phi_{\mathrm{d}} - \Phi_{\mathrm{c}}$ is the phase difference between these two detection pathways, and A is a proportionality constant. Note that the Purcell factor F_{ph} occurring in Eq. (3.32) is not identical to the total Purcell enhancement F_{c} of the hybrid cavity system. F_{c} can be interpreted as being composed of two components, namely a plasmonic contribution F_{pl} due to the plasmon resonance of the nanoantenna and a photonic contribution F_{ph} due to the mode of the bare photonic crystal cavity. In the present experiment the gold emission is primarily enhanced by the plasmonic resonance and only subsequently coupled to the cavity mode. Therefore, the three quantities are related via $F_{\mathrm{c}} = F_{\mathrm{pl}}F_{\mathrm{ph}} + F_{\mathrm{ph}} \approx F_{\mathrm{pl}}F_{\mathrm{ph}}$ and the observed interference effects are a measure for F_{ph}.

By fitting Eq. (3.32) to the experimental data in Fig. 3.20, the quality factor Q and the product $\xi\sqrt{F_{\mathrm{ph}}}$ can be determined independently of each other. In the following, only the $\mathrm{TE_y}$ mode is considered for simplicity. The corresponding values

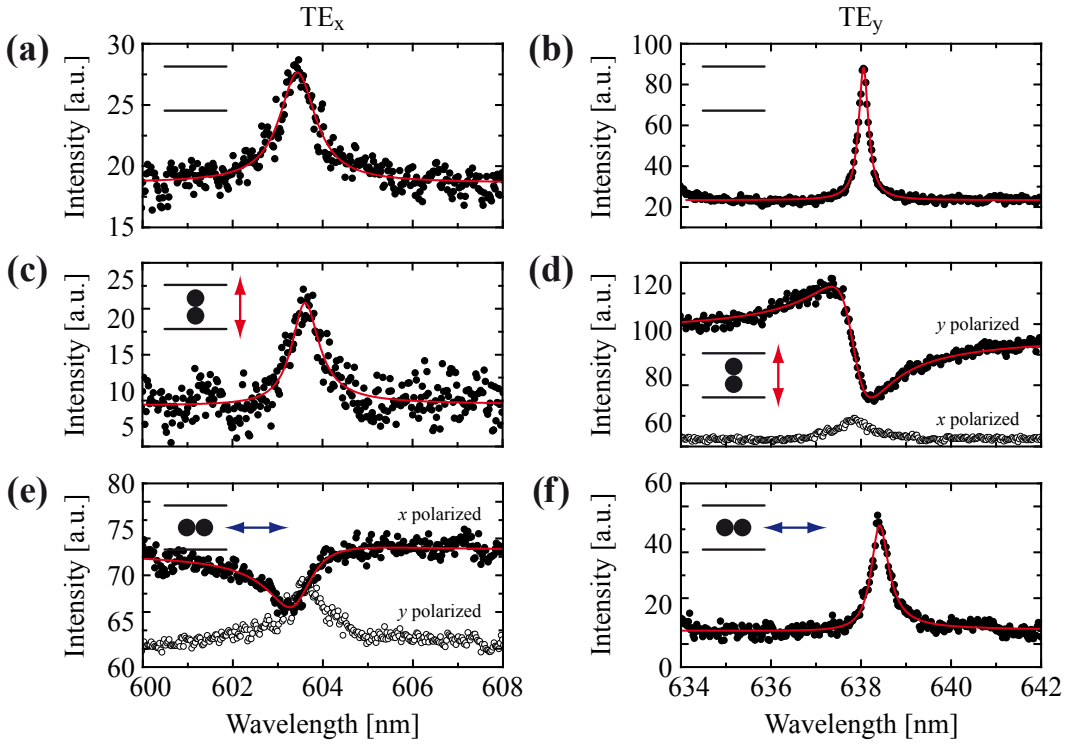

Figure 3.20: **(a,b)** Resonance peaks of the modes TE_x (a) and TE_y (b) for the bare double-heterostructure cavity (without nanoantenna). **(c,d)** Resonance peaks of the modes TE_x (c) and TE_y (d) for the configuration shown in Fig. 3.18a (see inset). The excitation light was polarized in y direction, i.e., perpendicular to the waveguide axis. In (d) additional polarization filtering in y (filled circles) or x direction (open circles) was applied in the detection path. **(e,f)** Resonance peaks of the modes TE_x (e) and TE_y (f) for the configuration shown in Fig. 3.18b (see inset). The excitation light was polarized in x direction, i.e., parallel to the waveguide axis. In (e) additional polarization filtering in x (filled circles) or y direction (open circles) was applied in the detection path. In each plot the red curves represent fits to the experimental data (black), which was flattened (by normalization to the unstructured background signal) prior to fitting.

of Q for the different cavity configurations are summarized and compared to the calculations in Tab. 3.2. Again, the observed reduction of the quality factor caused by the plasmon resonance is significantly larger than that predicted by the simulations, probably due to the same reasons as discussed in Sec. 3.6.1. However, for the configuration displayed in Fig. 3.18a, still a ≈ 10 times net enhancement of the Purcell factor F_c (compared to the bare cavity) is derived. Furthermore, the photonic contribution F_{ph} can be estimated if the ratio ξ of the collection efficiencies is known. For this purpose, corresponding FDTD simulations of the farfield radiation pattern were performed, providing a rough estimate $\xi \approx 1.5$ for the TE_y mode. Then, the fit in Fig. 3.20d yields a value $F_{ph} \approx 0.65$, which translates into a coupling efficiency $\beta = F_{ph}/(1+F_{ph}) \approx 0.4$ [see Eq. (2.41)]. This means that approximately 40% of the plasmon-enhanced emission from the nanoantenna couples into the cavity mode.

	$Q_{\mathrm{exp}}(\mathrm{TE_y})$	$Q_{\mathrm{theo}}(\mathrm{TE_y})$	$V_{\mathrm{eff}}(\mathrm{TE_y})$	$F_{\mathrm{exp}}(\mathrm{TE_y})$	$F_{\mathrm{theo}}(\mathrm{TE_y})$
	2490 ± 40	4300	$(1.16\ \mu\mathrm{m})^3$	≈ 30	55
●	1910 ± 40	3530			
● ●	720 ± 70	2610	$(0.37\ \mu\mathrm{m})^3$	≈ 300	1070
●●	1420 ± 30	3090	$(2.12\ \mu\mathrm{m})^3$	≈ 3	6.6

Table 3.2: Experimentally and theoretically obtained quality factors Q_{exp} and Q_{theo}, respectively, effective mode volumes V_{eff}, and associated Purcell factors F_{exp} and F_{theo} of the $\mathrm{TE_y}$ mode. The configurations (from top to bottom line) are: bare cavity without gold nanosphere, one nanosphere on top of the cavity center, nanosphere dimer oriented perpendicular to the waveguide axis, and nanosphere dimer oriented parallel to the waveguide axis. The Purcell factors F_{exp} and F_{theo} were calculated via $F = (3/4\pi^2)(Q/V_{\mathrm{eff}})(\lambda/n)^3$ using either Q_{exp} or Q_{theo}, respectively, and assuming a refractive index $n = 1$.

These results prove the general feasibility of a hybrid metal-dielectric cavity system and highlight some of its unique optical properties, such as the simultaneous occurrence of strong field localizations and relatively high quality factors. It must be noted, however, that the field localization was only derived from numerical calculations and corresponding experimental investigations should be conducted (using, e.g., optical near-field probes) to confirm these findings. The present work may thus be understood as a starting point, since a number of open questions concerning the potential of this type of hybrid cavity remain.

For example, it is not yet clear to which extend the local field enhancement can be boosted without degrading the quality factor too much. Certainly, an optimal tradeoff between both quantities exists, which has to be explored experimentally as well as in numerical simulations. The main task in future studies will therefore be the optimization of the metal nanostructures, which were so far not specifically designed, neither with regard to the spectral position nor the strength of the plasmon resonance. Chemically synthesized metal nanoparticles are well suited for this purpose, since they exhibit a high surface and bulk quality, providing low intrinsic damping. However, also ways have to be explored to fabricate these devices using scalable lithographic techniques, as the nanoassembly method employed here is not suitable for large-scale production, providing mainly a convenient way for studying the underlying physical processes. Finally, the controlled coupling of a single quantum emitter to such a plasmonic-photonic hybrid cavity has to be demonstrated. A first step towards this goal is presented in the next section.

3.7 Metal-diamond hybrid structures

As was already discussed in Sec. 3.3.3, the highly localized electromagnetic field of metal nanostructures can lead to significantly altered excitation and decay rates of nearby emitters. These effects have been investigated in a large number of studies, mainly employing dye molecules as fluorescent probes [187, 188, 203, 204, 241–243]. Integrating such a plasmon-coupled emitter into a more complex structure (e.g., the hybrid cavity system introduced in the previous section) seems very appealing, but the photobleaching and blinking inherent to most molecular species prevents the realization of long-term stable devices. The use of NV defect centers in diamond is an elegant solution to this problem, as they represent photostable single photon emitters operating even at room temperature (see Sec. 3.2.2). So far, however, no reports on the coupling of NV centers to plasmonic structures exist. In the following, the feasibility of this approach is demonstrated by using the nanomanipulation method introduced in Sec. 3.4.1 to assemble individual diamond nanocrystals and gold nanospheres to form combined nanophotonic elements. At first, the optical and mechanical properties of both constituents are investigated separately (Sec. 3.7.1). Subsequently, the various assembled configurations are characterized with regard to changes in the excitation and decay rate of the NV center as well as with respect to the single photon character of the emission (Sec. 3.7.2).

3.7.1 Properties of the individual constituents

For these studies diamond nanocrystals (20–35 nm in height) and gold nanospheres (60 nm in diameter) were spin-coated on a glass coverslip from an aqueous solution (containing 0.3% polyvinyl alcohol to prevent aggregation). Thereby, the use of a transparent substrate offered the advantage of a simultaneous manipulation and optical characterization of the particles, considerably simplifying the assembly process (see Sec. 3.4.2 for details of the experimental setup).

Prior to the assembly the emission properties of the individual constituents were investigated. Representative fluorescence spectra from a single NV defect center in a diamond nanocrystal and of a single gold nanosphere are shown in Fig. 3.21a. Approximately 1% of the diamond nanocrystals contained NV centers, most of which exhibited both zero phonon lines, that of the neutral NV^0 state at 575 nm and that of the negatively charged NV^- state at 637 nm. In all these cases the single photon character of the NV emission could be proved by corresponding measurements of the autocorrelation function $g^{(2)}(\tau)$ (see Sec. 3.2.2), hinting at a continuous charge transfer process during illumination [170, 171]. The excited state lifetime τ_2 of the investigated NV centers was determined from the corresponding fluorescence time traces (Fig. 3.21b), yielding typical values in the range 40–60 ns. This is considerably

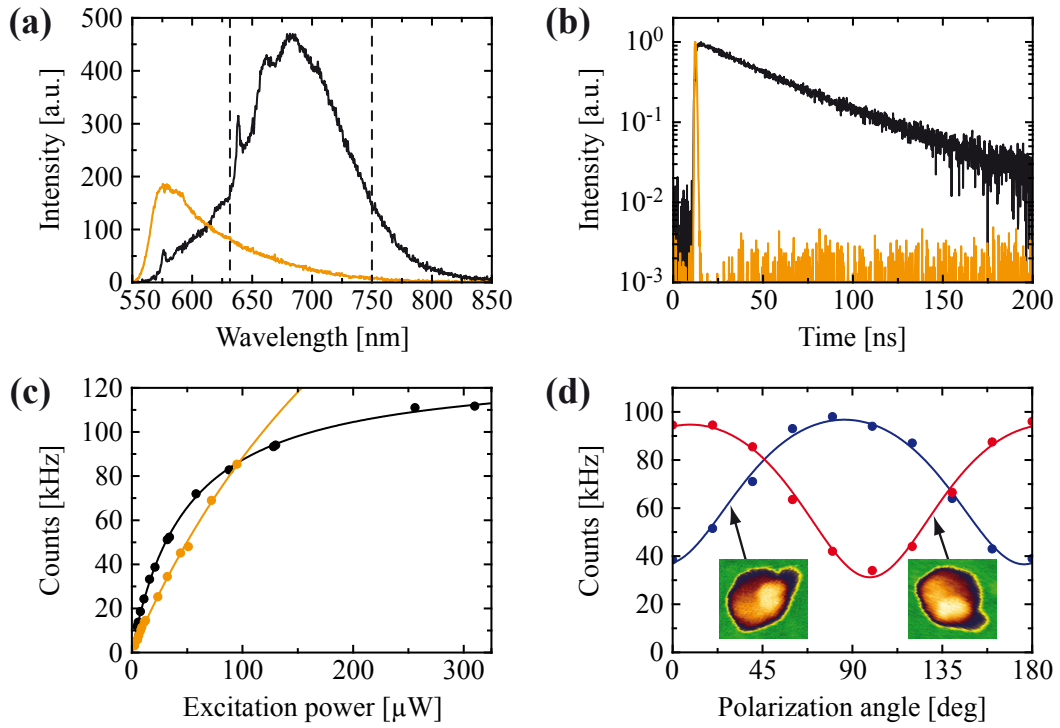

Figure 3.21: **(a)** Fluorescence spectra from a single NV defect center in a diamond nanocrystal (black) and from a single 60 nm gold nanosphere (orange). The horizontal dashed lines indicate the spectral detection window used in subsequent measurements. **(b)** Corresponding fluorescence time traces from the NV center (black) and the gold nanosphere (orange). **(c)** Photon count rate from the NV center (black) and the gold nanosphere (orange) as a function of the excitation power. The solid curves represent a fit to the experimental data using Eq. (3.33). **(d)** Photon count rate from the NV center as a function of the polarization angle θ of the excitation light. Blue and red circles refer to measurements on two different nanocrystal orientations, indicated by respective AFM images. The nanocrystal is 35 nm in height and ≈ 80 nm in width. The solid curves represent a modified $\cos^2(\theta)$ fit function, which also takes saturation effects into account.

longer than the lifetime $\tau_2 \approx 25$ ns found in other studies of diamond nanocrystals [174] and cannot simply be explained by the reduction of the refractive index of the environment (see Sec. 3.2.3). This discrepancy may be related to the conversion process $NV^- \leftrightarrow NV^0$ and/or the population of the metastable singlet state ^1A, leading to a longer effective lifetime observed in the measurements.

The fluorescence from the gold nanospheres results from a radiative decay of plasmons produced by interband transitions in the metal [240] and does not exhibit any photon antibunching. Its spectral position is directly linked to the plasmon resonance of the nanospheres, which lies at ≈ 560 nm on a glass substrate. This apparent mismatch with the emission wavelength of the NV center was chosen on purpose in order to be able to suppress a large amount of the unwanted background signal from the gold by spectral filtering (indicated in Fig. 3.21a). In time-resolved measurements the gold emission is easily distinguishable from the NV fluorescence

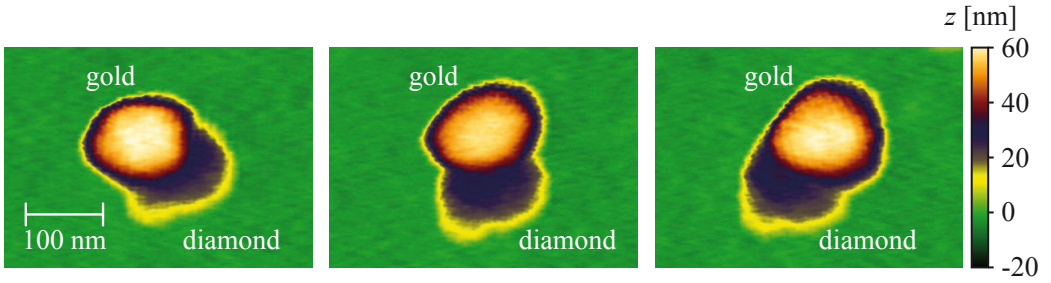

Figure 3.22: Series of AFM images demonstrating the controlled positioning of a 60 nm gold nanosphere relative the a diamond nanocrystal (same as the one shown in Fig. 3.21d). The nanocrystal stays fixed in its orientation (discernible from its characteristic shape) due to the stronger adhesion to the glass substrate. Distortions in the shape of the particles result from a degradation of the AFM tip.

due to its extremely short excited state lifetime below 10 ps (see Fig. 3.21b). Another difference between both types of emitters is related to their saturation behavior (Fig. 3.21c). While the fluorescence from the NV center saturates at excitation powers above 100 μW, the corresponding value for the gold emission is much higher (> 1 mW).

For almost all investigated NV centers a dependence of the detected fluorescence signal on the polarization direction of the excitation light could be observed. As seen in Fig. 3.21d, this is an inherent property of the diamond nanocrystals and not an artifact of the setup, since the angular variation of the emission intensity follows the orientation of the nanocrystal as the latter is rotated via the AFM tip. The excitation anisotropy is a result of the two-dimensional character of the transition dipole moment of the NV center, which lies in a plane perpendicular to the symmetry axis defined by the nitrogen atom and the vacancy [244].

In the assembled structure the distance and orientation of this dipole moment relative to the gold nanospheres is essential for an optimal plasmonic enhancement of the corresponding excitation and emission rate. However, as the NV center is located at a random position inside the diamond nanocrystal, both conditions (i.e., optimal distance and optimal orientation) can, in general, not be fulfilled at the same time. Consequently, a suitable tradeoff has to found, which was achieved in the experiment by moving a gold nanosphere around the diamond nanocrystal and monitoring the corresponding fluorescence signal, in this way exploring the optimal arrangement. A sequence of three successive manipulation steps is shown in Fig. 3.22. Note that only the gold nanosphere is moved while the diamond nanocrystal stays fixed in its position and orientation due to a stronger adhesion to the surface. The different mechanical interactions of both types of particles with the substrate and with each other are essential for a controlled assembly, as they allow a precise tailoring of the mutual orientation of the constituents.

3.7.2 Optical characterization of the assembled structures

Numerical analysis

Next, the optical properties of two specific assembled configurations are investigated, namely a diamond nanocrystal with one gold nanosphere attached (Fig. 3.23b) and the same nanocrystal sandwiched between two gold nanospheres (Fig. 3.23c). To estimate the plasmonic enhancement effects in these structures, corresponding FDTD simulations were performed using realistic material parameters (see Appendix A) and fully taking the influence of the glass substrate (with a refractive index $n = 1.51$) into account. The diamond nanocrystal was modeled as a truncated four-sided pyramid (with $n = 2.4$) and a mesh size of $(1\ \mathrm{nm})^3$ was chosen to accurately reproduce the electromagnetic fields near the metal surface. To simulate the excitation process the structures were illuminated by a tightly focused Gaussian laser beam with a wavelength $\lambda_{\mathrm{exc}} = 532$ nm. The resulting electric field intensity distributions $|\boldsymbol{E}|^2$ have been normalized to the respective calculation of the bare diamond nanocrys-

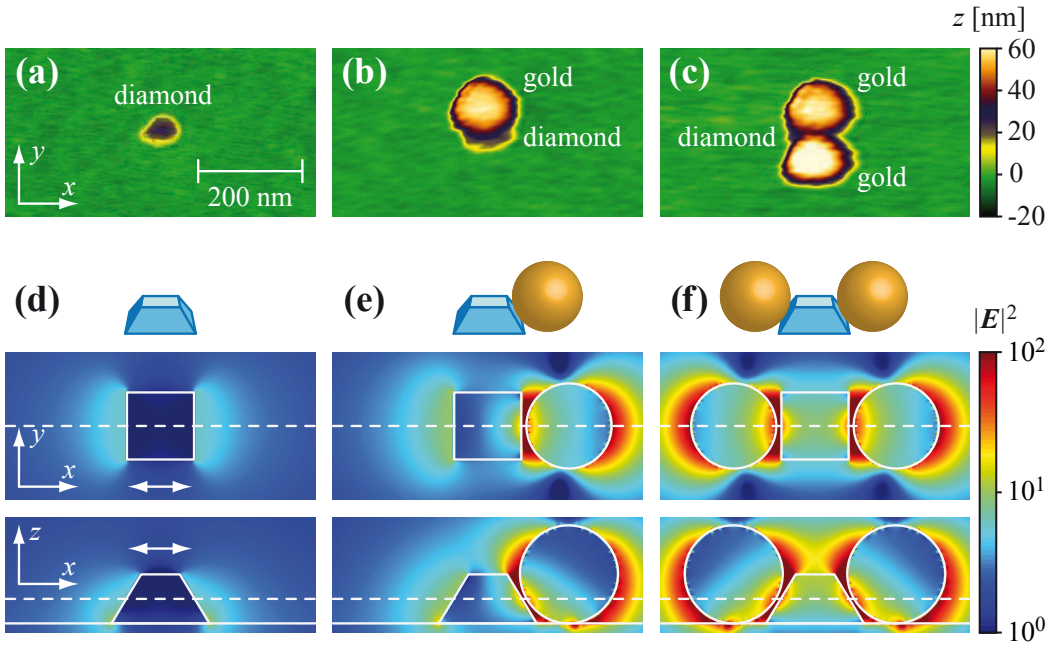

Figure 3.23: **(a–c)** AFM images of a single diamond nanocrystal (a) to which one (b) or two (c) 60 nm gold nanospheres are coupled. The nanocrystal is 30 nm in height and ≈ 40 nm in width. Distortions in the shape of the particles result from a degradation of the AFM tip. **(d–f)** Corresponding calculated electric field intensity distributions $|\boldsymbol{E}|^2$ of the excitation light (at a wavelength $\lambda_{\mathrm{exc}} = 532$ nm) for the configurations shown in (a–c). The Gaussian excitation beam is linearly polarized in x direction [indicated by arrows in (d)] and impinges from the negative z direction. Each panel displays x-y and x-z cross sections (indicated by dashed lines) through the center of the diamond nanocrystal, which is modeled as a truncated four-sided pyramid. The logarithmic color scale is always normalized to the respective $|\boldsymbol{E}|^2$ value at the center of the bare diamond nanocrystal shown in (d). Schematic representations of the particle configurations are also displayed for illustration.

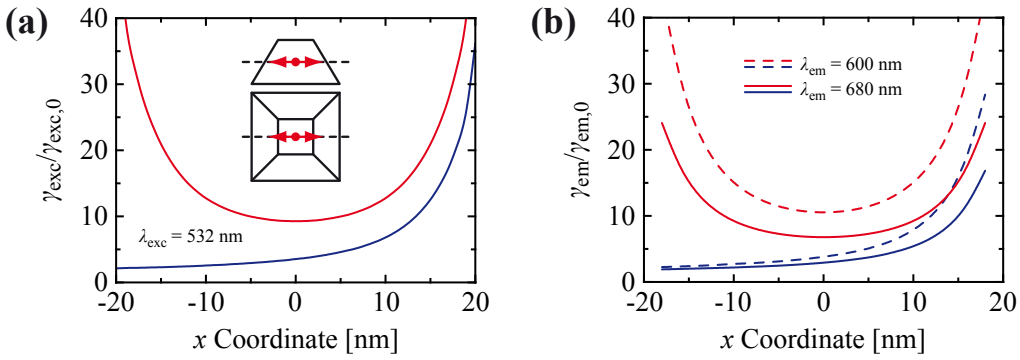

Figure 3.24: **(a)** Calculated enhancement of the excitation rate γ_{exc} (at a wavelength $\lambda_{exc} = 532$ nm) for a single dipole emitter as a function of its position within the diamond nanocrystal. The dipole is oriented in x direction and moved along the central x axis as indicated in the inset. Blue and red curves refer to configurations with one (Fig. 3.23e) or two gold nanospheres (Fig. 3.23f), respectively. **(b)** Calculated enhancement of the emission rate γ_{em} (at wavelengths $\lambda_{em} = 600$ nm and $\lambda_{em} = 680$ nm) for the same configurations as studied in (a). All rates are normalized to the respective values $\gamma_{exc,0}$ and $\gamma_{em,0}$ of the bare diamond nanocrystal (Fig. 3.23d).

tal (Fig. 3.23d) and are shown in Figs. 3.23e and 3.23f. Note that a strong field enhancement only occurs for polarizations in x direction, i.e., along the axis connecting the diamond nanocrystal and the gold nanospheres. In this case, pronounced hot spots are formed at the contact points between both particles due to the steep jump in refractive index, giving rise to an increased electric field inside the diamond nanocrystal.

The impact of this increased electric field on the excitation rate γ_{exc} of a dipole emitter is displayed in Fig. 3.24a. Clearly, a pronounced enhancement effect is observed, which decreases exponentially with increasing distance from the inner surface of the nanocrystal. The same holds for the enhancement of the emission rate $\gamma_{em} = \gamma_{rad}^2/(\gamma_{rad} + \gamma_{abs})$, which is shown in Fig. 3.24b and comprises changes in the radiative rate γ_{rad} as well as quenching effects due to absorption in the metal (at a rate γ_{abs}). Two emission wavelengths λ_{em} were simulated, namely 600 nm and 680 nm, corresponding to the peak wavelengths of the fluorescence from the NV^0 and NV^- state, respectively. Obviously, a stronger increase in the fluorescence intensity is expected for the NV^0 state, since it is better matched to the plasmon resonance of the gold nanospheres. Note that for both processes, excitation as well as emission, a pronounced enhancement only occurs if the dipole is align parallel to the x axis. For orientations in y or z direction, the change in the corresponding rates is much smaller and can even be slightly negative. It should further be noted that the values calculated here are only a rough estimate, since the true geometry of the diamond nanocrystal is much more irregular and the exact location and orientation of the NV center is unknown.

Experimental results

Spectroscopic, time-resolved, and photon correlation measurements were performed to investigate the optical properties of the assembled structures, indeed revealing strong modifications in the presence of the gold nanospheres. In the following, the arrangements shown in Figs. 3.23b and 3.23c are simply denoted as configurations A and B, respectively. A corresponding fluorescence spectrum from configuration A is displayed in Fig. 3.25a. Compared to the spectrum of the bare diamond nanocrystal, it exhibits a drastic change at its short wavelength side, which is a result of the different coupling efficiencies of the NV^0 and NV^- state to the plasmon resonance. Also, a pronounced dependence of the fluorescence signal on the polarization of the excitation light is observed (Fig. 3.25b), with an intensity contrast of a factor of 13 between polarization directions parallel and perpendicular to the x axis. In the latter case, no plasmonic enhancement of the NV emission occurs and the detected fluorescence signal is basically a mixture of the emission from the bare diamond nanocrystal and the gold nanosphere (see Figs. 3.21a and 3.25a). The results obtained for configuration B are similar, except that the relative intensity of the gold emission increases due to the presence of two gold nanospheres.

From time-resolved measurements (Fig. 3.26a) the excited state lifetime τ_2 of the NV center can be deduced, which is determined by all radiative and non-radiative decay processes. Assuming the level scheme and the corresponding transition rates shown in Fig. 3.1b, the lifetime is given by $\tau_2 = 1/(\gamma_{21} + \gamma_{23}^* + \gamma_{\mathrm{nr}})$, where $\gamma_{23}^* = \gamma_{23}\gamma_{31}/(\gamma_{32} + \gamma_{31})$ is the effective transition rate to the metastable state ^{1}A and γ_{nr} denotes all other non-radiative decay channels. Compared to the corresponding

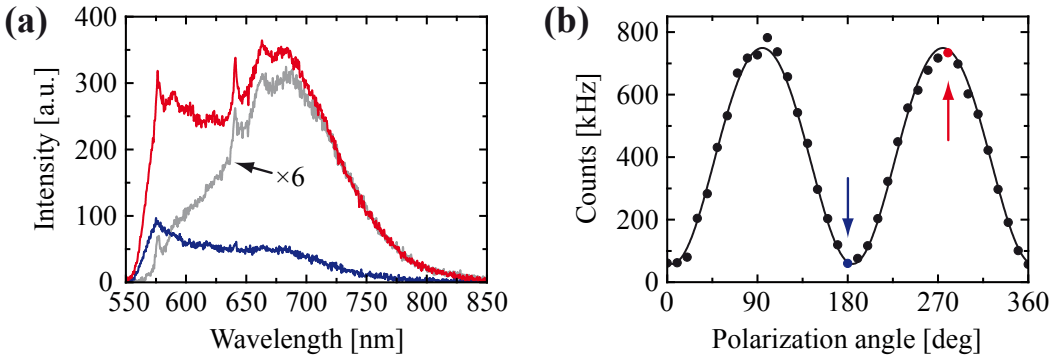

Figure 3.25: **(a)** Fluorescence spectra from the configuration shown in Fig. 3.23b, excited either in x direction (red) or in y direction (blue). For comparison, the spectrum from the bare diamond nanocrystal (scaled by a factor of 6) is displayed in gray. All measurements were performed at the same excitation power. **(b)** Photon count rate for the configuration shown in Fig. 3.23b as a function of the polarization angle θ of the excitation light. All data points were corrected for background emission from the gold. The solid curve represents a modified $\cos^2(\theta)$ fit function, which also takes saturation effects into account. The colored arrows indicate the values of θ for which the corresponding spectra in (a) were recorded.

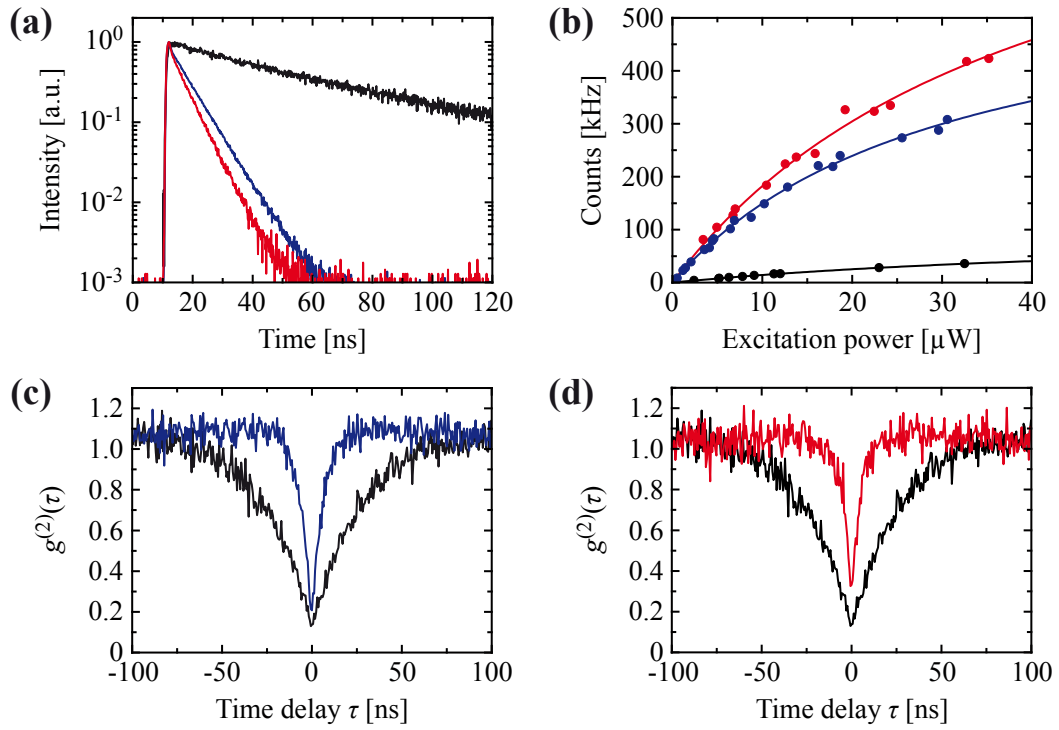

Figure 3.26: **(a)** Fluorescence time traces from the various configurations shown in Fig. 3.23, namely the bare diamond nanocrystal (black), with one gold nanosphere attached (blue), and sandwiched between two gold nanospheres (red). **(b)** Photon count rate as a function of the excitation power for the same configurations (and with the same color code) as in (a). All data points were corrected for background emission from the gold. The solid curves represent a fit to the experimental data using Eq. (3.33). **(c,d)** Measured autocorrelation functions $g^{(2)}(\tau)$ from the same configurations (and with the same color code) as in (a). Note that no background was subtracted in this case.

value $\tau_2 = 53$ ns of the bare diamond nanocrystal, a decrease of the excited state lifetime by factors of 7.5 and 9.5 is found for the configurations A and B, respectively.

To check whether this modification is due to radiative or non-radiative processes, additional power-dependent measurements were performed (Fig. 3.26b) and fitted by a saturation model of the form [245]

$$P = \frac{\xi\phi\gamma_{\mathrm{exc}}}{1 + \phi\gamma_{\mathrm{exc}}/\Gamma_{\mathrm{em}}} \,. \tag{3.33}$$

Here, ξ is the collection efficiency of the setup, ϕ is the fluorescence quantum yield of the NV center, $\gamma_{\mathrm{exc}} = \gamma_{12}$ is the excitation rate, and Γ_{em} is the (saturated) emission rate given by Eq. (3.10). Under strong excitation the maximum number of emitted photons is only restricted by Γ_{em} and Eq. (3.33) reduces to $P = \xi\Gamma_{\mathrm{em}}$. Since corresponding FDTD simulations show a negligible influence of the gold nanospheres on the far-field radiation pattern of the NV center, it is reasonable to assume the collection efficiency $\xi \approx 1\%$ to be constant throughout the measurements. Then,

an increase in the emission rate Γ_{em} by factors of 5.8 and 8.9 is deduced for the configurations A and B, respectively. If it is further assumed that the transition rates to and from the metastable state ^{1}A are not affected by plasmonic effects, this directly translates into a corresponding modification of the radiative rate $\gamma_{\mathrm{rad}} = \gamma_{21}$. By comparing these factors to those obtained from time-resolved measurements, quantum yields ϕ of 0.54 and 0.65 are derived for the configurations A and B, respectively, if a value $\phi = 0.7$ is assumed for the bare diamond nanocrystal [6].

Obviously, the first gold nanosphere induces an enhancement of γ_{rad}, but also a noticeable non-radiative decay rate γ_{abs} due to absorption in the metal, thus reducing the quantum yield. On the other hand, the second gold nanosphere predominantly enhances γ_{rad} without any severe absorption effects, thus partly restoring the original quantum yield. This can be attributed to the different distances of the nanospheres to the NV center, resulting in a different impact of fluorescence quenching (see Fig. 3.5). Note that the observed enhancement of Γ_{em} by nearly an order of magnitude is the highest achieved so far for NV centers and is equivalent to an increase of the maximum single photon rate by the same factor.

Far below saturation the number of emitted photons is not limited by Γ_{em}, but is proportional to the excitation rate γ_{exc}. From the power-dependent measurements displayed in Fig. 3.26b it is thus possible to deduce a 12- and 14-fold enhancement of γ_{exc} for the configurations A and B, respectively, in good agreement with the observations from polarization-dependent measurements (see Fig. 3.25b). For other diamond nanocrystals an increase of up to a factor of 18 was observed (data not shown). Again, the impact of the second gold nanosphere is rather modest compared to that of the first one, which is a result of the non-central location of the NV center inside the diamond nanocrystal. As a consequence of the employed assembly procedure (see Fig. 3.22), the first nanosphere is already placed at an optimal position with respect to the NV center and the effect of the second nanosphere is therefore much less pronounced.

Further inside into the decay dynamics of the assembled structures can be gained from photon correlation measurements (Figs. 3.26c and 3.26d). Apparently, the single photon character of the emission is still preserved, as the corresponding autocorrelation function $g^{(2)}(0)$ yields values well below 0.5 (see Sec. 3.2.2). The contribution f_{bg} of the background emission to the detected signal can be determined via $f_{\mathrm{bg}} = 1 - \sqrt{1 - g^{(2)}(0)}$ [166], yielding values of 7% and 14% for the configurations A and B, respectively. This background is dominated by the fluorescence from the gold nanospheres, but does not represent a fundamental limitation for the application as a single photon source. Since the decay time of the gold nanospheres is much faster than that of the NV center (see Fig. 3.21b), it can be eliminated through gated detection in a pulsed excitation scheme. By fitting Eq. (3.5) to the

correlation measurements and using the values of γ_{exc} and γ_{rad} obtained above as input parameters, the transition rates to and from the metastable state ^{1}A can be estimated. Although an exact determination turned out to be impossible due to the large number of fitting parameters, the obtained results are at least consistent with the assumption that these rates are not significantly influenced by plasmonic effects.

Finally, it should be noted that in the entire analysis presented here, the conversion to the neutral NV^0 state was completely ignored. Consequently, the derived values should be treated with care. However, it is believed that the general trend and the order of magnitude of the observed effects are correct, highlighting the potential of such a metal-diamond hybrid structure as a long-term stable single photon source. Furthermore, the plasmonic enhancement can boost the signal-to-noise ratio in single-spin read-out experiments [154, 155], considerably improving the performance of quantum information processing schemes.

3.8 Summary and conclusions

In this chapter an AFM-based nanomanipulation method for the controlled assembly of hybrid photonic and plasmonic elements was introduced and tested on three different systems. First, the deterministic coupling of dielectric nanoparticles to silicon nitride photonic crystal cavities was demonstrated, also studying the optical properties of these combined structures. Apparently, particle sizes below 20 nm would be ideal for an efficient coupling of external emitters to the cavities without a noticeable degradation of the cavity quality factor. On the other hand, larger (passive) particles may be employed for the precise tuning of the corresponding resonance wavelength. Attempts to investigate such a coupled emitter-cavity system using NV defect centers in a diamond nanocrystal failed due to the large background emission from the silicon nitride. In a second experiment the same manipulation technique was employed to realize a novel plasmonic-photonic hybrid cavity by placing metal nanoparticles on a photonic crystal structure. A coherent, polarization-selective coupling of the plasmon resonance to the various cavity modes could be observed, giving rise to an enhanced, precisely tailored light-matter interaction. Such a system also appears promising in conjunction with single photon emitters such as NV defect centers. Therefore, in a third series of experiments the controlled coupling of metal nanoparticles to diamond nanocrystals was studied, demonstrating an unprecedented boost in the excitation and emission rate of a single NV center by approximately one order of magnitude. The combination of all three elements (i.e., photonic crystal cavities, metal nanostructures, and NV centers) to realize a plasmonic-photonic single photon device could not be facilitated in the course of this thesis, but is subject of ongoing investigations.

Note that part of these findings have already been published in Barth *et al.* 2009a, 2009b, 2010b and Schietinger *et al.* 2009 (see List of Own Publications).

The great potential of the employed nanomanipulation method lies in its ability to realize multiple, precisely tailored nanophotonic elements, which can be linked in one and the same device. For example, the method is not restricted to a single emitter-cavity system as investigated here, but provides the means to create a whole network of coupled cavities with independently placed emitters (which need not to be of the same type) or other active materials. This paves the way for experimental investigations of the fundamental physics of coupled-cavity/coupled-emitter systems, which have not been possible so far employing only lithographic fabrication techniques [222]. Pioneering theoretical studies predict a strongly altered emission dynamics if two emitters are coupled to the same cavity mode [246] or to different cavities connected via an integrated waveguide [247].

Before being able to investigate such sophisticated cavity QED effects, some obvious drawbacks of the assembly technique have to be tackled. First and foremost, the nanoparticles can only be deposited on the surface of the photonic crystal structures, leading to a pure evanescent coupling and thus to a reduced emitter-cavity interaction. The proposed plasmonic-photonic hybrid cavity may present a solution to this problem, as the metal nanostructures act as a transceiver between the emitter and the corresponding cavity mode, effectively increasing the interaction. A different approach involves the incorporation of small molds into the photonic crystal slab, allowing the particles to be brought closer to the region of highest field intensity. First numerical simulations indicate that such molds would not reduce the cavity quality factor too much as long as their diameter is restricted to values below 50 nm.

Another drawback of the current assembly technique is the rather imprecise "dip-pen" deposition process, which still lacks control on a single particle level. However, various approaches to tackle this problem are available. Recently, several groups introduced a novel method which utilizes a manipulator tip in a scanning electron microscope to pick up and place individual nanoparticles under real-time imaging conditions [248, 249]. Alternatively, first experiments with platinum-coated AFM tips also yielded promising results concerning a reliable pick-and-place procedure, potentially simplifying the assembly process. This is essential in the case of diamond nanocrystals, among which only a small fraction usually contains a single defect center.

In this regard, the question whether NV defect centers in diamond nanocrystals are indeed suitable candidates for the proposed cavity QED applications should briefly be discussed. The strain-induced shift and spectral diffusion of the zero phonon transition may represent a severe obstacle for an efficient emitter-cavity

interaction. For this reason, growing efforts exist to directly couple NV centers in bulk diamond to optical microcavities [250–253]. However, these approaches provide much less control on the emitter-cavity coupling than the particle-based method introduced here. Therefore, other types of defect centers in diamond nanocrystals should be tested with respect to their suitability for cavity QED applications. A promising candidate has recently been reported by Aharonovich *et al.* [254] and further studies will certainly follow. Then, after the issues discussed above have been addressed, the nanomanipulation method can enable the realization of a multitude of hybrid nanophotonic and plasmonic devices operating on a single photon level. Although a large-scale production is not possible with this technique, it can provide invaluable insight into the underlying physical processes.

Chapter 4

Analysis of optical forces near photonic crystal cavities

4.1 Introduction

In the previous chapter it was shown that nanoscopic particles can influence the optical properties of photonic crystal cavities, inducing changes in the resonance wavelength, quality factor, and field distribution of the corresponding cavity modes. This sensitivity to the local dielectric environment is the key property which makes photonic crystal structures attractive for a variety of sensing applications, especially in the rapidly developing field of optofluidics [8, 9]. For example, refractive index sensing has been demonstrated by monitoring the transmission signal of photonic crystal cavities [255–258] or waveguides [259, 260], or by detecting spectral shifts in the emission from photonic crystal nanolasers [261–263]. Compared to bulk systems, these structures offer a compact and versatile design which is capable of performing measurements on ultra-small sample volumes (down to femtoliters) and which can potentially be integrated into so-called "lab-on-a-chip" devices for biochemical sensing.

In principle, it should be possible to detect individual biological objects (such as cells, bacteria, or even single macromolecules) by monitoring the spectral response of a photonic crystal cavity, as can be deduced from the numerical simulations presented in Sec. 3.5. The main challenge, however, lies in a targeted transport of the respective object and its subsequent immobilization on or near the cavity to ensure a sufficiently long interaction time. A corresponding manipulation scheme may be realized in an elegant way by exploiting the optical forces exerted on the object by the electromagnetic field of the cavity itself. Such a type of manipulation is well-known from optical tweezers, which utilize a strongly focused laser beam to trap and move dielectric particles [264] and have become one of the most versatile

tools in life science [265]. Apart from these trapping techniques, which rely on freely propagating beams, near-field optical methods have emerged in recent years, offering the advantage of better spatial confinement. Various different approaches exist, employing either evanescent wave illumination [266, 267], nanometric tips [268] or apertures [269], plasmonic nanostructures [270], or optical microcavities [271, 272] to generate the trapping field.

Photonic crystal cavities belong to the latter type of devices, providing the benefit of an additional enhancement of the trapping field due to the cavity resonance. However, apart from pioneering theoretical studies of the corresponding forces acting on nearly point-like particles [273, 274], no comprehensive investigation of the optomechanical phenomena occurring near photonic crystal cavities has been performed so far. Therefore, the third part of this thesis deals with a thorough numerical analysis of the forces exerted on dielectric particles of various sizes (ranging from several nanometers to micrometers) and the accompanied back-action on the optical properties of the photonic crystal cavities. It is demonstrated that an intricate interplay between both entities can arise, resulting in phenomena such as self-induced or bistable trapping, highlighting the unique optomechanical characteristics of these systems.

The chapter is organized as follows: In Sec. 4.2 the basic theory of electromagnetic forces is introduced, providing the background knowledge for the subsequent numerical analysis of the particle-cavity interaction. This analysis starts with the investigation of an idealized system in Sec. 4.3, exploring changes in the trapping behavior as the particle size varies. A more realistic geometry is then studied in Sec. 4.4, taking into account the resonance shift induced by the particle. A complicated collapse and revival of the trapping force is revealed, depending sensitively on the particle position. An application of these effects for the realization of size-selective trapping schemes is discussed. Finally, a short summary of this chapter as well as some concluding remarks are given in Sec. 4.5.

4.2 Theory of electromagnetic forces

The idea that light exerts a force when impinging upon matter dates back to Maxwell himself [275]. This optical force is simply a consequence of the conservation of momentum and can occur in different forms, either as radiation pressure, pushing objects away, or as an attractive force, pulling objects to the region of highest field intensity. In the following, the fundamental laws for these optical forces are derived in general terms (Sec. 4.2.1) as well as in the limit of small particles (Sec. 4.2.2). Furthermore, the specific conditions encountered in the geometries studied here (i.e., photonic crystal structures) are discussed (Sec. 4.2.3).

4.2.1 General expression for electromagnetic forces

The starting point for describing the force $\boldsymbol{F}$ exerted by an electromagnetic field on a dielectric body (with $\mu = 1$) is the Lorentz law [33]

$$\boldsymbol{F} = q(\boldsymbol{E} + \boldsymbol{v} \times \mu_0 \boldsymbol{H}) \,, \tag{4.1}$$

with q and $\boldsymbol{v}$ being the charge and velocity, respectively, of a specific volume element of the body. Equation (4.1) can be rewritten in terms of the charge density ρ and the current density $\boldsymbol{J}$, yielding the more general expression for the force density

$$\boldsymbol{f} = \rho \boldsymbol{E} + \boldsymbol{J} \times \mu_0 \boldsymbol{H} \,. \tag{4.2}$$

Using the Maxwell equations (2.1)–(2.4) as well as the vector relation $(\nabla \times \boldsymbol{V}) \times \boldsymbol{V} = (\boldsymbol{V} \cdot \nabla)\, \boldsymbol{V} - \nabla |\boldsymbol{V}|^2/2$, this can be transformed into

$$\begin{aligned} \boldsymbol{f} = \varepsilon_0 \varepsilon \Big[\boldsymbol{E}(\nabla \cdot \boldsymbol{E}) + (\boldsymbol{E} \cdot \nabla)\boldsymbol{E} \Big] + \mu_0 \Big[\boldsymbol{H}(\nabla \cdot \boldsymbol{H}) + (\boldsymbol{H} \cdot \nabla)\boldsymbol{H} \Big] \\ - \frac{1}{2} \nabla \Big(\varepsilon_0 \varepsilon |\boldsymbol{E}|^2 + \mu_0 |\boldsymbol{H}|^2 \Big) - \frac{\varepsilon}{c^2} \frac{\partial \boldsymbol{S}}{\partial t} \,, \end{aligned} \tag{4.3}$$

with $\boldsymbol{S} = \boldsymbol{E} \times \boldsymbol{H}$ denoting the Poynting vector. By defining the Maxwell stress tensor $\mathbf{T}$ via [33]

$$T_{ij} = \varepsilon_0 \varepsilon E_i E_j + \mu_0 H_i H_j - \frac{1}{2} \delta_{ij} \Big(\varepsilon_0 \varepsilon |\boldsymbol{E}|^2 + \mu_0 |\boldsymbol{H}|^2 \Big) \qquad (i, j = x, y, z) \,, \tag{4.4}$$

Eq. (4.3) takes the simple form

$$\boldsymbol{f} = \nabla \cdot \mathbf{T} - \frac{\varepsilon}{c^2} \frac{\partial \boldsymbol{S}}{\partial t} \,. \tag{4.5}$$

The total time-averaged force on a dielectric body of volume V is then given by

$$\langle \boldsymbol{F} \rangle = \int\limits_V \mathrm{d}\boldsymbol{r}\, \langle \nabla \cdot \mathbf{T} \rangle - \int\limits_V \mathrm{d}\boldsymbol{r}\, \frac{\varepsilon}{c^2} \left\langle \frac{\partial \boldsymbol{S}}{\partial t} \right\rangle \,. \tag{4.6}$$

In the case of a harmonically oscillating steady-state electromagnetic field, the time-averaged Poynting vector (averaged over one oscillation period $T = 2\pi/\omega$) does not vary with t and the second integral on the right hand side of Eq. (4.6) vanishes [276]. By applying the divergence theorem the first integral can be transformed into an integral over the surface A enclosing the volume V of the dielectric body, yielding the expression

$$\langle \boldsymbol{F} \rangle = \oint\limits_A \mathrm{d}s\, \langle \mathbf{T} \rangle \cdot \hat{\boldsymbol{n}} \,. \tag{4.7}$$

Here, $\hat{\boldsymbol{n}}$ is the unit normal vector (pointing outwards) on the surface element ds and the time-averaged Maxwell stress tensor is given by [276]

$$\langle T_{ij} \rangle = \frac{1}{2}\varepsilon_0\varepsilon \mathrm{Re}\{E_i E_j^*\} + \frac{1}{2}\mu_0 \mathrm{Re}\{H_i H_j^*\} - \frac{1}{4}\delta_{ij}\left(\varepsilon_0\varepsilon|\boldsymbol{E}|^2 + \mu_0|\boldsymbol{H}|^2\right) . \tag{4.8}$$

Note that the integration in Eq. (4.7) can be performed over any surface which encloses the object under consideration once the electromagnetic field distribution is known. In the complex geometries which are of interest here (i.e., photonic crystal cavities), these fields have to be calculated numerically. Then, the resulting optical force on any dielectric object (of arbitrary size) can be obtained by applying the Maxwell stress tensor formalism described above. However, it is instructive to consider the limiting case of very small particles to gain insight into the nature and order of magnitude of these forces, as is discussed next.

4.2.2 Dipole approximation for electromagnetic forces

In the following, a dielectric sphere of radius R and refractive index n_2 in a medium of refractive index n_1 is assumed. If R is much smaller than the corresponding wavelength λ/n_1 (the so-called Rayleigh regime), the variation of the electromagnetic field over the extend of the sphere can be neglected and the latter can be treated as an induced point dipole on which the external field acts. Then, according to the Lorentz law in Eq. (4.1), the force exerted on this dipole (located at position $\boldsymbol{r}_0$) is given by [33]

$$\boldsymbol{F} = (\boldsymbol{\mu}\cdot\nabla)\boldsymbol{E} + \frac{\partial \boldsymbol{\mu}}{\partial t} \times \mu_0 \boldsymbol{H} , \tag{4.9}$$

where $\boldsymbol{\mu}$ is the induced dipole moment, being equivalent to the (microscopic) polarization $\boldsymbol{P}(\boldsymbol{r}) = \boldsymbol{\mu}\delta(\boldsymbol{r}-\boldsymbol{r}_0)$ [277]. Using the relation $\boldsymbol{P} = \alpha\boldsymbol{E}$ for a linear dielectric medium with polarizability α as well as the Maxwell equation (2.3), one obtains an expression for the time-averaged force of the form [278]

$$\langle \boldsymbol{F} \rangle = \frac{1}{4}\mathrm{Re}\{\alpha\nabla|\boldsymbol{E}|^2\} . \tag{4.10}$$

Here, a harmonically oscillating electromagnetic field was assumed.

Equation (4.10) can be evaluated in various ways, yielding different notions of the force contributions which act upon the particle. For example, if the polarizability α is identified with the Clausius-Mossotti equation

$$\alpha_0 = 4\pi\varepsilon_0 n_1^2 R^3 \frac{n_2^2 - n_1^2}{n_2^2 + 2n_1^2} , \tag{4.11}$$

Eq. (4.10) takes the simple form [279]

$$\langle \boldsymbol{F} \rangle_{\mathrm{grad}} = \frac{1}{4}\alpha_0 \nabla |\boldsymbol{E}|^2 \, . \tag{4.12}$$

This so-called gradient force always pulls the particle towards the region of highest field intensity, provided that $n_2 > n_1$. It directly reflects the Lorentz force exerted on the point dipole. However, the expression in Eq. (4.12) is incomplete, since it does not account for the scattering field induced by the dipole and the accompanied change in the momentum of the (external) electromagnetic field. As the total momentum has to be conserved [280], a corresponding scattering force is exerted on the particle, which is given by [279]

$$\langle \boldsymbol{F} \rangle_{\mathrm{scat}} = \frac{n_1^2 |\boldsymbol{k}|^4}{12\pi\varepsilon_0} \alpha_0^2 |\boldsymbol{E}|^2 \hat{\boldsymbol{k}} \tag{4.13}$$

for the simple case of an impinging plane wave. Here, $\boldsymbol{k}$ and $\hat{\boldsymbol{k}}$ are the free-space wave vector of the plane wave and the corresponding unit vector, respectively.

This scattering force can directly be derived from Eq. (4.10) in a consistent way by employing the generalized expression

$$\alpha = \frac{\alpha_0}{1 - i n_1 |\boldsymbol{k}|^3 \alpha_0 / (6\pi\varepsilon_0)} \approx \alpha_0 + i \frac{n_1 |\boldsymbol{k}|^3}{6\pi\varepsilon_0} \alpha_0^2 \tag{4.14}$$

for the polarizability of the sphere, which includes the radiation-reaction term analogues to Eq. (3.21). The total force then reads [276]

$$\langle \boldsymbol{F} \rangle = \frac{1}{4}\mathrm{Re}\{\alpha\} \nabla |\boldsymbol{E}|^2 + \frac{1}{2} n_1 \boldsymbol{k}\, \mathrm{Im}\{\alpha\} |\boldsymbol{E}|^2 - \frac{1}{2}\mathrm{Im}\{\alpha\}\mathrm{Im}\{\boldsymbol{E} \cdot \nabla \boldsymbol{E}\} \, , \tag{4.15}$$

with the first term being the gradient force [Eq. (4.12)] and the second term representing the scattering force for a single plane wave [Eq. (4.13)]. The third term accounts for scattering arising from all other field contributions.

As is seen from Eqs. (4.12) and (4.13), the gradient and scattering force exhibit different dependencies on the radius R of the dielectric sphere. While $|\boldsymbol{F}_{\mathrm{grad}}|$ increases proportional to R^3, $|\boldsymbol{F}_{\mathrm{scat}}|$ grows with R^6. This, however, is only true for small radii $R < \lambda/(20 n_1)$, above which the Rayleigh approximation becomes inaccurate and strongly overestimates the contribution of $\boldsymbol{F}_{\mathrm{scat}}$ [279]. The correct results for spheres of arbitrary size are obtained from Mie theory [281], which, in turn, converges to the classical ray optics description for very large particle radii $R \gg \lambda/n_1$ [282]. Nonetheless, the dipole approximation can also be applied to larger dielectric objects (of arbitrary shape) by treating the particle as being composed of a continuous distribution of dipoles and integrating over its entire volume [283].

4.2.3 Application to photonic crystal structures

The question which force ($\boldsymbol{F}_{\mathrm{grad}}$ or $\boldsymbol{F}_{\mathrm{scat}}$) dominates for a particular particle size and, consequently, determines whether the particle is spatially trapped or propelled in a certain direction depends on the specific field distribution $\boldsymbol{E}(\boldsymbol{r})$. The original ideas of manipulating dielectric particles by optical forces mainly relied on freely propagating beams [264, 284, 285]. For example, in the case of a tightly focused laser beam (Fig. 4.1a) the gradient force pulls the particle towards the center of the focus, while the scattering force pushes it in the direction of beam propagation. A stable three-dimensional optical trapping is only possible if $|\boldsymbol{F}_{\mathrm{grad}}| > |\boldsymbol{F}_{\mathrm{scat}}|$ for all directions and if the resulting trapping potential W exceeds the kinetic energy of the particle due to Brownian motion. The latter criterion is fulfilled if $\exp(-W/k_{\mathrm{B}}T) \ll 1$, where k_{B} denotes the Boltzmann constant and T is the temperature of the surrounding medium. Typically, a value $W > 10k_{\mathrm{B}}T$ is considered sufficient for a stable optical trapping [264].

If the laser beam is not propagating in free space, but is guided within a dielectric waveguide (Fig. 4.1b), the particle mainly interacts with the evanescent part of the field distribution, experiencing a steep intensity gradient and thus a large gradient force directed towards the surface of the waveguide. In addition, a scattering force

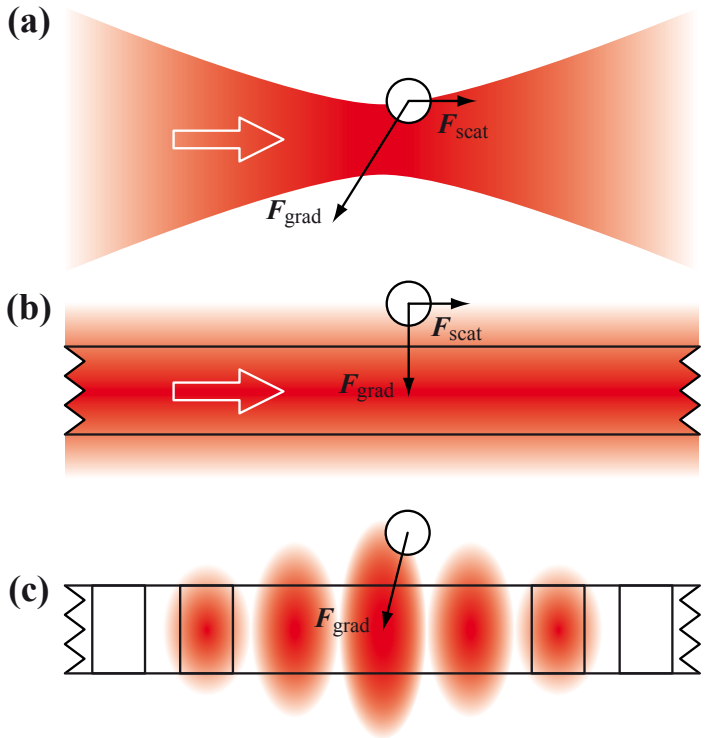

Figure 4.1: Schematic illustration of the optical forces acting on a dielectric sphere in various environments: **(a)** near the focus of a free-space laser beam, **(b)** near the surface of a dielectric waveguide, and **(c)** near the surface of a planar photonic crystal cavity.

occurs, which propels the particle along the direction of mode propagation. This behavior can be utilized to assemble and simultaneously transport multiple objects on predefined pathways [286–288] and has even been applied for particle sorting [289].

In the case of a planar photonic crystal cavity (Fig. 4.1c), the electromagnetic field is not only vertically confined to the dielectric slab, but is also localized in a small region within the plane of the slab, forming a standing wave. Consequently, all scattering forces in the lateral direction balance on average, while scattering forces in the vertical direction can be neglected as long as radiative cavity losses are small. Then, the only remaining significant contribution is the gradient force pulling the particle toward the surface of the cavity, where it stays fixed in its position. If the cavity mode is engineered such that the intensity maximum is located within one of the holes, the particle might actually get trapped inside the latter. Therefore, photonic crystal cavities can be employed to immobilize and detect dielectric objects, provided that a suitable input channel exists on which light can efficiently be coupled into the cavity in order to create a sufficiently large trapping potential.

4.3 Dependence of optical forces on particle size and cavity geometry

The few theoretical studies investigating the optical forces near photonic crystal cavities have all been limited to very small particles [273, 274], while no reports on the trapping behavior of larger objects beyond the dipole approximation exist so far. Such an analysis would be of high interest, especially with regard to biological applications, where the typical particle dimensions span ranges from a few nanometers up to several micrometers. Therefore, the purpose of this section is a detailed investigation of the optical forces in this yet unexplored regime, focusing on changes in the trapping behavior as the particle size and cavity geometry varies. Other aspects, such as the impact of the particles on the quality factor and resonance wavelength of the cavities, are neglected in this analysis, but will be taken into account in Sec. 4.4.

As in the previous chapters, FDTD simulations were employed to calculate the field distribution in the photonic crystal cavities, using simulation parameters similar to those described in Sec. 2.4.1. However, several important changes regarding the cavity design were made. The entire photonic crystal structure is now immersed in an aqueous medium with a refractive index $n = 1.33$ and silicon (with $n = 3.46$) is used as slab material instead of silicon nitride to ensure a sufficiently large index contrast. To reduce the complexity of the field distribution, the so-called H1 cavity design is employed, featuring a single modified hole in the otherwise periodic photonic crystal lattice. Two different versions of this cavity are studied, with the central hole being

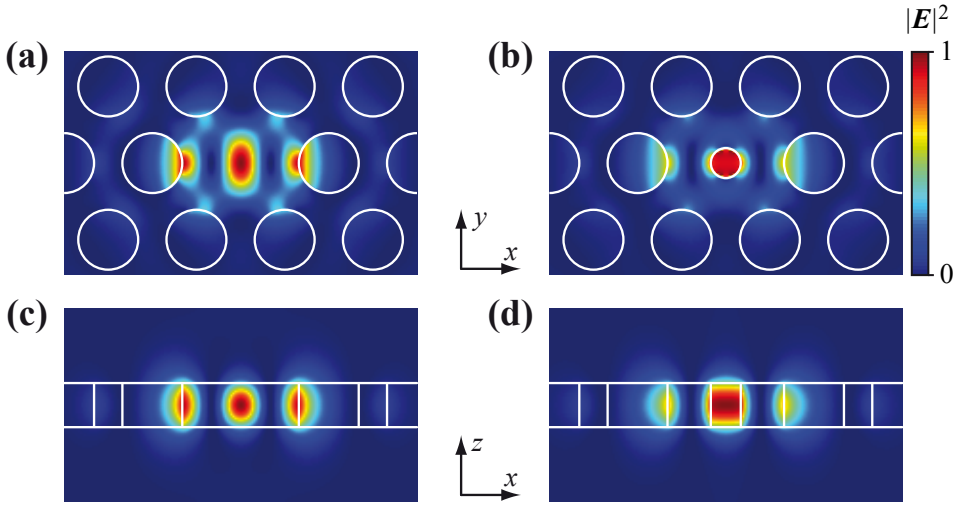

Figure 4.2: (a,c) Calculated electric field intensity distribution $|\boldsymbol{E}|^2$ of the $\mathrm{TE_y}$ mode of the cavity H1a, i.e., a single missing hole. The lattice parameters are $a = 460$ nm, $t = 0.5a$, and $r = 0.35a$. The slab material is silicon (refractive index $n = 3.46$) immersed in an aqueous medium ($n = 1.33$). **(b,d)** Corresponding intensity distribution of the cavity H1b with a central hole of reduced radius $r' = 0.5r$. For both types of cavities cross sections through the central x-y (a,b) and x-z planes (c,d) are displayed, respectively.

either completely omitted (termed cavity H1a) or having a reduced radius $r' = 0.5r$ (termed cavity H1b). Both structures support two orthogonal, nearly degenerate cavity modes. In the following, only the one shown in Fig. 4.2 is considered, being denoted as $\mathrm{TE_y}$ due to its polarization in y direction (at the center of the cavity). The corresponding resonance wavelength lies near 1550 nm. It should be emphasized that this is an arbitrary choice and that the results discussed below are scalable to other wavelengths as long as a suitable high-index material is available. Therefore, all length scales are given in units of the lattice constant a throughout this section.

To study the optical forces near the cavities, polystyrene beads with a refractive index $n = 1.59$ serve as model particles, being placed at different locations above the surface of the photonic crystal slab. Once the electromagnetic field distribution in each of these configurations is known from the FDTD simulations, the resulting force $\boldsymbol{F}$ can be calculated by applying Eq. (4.7). Note that a small gap had to be introduced between the surface of the bead and that of the slab in order to properly evaluate the corresponding surface integral. The results for a bead of diameter $d = 0.5a$ are shown in Fig. 4.3. All values were scaled with respect to the power $P = cU/V_{\mathrm{eff}}^{1/3}$ inside the cavity, yielding the normalized force $\boldsymbol{K} = \boldsymbol{F}/P$. Here, U is the mode energy according to Eq. (2.17) and V_{eff} is the mode volume defined by Eq. (2.21). Note that this normalization obscures any effects due to changes in the quality factor or resonance wavelength of the cavity, but provides a clearer picture of the underlying optical forces.

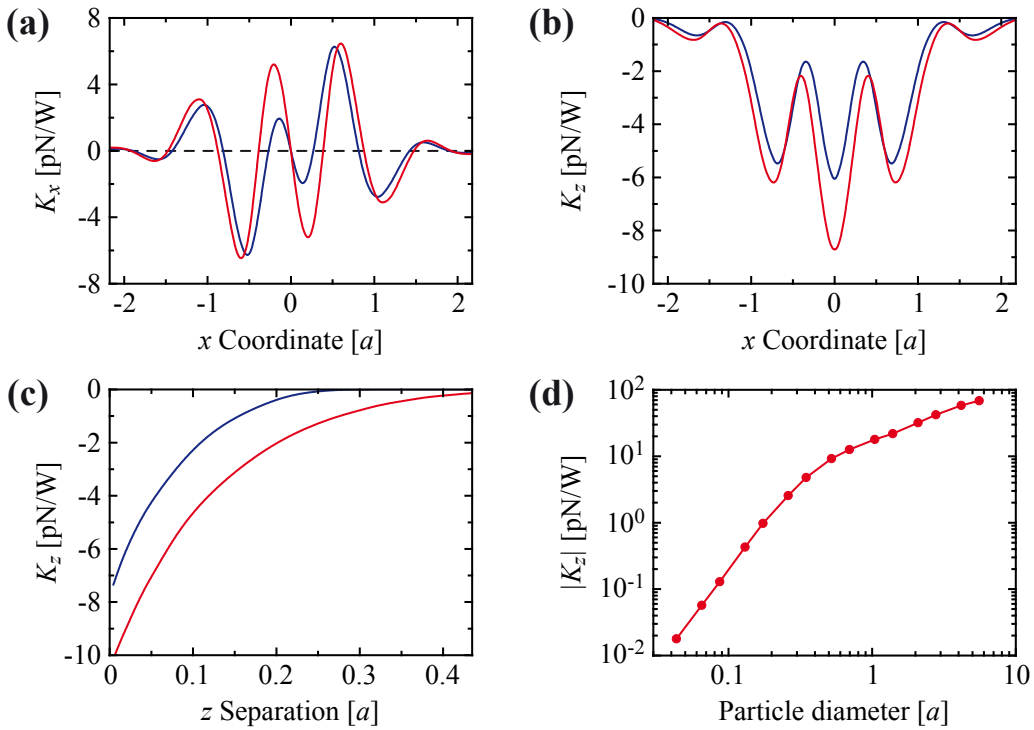

Figure 4.3: **(a,b)** Normalized force components K_x (a) and K_z (b) for a polystyrene bead (diameter $d = 0.5a$) located above the surface of an H1 photonic crystal cavity as a function of the position on the central x axis. Blue and red curves refer to the cavities H1a and H1b shown in Figs. 4.2a and 4.2b, respectively. A small gap of width $a/50$ was introduced between the bead and the slab surface. **(c)** Corresponding forces K_z for the same bead located above the center of the respective cavities as a function of the separation between the bead and the slab surface. **(d)** Normalized force K_z for beads of different diameters located above the center of the cavity H1b. The separation between the bead and the slab surface is held constant at $a/50$.

As is evident from Figs. 4.3a and 4.3b, the force mainly follows the electric field distribution, exhibiting clear differences between the cavities H1a and H1b. In the case of cavity H1b, the concentration of the electric field in the central hole results in a stronger force at this location. Additionally, the evanescent field penetrates farther into the surrounding medium due to the reduced effective refractive index of the photonic crystal slab, leading to an extended trapping range in z direction (see Fig. 4.3c). In general, it can be concluded that all design modifications which expel a part of the field intensity from the high-index material (i.e., the silicon slab) into the surrounding medium are favorable for an efficient optical trapping, provided that a sufficiently large cavity quality factor is maintained. In this regard, slot-based waveguide and cavity structures have recently attracted considerable attention [290–294], since they allow a large fraction of the electric field to be located in the low-index medium.

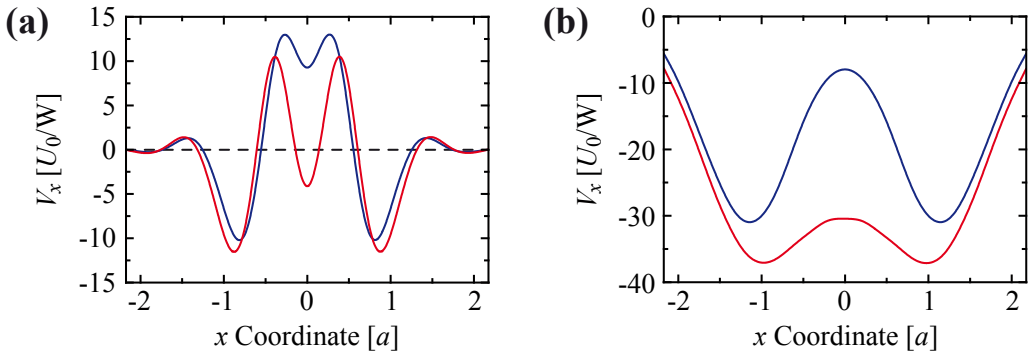

Figure 4.4: **(a)** Normalized trapping potential V_x on the central x axis for a polystyrene bead of diameter $d = 0.5a$, located above the cavities H1a (blue) and H1b (red) shown in Figs. 4.2a and 4.2b, respectively. **(b)** Corresponding trapping potentials V_x for a larger bead of diameter $d = 5a$. For both particles the separation between the bead and the slab surface is $a/50$.

To investigate size-dependent changes in the trapping behavior, the calculations presented above were repeated with beads of different diameters d. As is seen in Fig. 4.3d, the maximum force component F_z varies proportional to d^3 for particles within the Rayleigh limit (i.e., $d < 0.2a$), which is in accordance with Eq. (4.12). With growing diameter the particles start to extends beyond the decay length of the evanescent field in z direction, at the same time overlapping with multiple field lobes in the lateral direction. Therefore, the corresponding force increases approximately proportional to d^2 in this size regime. For even larger particles exceeding the cavity mode volume, a saturation of the force is expected. The final trapping position in z direction is either located on top of the photonic crystal slab or at its center, depending on whether the bead is small enough to be drawn into one of the holes. As described in Sec. 4.2.3, the depth of the corresponding trapping potential W_z has to exceed the kinetic energy $U_0 = 10k_\mathrm{B}T$ of the particle due to Brownian motion to ensure a stable trapping. At room temperature $U_0 = 4.1 \times 10^{-20}$ J, which translates into a necessary force $|F_z| \approx 1$ pN.

The situation is much more complicated if the trapping position in the lateral direction is considered. For example, the normalized potential $V_x = W_x/P$ (in units of U_0) for a bead of diameter $d = 0.5a$ is shown in Fig. 4.4a. As can be seen, there are three potential wells of nearly equal depth in the case of cavity H1b, being associated with the three lobes in the electric field intensity distribution (see Fig. 4.2d). In the case of cavity H1a, the central potential minimum is much shallower, which is a result of the smaller penetration length of the corresponding field lobe into the surrounding medium (see Fig. 4.2c). Therefore, a small particle would preferentially get trapped near the outer holes of cavity H1a, while there is a high probability for getting trapped at the center of cavity H1b.

This behavior changes drastically as the bead diameter increases and the particle starts to overlap multiple field lobes. In Fig. 4.4b the corresponding results for a diameter $d = 5a$ are displayed. Obviously, there is no narrow potential well in the case of cavity H1b, as all three field lobes are comparable in strength and cancel each other. Consequently, the particle may easily hop between different positions along the whole length of the cavity. Contrary to this, there are still two distinct and well-defined trapping sites in the case of cavity H1a, providing a much better spatial confinement of the particle in the lateral direction. This example illustrates that there is not necessarily an optimal cavity design for the entire range of particle diameters. Instead, a careful optimization for each size regime may be required, depending on the specific application and the associated trapping demands.

As a final point in this section the obtained results shall be put into perspective regarding the achievable trapping performance. The optical forces and potentials displayed in Figs. 4.3 and 4.4 are all normalized to the power P inside the cavity. Under resonant conditions P is related to the input power P_0 via $P = \eta Q P_0$, where η is the coupling efficiency of light into the cavity. Consequently, the trapping performance of the photonic crystal cavity is enhanced by a factor ηQ compared to a free-space beam. For example, a power $P = 100$ mW is required to reliably trap a medium-sized bead of diameter $d = 0.5a$ according to the simulations presented above. Assuming moderate values $\eta = 0.1$ and $Q = 10^4$, this corresponds to an input power of 0.1 mW, which is orders of magnitude smaller than in conventional optical tweezers.

4.4 Influence of particle-induced resonance shifts on the trapping behavior

In the previous section the photonic crystal cavities were mainly treated as an idealized system, focusing only on the field distribution, but neglecting other properties such as the quality factor and the resonance wavelength. However, in any real implementation the surrounding medium and the particle will have a noticeable influence on both, eventually diminishing the achievable trapping performance discussed above. Therefore, this section deals with a more sophisticated analysis of the trapping behavior, fully taking the impact of the particle on the cavity properties into account.

The particular system to be studied is a silicon double-heterostructure cavity (see Sec. 2.2.3), which was chosen for two reasons. First, it exhibits ultra-high intrinsic quality factors $Q > 10^6$ (in air), which are an essential prerequisite for a large enhancement of the corresponding trapping force. Second, the integrated waveguide offers interesting possibilities for a simultaneous optical transport of particles

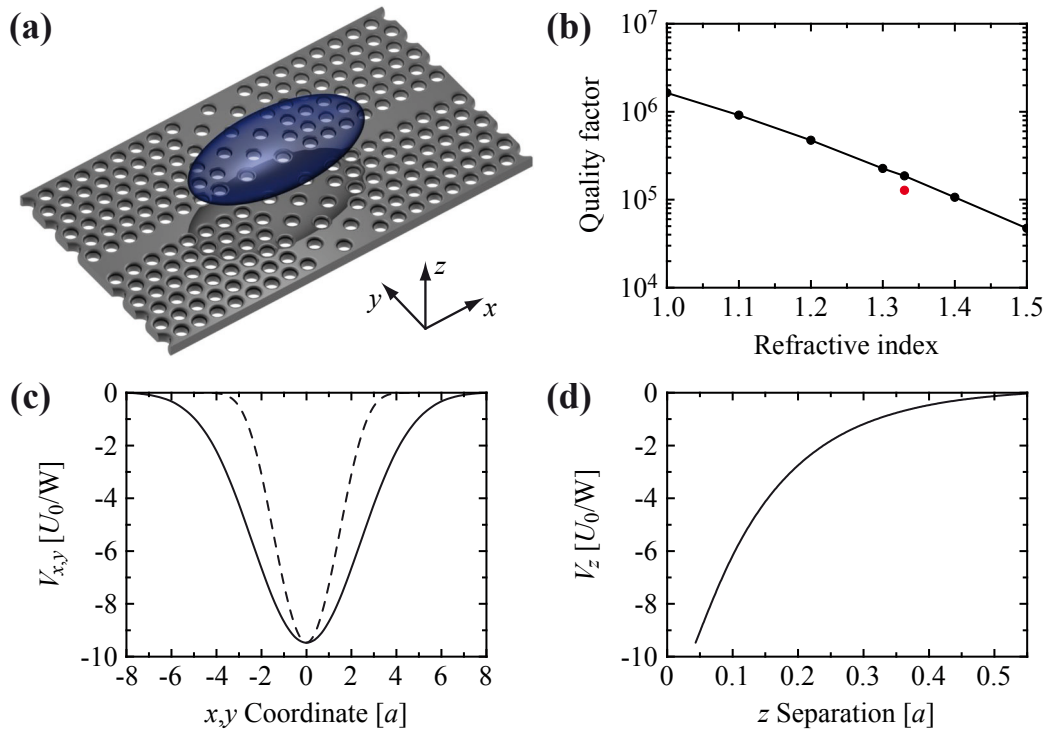

Figure 4.5: **(a)** Schematic illustration of the silicon double-heterostructure cavity (refractive index $n = 3.46$) and the cell to be trapped ($n = 1.38$). The lattice parameters are $a = 400$ nm, $a' = 410$ nm, $t = 0.625a$, and $r = 0.29a$. The cell is modeled as an ellipsoid with dimensions $4a$, $2a$, and a in x, y, and z direction, respectively. **(b)** Quality factor Q of the cavity (black) as a function of the refractive index of the surrounding medium (without cell). The red data point indicates the value for water ($n = 1.33$) in the presence of the cell (located above the center of the cavity). **(c)** Normalized trapping potentials V_x (solid curve) and V_y (dashed curve) on the central x and y axis, respectively, for an aqueous environment. The separation between the cell and the slab surface is $a/20$. **(d)** Corresponding trapping potential V_z for a central location of the cell above the cavity.

to/from the cavity, as is discussed at the end of this section. Instead of polystyrene beads, a more realistic object is used to simulate the trapping behavior, namely a biological cell, modeled as an ellipsoid with dimensions $4a \times 2a \times a$ (see Fig. 4.5a) and a refractive index $n = 1.38$ [295]. The calculated quality factors Q of the bare cavity in various liquid environments as well as in the presence of the cell are displayed in Fig. 4.5b. Obviously, quality factors $Q > 10^5$ can still be maintained if the cavity is immersed in water ($n = 1.33$) and the cell is directly positioned on top of it. The resulting (normalized) trapping potentials shown in Figs. 4.5c and 4.5d are not as deep as those obtained in the previous section (for an object of comparable size) owing to the smaller refractive index contrast between the cell and the aqueous environment. Also, any features due to the individual field lobes of the cavity mode are averaged out because of the large size of the cell, leading to a Gaussian shape of the trapping potential in the lateral direction (see Fig. 4.5c).

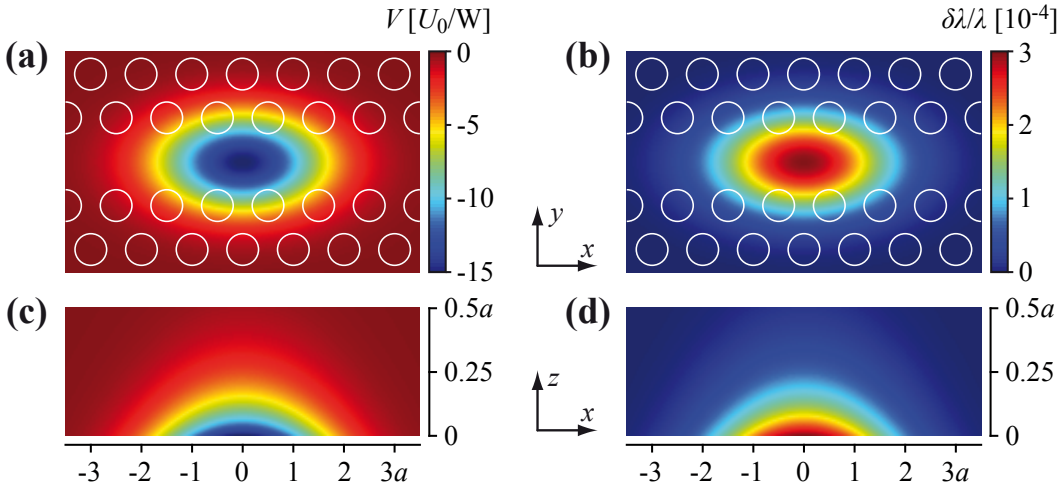

Figure 4.6: **(a,c)** Normalized three-dimensional trapping potential V, derived from the data shown in Fig. 4.5. **(b,d)** Corresponding shift $\Lambda = \delta\lambda/\lambda$ of the resonance wavelength due to the presence of the cell. In both plots cross sections through the x-y plane directly at the surface of the cavity (a,b) and through the central x-z plane (c,d) are displayed, respectively. The coordinates in x and y direction refer to the center of the cell, while in z direction the separation between the cell and the slab surface is used. Note that the length scale in z direction is stretched by a factor of 10 compared to the other directions.

In order to investigate the trapping dynamics of the cell, it would be beneficial to know the entire three-dimensional potential V in the half-space above the photonic crystal cavity. However, corresponding simulations with a sufficiently high spatial resolution would have been far too time-consuming. Therefore, an approximated potential of the form

$$V(x,y,z) = A\exp\left[-\left(\frac{x^2}{\sigma_x^2}+\frac{y^2}{\sigma_y^2}+\frac{z-a/20}{\sigma_z}\right)\right] \tag{4.16}$$

is used in the subsequent analysis, with the proportionality factor A and the decay constants σ_x, σ_y, and σ_z being determined from the calculated data shown in Figs. 4.5c and 4.5d. Likewise, the relative shift $\delta\lambda/\lambda$ of the resonance wavelength (due to the presence of the cell) was deduced from the simulations and fitted by a three-dimensional function $\Lambda(x,y,z)$ of the same form as Eq. (4.16). Cross sections of $V(x,y,z)$ and $\Lambda(x,y,z)$ are displayed in Fig. 4.6. Note that although these idealized functions might deviate from the true values at positions away from the coordinate axes, the general conclusions derived below should not be affected.

The resonance shift $\Lambda = \delta\lambda/\lambda$ directly influences the power $P = \eta Q P_0$ stored inside the cavity, as the corresponding coupling efficiency η decreases (at least for a fixed input wavelength). The impact of this effect on the trapping performance depends on the linewidth $\Delta\lambda = \lambda/Q$ of the respective cavity mode. If a Lorentzian

spectrum is assumed, P can be expressed as

$$P(x,y,z) = \eta_0 Q P_0 \frac{(\Delta\lambda/2)^2}{[\lambda\Lambda(x,y,z) - s]^2 + (\Delta\lambda/2)^2} \,, \tag{4.17}$$

where an additional detuning s of the input wavelength with respect to the resonance wavelength λ of the bare cavity was introduced. Since the impact of the cell on the quality factor Q (and thus on the linewidth $\Delta\lambda$) is relatively small (see Fig. 4.5b), it can be neglected in the current analysis. The force experienced by the cell is then given by

$$\boldsymbol{F}(\boldsymbol{r}) = -P(\boldsymbol{r}) \frac{\mathrm{d}V(\boldsymbol{r})}{\mathrm{d}\boldsymbol{r}} \qquad (\boldsymbol{r} = \{x,y,z\}) \,. \tag{4.18}$$

The resulting force distributions in the central x-z plane for different detunings s are shown in Fig. 4.7. A realistic quality factor $Q = 5 \times 10^4$ was assumed, which is about half the theoretically possible value and corresponds to a mode linewidth $\Delta\lambda$ approximately 14 times smaller than the maximum resonance shift $\delta\lambda$. If the detuning s is adjusted such that the input wavelength always matches the resonance wavelength (i.e., $s = \delta\lambda$, Fig. 4.7a), the force is maximized at each point and the associated potential is identical to the one shown in Fig. 4.6c. For a fixed input wavelength without detuning (i.e., $s = 0$, Fig. 4.7b), the cell experiences a small attractive force as it approaches, which rapidly ceases with decreasing distance to the cavity center due to the induced resonance shift $\delta\lambda$. Consequently, the associated trapping potential becomes flat and the cell is free to move inside this force barrier. By introducing a finite (fixed) detuning to longer wavelengths (i.e., $s > 0$, Figs. 4.7c–4.7e), the strength of the barrier increases while its effective radius decreases, thus reducing the motion of the cell.

This peculiar dependence of the optical force on the particle-induced resonance shift has important consequences for the possible trapping schemes. Small particles, which do not affect the resonance wavelength significantly, can simply be trapped by operating the cavity without detuning (i.e., $s = 0$). In this case, larger objects may either show a complicated bistable behavior due to the position-dependent collapse and revival of the force as displayed in Fig. 4.7b, or may not be trapped at all if the corresponding force barrier is too weak. Contrary to this, a detuning $s > 0$ prevents the trapping of small particles (which are unable to induce a sufficiently large resonance shift), while larger objects of a certain size can be pinned to the cavity owing to their own back-action on the optical properties of the latter. A similar behavior was recently observed in the context of optical forces near metal nanoapertures [296]. Consequently, a size-selective, self-induced trapping is possible using initially detuned photonic crystal cavities.

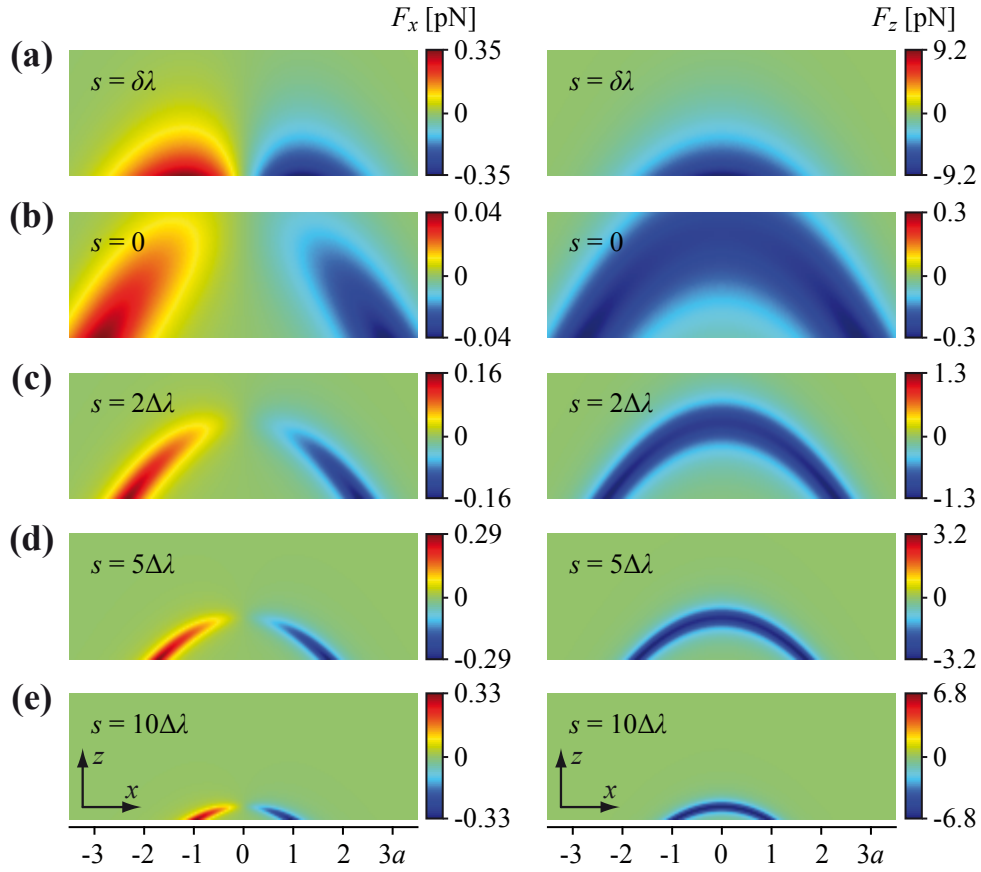

Figure 4.7: Force components F_x (left) and F_z (right) in the central x-z plane for different detunings s of the input wavelength with respect to the resonance wavelength λ of the bare cavity (without cell). In **(a)** the input wavelength is always tuned such that the resonance shift $\delta\lambda$ induced by the cell is compensated. The power stored inside the cavity is assumed to be $P = 1$ W. In **(b–e)** the input wavelength is fixed at values $\lambda + s$ as indicated in each panel and P is scaled with $\delta\lambda$ according to Eq. (4.17), assuming a cavity quality factor $Q = 5 \times 10^4$. Note the different color scales in each panel. The length scales are the same as in Figs. 4.6c and 4.6d.

A severe drawback of this proposal is the extremely short interaction range between the particle and the cavity, as the cell has to be brought very close to the latter in order to experience a noticeable force (see Fig. 4.7e). This problem may be tackled by exploiting the waveguide structure itself as a type of conveyor belt, delivering particles directly to the cavity. For this purpose, light from a blue-shifted laser, which is able to propagate through all waveguide sections (including the cavity), can be coupled into the structure in addition to the resonant laser beam. While the blue-shifted light is used to trap and transport objects along the entire length of the modulated waveguide [286–288], the resonant light (injected through a second, evanescently coupled waveguide) pins them as soon as they cross the cavity. Switching the resonant laser on and off would allow the trapping and release of consecutive objects, enabling a whole series of manipulation and measurement procedures.

4.5 Summary and conclusions

In this chapter a thorough numerical analysis of the optical forces exerted on dielectric particles in the near-field of photonic crystal cavities was reported. It could be shown that changes in the particle size and cavity geometry can significantly alter the trapping behavior and that designs are favorable which concentrate a large fraction of the field intensity in the surrounding medium. Furthermore, by taking the back-action of the particles on the cavity properties into account, a complicated dynamics due to the induced resonance shift was revealed, potentially enabling sophisticated approaches such as self-induced trapping. Thereby, realistic cavity parameters were assumed, demonstrating the general feasibility of photonic crystal-based trapping schemes, which should be realizable with state-of-the-art fabrication techniques and lasers. Indeed, a first experimental implementation employing waveguide-coupled one-dimensional photonic crystal cavities was recently reported [297] and other systems will hopefully be developed in the near future.

Note that part of these findings have already been published in Barth *et al.* 2006a (see List of Own Publications).

As briefly outlined in Sec. 4.1, the great potential of such integrated photonic crystal devices lies in the possible combination of optical trapping and sensing. If light is launched into the cavity via a coupled waveguide, the corresponding transmission signal may be used to detect the presence of particles by means of the induced resonance shift and appropriate lock-in techniques may be employed to adjust the laser frequency with respect to the cavity resonance, enabling a stable trapping configuration. Then, the strong interaction of the trapped object with the high field intensity inside the cavity may be exploited to collect the generated Raman or fluorescence signal via the same waveguide. In this way, spectroscopic information can be gathered in addition to a mere index sensing, potentially allowing the identification of the trapped object. Together with an optical transportation scheme as discussed at the end of the previous section, a fully automated and integrated microfluidic particle detection and measurement system can be envisaged.

Furthermore, photonic crystal devices might also be employed in combination with conventional optical tweezers, serving as "work boards" for the simultaneous storage, arrangement, and manipulation of particles, since multiple cavities can be arrayed and individually addressed in an integrated system. Manifold other designs and applications are imaginable, making photonic crystal structures a versatile tool for future optofluidic devices.

Chapter 5

Optofluidic sensing with photonic crystal fibers

5.1 Introduction

The basic concept of optofluidics is to control the flow of liquids and light at the micron scale in a combined system, enabling the realization of compact and versatile devices, e.g., for biochemical sensing [8, 9]. The previous chapter already gave an example of how photonic crystal cavities may be employed for this purpose. Optical fibers are another candidate for these kinds of applications, since they provide the means to confine light in microscopic dimensions while guiding it over macroscopic distances. This allows the realization of strong and well-controlled interactions with fluidic systems, especially if the fiber itself contains microfluidic channels to facilitate and control the liquid flow.

The idea of using optical fibers for sensing applications has been pursued for several decades, promising significant advantages compared to conventional devices which rely on free-space optics. First and foremost, fibers offer a much longer interaction length between the guided light and the sample material (e.g., gases or liquids), which is basically limited by the length of the fiber itself. This, in turn, leads to an enhancement of the corresponding detection signal and sensitivity. In order to make a fiber suitable for sensing, the guided optical field has to have a certain overlap with the sample material such that an efficient interaction can take place. In the first practical implementations with standard step-index fibers this was achieved by completely removing the cladding of the fiber, exposing the bare core [298, 299]. The latter can then by immersed into the sample liquid which interacts with the guided light via the evanescent part of the field [300]. The drawback of this method, however, is that the bare core is usually very fragile and only a very small fraction ($< 1\%$) of the light intensity is actually located within the liquid.

Only since the advent of microstructured optical fibers [301, 302] it has become possible to deliver sample material directly to the light-guiding region of the fiber (via the holey structure) without the need to strip its cladding. This considerably improves the robustness of the device and provides a vast range of design possibilities to optimize the light-sample interaction. Usually, this interaction is evanescent in character if the light is guided via total internal reflection in the higher dielectric material of the fiber. However, hollow-core photonic crystal fibers [303] (which represent a special class of microstructured optical fibers) possess the ability to confine and guide light within the lower dielectric material due to the photonic band gap effect. This opens the possibility to achieve a much stronger light-sample interaction (and thus higher detection sensitivities) by infiltrating the hollow core with gases or liquids such that most of the field energy propagates in the sample material itself.

There have been several reports on the application of microstructured optical fibers as biochemical sensing devices, using either evanescent detection schemes [304–308] or direct propagation inside the infiltrated sample material [309–311]. However, a comprehensive study and comparison of the sensing performance of the various types of fibers and detection methods has not been performed so far, nor has the achievable detection limit been explored. Therefore, a detailed analysis of absorption and fluorescence measurements on dye solutions infiltrated into solid-core as well as hollow-core photonic crystal fibers is presented in the fourth part of this thesis. Thereby, the same experimental setup is used for all measurements, enabling a direct comparison between both types of fibers and allowing conclusions on the practicality of the different sensing schemes.

The chapter is organized as follows: In Sec. 5.2 a theoretical overview on the fundamental optical properties of photonic crystal fibers as well as their basic sensing characteristics is provided. Experimental details of the fiber preparation and the optical setup are described in Sec. 5.3, accompanied by a brief outline of the employed computational method. The results obtained from absorption and fluorescence measurements are then presented in Sec. 5.4, demonstrating a clear superiority of the hollow-core fiber in comparison to the solid-core design with regard to the achievable detection sensitivity. The respective interaction coefficients between the guided light and the sample material are determined and found to be in good agreement with the results from corresponding numerical calculations. Furthermore, additional measurements on selectively coated hollow-core fibers are presented and discussed. Finally, a short summary of this chapter as well as some concluding remarks are given in Sec. 5.5.

5.2 Theory of sensing with photonic crystal fibers

Photonic crystal fibers [10, 11] have revolutionized the concept of light guiding in optical fibers, since their holey structure allows to tailor the optical properties in unprecedented ways and enables guiding mechanisms which are not possible in standard fibers. This has lead to a rapidly increasing number of applications in the fields of telecommunication, nonlinear optics, as well as chemical and biological sensing. The latter application requires a detailed knowledge on the ways in which infiltrated sample material changes the characteristics of the fiber and interacts with the guided light. Therefore, in this section the basic optical properties of photonic crystal fibers are derived in general terms (Sec. 5.2.1) as well as with regard to different sensing schemes (Sec. 5.2.2). Furthermore, the problem of fluid injection into the fiber is addressed (Sec. 5.2.3).

5.2.1 Basis optical properties of photonic crystal fibers

Similar to the planar photonic crystal structures discussed in Sec. 2.2.2, photonic crystal fibers exhibit a two-dimensional periodicity in the x-y plane, but have a much larger extend in z direction (which can be considered infinite for modeling purposes). A typical example would be a filament of dielectric material with a periodic arrangement of air holes running along its entire length. In contrast to planar system, one is interested in modes predominantly propagating in z direction (i.e., along the fiber) rather than in the plane of periodicity. Also in this case band gaps can occur and light can be guided along defects in the fiber cladding, as is discussed in the following.

Characteristics of the cladding structure

In a first step it is instructive to study the bare periodic cladding structure of a photonic crystal fiber without any defects (i.e., without a fiber core) as shown in Fig. 5.1a. Similar to the analysis in Sec. 2.2.2, the optical properties of this system can be obtained from the projected band structure $\omega(k_z)$, where k_z is the wave vector component along the fiber, also termed the propagation constant β. The latter is related to the wave vector $\boldsymbol{k}$ in free space via $\beta = n_{\text{eff}}|\boldsymbol{k}|$, with n_{eff} being the effective refractive index of a particular optical mode. In principle, the band structure and the corresponding mode profiles

$$\boldsymbol{E}(\boldsymbol{r}) = \boldsymbol{E}(x,y)\mathrm{e}^{i\beta z} \qquad \text{and} \tag{5.1}$$

$$\boldsymbol{H}(\boldsymbol{r}) = \boldsymbol{H}(x,y)\mathrm{e}^{i\beta z} \tag{5.2}$$

can be calculated from Eqs. (2.7) and (2.8), yielding a set of eigenmodes with different frequencies ω for each given value of β. In the case of optical fibers, however, one is often interested in the inverse problem of finding the various modes with different values β which can exist at a specific frequency ω. It is therefore more convenient to rearrange Maxwell's equations (2.1)–(2.4) such that they yield eigenvalue problems of the form [312]

$$\beta^2 \boldsymbol{E}(x,y) = \left(\nabla^2 + \varepsilon|\boldsymbol{k}|^2\right)\boldsymbol{E}(x,y) + \nabla\left[\boldsymbol{E}(x,y)\cdot\nabla\ln\varepsilon\right] \qquad \text{and} \tag{5.3}$$

$$\beta^2 \boldsymbol{H}(x,y) = \left(\nabla^2 + \varepsilon|\boldsymbol{k}|^2\right)\boldsymbol{H}(x,y) + \nabla\ln\varepsilon\times\left[\nabla\times\boldsymbol{H}(x,y)\right], \tag{5.4}$$

with β^2 as eigenvalue and $|\boldsymbol{k}| = \omega/c$ as free input parameter.

Some general properties of the photonic crystal fiber can already be deduced from Eqs. (5.3) and (5.4) by applying the paraxial scalar approximation, i.e., by neglecting the second terms on the right hand side which couple the different field components to each other. This is equivalent to ignoring any vector effects and yields the scalar wave equations [312]

$$\left(\nabla^2 + \varepsilon|\boldsymbol{k}|^2 - \beta^2\right)\boldsymbol{E}(x,y) = \left(\Lambda^2\nabla^2 + V^2\right)\boldsymbol{E}(x,y) = 0 \qquad \text{and} \tag{5.5}$$

$$\left(\nabla^2 + \varepsilon|\boldsymbol{k}|^2 - \beta^2\right)\boldsymbol{H}(x,y) = \left(\Lambda^2\nabla^2 + V^2\right)\boldsymbol{H}(x,y) = 0\,. \tag{5.6}$$

Here, the so-called generalized V-parameter [313]

$$V = \Lambda\sqrt{n^2|\boldsymbol{k}|^2 - \beta^2} = \Lambda|\boldsymbol{k}|\sqrt{n^2 - n_{\text{eff}}^2} \tag{5.7}$$

was introduced, where Λ is a characteristic transverse length of the fiber geometry (usually identified with the lattice constant a) and $n = \sqrt{\varepsilon}$ denotes either the refractive index in the high- or low-index material, depending on where the fields are evaluated. In addition to the scaling law presented in Sec. 2.2.1, which predicts identical band structures and mode profiles if all lengths are scaled accordingly, the V-parameter represents another invariant connecting the optical properties of the fiber with the index contrast in its cladding [314]. As long as V is held constant, the mode profiles and dispersion relations are also (approximately) the same, which means that band gaps can exist even if the index contrast is very small, provided that the transverse dimensions of the fiber are sufficiently large.

It should be emphasized that Eqs. (5.5) and (5.6) are strictly valid only in the homogeneous parts of the fiber and not at the boundaries between different materials. However, in the short-wavelength limit ($\Lambda|\boldsymbol{k}| \to \infty$) most of the field energy is located in the high-index material anyway and boundary effects become negligible, while in the long-wavelength limit ($\Lambda|\boldsymbol{k}| \to 0$) the entire cladding structure can be treated

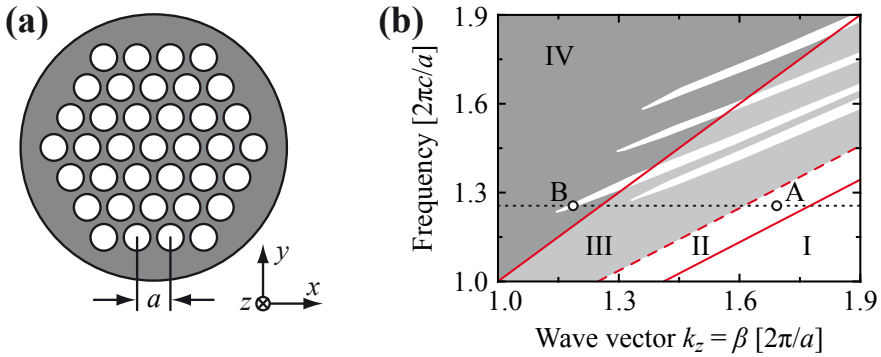

Figure 5.1: **(a)** Schematic cross section through a photonic crystal fiber with a hexagonal cladding structure (but without core) consisting of air holes in a silica rod. **(b)** Corresponding projected band structure (adopted from Ref. [315]) along the propagation direction of the fiber. The upper/lower solid red line represents the light line in air/silica and the dashed red line indicates the fundamental cladding modes. The darker gray shaded area corresponds to the continuum of extended states which can propagate in air, while the lighter gray shaded area marks the continuum of modes guided in the photonic crystal cladding. Both areas are intersected by photonic band gaps (white fingers) in which no modes exist. The dotted black line indicates a specific frequency at which defect modes can be guided in a solid core (via total internal reflection, point A) or in a hollow core (via the band gap effect, point B), respectively.

as an effective homogeneous medium and the V-parameter (for the fundamental cladding mode) takes the form [313]

$$V = \Lambda |\boldsymbol{k}| \sqrt{f(n_2^2 - n_1^2)} \, . \tag{5.8}$$

Here, f is the air filling fraction (i.e., the fraction of space occupied by the holes in the fiber cladding) and n_1 and n_2 are the refractive indices of the lower and higher dielectric material, respectively. Therefore, once the band structure of a particular fiber design is known, the optical properties of any related structure can roughly be approximated by applying the corresponding scaling laws.

A representative band structure, adopted from Ref. [315], is shown in Fig. 5.1b. It is divided into four regions of different modal behavior by the light line in air (i.e., $\omega = c\beta$, upper solid red line), the cladding modes of lowest frequency (dashed red line), and the light line in the fiber material (i.e., $\omega = c\beta/n_2$, lower solid red line). The fiber material is assumed to be silica with $n_2 = 1.45$. In region I (below the silica light line) no propagating modes can exist whatsoever, while in region II (above the silica light line) modes are in principle allowed in the high-index material but are not supported by the periodic cladding structure. This is the region where donor-type defect modes can be introduced (point A), which are then guided along the fiber via total internal reflection. Region III (below the air light line) is populated by a continuum of cladding modes (lighter gray shaded area), which can propagate within the entire fiber cladding, but are not allowed to radiate into free space. Finally, in

region IV (above the air light line) a continuum of extended free-space states exists (darker gray shaded area), which are able to propagate everywhere. As a result of the periodic cladding structure, regions III and IV are both intersected by narrow band gap features (white fingers) in which no modes are supported within the fiber. It is the existence of these band gaps in region IV that enables the creation of acceptor-type defect modes (point B), which are guided in air rather than in the high-index material, as is discussed next.

Light guiding mechanisms

In analogy to defects in planar photonic crystals (Sec. 2.2.3), local distortions of the periodic cladding structure can induce defect modes in the photonic crystal fiber. If such a defect (usually termed the fiber core) runs uniformly along the whole length of the fiber, the corresponding modes are confined in the x-y plane but can propagate freely in z direction. In analogy to planar photonic crystal waveguides, the wave vector component k_z is thus conserved and the core modes exhibit dispersion.

The mechanism by which light is guided along the fiber core depends on the geometry of the defect structure. Some examples are shown in Fig. 5.2. If the dielectric constant is locally increased such that the effective refractive index of the core mode is larger than that of the fundamental cladding mode, light can be guided via total internal reflection [316]. This corresponds to the region marked by point A in the band structure of Fig. 5.1b and can be achieved, e.g., by omitting one or several holes (Fig. 5.2a) or decreasing their size (Fig. 5.2b). These kinds of defects are denoted as solid cores or microstructured solid cores, respectively. As the photonic band gaps due not play any role for this type of guidance, a periodic cladding structure is in fact not necessary and other designs from the broader class of microstructured optical fibers [301] can also be employed.

If light shall be guided in the lower dielectric material without severe losses, photonic band gaps are an essential prerequisite. The corresponding modes have to fulfill the condition $\beta < n_1|\boldsymbol{k}|$ (and thus $n_{\text{eff}} < n_1$) to be able to propagate in the low-index medium (usually air), while at the same time being rejected from the cladding structure by the band gap effect. These requirements are met at point B in Fig. 5.1b and the respective core modes can be induced, e.g., through incorporation of a large central hole into the fiber cladding (Fig. 5.2c). This so-called hollow-core photonic crystal fiber allows the guiding of light almost entirely in air [303], a feature which is not possible with conventional waveguides relying on total internal reflection. If the hollow core is selectively filled with a material of higher dielectric constant (e.g., a liquid or a polymer, Fig. 5.2d), the guiding mechanism can be reverted to total internal reflection, provided that the effective refractive index of the (new) core mode exceeds that of the cladding modes [317].

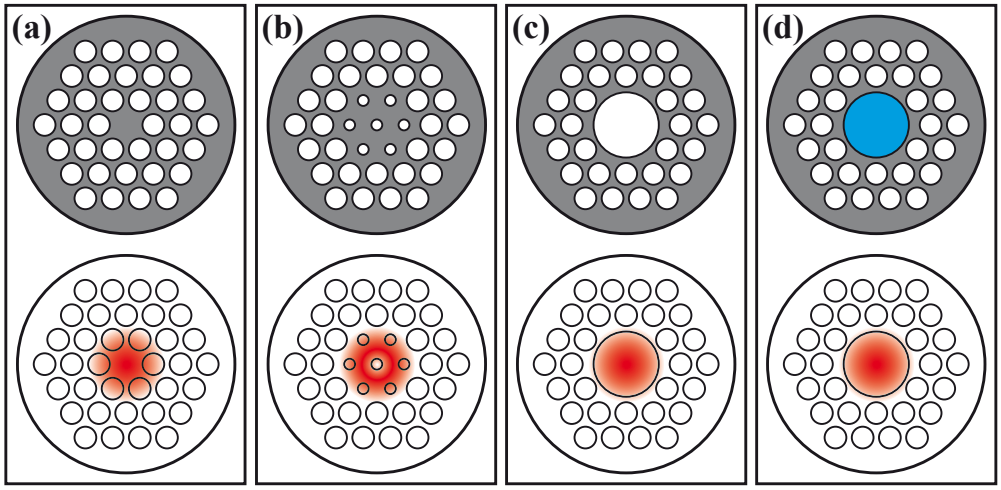

Figure 5.2: Schematic cross sections (upper row) and corresponding fundamental core modes (lower row) for various designs of photonic crystal fibers: **(a)** solid core, **(b)** microstructured solid core, **(c)** hollow core, and **(d)** hollow core filled with a liquid (cyan). In (a,b,d) guidance occurs by means of total internal reflection, while in (c) the light is confined to the core hole by the photonic band gap effect.

Although the guidance of light by total internal reflection in a solid-core photonic crystal fiber resembles that in conventional step-index fibers (with a homogeneous core and cladding structure), a striking difference occurs regarding the number of modes N guided in the core. This number is approximately related to the V-parameter via [312]

$$N \approx \frac{V^2}{2} \,. \tag{5.9}$$

In a step-index fiber the V-parameter is defined as [312]

$$V_{\mathrm{si}} = R|\boldsymbol{k}|\sqrt{n_{\mathrm{core}}^2 - n_{\mathrm{clad}}^2} \,, \tag{5.10}$$

with R and n_{core} denoting the radius and refractive index of the core, respectively, and n_{clad} being the refractive index of the cladding. As $(n_{\mathrm{core}}^2 - n_{\mathrm{clad}}^2)$ does not vary significantly over a wide range of frequencies (except due to the intrinsic material dispersion), V_{si} is mainly determined by $|\boldsymbol{k}| = 2\pi/\lambda$ and thus the number of modes N continuously grows with decreasing wavelength. Contrary to this, the V-parameter in a solid-core photonic crystal fiber is given by [313]

$$V_{\mathrm{sc}} = R|\boldsymbol{k}|\sqrt{n_2^2 - n_{\mathrm{eff}}^2} \,, \tag{5.11}$$

where n_{eff} is determined by the fundamental cladding mode as in Eq. (5.7). n_{eff} depends explicitly on λ and approaches n_2 for short wavelengths, because most of the

field energy becomes localized in the high-index material. Consequently, $(n_2^2 - n_{\mathrm{eff}}^2)$ tends to zero at high frequencies and imposes an upper bound on N, as higher-order modes are not guided anymore due to the vanishing index contrast between the core and the cladding. This enables the realization of endlessly single-mode fibers [313], even for large core diameters [318].

In the case of a hollow-core photonic crystal fiber, the V-parameter has to be defined as [303]

$$V_{\mathrm{hc}} = R|\boldsymbol{k}|\sqrt{n_{\mathrm{up}}^2 - n_{\mathrm{low}}^2}\,, \tag{5.12}$$

with n_{up} and n_{low} being the refractive index at the upper and lower edge of the photonic band gap, respectively. Note that for $n_{\mathrm{up}} > n_1$, n_{up} must be set equal to n_1. Since the width $(n_{\mathrm{up}}^2 - n_{\mathrm{low}}^2)$ of the band gap is usually quite small (see Fig. 5.1b), the hollow core has to be sufficiently large (typically $R > \Lambda$) to support at least one guided mode according to Eq. (5.9) [303].

5.2.2 Sensing schemes for photonic crystal fibers

Within this thesis the main field of application of photonic crystal fibers is related to optofluidic sensing, exploiting the fact that the holey structure can be filled with arbitrary sample materials (e.g., a solution containing some molecular species of interest). The interaction of the guided light with the sample material depends on whether a solid-core or a hollow-core fiber is employed as well as on the type of infiltration scheme which is used. In the following, the basic operation principles of various configurations of liquid-filled photonic crystal fibers are discussed and some important figures of merit, needed to evaluate and compare their sensing performance, are derived.

General operation principles

Depending on the structure of the photonic crystal fiber and the method used for liquid infiltration, different light-guiding regimes can be distinguished. Here, these regimes shall exemplarily be illustrated for the solid-core fiber shown in Fig. 5.2a and for the hollow-core fiber shown in Fig. 5.2c. When filled with air, the former guides light predominantly in the core via total internal reflection, while the latter supports a mode which is mainly confined to the central hole via the photonic band gap effect (see Sec. 5.2.1). Both fibers may readily be employed as gas sensors, with the key difference that in the case of the solid-core fiber the interaction of the guided light with the gas only takes place via the evanescent part of the field [319], while in the case of the hollow-core fiber nearly the entire field participates in the interaction [320–322].

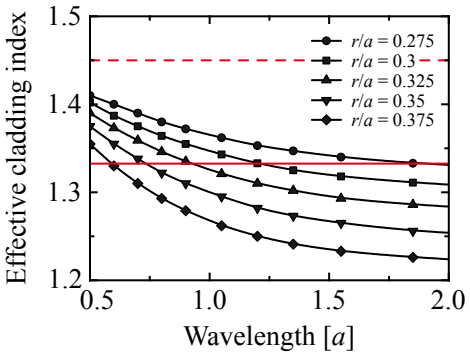

Figure 5.3: Calculated effective refractive index (adopted from Ref. [317]) of the fundamental cladding mode of photonic crystal fibers (similar to the one shown in Fig. 5.1a) with different hole radii r. The solid and dashed red lines indicate the refractive index of water and silica, respectively.

When all holes are filled with a low-index liquid, the principal behavior stays the same for both types of fibers as long as the refractive index n_{liq} of the liquid is smaller than that of the fiber material (i.e., n_2). The light confinement will in general be reduced due to the smaller refractive index contrast in the holey structure. This weaker confinement can be advantageous in the case of the solid-core fiber, since the evanescent field penetrates further into the liquid, increasing the light-sample interaction. Therefore, this is the regime in which evanescent fiber devices are typically operating [302].

In the case of the hollow-core fiber, a complete filling of the holey structure shifts the spectral position λ_{gap} of the photonic band gap to smaller wavelengths. According to the scaling law derived in Sec. 5.2.1, the shifted wavelength is approximately given by [311]

$$\lambda_{\mathrm{gap}} = \lambda^0_{\mathrm{gap}} \sqrt{\frac{n_2^2 - n_{\mathrm{liq}}^2}{n_2^2 - n_1^2}} \,, \tag{5.13}$$

where λ^0_{gap} is the original band gap position of the air-filled fiber. The spectral shift is usually accompanied by a strong narrowing of the width of the photonic band gap, severely limiting the wavelength range in which the device is able to operate.

This drawback can be circumvented by injecting liquid into the core hole only, thus creating a liquid-core/air-cladding hybrid fiber (see Fig. 5.2d). As was already mentioned in Sec. 5.2.1, such a selective infiltration changes the light-guiding mechanism from band gap to index guiding, provided that the effective refractive index of the core mode is larger than that of the corresponding cladding modes. To fulfill this condition the radius r of the cladding holes as well as the wavelength λ of the guided light have to exceed a certain value relative to the lattice constant a. As can be seen in Fig. 5.3, the effective refractive index n_{eff} of the fundamental cladding mode

drops below that of water ($n_{\mathrm{liq}} = 1.33$) above a certain wavelength for $r/a > 0.27$. A more detailed analysis shows that values of $r/a > 0.35$ are in fact necessary to ensure a sufficiently strong confinement of the guided mode to the core and to reduce propagation losses [317]. Then, the key difference to solid-core fibers is that the light is almost entirely propagating within the liquid filament itself, providing a much more intensive interaction with the sample material.

Figures of merit for fiber sensors

When considering a specific application, the most suitable choice among the different operation schemes described above depends on several factors, such as the quantity which is detected (intensity, phase, or polarization), the way in which light is launched and extracted into/from the fiber (forwards, backwards, or sideways), and restrictions imposed by the sample material itself (refractive index, viscosity, etc.). However, there are some general criteria which can help to evaluate and compare the sensing performance of various types of photonic crystal fibers, some of them being also of relevance for the experimental part of this chapter. These figures of merit are introduced in the following.

Spatial overlap The most important figure of merit is the fraction of optical field energy propagating within the sample material, also termed the interaction coefficient or spatial overlap α, which is defined as [308]

$$\alpha = \frac{\iint_{\mathrm{sample}} \mathrm{d}x\,\mathrm{d}y\,\mathrm{Re}\{\boldsymbol{E}(x,y) \times \boldsymbol{H}^*(x,y)\} \cdot \hat{\boldsymbol{z}}}{\iint_{\mathrm{total}} \mathrm{d}x\,\mathrm{d}y\,\mathrm{Re}\{\boldsymbol{E}(x,y) \times \boldsymbol{H}^*(x,y)\} \cdot \hat{\boldsymbol{z}}} \,. \tag{5.14}$$

Here, $\hat{\boldsymbol{z}}$ is the unit vector pointing in z direction and the integration is performed over the region containing sample material and over the total cross section of the fiber, respectively. α is the dominant factor for all sensing schemes relying on the detection of transmission signals, such as absorption or phase measurements. It directly determines how much attenuation or phase shift the guided light accumulates when propagating through a specific length L of the fiber.

Consequently, the Beer-Lambert law, which relates the outgoing light intensity I to the incoming intensity I_0 in an absorption measurement, has to be modified such that [304]

$$I(\lambda) = I_0(\lambda)\,\mathrm{e}^{-\epsilon(\lambda)c\alpha L} = I_0(\lambda)\,\mathrm{e}^{-\epsilon(\lambda)cL_{\mathrm{eff}}} \,. \tag{5.15}$$

Here, $\epsilon(\lambda)$ and c are the wavelength-dependent molar extinction coefficient and the concentration of the absorbing material (e.g., molecules in a solution), respectively. $L_{\mathrm{eff}} = \alpha L$ can be interpreted as an effective interaction length that a free-space

setup (for which $\alpha = 1$) with a comparable absorption sensitivity would have. From Eq. (5.15) it is apparent that the main advantage of fiber sensors, namely the longer interaction length between the guided light and the sample material, can completely diminish if the overlap α is very small.

Propagation loss Another important property is the propagation loss κ of the fiber, which includes leakage of the guided modes, scattering due to surface roughness and fabrication imperfections, as well as parasitic absorption in the fiber material itself. With regard to the expression in Eq. (5.15), it leads to an additional reduction of the detected signal according to

$$I(\lambda) = I_0(\lambda)\, \mathrm{e}^{-\left[\epsilon(\lambda) c\alpha + \kappa(\lambda)\right] L} \tag{5.16}$$

and may thus limit the maximal fiber length L which can be employed in the sensing device. To achieve a good sensing performance $\kappa(\lambda) \ll \epsilon(\lambda) c\alpha$ should be fulfilled.

Collection efficiency While in pure transmission measurements α and κ are usually sufficient to characterize the sensing efficiency of a photonic crystal fiber, additional criteria need to be taken into account if the detected signal is generated inside the fiber, e.g., in fluorescence measurements. In this case, α not only determines the excitation efficiency of these signals, but also their coupling strength to the guided modes of the fiber. The fraction of light which is actually radiated into these guided modes and finally channeled to the detector can then be expressed through the collection efficiency ξ. In general, ξ depends on the specific optical mode structure of the fiber, as the spatial radiation pattern of the emitting species is altered compared to the free-space behavior due to the modified local density of optical states.

If an isotropic radiation pattern is assumed for simplicity, the fraction of emitted light guided by the fiber mainly depends on the acceptance angle θ of the various core modes, usually expressed through the numerical aperture $\mathrm{NA} = \sin\theta$. NA is directly related to the V-parameter via $V = |\boldsymbol{k}|\Lambda\mathrm{NA}$ and is accordingly defined by Eqs. (5.10)–(5.12) for the different types of fibers. In the case of guidance by total internal reflection, the collection efficiency can be approximated by

$$\xi = \frac{1}{2} \int_0^{\theta_{\max}} \mathrm{d}\theta\, \sin\theta = \frac{1}{2}\left(1 - \frac{n_{\mathrm{eff}}^{\mathrm{clad}}}{n_{\mathrm{eff}}^{\mathrm{core}}}\right), \tag{5.17}$$

provided that the number of core modes N is sufficiently large to cover the entire angular range (with respect to the z axis) between zero and the maximum angle $\theta_{\max}$ determined by the fundamental core mode. Here, $n_{\mathrm{eff}}^{\mathrm{core}}$ and $n_{\mathrm{eff}}^{\mathrm{clad}}$ are the effective

refractive indices of the fundamental core mode and the fundamental cladding mode, respectively. The factor 1/2 accounts for the detection of the emitted signal at only one output port of the fiber. In the case of band gap guidance, also a minimum acceptance angle θ_{min} can exist [323] and Eq. (5.17) has to be modified to

$$\xi = \frac{1}{2}\left(\frac{n_{\mathrm{up}}}{n_1} - \frac{n_{\mathrm{low}}}{n_1}\right) . \tag{5.18}$$

Here, the definitions of the refractive indices are identical to those used in Eq. (5.12), including the rule that n_{up} must be set equal to n_1 for $n_{\mathrm{up}} > n_1$.

5.2.3 Model of capillary filling in photonic crystal fibers

Having introduced the basic concepts and criteria for optofluidic sensing, the practical problem of injecting liquids into the holey structure of a photonic crystal fiber has to be considered. The speed with which the holes can be infiltrated directly determines the time needed for filling and, consequently, affects the practicality of the fiber sensor. In the following, a corresponding capillary filling model (adopted from Ref. [324]) is derived and applied to the specific geometries encountered in the experimental part of this chapter.

In the absence of external pressure the driving mechanism for capillary filling is the surface tension σ of the liquid at the interface to the capillary wall. Depending on the characteristic contact angle θ between the rim of the liquid and the wall, this surface tension leads to the capillary force

$$F_{\mathrm{cap}} = 2\pi\sigma R\cos\theta , \tag{5.19}$$

where R is the radius of the (circular) capillary tube. If external pressure is applied, an additional force

$$F_{\mathrm{p}} = \pi R^2 \Delta p \tag{5.20}$$

has to be taken into account, with Δp being the pressure difference between the liquid column and the open end of the capillary. As the typical hole radii encountered in photonic crystal fibers are on the order of a few micrometers, the flow inside the holes can be assumed to be laminar. In this case, the motion of the (incompressible) fluid is governed by Poiseuille's law and a liquid column of length L inside the capillary will encounter a friction force

$$F_{\mathrm{r}} = -8\pi\eta L\frac{\mathrm{d}L}{\mathrm{d}t} , \tag{5.21}$$

where η denotes the dynamic viscosity of the liquid.

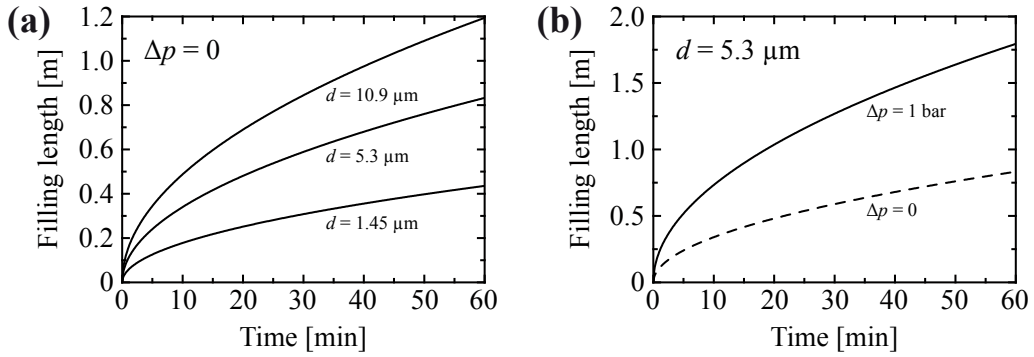

Figure 5.4: (a) Calculated filling length L versus time according to Eq. (5.23) for a silica capillary infused with water in the absence of external pressure. The assumed material parameters are $\rho = 1$ g/cm^3, $\sigma = 72.7$ mN/m, $\eta = 1$ mPa s, and $\theta = 0°$ [324]. The different capillary diameters $d = 2R$ are indicated at each curve. **(b)** Corresponding plot for a fixed diameter $d = 5.3$ µm and an additional external pressure $\Delta p = 1$ bar (solid curve). The case without pressure (dashed curve) is also shown for comparison.

The equation of motion for the filling of a capillary tube with a liquid of density ρ is then given by

$$\frac{\mathrm{d}}{\mathrm{d}t}\left(\pi\rho R^2 L\frac{\mathrm{d}L}{\mathrm{d}t}\right) = 2\pi\sigma R\cos\theta + \pi R^2\Delta p - 8\pi\eta L\frac{\mathrm{d}L}{\mathrm{d}t}\ . \tag{5.22}$$

Note that the action of gravity on the liquid has been neglected, which is only valid for horizontally oriented fibers and/or small hole radii $R < 5$ µm. For vertically oriented fibers and larger holes, one would have to add the gravitational force $F_\mathrm{g} = -\pi g\rho R^2 L$ (with g being the gravitational constant) on the right hand side of Eq. (5.22). In this case, the equation becomes nonlinear and has to be solved numerically. However, for the fiber geometries studied in the experimental part of this chapter, the influence of gravity can be neglected and Eq. (5.22) has the analytical solution [324]

$$L(t) = \sqrt{\frac{A}{B^2}\mathrm{e}^{-Bt} + \frac{At}{B} - \frac{A}{B^2}}\ , \tag{5.23}$$

with the coefficients

$$A = \frac{4\sigma\cos\theta + 2R\Delta p}{\rho R} \qquad \text{and} \qquad B = \frac{8\eta}{\rho R^2}\ . \tag{5.24}$$

Based on this solution the expected filling behavior for water in silica tubes of different diameters d is shown in Fig. 5.4a, assuming the absence of external pressure. Thereby, the values chosen for d correspond to typical holes sizes encountered in the experiment. It is apparent that small fiber lengths $L \approx 10$ cm can be infiltrated on a relatively fast time scale of a few minutes, while for longer fibers the filling time

soon reaches rather impractical values of hours or more. In this case, the application of overhead pressure is inevitable to increase the filling speed (Fig. 5.4b). However, even for pressures of several bars the infiltration length is practically limited to a few meters unless very large holes are used.

This simple analysis sets one of the main advantages of fiber-based sensors, namely the long interaction length between the guided light and the sample material, into a new perspective. Due to the unavoidably large impact of friction in such micrometer-sized fluid channels [325], the actual sample length (although still much larger than in corresponding free-space devices) will be limited in most practical applications. This underlines the necessity to optimize the sensing efficiencies as stated in Sec. 5.2.2, since a low interaction coefficient α cannot simply be compensated by increasing L arbitrarily.

5.3 Experimental and computational methods

This section contains a detailed description of the experimental techniques employed for the preparation and subsequent infiltration of photonic crystal fibers (Sec. 5.3.1) as well as a description of the optical setup used for corresponding absorption and fluorescence measurements (Sec. 5.3.2). Furthermore, a brief introduction into the finite element method is provided (Sec. 5.3.3), which was employed for calculating the optical mode profiles of the fibers.

5.3.1 Preparation and infiltration of photonic crystal fibers

For the experiments presented in this chapter, two different types of photonic crystal fibers were employed, namely the hollow-core fiber shown in Fig. 5.5a (provided by Crystal Fibre) and the solid-core fiber shown in Fig. 5.5b (provided by the Institute for Photonic Technology Jena, courtesy of Dr. J. Kobelke). Both are made of fused silica (refractive index $n_2 = 1.45$) and produced from a preform by a heating and stretching process in a drawing tower (so-called stack-and-draw method). The hollow-core fiber is designed for operation in air via the photonic band gap effect at a central wavelength of 510 nm with a transmission bandwidth larger than 60 nm. Its cladding structure exhibits an air filling fraction $f > 90\%$ and the core has a diameter $d = 5.3$ µm. The solid-core fiber is designed for index guiding in a broad wavelength range in the visible as well as in the near infrared. The (microstructured) core is created by reducing the diameter of the seven central holes from 3.7 µm to 1.6 µm and locally increasing the refractive index of the surrounding silica to $n_2 = 1.46$ via doping with germanium. Note that the periodic cladding structure is not essential for the operation of this fiber in the visible, as photonic band gap effects do not contribute to the guiding process in this wavelength range.

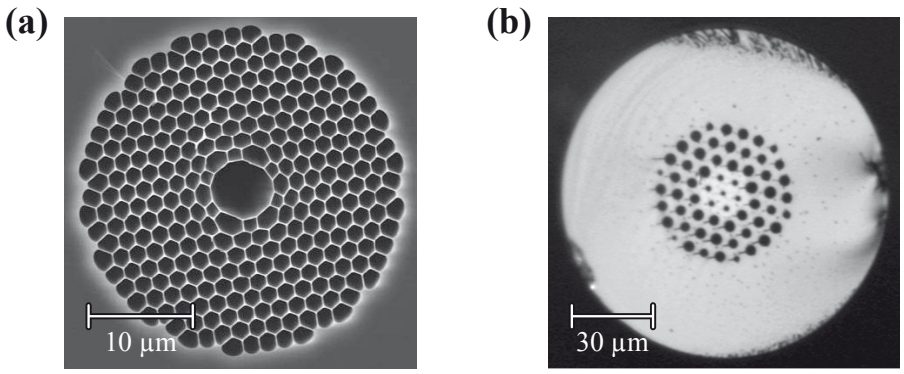

Figure 5.5: **(a)** Scanning electron microscope image of the employed hollow-core photonic crystal fiber. The diameter of the core and cladding holes is 5.3 µm and 1.45 µm, respectively, with a fiber pitch $\Lambda = 1.6$ µm. **(b)** Optical microscope image of the employed solid-core fiber. The diameter of the (microstructured) core and cladding holes is 1.6 µm and 3.7 µm, respectively, with a fiber pitch $\Lambda = 6.3$ µm.

When preparing the solid-core fiber for optofluidic sensing, it is sufficient to infuse the sample liquid into the entire holey structure, since the basic light-guiding mechanism (i.e., total internal reflection) is not affected as long as $n_{\mathrm{liq}} < n_2$ (see Sec. 5.2.2). Therefore, various liquids (such as water, ethanol, or ethylene glycol) could simply be injected into the fiber via a syringe (with a pressure of ≈ 2 bar) without any additional preparation steps. In the case of the hollow-core fiber, a complete infiltration would result in a strong spectral narrowing of the photonic band gap, thus severely limiting the transmission bandwidth. For this reason, a liquid-core/air-cladding design (see Fig. 5.2c) was chosen instead, changing the guiding mechanism to index guiding and enabling a broad transmission window in the entire visible wavelength range. This, however, requires liquid to be selectively injected into the core hole only and therefore necessitates additional preparation steps prior to the infiltration.

Two different approaches to facilitate such a selective infiltration scheme have been reported in the literature. The first one exploits the dependence of the infusion speed on the different hole diameters (see Fig. 5.4) to achieve the selective sealing of the cladding holes through polymer insertion [326]. It requires multiple infiltration and cleaving steps to reach the final configuration and is thus rather time- and material-consuming.

The second approach relies on the selective melting of the cladding holes when the fiber is exposed to the arc discharge of a conventional fusion splicer [327], as is shown in Fig. 5.6a. Since the temperature is lowest in the central region of the arc discharge (where the fiber core is located) and the heat transfer from the outer to the inner parts of the fiber is hindered due to the holey cladding structure, a temperature gradient builds up across the fiber profile. This leads to a corresponding gradient

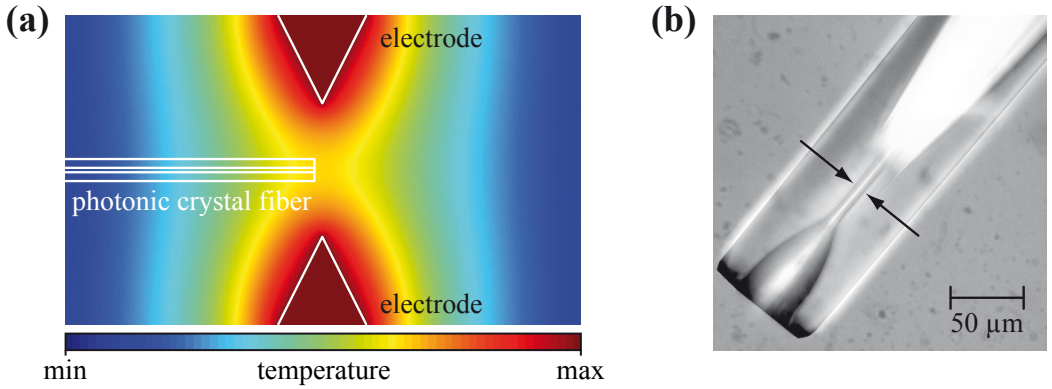

Figure 5.6: **(a)** Illustration of the temperature profile in an arc fusion splicer which is used to selectively melt the outer cladding holes of a hollow-core photonic crystal fiber. **(b)** Optical microscope image of a hollow-core fiber (side view) after the treatment in the fusion splicer. The arrows indicate the region where only the core hole is open, while all other holes have been sealed.

in the viscosity of the silica. Furthermore, the smaller size of the cladding holes in comparison to the core hole makes them more susceptible to a structural collapse. Consequently, by properly adjusting the fusion parameters (such as the applied current and duration as well as the position of the fiber), a selective melting and sealing of the cladding holes can be achieved, while the central core hole remains open. This approach turned out to be much faster and more reliable than the first one and was therefore employed in all experiments presented in this chapter.

An image of a hollow-core fiber after the treatment in the fusion splicer is displayed in Fig. 5.6b, clearly showing the melted cladding holes and the open core. After this initial preparation step, which was usually performed at both ends of the fiber, the latter could be infiltrated with liquids in the same way as the solid-core

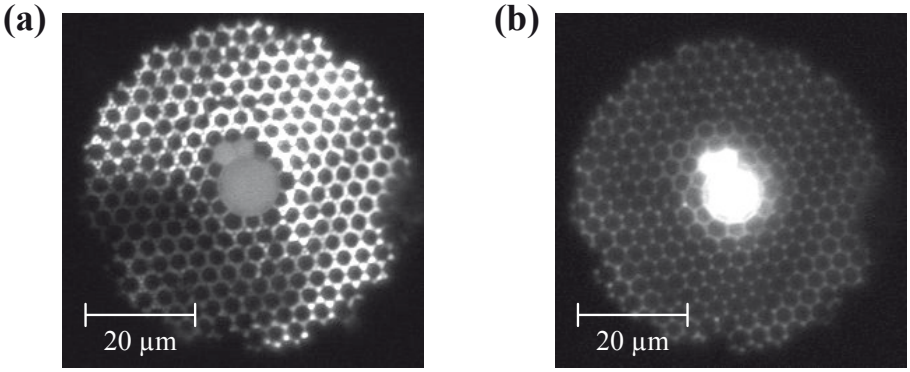

Figure 5.7: **(a)** Optical microscope image (under front illumination) of a hollow-core photonic crystal fiber selectively filled with ethylene glycol. The diameter of the core hole is $d = 10.9$ µm. **(b)** Image of the same fiber when white light is transmitted from the back side. Note that two adjacent cladding holes are filled in addition to the core hole, clearly demonstrating index guiding.

fiber. A corresponding image after infiltration and cleaving is displayed in Fig. 5.7a (note that a fiber with a larger core diameter than the one in Fig. 5.5a was employed here for test purposes). In this particular case, the fusion parameters were slightly inaccurate, leaving two cladding holes open in addition to the core hole. This, however, provides the opportunity to demonstrate the index guiding character of the liquid filament, as can be seen in Fig. 5.7b. Clearly, white light is likewise transmitted in all liquid-filled holes, which would not be possible if the guiding mechanism was primarily based on the photonic band gap effect.

5.3.2 Fiber absorption and fluorescence measurements

To investigate their sensing performance the photonic crystal fibers were filled with a solution of rhodamine 6G, with concentrations ranging from 10^{-4} M down to 10^{-10} M. Different types of solvents were tested for this purpose, namely water, ethanol, and ethylene glycol. The latter turned out to be the most suitable one due to its very low evaporation rate, enabling a long-term use of the filled fibers without connection to a fluid reservoir. A typical fiber length $L \approx 10$ cm was chosen for ease of handling. Absorption and fluorescence measurements on these fibers could be performed in one and the same setup, which is schematically shown in Fig. 5.8 and is described in more detail in the following.

Both ends of the fiber were mounted on mechanical translation stages (positioning accuracy ≈ 0.5 µm, Thorlabs) and light was coupled in and out of the fiber via 20×/0.4 NA microscope objectives (Olympus). For absorption measurements a white LED was used as light source and the transmitted intensity was spectrally dispersed in a spectrograph (SpectraPro 500i, Princeton Instruments) and subse-

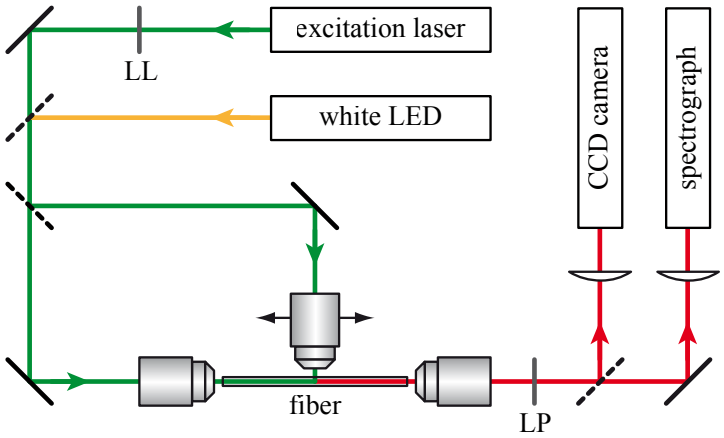

Figure 5.8: Schematic illustration of the experimental setup for absorption and fluorescence measurements on photonic crystal fibers. The abbreviations are defined as follows: LL – laser line filter, LP – long-pass filter, LED – light-emitting diode, CCD – charge-coupled device.

quently detected by a CCD camera (SPEC-10, Roper Scientific), with typical integration times of ≈ 1 s. The transmitted signal could also directly be channeled to a CCD camera (ORCA, Hamamatsu) to monitor the end facet of the fiber. In all cases the fiber was first filled with pure solvent to record a corresponding reference spectrum and was refilled afterwards with the desired dye concentration.

For fluorescence measurements a Beam-Lok 2080 Ar^+ laser (emission wavelength $\lambda = 514$ nm, Spectra Physics) was used to excite the dye molecules, with typical excitation powers of ≈ 2 µW coupled into the fiber. The fluorescence light was then collected in forward direction and (after passing a 540 nm long-pass filter) could be sent to the same detection system as described above for the absorption measurements. Depending on the dye concentration, integration times of 0.01–1 s were used for recording corresponding fluorescence spectra.

Instead of coupling laser light into the end facet of the fiber, a sideways, point-like excitation of the dye fluorescence could be facilitated by using a third microscope objective of the same type, mounted on a translation stage and being moveable along the length of the fiber. Also in this case the resulting fluorescence signal was collected at one end of the fiber, as is shown in Fig. 5.8. This type of excitation scheme was mainly employed to study the impact of reabsorption effects on the recorded spectra.

It should be noted that one and the same piece of fiber was usually used for a whole series of measurements with different dye concentrations. Thereby, the series always started with the lowest concentration, which was then gradually increased in subsequent measurements. In between, the fiber was rinsed with pure solvent, thus keeping the influence of previous infiltrations on the dye concentration small. Investigations of the fluorescence emission after such a rinsing procedure verified that only concentrations $c < 10^{-8}$ M remained in the fiber. Also, a comparison of the fluorescence spectra from freshly filled photonic crystal fibers with those of refilled ones did not yield any significant differences, justifying the suitability of this method.

5.3.3 Finite element simulations

So far, the numerical simulations performed within this thesis were either based on the plane wave expansion method (see Sec. 2.3.3) or on the finite-difference time-domain method (see Sec. 2.3.4). Both of these computational techniques may also be used to calculate the optical modes existing in a photonic crystal fiber. However, the finite element method (FEM) is much better suited for this purpose, as it provides the possibility to implement structures with spatially varying resolution, which is of particular importance for the rather large-scale geometries (compared to the corresponding wavelength) encountered in optical fibers. Therefore, the FEM

software package Comsol Multiphysics (Comsol) was employed for the numerical simulations in this chapter, the basic calculation principles of which are introduced in the following.

General principles

FEM calculations are a versatile tool for the numerical solution of partial differential equations in complex geometries, which also includes the Maxwell equations in microstructured dielectric materials [328]. In this case, the eigenvalue problems stated in Eqs. (2.7) and (2.8) have to be solved, yielding the optical mode profiles $\boldsymbol{E}(\boldsymbol{r})$ and $\boldsymbol{H}(\boldsymbol{r})$, respectively. In order to apply the finite element algorithm, these equations need to be restated in their variational form (also termed the weak formulation), which shall be derived here for the electric field eigenvalue problem

$$\nabla \times \big[\nabla \times \boldsymbol{E}(\boldsymbol{r})\big] - \frac{\omega^2 \varepsilon(\boldsymbol{r})}{c^2} \boldsymbol{E}(\boldsymbol{r}) = 0 \,. \tag{5.25}$$

For this purpose, Eq. (5.25) is multiplied by a test function $\boldsymbol{u}(\boldsymbol{r}) \in H$ and integrated over the computational domain Ω:

$$\int\limits_{\Omega} \mathrm{d}\boldsymbol{r} \left\{ \boldsymbol{u}^*(\boldsymbol{r}) \cdot \Big\{ \nabla \times \big[\nabla \times \boldsymbol{E}(\boldsymbol{r})\big] \Big\} - \frac{\omega^2 \varepsilon(\boldsymbol{r})}{c^2} \boldsymbol{u}^*(\boldsymbol{r}) \cdot \boldsymbol{E}(\boldsymbol{r}) \right\} = 0 \,. \tag{5.26}$$

Thereby, $\boldsymbol{u}(\boldsymbol{r})$ belongs to the same Hilbert space H as the functions $\boldsymbol{E}(\boldsymbol{r})$. Then, a partial integration yields the weak formulation

$$\begin{aligned} \int\limits_{\Omega} \mathrm{d}\boldsymbol{r} \left\{ \big[\nabla \times \boldsymbol{u}(\boldsymbol{r})\big]^* \cdot \big[\nabla \times \boldsymbol{E}(\boldsymbol{r})\big] - \frac{\omega^2 \varepsilon(\boldsymbol{r})}{c^2} \boldsymbol{u}^*(\boldsymbol{r}) \cdot \boldsymbol{E}(\boldsymbol{r}) \right\} = \\ \int\limits_{\partial\Omega} \mathrm{d}s \, \boldsymbol{u}^*(\boldsymbol{r}) \cdot \Big\{ \big[\nabla \times \boldsymbol{E}(\boldsymbol{r})\big] \times \boldsymbol{n}(\boldsymbol{r}) \Big\} \,, \end{aligned} \tag{5.27}$$

where $\boldsymbol{n}(\boldsymbol{r})$ denotes the unit normal vector (pointing outwards) on the boundary $\partial\Omega$ of the domain Ω. Note that the expression on the right hand side of Eq. (5.27) corresponds to an integral over the respective Neumann boundary condition

$$\boldsymbol{F}(\boldsymbol{r}) = \big[\nabla \times \boldsymbol{E}(\boldsymbol{r})\big] \times \boldsymbol{n}(\boldsymbol{r}) \qquad (\text{defined on } \partial\Omega) \,, \tag{5.28}$$

which is supposed to be a given function in the problem under consideration.

If $\boldsymbol{E}(\boldsymbol{r})$ solves Eq. (5.27) for any $\boldsymbol{u}(\boldsymbol{r}) \in H$, it is also a solution of the original problem (5.25). The basic idea of the finite element method is now to approximate the solution of Eq. (5.27) by restricting the functions $\boldsymbol{E}(\boldsymbol{r})$ and $\boldsymbol{u}(\boldsymbol{r})$ to a subspace $V \subset H$ of finite dimension N. This is achieved by discretizing the domain Ω into

small patches, e.g., triangles (in two dimension) or tetrahedrons (in three dimensions). The basis of V is typically formed by polynomials $\{\boldsymbol{\nu}_i(\boldsymbol{r})\}$ of degree p, which are defined such that they have finite values only on or near the respective patch i and are zero otherwise. The approximate solution for the electric field distribution is then a superposition of these local polynomials, i.e.,

$$\boldsymbol{E}(\boldsymbol{r}) = \sum_{i=1}^{N} a_i \boldsymbol{\nu}_i(\boldsymbol{r}) \; . \tag{5.29}$$

Inserting Eq. (5.29) into the weak formulation (5.27), this yields a set of linear equations

$$\sum_{i=1}^{N} a_i \phi(\boldsymbol{\nu}_i, \boldsymbol{\nu}_j) = f(\boldsymbol{\nu}_j) \qquad \forall j = 1, \ldots, N \; , \tag{5.30}$$

from which the coefficients a_i can be determined. Here, the bilinear functionals

$$f(\boldsymbol{\nu}_j) = \int_{\Gamma} \mathrm{d}s \, \boldsymbol{\nu}_j^*(\boldsymbol{r}) \cdot \boldsymbol{F}(\boldsymbol{r}) \qquad \text{and} \tag{5.31}$$

$$\phi(\boldsymbol{\nu}_i, \boldsymbol{\nu}_j) = \int_{\Omega} \mathrm{d}\boldsymbol{r} \left\{ \left[\nabla \times \boldsymbol{\nu}_j(\boldsymbol{r})\right]^* \cdot \left[\nabla \times \boldsymbol{\nu}_i(\boldsymbol{r})\right] - \frac{\omega^2 \varepsilon(\boldsymbol{r})}{c^2} \boldsymbol{\nu}_j^*(\boldsymbol{r}) \cdot \boldsymbol{\nu}_i(\boldsymbol{r}) \right\} \tag{5.32}$$

were defined, which can readily be evaluated. In fact, due to the local definition of the basis functions $\{\boldsymbol{\nu}_i(\boldsymbol{r})\}$, most of the entries $\phi(\boldsymbol{\nu}_i, \boldsymbol{\nu}_j)$ in Eq. (5.30) vanish for $i \neq j$, allowing the system of linear equations to be solved very efficiently. This makes the FEM approach superior to the plane wave expansion method, where the basis functions (i.e., plane waves) are spread over the entire domain Ω, leading to much longer computation times.

Application to photonic crystal fibers

As was already stated in Sec. 5.2.1, the mode profiles in a photonic crystal fiber can be expressed as

$$\boldsymbol{E}(\boldsymbol{r}) = \boldsymbol{E}(x, y) \mathrm{e}^{i\beta z} \; , \tag{5.33}$$

effectively reducing Eq. (5.27) as well as the corresponding formulation for $\boldsymbol{H}(\boldsymbol{r})$ to a two-dimensional problem [329]. Then, pairs of $\boldsymbol{E}(x, y)$ and $\beta = n_{\mathrm{eff}}|\boldsymbol{k}|$ are obtained for each given frequency ω. An example of such a calculation is shown in Fig. 5.9. Note that the employed mesh (Fig. 5.9a) has a different spatial resolution in the various parts of the fiber and can selectively be refined after each computational run to increase the resolution in regions where the electromagnetic field varies rapidly. Such

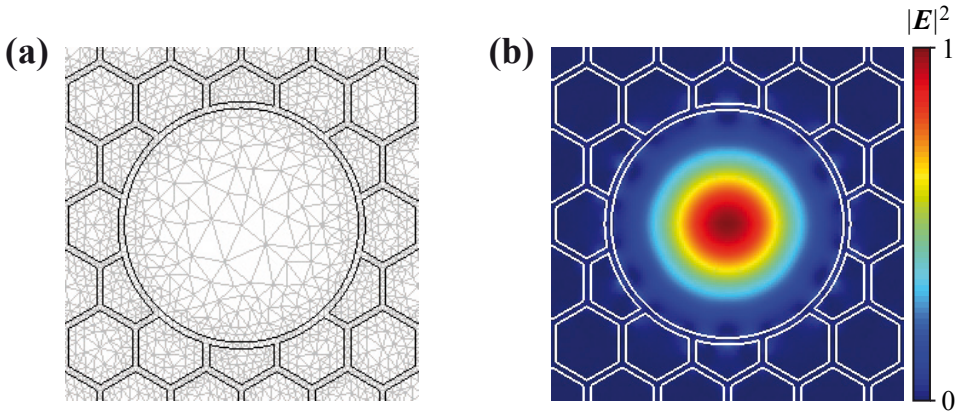

Figure 5.9: (a) Example of the triangular mesh used to calculate the optical mode profiles of a hollow-core photonic crystal fiber. The core diameter is $d = 5.3$ µm. **(b)** Corresponding electric field intensity distribution $|\boldsymbol{E}|^2$ of the fundamental guided mode (with $n_{\text{eff}} \approx 0.99$) at a wavelength $\lambda = 530$ nm.

adaptive meshing strategies are one of the main advantages of the FEM approach compared to the FDTD method, efficiently reducing computational time (at least for steady-state electromagnetic problems in the frequency domain). This particularly applies to photonic crystal fibers, where most of the field energy is concentrated inside the core, but a large part of the cladding structure has nonetheless to be taken into account in order to accurately model the band gap effect.

In the calculations presented in this chapter, the simulated cladding structure consisted of six layers of holes, which is sufficient to achieve a good spatial confinement of the guided modes inside the core. The number of meshing nodes was typically on the order of 10^5 and second-order polynomials (i.e., $p = 2$) were used as basis functions for the computation. These settings turned out to be suitable for obtaining smooth intensity profiles as the one displayed in Fig. 5.9b. In principle, transparent boundary conditions can also be implemented in the FEM simulations by using perfectly matched layers (see Sec. 2.3.4) or other methods [330], allowing the calculation of radiation losses. However, in the case of the short propagation lengths $L \approx 10$ cm considered here, these losses are negligibly small and not relevant for the analysis of the experimental data. Therefore, the simply boundary condition $\boldsymbol{F}(\boldsymbol{r}) = 0$ was employed in most of the simulations.

5.4 Investigation of the sensing performance

The two types of photonic crystal fibers employed in this thesis were already introduced in Sec. 5.3.1, namely the hollow-core fiber shown in Fig. 5.5a and the (microstructured) solid-core fiber shown in Fig. 5.5b. As discussed in Sec. 5.2.2, they represent different approaches for optofluidic sensing, relying either on a di-

rect or an evanescent light-sample interaction, respectively. Both types of fibers and sensing schemes have their advantages and drawbacks, which need to be taken into account when designing devices for a specific application. For example, evanescent field sensors do not require a selective filling technique, which simplifies the preparation and handling considerably. As the solid core can be made very small, single-mode operation is easily maintained, being important for applications where phase information is crucial. However, the main drawback is the relatively weak interaction of the propagating light with the sample material, which is expected to be much higher in selectively filled hollow-core fibers. However, the achievable sensing performance of the latter has never been studied in detail and the true benefit compared to evanescent field devices is yet unknown.

In the following, the sensing performance of both types of fibers is analyzed and directly compared using absorption (Sec. 5.4.1) as well as fluorescence measurements (Sec. 5.4.2). The experiments are accompanied by corresponding numerical calculations of the most relevant sensing parameters. Furthermore, the possibility of using a selectively coated hollow-core fiber instead of a liquid-filled one is explored (Sec. 5.4.3).

5.4.1 Absorption measurements

Numerical simulations

As described in Sec. 5.2.2, the most important figure of merit in absorption measurements is the interaction coefficient α, which represents a measure for the fraction of field intensity located inside the sample material. According to Eq. (5.15), it directly determines the absorbance

$$A(\lambda) = -\ln\left[\frac{I(\lambda)}{I_0(\lambda)}\right] = \alpha\epsilon(\lambda)cL \tag{5.34}$$

observed experimentally. To estimate the expected value of α in the two types of fibers, corresponding finite element simulations of the respective optical mode profiles were performed using different kinds of sample liquids. Thereby, it was assumed that only the central hole of the hollow-core fiber is filled (see Fig. 5.10a), while the solid-core fiber is completely infiltrated (see Fig. 5.10b). For the case of ethylene glycol (refractive index $n_{\mathrm{liq}} = 1.43$), the resulting intensity distributions $|\boldsymbol{E}|^2$ of the fundamental guided modes are shown in Figs. 5.10c and 5.10d, respectively. Note that the mode profile of the liquid-filled hollow-core fiber resembles that of the air-filled version shown in Fig. 5.9b. However, one has to keep in mind that the underlying guiding mechanisms are quite different, being based on total internal reflection and the photonic band gap effect, respectively.

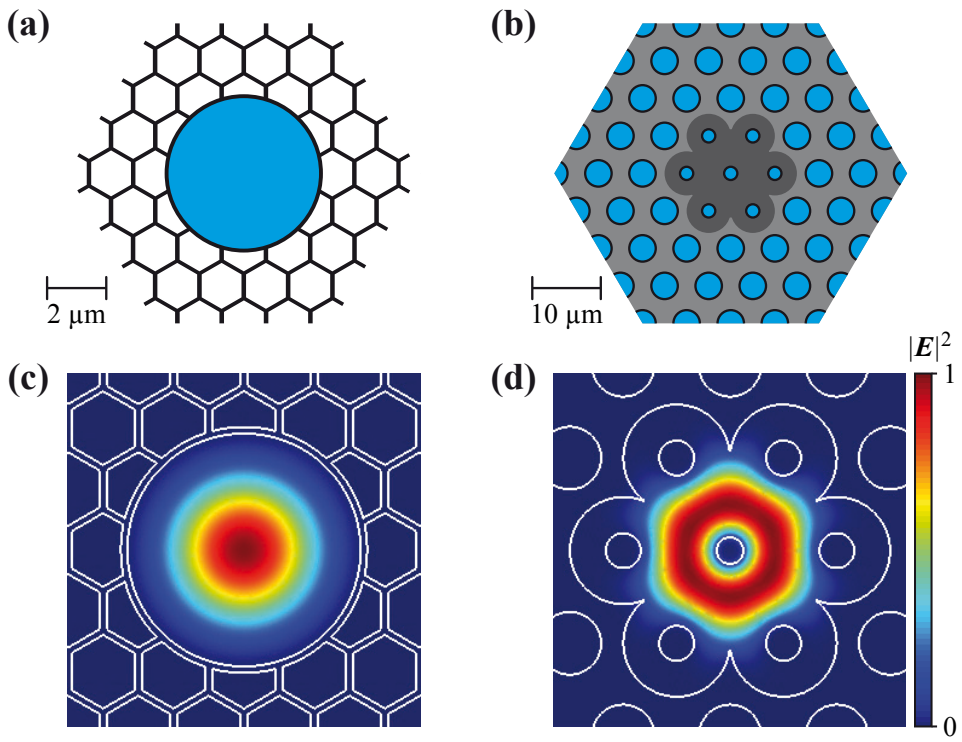

Figure 5.10: **(a,b)** Schematic illustration of the selectively filled hollow-core fiber (a) and of the completely filled (microstructured) solid-core fiber (b). Both structures are approximations of the fibers shown in Figs. 5.5a and 5.5b, respectively. **(c,d)** Corresponding calculated electric field intensity distributions $|\boldsymbol{E}|^2$ of the fundamental guided mode (at a wavelength $\lambda = 530\,\text{nm}$) of the hollow-core design (c) and the solid-core design (d), respectively. Ethylene glycol with a refractive index $n_{\text{liq}} = 1.43$ is assumed as filling liquid.

By integrating the calculated electromagnetic fields over the liquid-filled regions of the fiber and comparing these values to the total amount of energy stored in the guided mode, α can be deduced according to Eq. (5.14). The corresponding values for the fundamental guided mode and three different kinds of injected liquids (i.e., water, ethanol, and ethylene glycol) are summarized in Tab. 5.1. In the case of the hollow-core fiber, light is almost completely guided within the liquid filament, leading to extremely high interaction coefficients α close to unity. Thereby, the exact value of α depends only weakly on the refractive index n_{liq}. The same holds for the

solvent	n_{liq}	α_{hc}	α_{sc}
water	1.33	98.3%	0.05%
ethanol	1.36	99.3%	0.06%
ethylene glycol	1.43	99.8%	0.30%

Table 5.1: Interaction coefficients α (at a wavelength $\lambda = 530\,\text{nm}$) for the fundamental mode of the selectively filled hollow-core (hc) fiber and the completely filled solid-core (sc) fiber for different infiltrated solvents.

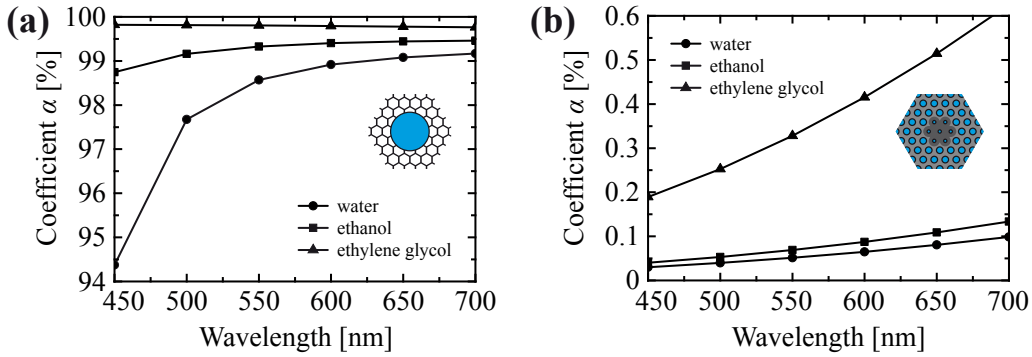

Figure 5.11: Calculated interaction coefficient α as a function of the wavelength λ for the fundamental guided mode in **(a)** the hollow-core fiber and **(b)** the solid-core fiber when infiltrated with different liquids. The values assumed for the refractive index n_{liq} are provided in Tab. 5.1.

wavelength λ (at least in the spectral range above 500 nm), as can be seen from Fig. 5.11a. If higher-order modes are taken into account, α decreases slightly (data not shown), yielding a mean value $\alpha \approx 92\%$ (for $\lambda = 530$ nm and $n_{\mathrm{liq}} = 1.43$) when averaging over the 20 modes of lowest energy.

In the case of the solid-core fiber, over 99% of the light intensity is guided in the silica and only the small evanescent part of the field penetrates into the surrounding holes. Thereby, the penetration depth (and thus α) increases with growing n_{liq} due to the decreasing index contrast between the silica and the holes (see Tab. 5.1). Likewise, α increases with growing wavelength λ of the guided light (see Fig. 5.11b). If again higher-order modes are considered, the interaction coefficient exhibits large fluctuations between $\alpha = 0.2\%$ and $\alpha = 1\%$ among the 50 modes of lowest energy (data not shown), with a mean value of $\alpha \approx 0.5\%$ (for $\lambda = 530$ nm and $n_{\mathrm{liq}} = 1.43$).

It should be noted that the specific type of solid-core fiber employed here does not represent the most suitable design for evanescent field sensing due to the relatively large size of the core area ($\approx$ 19 µm in diameter). Other designs using smaller microstructured cores [308] or so-called steering-wheel fibers [331] predict much higher interaction coefficients α on the order of 10% in the visible wavelength range. However, even in these optimized structures the extremely high values of α provided by hollow-core fibers are not within reach due to the evanescent character of the interaction.

It should further be noted that the second important sensing parameter in absorption measurements, namely the propagation loss κ (see Sec. 5.2.2), is small enough to be neglected in the present analysis. In finite element simulations with transparent boundary conditions it was verified that the requirement $\kappa(\lambda) \ll \alpha\epsilon(\lambda)c$ is fulfilled for all fiber designs and dye concentrations c considered in the experiment, the results of which are discussed next.

Experimental results

Absorption measurements were performed on both types of fibers using the experimental methods described in Secs. 5.3.1 and 5.3.2. Thereby, ethylene glycol proved to be the most suitable liquid for infiltration due to its low evaporation rate and the high refractive index, which promises the best sensing performance according to the simulations presented above. Corresponding absorption spectra of rhodamine 6G are shown in Fig. 5.12. It can be seen that, apart from slight modulations, the overall spectral shape is almost identical to that observed in respective free-space measurements (red curves). The latter were performed by means of a conventional absorption/fluorescence spectrometer (UV3101PC, Shimadzu).

One of the main problems in fiber-based absorption measurements is the need for a suitable reference spectrum, which has to be recorded in advance from the same piece of fiber filled with pure solvent. In the current experimental setup each refilling procedure also required a readjustment of the light input, resulting in spectral fluctuations of the corresponding transmission signal due to slightly different coupling conditions. This turned out to be most critical in the case of the solid-core fiber, where cladding modes are easily excited in addition to the core modes, the former being extremely sensitive to variations of the fiber coupling. In the case of the hollow-core fiber, the effect was less severe, since no cladding modes can exist in the relevant wavelength range around 530 nm due to the photonic band gap effect. Nonetheless, the detection sensitivity was still limited to a minimum absorbance $A \approx 0.1$ required to distinguish between coupling-induced changes in the transmission spectrum and the actual absorption signal of the dye.

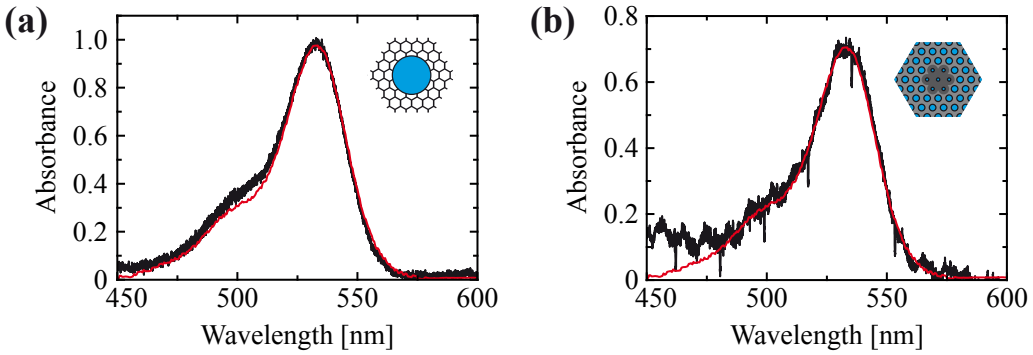

Figure 5.12: **(a)** Absorption spectrum from a hollow-core fiber (black) selectively filled with a solution of rhodamine 6G in ethylene glycol. The dye concentration and fiber length are $c = 5 \times 10^{-7}$ M and $L = 10.3$ cm, respectively. **(b)** Corresponding absorption spectrum from a completely filled solid-core fiber (black). The dye concentration and fiber length are $c = 5 \times 10^{-5}$ M and $L = 10.7$ cm, respectively. In both plots the red curves represent a free-space reference spectrum of rhodamine 6G in ethylene glycol (at a concentration $c = 1.7 \times 10^{-6}$ M), which was scaled accordingly.

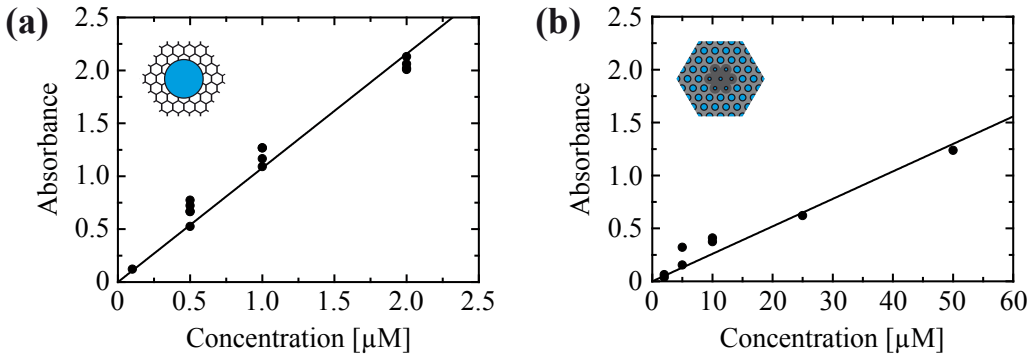

Figure 5.13: Peak absorbance A (at a wavelength $\lambda = 530$ nm) for different dye concentrations in **(a)** the hollow-core fiber and **(b)** the solid-core fiber. In all measurements (symbols) ethylene glycol was used as solvent and the results were normalized to a fiber length of 10 cm. The solid lines are a linear fit to the experimental data, from which the interaction coefficient α can be deduced. Note the different scales on the abscissa.

To estimate the interaction coefficient α in both types of fibers, the corresponding peak absorbance $A(\lambda = 530\,\text{nm})$ for different dye concentrations is displayed in Fig. 5.13. Apparently, relatively large fluctuations in the measured values of A can occur, which might be attributed to local accumulations of dye molecules near the end facets of the fibers as well as to uncertainties in the fiber coupling as described above. Therefore, a linear regression of the experimental data was performed, from which α can be deduced according to Eq. (5.34) if the molar extinction coefficient $\epsilon(\lambda)$ is known. The latter is well documented as $\epsilon(\lambda = 530\,\text{nm}) = 1.16 \times 10^4\ \text{m}^2/\text{mol}$ for rhodamine 6G solved in ethanol. In the following, the same value is also assumed for ethylene glycol, since both solvents produced nearly the same results in free-space absorption measurements. Then, the linear fit in Fig. 5.13a yields an interaction coefficient $\alpha_{\text{hc}} = (93 \pm 3)\%$ for the hollow-core fiber, which is in excellent agreement with the theoretical prediction. Note that this is the first experimental demonstration of a liquid-core fiber sensor with values of α close to unity.

In the case of the solid-core fiber, an interaction coefficient $\alpha_{\text{sc}} = (2.2 \pm 0.2)\%$ is deduced from the linear fit in Fig. 5.13b, being significantly larger than the predicted value of $\approx 0.5\%$. This discrepancy may be attributed to additional cladding modes, which have not been taken into account in the simulation, but can also interact with the dye solution due to the complete infiltration of the fiber. Furthermore, dye molecules might get attached to the walls of the holes, thus locally increasing the dye concentration where the evanescent field is largest.

Due to the larger interaction coefficient α, the minimal concentration $c_{\text{min}} = 5 \times 10^{-8}$ M which could reliably be detected (via absorption) in the hollow-core fiber was 40 times lower than the corresponding value $c_{\text{min}} = 2 \times 10^{-6}$ M in the solid-core design. This detection sensitivity may further be improved by using an

integrated optofluidic system, where liquid can be pumped through the fiber while simultaneously launching light into the latter. Such a configuration was already demonstrated by Rindorf *et al.* [306] and makes readjustment procedures between measurements obsolete, thus avoiding distortions in the reference spectrum due to different coupling conditions.

5.4.2 Fluorescence measurements

Numerical simulations

Contrary to sensing methods which rely on absorption or extinction, fluorescence measurements do not require additional reference spectra and may thus inherently provide higher detection sensitivities. In this case, not only the interaction coefficient α, but also the collection efficiency ξ is of utmost importance (see Sec. 5.2.2). While α determines the efficiency of the excitation process and the coupling of the emission to the guided modes, ξ is a measure for the fraction of all available optical modes which are actually guided by the fiber. For the configurations studied here, ξ can well be approximated by Eq. (5.17), since both types of fibers are highly multimode and the emission can be assumed as isotropic due to the random orientation of the dye molecules. Therefore, finite element simulations were performed to calculate the effective refractive indices of the fundamental core and cladding modes, $n_{\mathrm{eff}}^{\mathrm{core}}$ and $n_{\mathrm{eff}}^{\mathrm{clad}}$, respectively, whose ratio directly determines the collection efficiency. The resulting values of ξ for the different kinds of liquids are summarized in Tab. 5.2.

In the case of the hollow-core fiber, the collection efficiency clearly increases with growing refractive index of the injected liquid, since $n_{\mathrm{eff}}^{\mathrm{core}}$ directly scales with n_{liq}, while $n_{\mathrm{eff}}^{\mathrm{clad}}$ is unaffected due to the selective infiltration of the core. As the same trend holds for the interaction coefficient α (see Tab. 5.1), a simultaneous optimization of α and ξ is possible by using high-index liquids, providing ideal conditions for an efficient fluorescence sensing. Contrary to this, ξ decreases with growing n_{liq} in the case of the solid-core fiber, because the index contrast between the core and the cladding region becomes smaller. Consequently, α and ξ cannot simultaneously be maximized and an appropriate tradeoff has to be found.

solvent	n_{liq}	ξ_{hc}	ξ_{sc}
water	1.33	6.7%	1.2%
ethanol	1.36	7.6%	1.0%
ethylene glycol	1.43	9.6%	0.5%

Table 5.2: Collection efficiencies ξ (at a wavelength $\lambda = 530$ nm) of the selectively filled hollow-core (hc) fiber and the completely filled solid-core (sc) fiber for different infiltrated solvents.

A suitable figure of merit for the total sensing performance in fluorescence measurements would be the expression $\Phi = \alpha^2 \xi$, which reflects the double role of the interaction coefficient for excitation and emission processes. From a comparison of the respective values of α and ξ in Tabs. 5.1 and 5.2, respectively, it is apparent that ethylene glycol represents the best choice for both types of fibers. However, the corresponding sensing performance Φ of the hollow-core design is expected to exceed that of the solid-core fiber by a factor of $\approx 4 \times 10^4$ (when using the experimentally deduced values of α), highlighting the superiority of the liquid-core/air-cladding concept. It should be noted that this figure of merit does not only apply to fluorescence sensing, but to all processes (such as Raman scattering) where the sample material is actively emitting.

Experimental results

To test the theoretical predictions fluorescence measurements were performed on both types of fibers using the same experimental setup as employed for the absorption measurements, except that the white light source was substituted by a 514 nm laser (see Sec. 5.3.2). Corresponding fluorescence spectra of rhodamine 6G (solved in ethylene glycol) are shown in Fig. 5.14. Again, the observed spectral shapes and peak positions agree well with those obtained from free-space measurements (red curves), indicating that reabsorption effects and interactions of the dye molecules with the inner walls of the holes play a minor role. In the case of the hollow-core fiber, reabsorption effects only become significant at concentrations exceeding $c = 10^{-6}$ M (for a fiber length of 10 cm), leading to a red-shift of the emission maximum. The corresponding value for the solid-core design is much higher due to the smaller in-

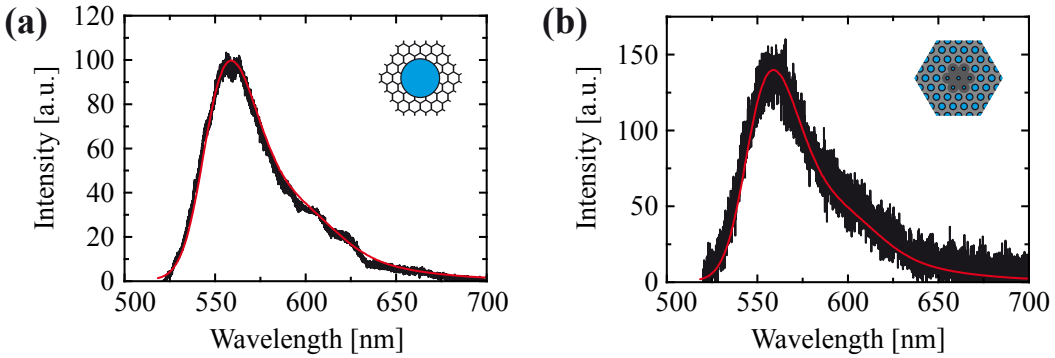

Figure 5.14: **(a)** Fluorescence spectrum from a hollow-core fiber (black) selectively filled with a solution of rhodamine 6G in ethylene glycol. The dye concentration and fiber length are $c = 1 \times 10^{-9}$ M and $L = 12.4$ cm, respectively. **(b)** Corresponding fluorescence spectrum from a completely filled solid-core fiber (black). The dye concentration and fiber length are $c = 5 \times 10^{-6}$ M and $L = 10.7$ cm, respectively. In both plots the red curves represent a free-space reference spectrum of rhodamine 6G in ethylene glycol (at a concentration $c = 1.7 \times 10^{-6}$ M), which was scaled accordingly.

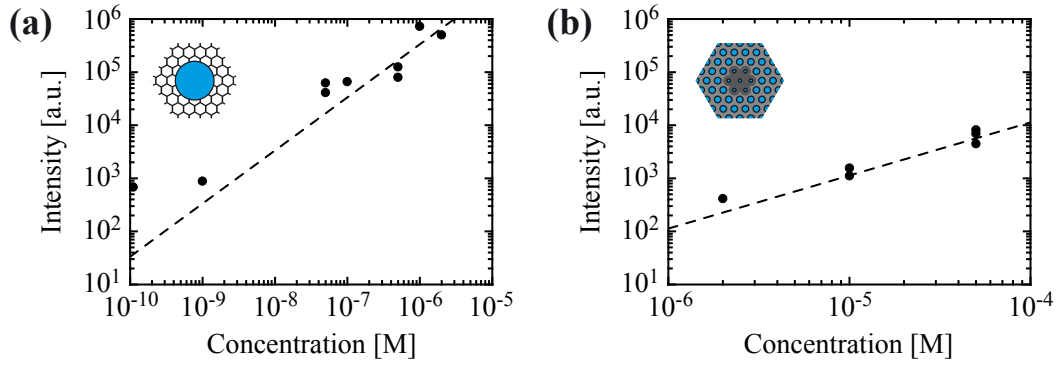

Figure 5.15: Peak fluorescence (at a wavelength $\lambda = 560$ nm) for different dye concentrations in **(a)** the hollow-core fiber and **(b)** the solid-core fiber. In all measurements (symbols) ethylene glycol was used as solvent and the results were normalized to a fiber length of 10 cm and to integration times of 1 s. The dashed lines are a linear fit to the experimental data and serve as a guide to the eye. Note the different scales on the abscissa.

teraction coefficient α and therefore not relevant for the range of concentrations considered here. The negligible influence of interactions with the hole walls is not self-evident, as is discussed in more detail in Sec. 5.4.3. Obviously, the situation here seems to be comparable to that in a macroscopic cuvette, where absorption and emission processes are dominated by volume rather than surface effects. However, the key difference to a macroscopic measurement is the much smaller sample volume, which is only 2.2 nL in a 10 cm piece of the selectively filled hollow-core fiber and 58 nL in the case of the solid-core fiber.

The peak fluorescence values (recorded at a wavelength $\lambda = 560$ nm) for different dye concentrations are displayed in Fig. 5.15. Thereby, the investigated range of concentrations for each type of fiber was chosen such that reabsorption effects are negligible. As expected from the numerical simulations discussed above, the sensing performance Φ of the hollow-core design exceeds that of the solid-core fiber by several orders of magnitude. The exact gain in sensitivity is hard to evaluate due to the rather large fluctuations in the detected intensity, but seems to be ≈ 10 times smaller than the theoretical prediction of 4×10^4. This discrepancy may be attributed to additional scattering at the melted end facet of the hollow-core fiber, leading to increased output losses and thus to a reduction of the collection efficiency.

Nonetheless, it should be noted that the achieved detection sensitivity outperforms that of any previously reported fiber-based sensing devices [304]. Thereby, the minimal detectable dye concentration c_{min} was not limited by the collection efficiency, but by a parasitic background signal originating from the fiber material itself, which becomes comparable in intensity for concentrations $c \approx 5 \times 10^{-10}$ M (see Fig. 5.15a). Similar problems also occurred in other recent reports [332] and seem to be the major obstacle for further improvements in the sensing performance.

5.4.3 Selective coating of the hollow core

Instead of directly using the liquid-filled fibers for sensing, there is also the possibility to coat the inner walls of the holes with sample material by allowing the solvent to evaporate after the infiltration. Such a scheme may be of interest, e.g., for applications involving surface-enhanced Raman scattering [333]. While for the solid-core design the character of the light-sample interaction is not significantly affected by the evaporation, the guiding mechanism is completely changed in the case of the hollow-core fiber, being again reverted to photonic band gap guidance (in air). Although this strongly limits the available wavelength range, it can provide valuable insight into the interaction between the dye molecules and the optical modes of the fiber, as is discussed in the following.

For these experiments the hollow-core fiber was selectively filled with a solution of rhodamine 6G in ethanol, since the latter exhibits a high evaporation rate. Although also a complete infiltration scheme would have been possible, the same preparation procedure as in the previous experiments was employed to ensure comparability, with the exception that the end facets of the fiber were cleaved prior to the measurements. Using the evaluation method described in Sec. 5.4.1, the interaction coefficient α of the hollow-core fiber was deduced from corresponding absorption measurements (data not shown), yielding a value $\alpha = (10 \pm 2)\%$. This agrees with the expected order of magnitude derived from numerical simulations (see Fig. 5.9b), although a precise theoretical prediction is non-trivial due to the jump of the electromagnetic field at the air/silica interface of the hole walls.

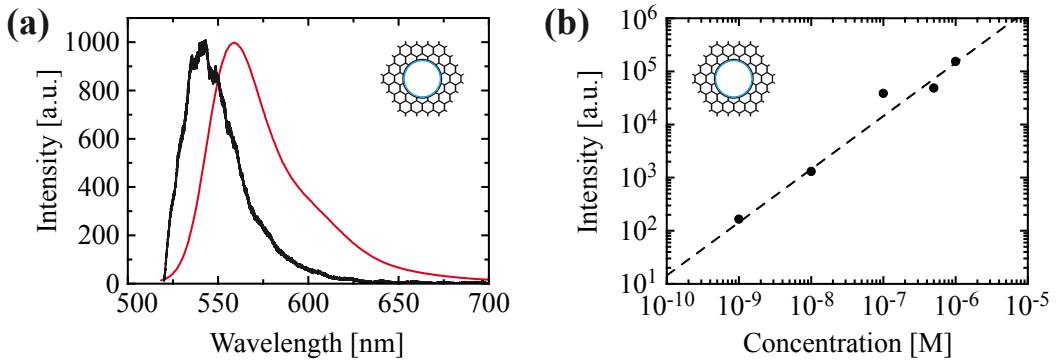

Figure 5.16: **(a)** Fluorescence spectrum from a hollow-core fiber (black) selectively coated with rhodamine 6G. The (injected) dye concentration and fiber length are $c = 1 \times 10^{-9}$ M and $L = 13.7$ cm, respectively. The red curve represents a free-space reference spectrum of rhodamine 6G in ethylene glycol (at a concentration $c = 1.7 \times 10^{-6}$ M), which was scaled accordingly. **(b)** Corresponding peak fluorescence (at a wavelength $\lambda = 535$ nm) for different dye concentrations injected into the fiber. All measurements (symbols) were normalized to a fiber length of 10 cm and to integration times of 1 s. The dashed line is a linear fit to the experimental data and serves as a guide to the eye.

Likewise, fluorescence measurements were performed on the selectively coated hollow-core fiber. A typical spectrum is shown in Fig. 5.16a, exhibiting a clear blue-shift of the peak wavelength compared to the respective free-space measurement (red curve). This apparent change in the spectral shape is simply a result of the limited bandwidth (≈ 60 nm) of the air-guiding hollow-core fiber, which has its central wavelength at 510 nm, thus leading to a spectral filtering effect. However, if the concentration c of the injected dye solution is increased, a sudden red-shift of the peak wavelength (by ≈ 10 nm) occurs at concentrations around 10^{-6} M. This shift is not due to reabsorption effects, which are smaller in magnitude and increase continuously with c. It may rather be suspected that the sudden spectral change results from intermolecular effects. Once a critical coverage of dye molecules on the silica surface is reached, they might undergo conformational changes, forming dimers or other supermolecular structures. Similar effects were also observed in other studies [308] and need to be taken into account when aiming at quantitative sensing applications.

The peak fluorescence values (recorded at a wavelength $\lambda = 535$ nm) for those concentrations at which no red-shift occurred are displayed in Fig. 5.16b. Astonishingly, the detected intensities were only about one order of magnitude lower than the corresponding values obtained for the liquid-core fiber (see Fig. 5.15a), although both, the interaction coefficient α and the collection efficiency ξ, are expected to be much smaller in the air-core version. Numerical simulations as well as specifications of the manufacturer predict $\xi = 0.4\%$ for the coated fiber. Together with an interaction coefficient $\alpha \approx 10\%$, this yields a total sensing performance Φ which should be ≈ 2000 times lower than that of the liquid-core design. This discrepancy cannot simply be explained by a better out-coupling efficiency of the coated fiber due to its cleaved end facets. It may be suggested that the silica surface takes an active role in enhancing the coupling of the dye emission to the guided optical modes through local field effects. Alternatively, the fluorescence detected from the liquid-filled fibers may be lower than expected for reasons yet unknown. At this time, no clear indication exists regarding the origin of the observed discrepancy, requiring further studies.

5.5 Summary and conclusions

In this chapter the optofluidic sensing performance of different types of photonic crystal fibers was investigated and directly compared by conducting numerical simulations as well as absorption and fluorescence measurements. Regarding the achievable detection sensitivity, a clear superiority of liquid-core designs could be demonstrated, resulting from a much more efficient light-sample interaction in comparison to solid-core devices, which rely on evanescent fields. The minimal molecular concen-

tration which could reliably be detected was on the order of 10^{-9} M, being limited by fluctuations of the coupling conditions in the case of absorption measurements and by unwanted background emission in the case of fluorescence measurements. Additional experiments on selectively coated hollow-core fibers revealed an unusually high detection sensitivity, exceeding the theoretical prediction by two orders of magnitude. Understanding the origin of this effect may enable the realization of devices with even better sensing performances.

Note that part of these findings have already been published in Barth *et al.* 2010a and Smolka *et al.* 2007a, 2007b (see List of Own Publications).

Despite the clear advantages of liquid-core fibers regarding the detection sensitivity, their true potential is often limited by practical issues as those discussed above. Meanwhile, other studies of optimized solid-core fibers, especially those of the steering-wheel type [332, 334–336], have also demonstrated the detection of molecular concentrations on the order of 10^{-9} M, providing the additional benefit of an easier preparation and handling. Thus, it is not yet clear what the optimum design for a fiber-based optofluidic sensor has to look like. Most probably, each specific application will require a slightly different design, balancing the need for sensitivity, robustness, and cost-effectiveness.

One specific application, which has attracted considerable attention in recent years, is the use of photonic crystal fibers as sensors for surface-enhanced Raman scattering (SERS). Various implementations have been realized by infiltrating mixtures of molecules and metal nanoparticles into the fibers [333, 337–339]. Although the achieved sensitivities were so far limited to molecular concentrations on the order of 10^{-7} M, the great advantage of fiber-based SERS sensors (compared to single-molecule SERS studies [184, 185]) is the ability to excite and detect multiple nanoparticle-molecule aggregates at the same time, instantly providing an average signal without the need to search for specific "active" sites on the sample. This should not only help to improve the reproducibility of SERS measurements, but would also allow for a much better quantitative analysis even when analyte concentrations are small.

Regarding practical implementations, an essential drawback of the fiber-based detection schemes used here and in many other studies is the insertion of the liquid at the end facet of the fiber, where also light has to be coupled in and out. Thus, it is often difficult to achieve optical and fluidic access simultaneously. This may be tackled by providing a side access to the holes of the fiber, as has recently been demonstrated by using melting techniques [340] or focused ion beam milling [341]. Alternatively, the core region may completely be exposed [342, 343], allowing much faster liquid flow and response times.

Another issue concerns the reusability of fiber sensors once they have been infiltrated, since the removal of residual analytes from the holes is usually very time consuming or may be impossible at all. In some cases an appropriate functionalization of the inner walls of the holes can prevent the unwanted binding of molecules to the surface. This is crucial for all applications where the fiber is permanently integrated into a more complex optofluidic network and cannot simply be replaced. In other cases a single-use design might be more suitable, especially as production costs will drop once fabrication methods have evolved to the state of mass production. Then, a type of "plug-and-play" device can be envisaged, using exchangeable pieces of fiber which are connected to an optical detection unit through appropriate plugs, requiring no complicated alignment procedures.

Chapter 6

Summary and Outlook

6.1 Summary

Within this thesis a variety of novel photonic crystal structures was developed and investigated with regard to applications in nanophotonics and optofluidics. In particular, four major topics were discussed, dealing with (1) the fabrication and optimization of photonic crystal cavities in the visible, (2) the controlled deposition of nanoparticles on these cavities to create hybrid nanophotonic elements, (3) the theoretical study of optical forces near photonic crystal cavities for particle trapping, and (4) the investigation of liquid-filled photonic crystal fibers for biochemical sensing. Thereby, a broad range of research areas was covered, including nanophotonics, cavity quantum electrodynamics (QED), plasmonics, and optofluidics.

In the first part planar photonic crystal cavities made from silicon nitride were developed and subsequently characterized by means of fluorescence spectroscopy. These structures are capable of operating in the visible wavelength range, a spectral region which had barely been tapped so far. The main focus lay on the optimization of the cavity quality factor in order to allow for sophisticated cavity QED experiments with these devices. By exploring different design strategies quality factors exceeding 1000 could be demonstrated for the first time (Barth *et al.* 2007a), with an unprecedented maximum value of 3400 for cavities of the double-heterostructure type (Barth *et al.* 2008a). Spectroscopic and time-resolved measurements on ensembles of cavity-coupled dye molecules showed clear evidence for QED effects (in the weak coupling regime), although studies on a single emitter level would be required for a quantitative analysis, a goal which was subsequently pursued in the second part of this thesis.

In the second part the fabricated double-heterostructure cavities were employed as platforms for the creation of hybrid nanophotonic elements, targeting, among other things, at the controlled and efficient coupling of single defect centers

in diamond to the cavity modes. For this purpose, a versatile AFM-based nanomanipulation method was developed, being capable of depositing and assembling arbitrary types of nanoparticles on the photonic crystal structures with high precision (Barth *et al.* 2009b). This method allowed the realization of three, so far unexplored hybrid systems.

(1) For the first time the deterministic coupling of a single diamond nanocrystals to a photonic crystal cavity was demonstrated (Barth *et al.* 2009a). It could be shown that particle sizes below 20 nm would be ideal for an efficient coupling of fluorescent defect centers to the cavity modes without a noticeable degradation of the corresponding quality factor. On the other hand, the variation of the particle position with respect to the cavity field revealed the tuning capabilities of larger nanocrystals, allowing for a spectral adjustment of the cavity resonance while keeping the impact on the quality factor small. A coupling of single/few nitrogen-vacancy (NV) defect centers to the cavity could be facilitated, although background luminescence from the silicon nitride prevented further investigations of cavity QED effects in this system.

(2) For the first time individual metal nanoparticles were coupled to a photonic crystal cavity, creating a novel plasmonic-photonic hybrid device (Barth *et al.* 2010b). Such a system combines the high quality factors achievable with dielectric cavities with the plasmonic field enhancement inherent to metal structures. A coherent, polarization-selective interaction of the cavity field with the plasmon resonances of gold nanorods and -spheres could be observed, with a coupling efficiency of $\approx 40\%$. Contrary to most previous implementations of purely plasmonic cavities, relatively high quality factors of up to 900 were maintained. In combination with the strong field localization near the metal nanoparticles, this gives rise to a ≈ 10 times enhancement of the achievable Purcell factor (compared to the bare cavity), promising higher efficiencies for the coupling of external emitters to photonic crystal cavities.

(3) For the first time a single NV defect center in a diamond nanocrystal was coupled to metal nanoparticles, yielding a plasmonic enhancement of the corresponding excitation and emission process (Schietinger *et al.* 2009). An unprecedented boost in the excitation and emission rate by approximately one order of magnitude could be demonstrated, resulting in a total enhancement of the emission efficiency by a factor of ≈ 100. Thereby, the single photon characteristics were maintained, proving the suitability of this approach to create highly efficient single photon sources operating at room temperature. All three of the above-mentioned systems represent milestones toward the realization of a diamond-coupled plasmonic-photonic hybrid cavity as a fundamental building block for integrated nanophotonic devices.

In the third part another field of application for photonic crystal cavities was theoretically studied, namely their use as sophisticated optical traps for microscopic particles. Such a trapping approach may be of high value for the realization of integrated optofluidic devices with novel sensing functionalities, but had not been investigated in detail so far. For this purpose, a thorough numerical analysis of the optical forces exerted on objects in the near-field of photonic crystal cavities was conducted (Barth *et al.* 2006a). It could be shown that changes in the object size and cavity geometry can significantly alter the trapping behavior and that designs are favorable which concentrate a large fraction of the field intensity in the surrounding medium. For the first time the back-action of particles on the cavity properties was fully taken into account, revealing a complicated dynamics due to the induced resonance shift. Based on these findings, a novel self-induced trapping scheme was proposed, allowing for a highly size-selective particle trapping. Note that the feasibility of optical traps based on photonic crystals as well as the general principle of the proposed self-induced trapping scheme have both been proven in recent experiments [296, 297].

In the fourth part another promising system for optofluidic sensing was studied, namely liquid-filled photonic crystal fibers. These structures offer a much longer interaction length between the guided light and the infiltrated sample material, potentially resulting in higher detection sensitivities than possible with conventional free-space devices. The corresponding sensing performance was explored in numerical simulations as well as absorption and fluorescence measurements (Smolka *et al.* 2007a, 2007b). Thereby, several important figures of merit were identified, for the first time allowing the direct comparison of the detection efficiencies of different fiber designs (Barth *et al.* 2010a). A clear superiority of liquid-core devices in comparison to solid-core fibers could be demonstrated, enabling the reliable detection of molecular concentrations on the order of 10^{-9} M, outperforming previous implementations of fiber-based sensors by almost two orders of magnitude.

6.2 Outlook

It was the intention of this work to promote the development of novel building blocks for future nanophotonic and optofluidic devices. In large parts this goal could indeed be achieved. For example, the introduced nanoassembly method provides a powerful tool for the creation of hybrid nanophotonic structures, whose fabrication and investigation has not been possible so far. Also, the theoretical analysis of optical traps near photonic crystal cavities has inspired recent experimental work on this topic [297]. On the other hand, silicon nitride photonic crystals turned out to be not very well suited for cavity QED experiments due to their large intrinsic emission.

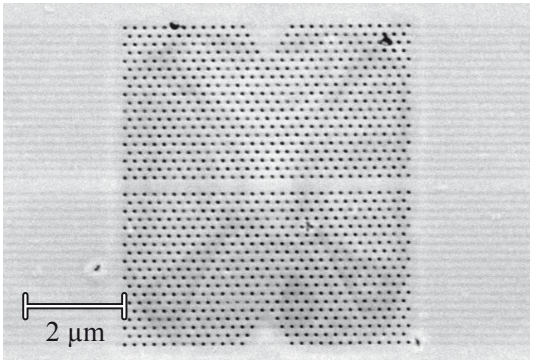

Figure 6.1: Scanning electron microscope image of one of the first gallium phosphide double-heterostructure cavities. The lattice constant and membrane thickness are 200 nm and 70 nm, respectively.

Likewise, the full potential of photonic crystal fiber sensors based on the liquid-core design was hampered by background fluorescence. Thus, not all approaches used within this thesis will persist in future implementations of similar systems. In the following, ways to tackle some of the existing problems are discussed and a number of ideas for further experiments and applications is collected, whose realization should be feasible by exploiting the methods and findings presented in this thesis.

As was already stated in Sec. 2.6, gallium phosphide is a promising material system for the fabrication of photonic crystal structures in the visible, providing a high refractive index ($n \approx 3.4$) and low intrinsic fluorescence. Consequently, large improvements in the device performance may readily be achieved by using gallium phosphide instead of silicon nitride for the realization of the proposed hybrid elements. First attempts to fabricate corresponding double-heterostructure cavities which are capable of operating in the wavelength range 600–700 nm have already been successful (see Fig. 6.1). Once the current fabrication procedure has been optimized to reduce remaining structural imperfections, these devices will allow for a whole series of cavity QED experiments with single NV defect centers.

In the field of solid-state cavity QED each new approach has to compete with the great achievements in semiconductor systems, which usually employ self-assembled quantum dots as emitters. In this regard, the state-of-the-art concerning defect centers in diamond is still behind, but their unique optical properties offer great potentials for applications in quantum information processing [344] and communication [345] which are currently beyond the capabilities of semiconductor quantum dots. In the case of NV defect centers, this includes the possibility for operation at room temperature as well as the existence of a triplet ground state with ultra-long spin coherence times on the order of 10^{-5}–10^{-3} s, which would allow for a multitude of spin qubit operations before dephasing processes destroy the coherent state. Two recent proposals for the implementation of cavity-enhanced quantum devices based

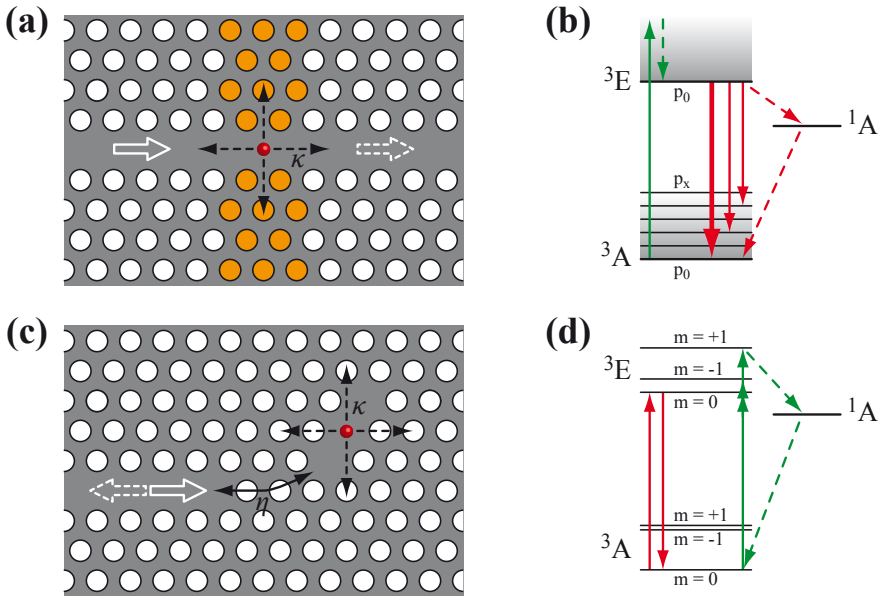

Figure 6.2: **(a)** Schematic illustration of a (high-Q) cavity-enhanced single photon source based on a single NV center. **(b)** Corresponding scheme showing the relevant energy level structure of the NV center. While excitation (green) occurs non-resonantly, the emission (red) is strongly enhanced at the frequency of the zero phonon transition ${}^3\mathrm{A}_{\mathrm{p}_0} \leftrightarrow {}^3\mathrm{E}_{\mathrm{p}_0}$ (thick arrow) due to resonant coupling to the cavity mode, effectively suppressing emission into phonon sidebands (thin arrows) and non-radiative decay channels (dashed arrows). **(c)** Schematic illustration of a (low-Q) cavity-enhanced spin measurement on a single NV center. **(d)** Corresponding scheme showing the relevant energy level structure of the NV center. The system is prepared into the spin state $m = 0$ through illumination with a broad-band laser (green) and the spin state is probed via a narrow-band laser (red) in resonance with the transition ${}^3\mathrm{A}_{m=0} \leftrightarrow {}^3\mathrm{E}_{m=0}$.

on NV defect centers might be realized using gallium phosphide photonic crystal structures and diamond nanocrystals, as is described in the following.

First, a high performance single photon source for linear optical quantum computing and quantum key distribution was proposed by Su *et al.* [346], exploiting the resonant coupling to a photonic crystal cavity mode to enhance the zero phonon transition of the NV center, while suppressing all other decay channels (see Fig. 6.2b). This requires operation in the so-called strong Purcell regime $\kappa > g \gg \gamma$ (see Sec. 2.2.5), which can be achieved using a double-heterostructure cavity design with a quality factor Q on the order of 10^4–10^5 and a precisely positioned diamond nanocrystal (see Fig. 6.2a). Thereby, the cavity may be tuned through the deposition of additional nanoscopic particles, as described in Sec. 3.5.2.

Second, a scheme for a quantum non-demolition measurement of the spin state of the NV center was proposed by Young *et al.* [347], using the reflection signal from a waveguide-coupled photonic crystal cavity (see Fig. 6.2c) to distinguish between the spin states $m = 0$ and $m = \pm 1$ while keeping the probability for a spin flip extremely small. This requires only low (total) quality factors $Q \approx 50$ and large

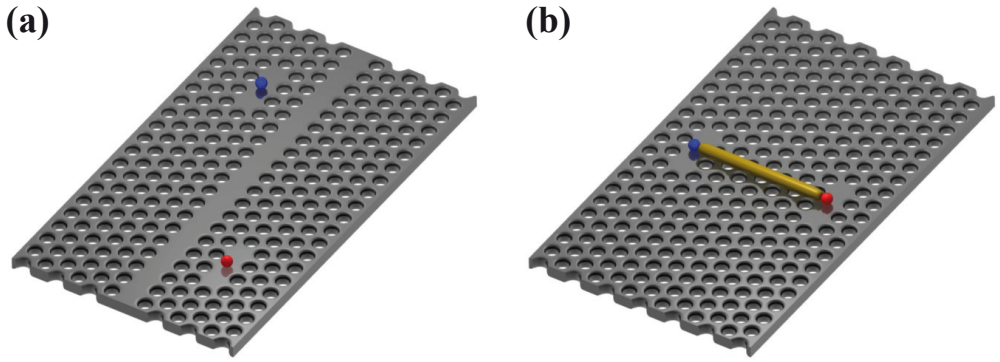

Figure 6.3: **(a)** Illustration of two emitters coupled to separate cavities which are link via a photonic crystal waveguide. **(b)** Corresponding implementation using a metal nanowire to connect both cavities.

cavity-waveguide coupling constants $\eta \approx 50\kappa$, which should readily be achievable with established cavity and waveguide designs. Note that this approach not only allows for a read-out of the spin state, but also for an initialization of the latter by employing a broad-band laser in addition to the probe laser (see Fig. 6.2d), and therefore constitutes an important building block for storing and processing quantum information.

Even the most fundamental schemes in quantum information processing require photons to be transferred between individual emitters/cavities in a coherent way [344], a problem which has not been tackled so far. Also in this regard the presented nanoassembly technique can open routes for the realization of such systems, since it is much more versatile than lithographic methods alone. First experiments may investigate the (incoherent) energy transfer from a donor cavity (containing one type of emitter) to an acceptor cavity (containing a second type of emitter) linked via a photonic crystal waveguide (see Fig. 6.3a). This would allow the exploration of various design strategies for optimal emitter-emitter coupling. In a second stage one might then target the coherent coupling regime with identical types of emitters, enabling, e.g., the creation of entangled states [348]. This, however, requires methods to energetically tune the individual constituents (cavities and emitters) relative to each other. With regard to NV defect centers, such a tuning can be facilitated by incorporating small electrodes near each cavity in order to locally induce a corresponding Stark shift [177].

Apart from pure dielectric photonic crystal structures, one might also envisage the combination with plasmonic components, e.g., to efficiently couple separate emitters as shown in Fig. 6.3b. Considerable progress has recently been made concerning low-loss metal-dielectric hybrid waveguides [349, 350] and also the conversion of single photons into single propagating plasmons (and *vice versa*) has successfully been demonstrated [351, 352]. Experiments to facilitate such a coupling in a con-

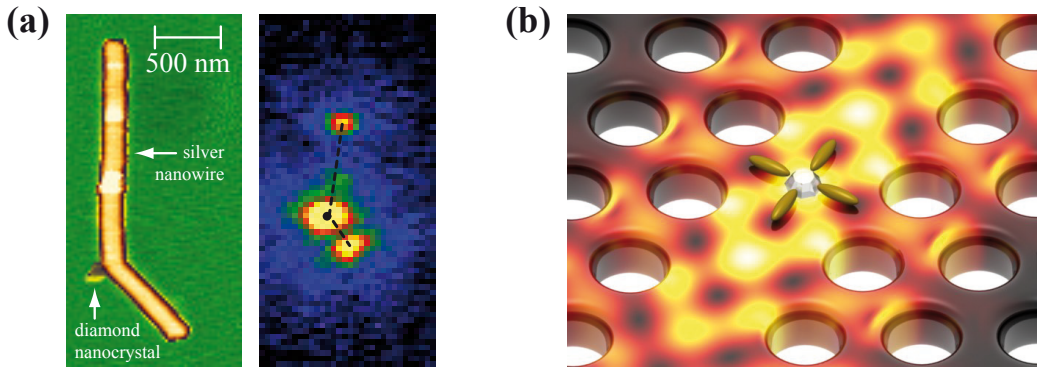

Figure 6.4: **(a)** AFM (left) and corresponding fluorescence image (right) of a silver nanowire (100 nm in diameter, 2.8 µm in length) to which a diamond nanocrystal (containing a single NV defect center) is coupled. The dashed line and the black dot in the fluorescence image indicate the silver nanowire and the diamond nanocrystal, respectively, the latter being locally excited. Note the fluorescence signal at both ends of the nanowire, resulting from the plasmon-mediated single photon emission of the NV center. **(b)** Illustration of a diamond nanocrystal coupled to a photonic crystal cavity with cross-resonant optical antenna.

trolled manner using nanoassembled diamond nanocrystals and metal nanowires are currently in progress (see Fig. 6.4a). The implementation of similar systems in combination with photonic crystal cavities and waveguides is within reach and would pave the way to a whole new class of optoplasmonic devices, merging the broad spectral response and extreme field localization of metal nanostructures with the narrow resonances of dielectric cavities.

As discussed in Sec. 3.6, most of these optoplasmonic structures feature a strong inherent polarization selectivity, which is certainly advantageous in some cases, but may be undesired in others. Therefore, novel plasmonic designs should be tested which allow a polarization-independent excitation and coupling to the cavity modes. A promising candidate for this purpose is the cross-resonant optical antenna proposed by Biagioni *et al.* [353], which can be realized by assembling individual metal nanorods on the photonic crystal surface as shown in Fig. 6.4b. Such a geometry may be employed to boost the excitation and radiative rate of NV centers with arbitrary dipole orientations and facilitate the simultaneous coupling to different cavity modes.

Apart from applications in quantum computing and communication, plasmonic-photonic hybrid cavities are also appealing for the realization of novel sensing devices, exploiting, e.g., the surface-enhanced Raman signal generated in hot spots near the metal nanostructures. If such a system is embedded in a microfluidic environment, the associated strongly localized electromagnetic fields may further be used to enhance the optical forces acting on nanoscopic particles (see Chapter 4). Such a scheme represents a fusion of so far distinct approaches relying on trapping near

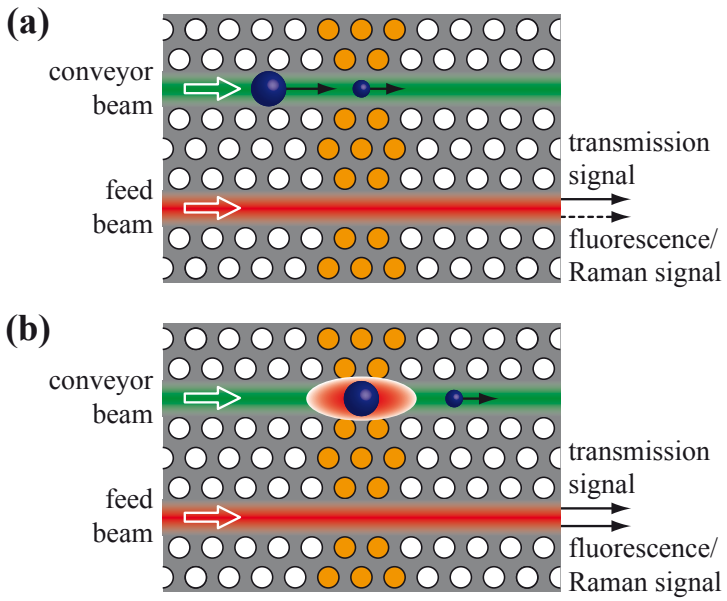

Figure 6.5: Schematic illustration of a photonic crystal trapping device for optofluidic sensing, featuring a conveyor waveguide which includes the trapping cavity and a feed waveguide which serves as input and collection channel. The feed beam (red) is detuned from the cavity resonance to enable the self-induced trapping of large particles. **(a)** Situation if no or only small particles are close to the cavity. No resonant enhancement of the feed beam occurs, hence no stable trapping is possible. **(b)** Situation if a large particle comes close to the cavity. The induced resonance shift enables a resonant enhancement of the feed beam, leading to a strong trapping force. The generated fluorescence/Raman light is collected through the feed waveguide.

plasmonic structures [270] and photonic crystal cavities [297], respectively, and potentially enables the simultaneous trapping and detection of single macromolecules with sizes on the order of 10 nm or below.

Also with regard to larger particles devices based on photonic crystals provide novel means to realize sophisticated optofluidic sensing schemes. One particular example, which was briefly discussed at the end of Sec. 4.4, is a fully integrated and automated particle detection and measurement system, which should be realizable with state-of-the-art technology and whose functionality shall be outlined in some more detail in the following (see Fig. 6.5). The key element is a double-heterostructure cavity constituting the optical trap. The associated waveguide simultaneously acts as a particle conveyor when light of an appropriate frequency (which is able to propagate through the waveguide and cavity regions) is coupled in. The cavity itself is fed through a second, evanescently coupled waveguide, being somewhat wider than the first one in order to guide light near the resonance frequency of the cavity.

The basic idea is now to inject light into the feed waveguide which is slightly detuned from the cavity resonance and monitor the corresponding transmission signal. If no or only small particles cross the cavity on the conveyor waveguide, the power

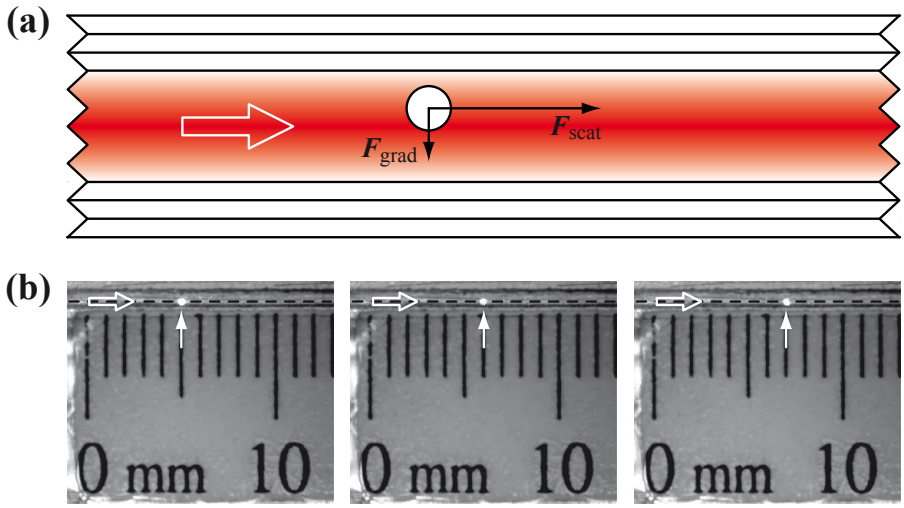

Figure 6.6: **(a)** Schematic illustration of the optical forces acting upon a dielectric particle in a liquid-core photonic crystal fiber. **(b)** Sequence of optical microscope images showing a 2 µm polystyrene particle (marked by arrows) which is propelled through a liquid-core fiber (indicated by dashed lines) filled with ethanol.

coupled into the cavity is insufficient to produce a strong trapping field (Fig. 6.5a). If a larger particle approaches, it shifts the cavity into resonance with the feed laser, leading to a resonant enhancement of the trapping field (Fig. 6.5b) and a simultaneous drop in the transmission signal. Once a particle is pinned through this self-induced trapping process, its interaction with the strong cavity field leads to the generation of a corresponding fluorescence or Raman signal, a fraction of which can be collected through the feed waveguide. Consequently, the device would not only be capable of detecting the presence of a particle (via the transmission signal), but may also allow for its identification. The whole procedure can be steered by switching the laser beams on and off as needed, enabling a whole series of trapping and measurement steps. It should be noted that the holey structure of this system would also allow the efficient removal of stuck particles by applying a sufficiently strong liquid flow through the photonic crystal membrane.

Apart from such micron-scaled optical traps, there has been growing interest in the application of optical forces in hollow-core photonic crystal fibers to transport particles over distances of several centimeters or more along well-defined pathways [354–356]. Thereby, the scattering force propels the particle in forward direction, while the gradient force draws it to the maximum of the intensity distribution inside the core (see Fig. 6.6a). Own first attempts to realize such a transport scheme in a liquid-core fiber were indeed successful (see Fig. 6.6b), but the achieved particle velocity was restricted to values on the order of 10 µm/s, being limited by collisions between the particle and the core wall. This can be prevented by designing the fiber for single-mode operation with a Gaussian-like intensity profile, as was demonstrated

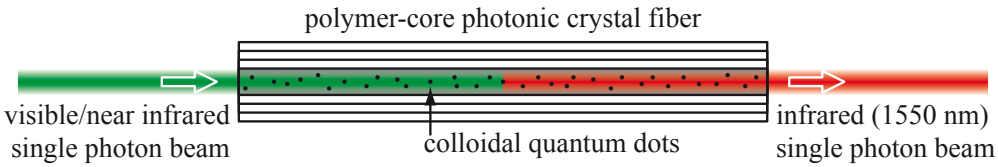

Figure 6.7: Schematic illustration of the single photon conversion principle. A beam of single photons in the visible/near infrared wavelength range is coupled into a photonic crystal fiber whose core is selectively filled with a mixture of polymer and colloidal quantum dots. The latter absorb the incoming photons and re-emit them at infrared wavelengths, thereby preserving the single photon statistics.

recently [356]. Combining such a transport scheme with the sensing capabilities of liquid-filled photonic crystal fibers (see Chapter 5) offers new possibilities for the manipulation, sorting, and investigation of biological particles in a continuous flow.

Finally, a somewhat different application of selectively infiltrated hollow-core photonic crystal fibers shall be outline, namely their use as a tool to convert the wavelength of single photons via an efficient absorption and re-emission process. Such a scheme is particularly appealing with regard to the spectral region around 1550 nm, where the performance of existing single photon sources is rather limited. In principle, individual lead chalcogenide colloidal quantum dots (such as PbS or PbSe) can provide single photons in this wavelength range, but they are not photostable over longer periods of time [357]. In the visible, however, such stable sources are available in the form of defect centers in diamond. Thus, the basic idea is to launch these visible photons into a photonic crystal fiber whose core is selectively filled with a mixture of polymer and colloidal quantum dots (see Fig. 6.7). The latter absorb the incoming photons with almost 100% probability (due to the long interaction length) and the resulting (infrared) fluorescence emission is collected with relatively high efficiency due to the large numerical aperture of the polymer-core fiber (see Sec. 5.4.2). Thereby, the single photon statistics is preserved as long as the decay rate of the quantum dots is considerably faster than the photon rate of the incoming beam. Assuming a fluorescence quantum yield of ≈ 0.5, a total conversion efficiency on the order of 5% should be feasible with such a device.

The above-mentioned proposals represent only a small selection of what might be possible in this exciting field on the borderline between nanophotonics, plasmonics, and optofluidics. A vast range of other experiments and applications can be envisaged, and almost daily novel findings broaden the available toolbox of materials, fabrication techniques, and characterization methods. Which of the approaches will turn out fruitful is hard to predict, as new ideas often find surprising applications in areas other than those initially intended. So the best way is to keep on exploring. Let's see what comes out!

Appendix A

Dielectric function of gold

For all calculations within this thesis involving gold structures, the values assumed for the corresponding dielectric function were taken from Johnson *et al.* [358]. A plot of the real and imaginary part of this function is shown in Fig. A.1, together with the respective curves obtained from the simple Drude model [see Eq. (3.15)].

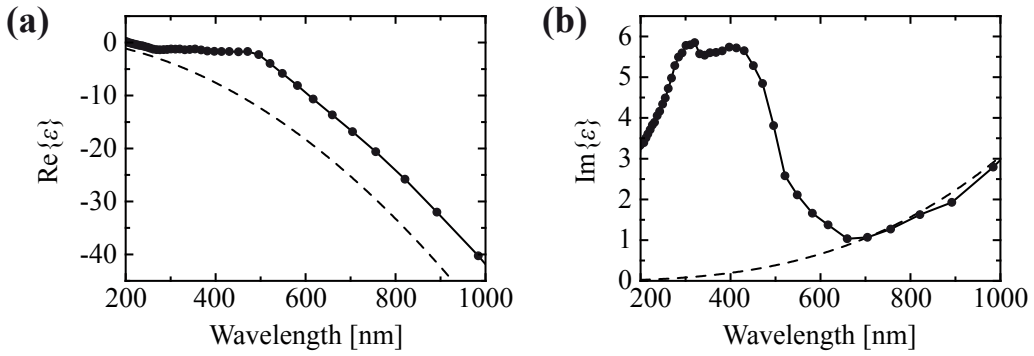

Figure A.1: **(a)** Real part and **(b)** imaginary part of the dielectric function of gold according to Ref. [358] (symbols). The dashed curves represent the corresponding values derived from the Drude model [Eq. (3.15)], assuming $\omega_\mathrm{p} = 1.38 \times 10^{15}$ s^{-1} and $\kappa = 1.075 \times 10^{14}$ s^{-1} [182].

Appendix B

Synthesis and optical properties of gold nanorods

The gold nanorods employed in Chapter 3 were synthesized in batch according to Ref. [359]. 12 µL of preformed small spherical seeds were added to a growth solution containing 5 mL deionized water, 50 µL $HAuCl_4$ (0.1 M, Sigma-Aldrich), 20 µL $AgNO_3$ (0.04 M, Sigma-Aldrich), 70 µL of a mild reducing agent (l-ascorbic acid, 0.0788 M, Sigma-Aldrich), and 5 mL cetyl-trimethyl-ammonium bromide (CTAB, 0.2 M, Sigma-Aldrich) as surfactant.

A typical transmission electron microscope image of the synthesized nanorods is shown in Fig. B.1a. From a statistical analysis the mean diameter and length of the nanorods is determined as (17 ± 2) nm and (56 ± 11) nm, respectively. A corresponding extinction spectrum from an ensemble measurement (in aqueous solution) is displayed in Fig. B.1b, revealing a maximum of the plasmon resonance at a wavelength of 727 nm.

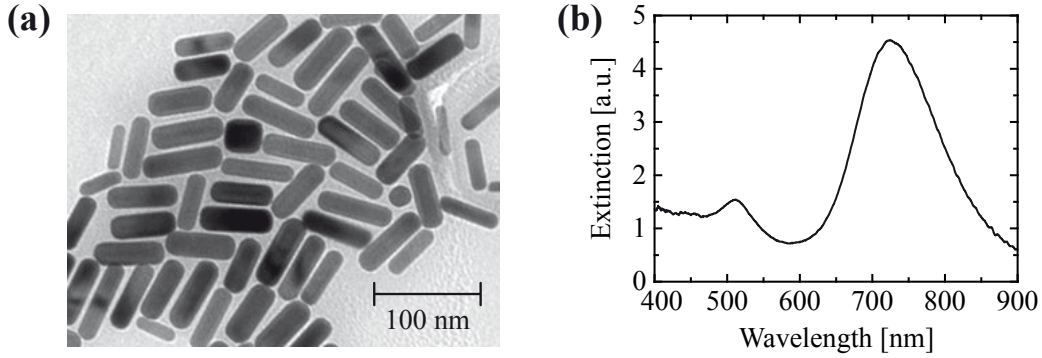

Figure B.1: **(a)** Transmission electron microscope image of the synthesized gold nanorods. **(b)** Corresponding extinction spectrum in aqueous solution.

Acknowledgement

This is it. It's finally done. Mission accomplished.

It has taken a long time, much longer than I would have dared to believe at the beginning of this thesis. But, on the other hand, good things come to those who wait. And I can say that, after all, I'm satisfied with the result. So here and now is the time to thank all those people who contributed to this work or supported me in other ways during 4 1/2 years of constant joy and pleasure (with short periods of lesser joy and pleasure).

First of all, I have to express my deep gratitude to Prof. Oliver Benson, who guided me through all these years, always providing advice and, most importantly, fresh ideas if needed. Fortunately, I was able to implement at least some of them.

I further want to thank my dear former diploma/bachelor students Stephan Smolka, Johannes Stingl, and Sebastian Knauer, who contributed a lot to the work presented in this thesis. The same holds for Stefan Schietinger, without whom diamonds would never have shone so brightly.

My gratitude also goes to our collaborators Josef Kouba, Nils Nüsse, and Dr. Bernd Löchel at the Helmholtz-Centre Berlin for Materials and Energy, who mastered the art of making a lot of tiny holes, as well as Jan Becker and Prof. Carsten Sönnichsen at the University of Mainz, who know how gold likes to be treated.

Dr. Thomas Aichele and Andreas Schell provided some nice prospects for future plasmonic research, for which a want to thank them. Tim Schröder took over my old lab and had the decency not to rebuild everything. Thank you and good luck!

This is where the scientific part ends. The other part was mainly occupied by my dear office colleagues Malte Schmidt, Alex Senger, and Moritz Nagel, who saw to it that there was enough chit-chat to lengthen my graduation by, roughly speaking, 4 years. Admittedly, this is not totally fair, since there were also my *other* colleagues, let's call them Gesine S., Alex K., Katharina M., Markus K., Klaus K., Matthias H., Martin G., Björn L., Andrea M., Rico H., Markus G., and Mr. Coffee (who always made my tea). Yes, we had a lot of fun. But my very special thanks go to Matthias "Granatsplitter" Leifgen and the (anonymous) Quark maker at the local cafeteria, who both helped me keeping my spirits high.

Finally, I want to thank my beloved Sabine, who gave me so much in this last year, and my family, who constantly reminded me that I should finish my thesis and find a decent job.

Thank you all so very much!

Bibliography

[1] E. Yablonovitch. Inhibited spontaneous emission in solid-state physics and electronics. *Phys. Rev. Lett.*, 58(20):2059–2062, 1987.

[2] S. John. Strong localization of photons in certain disordered dielectric superlattices. *Phys. Rev. Lett.*, 58(23):2486–2489, 1987.

[3] S. Noda, M. Fujita, and T. Asano. Spontaneous-emission control by photonic crystals and nanocavities. *Nature Photon.*, 1(8):449–458, 2007.

[4] C. H. Bennett and D. P. DiVincenzo. Quantum information and computation. *Nature*, 404(6775):247–255, 2000.

[5] E. Knill, R. Laflamme, and G. J. Milburn. A scheme for efficient quantum computation with linear optics. *Nature*, 409(6816):46–52, 2001.

[6] F. Jelezko and J. Wrachtrup. Single defect centres in diamond: A review. *Phys. Status Solidi A*, 203(13):3207–3225, 2006.

[7] W. L. Barnes, A. Dereux, and T. W. Ebbesen. Surface plasmon subwavelength optics. *Nature*, 424(6950):824–830, 2003.

[8] D. Psaltis, S. R. Quake, and C. Yang. Developing optofluidic technology through the fusion of microfluidics and optics. *Nature*, 442(7101):381–386, 2006.

[9] C. Monat, P. Domachuk, and B. J. Eggleton. Integrated optofluidics: A new river of light. *Nature Photon.*, 1(2):106–114, 2007.

[10] J. C. Knight. Photonic crystal fibres. *Nature*, 424(6950):847–851, 2003.

[11] P. S. J. Russell. Photonic crystal fibers. *Science*, 299(5605):358–362, 2003.

[12] O. Painter, R. K. Lee, A. Scherer, A. Yariv, J. D. O'Brien, P. D. Dapkus, and I. Kim. Two-dimensional photonic band-gap defect mode laser. *Science*, 284 (5421):1819–1821, 1999.

[13] K. Nozaki, S. Kita, and T. Baba. Room temperature continuous wave operation and controlled spontaneous emission in ultrasmall photonic crystal nanolaser. *Opt. Express*, 15(12):7506–7514, 2007.

[14] S. Laurent, S. Varoutsis, L. Le Gratiet, A. Lemaître, I. Sagnes, F. Raineri, A. Levenson, I. Robert-Philip, and I. Abram. Indistinguishable single photons from a single-quantum dot in a two-dimensional photonic crystal cavity. *Appl. Phys. Lett.*, 87(16):163107, 2005.

[15] J. Vučković, D. Englund, D. Fattal, E. Waks, and Y. Yamamoto. Generation and manipulation of nonclassical light using photonic crystals. *Physica E*, 32 (1–2):466–470, 2006.

[16] T. Yoshie, A. Scherer, J. Hendrickson, G. Khitrova, H. M. Gibbs, G. Rupper, C. Ell, O. B. Shchekin, and D. G. Deppe. Vacuum Rabi splitting with a single quantum dot in a photonic crystal nanocavity. *Nature*, 432(7014):200–203, 2004.

[17] K. Hennessy, A. Badolato, M. Winger, D. Gerace, M. Atatüre, S. Gulde, S. Fält, E. L. Hu, and A. Imamoğlu. Quantum nature of a strongly coupled single quantum dot-cavity system. *Nature*, 445(7130):896–899, 2007.

[18] D. Englund, D. Fattal, E. Waks, G. Solomon, B. Zhang, T. Nakaoka, Y. Arakawa, Y. Yamamoto, and J. Vučković. Controlling the spontaneous emission rate of single quantum dots in a two-dimensional photonic crystal. *Phys. Rev. Lett.*, 95(1):013904, 2005.

[19] A. Badolato, K. Hennessy, M. Atatüre, J. Dreiser, E. Hu, P. M. Petroff, and A. Imamoğlu. Deterministic coupling of single quantum dots to single nanocavity modes. *Science*, 308(5725):1158–1161, 2005.

[20] A. Kress, F. Hofbauer, N. Reinelt, M. Kaniber, H. J. Krenner, R. Meyer, G. Bohm, and J. J. Finley. Manipulation of the spontaneous emission dynamics of quantum dots in two-dimensional photonic crystals. *Phys. Rev. B*, 71(24): 241304, 2005.

[21] W.-H. Chang, W.-Y. Chen, H.-S. Chang, T.-M. Hsu, T.-P. Hsieh, and J.-I. Chyi. Optical emission from individual InGaAs quantum dots in single-defect photonic crystal nanocavity. *J. Appl. Phys.*, 98(3):034306, 2005.

[22] I. Fushman, D. Englund, and J. Vučković. Coupling of PbS quantum dots to photonic crystal cavities at room temperature. *Appl. Phys. Lett.*, 87(24): 241102, 2005.

[23] M. Nomura, S. Iwamoto, T. Yang, S. Ishida, and Y. Arakawa. Enhancement of light emission from single quantum dot in photonic crystal nanocavity by using cavity resonant excitation. *Appl. Phys. Lett.*, 89(24):241124, 2006.

[24] R. Bose, X. Yang, R. Chatterjee, J. Gao, and C. W. Wong. Weak coupling interactions of colloidal lead sulphide nanocrystals with silicon photonic crystal nanocavities near 1.55 μm at room temperature. *Appl. Phys. Lett.*, 90(11): 111117, 2007.

[25] Z. Wu, Z. Mi, P. Bhattacharya, T. Zhu, and J. Xu. Enhanced spontaneous emission at 1.55 μm from colloidal PbSe quantum dots in a Si photonic crystal microcavity. *Appl. Phys. Lett.*, 90(17):171105, 2007.

[26] C. Meier, K. Hennessy, E. D. Haberer, R. Sharma, Y. S. Choi, K. McGroddy, S. Keller, S. P. DenBaars, S. Nakamura, and E. L. Hu. Visible resonant modes in GaN-based photonic crystal membrane cavities. *Appl. Phys. Lett.*, 88(3): 031111, 2006.

[27] Y. S. Choi, K. Hennessy, R. Sharma, E. Haberer, Y. Gao, S. P. DenBaars, S. Nakamura, E. L. Hu, and C. Meier. GaN blue photonic crystal membrane nanocavities. *Appl. Phys. Lett.*, 87(24):243101, 2005.

[28] M. Arita, S. Ishida, S. Kako, S. Iwamoto, and Y. Arakawa. AlN air-bridge photonic crystal nanocavities demonstrating high quality factor. *Appl. Phys. Lett.*, 91(5):051106, 2007.

[29] Z. Zhang, T. Yoshie, X. Zhu, J. Xu, and A. Scherer. Visible two-dimensional photonic crystal slab laser. *Appl. Phys. Lett.*, 89(7):071102, 2006.

[30] M. Kitamura, S. Iwamoto, and Y. Arakawa. Enhanced light emission from an organic photonic crystal with a nanocavity. *Appl. Phys. Lett.*, 87(15):151119, 2005.

[31] M. Makarova, J. Vučković, H. Sanda, and Y. Nishi. Silicon-based photonic crystal nanocavity light emitters. *Appl. Phys. Lett.*, 89(22):221101, 2006.

[32] J. D. Joannopoulos, S. G. Johnson, J. N. Winn, and R. D. Meade. *Photonic crystals: Molding the flow of light.* Princeton University Press, 2008.

[33] J. D. Jackson. *Classical electrodynamics.* John Wiley & Sons, 1999.

[34] N. W. Ashcroft and N. D. Mermin. *Solid state physics.* Thomson Learning, 1976.

[35] S. G. Johnson, S. H. Fan, P. R. Villeneuve, J. D. Joannopoulos, and L. A. Kolodziejski. Guided modes in photonic crystal slabs. *Phys. Rev. B*, 60(8): 5751–5758, 1999.

[36] J. S. Foresi, P. R. Villeneuve, J. Ferrera, E. R. Thoen, G. Steinmeyer, S. Fan, J. D. Joannopoulos, L. C. Kimerling, H. I . Smith, and E. P. Ippen. Photonic-bandgap microcavities in optical waveguides. *Nature*, 390(6656):143–145, 1997.

[37] S. Noda, A. Chutinan, and M. Imada. Trapping and emission of photons by a single defect in a photonic bandgap structure. *Nature*, 407(6804):608–610, 2000.

[38] S. M. Barnett and R. Loudon. Sum rule for modified spontaneous emission rates. *Phys. Rev. Lett.*, 77(12):2444–2446, 1996.

[39] E. Yablonovitch, T. J. Gmitter, R. D. Meade, A. M. Rappe, K. D. Brommer, and J. D. Joannopoulos. Donor and acceptor modes in photonic band structure. *Phys. Rev. Lett.*, 67(24):3380–3383, 1991.

[40] T. Yoshie, J. Vučković, A. Scherer, H. Chen, and D. Deppe. High quality two-dimensional photonic crystal slab cavities. *Appl. Phys. Lett.*, 79(26):4289–4291, 2001.

[41] K. Srinivasan, P. E. Barclay, O. Painter, J. X. Chen, A. Y. Cho, and C. Gmachl. Experimental demonstration of a high quality factor photonic crystal microcavity. *Appl. Phys. Lett.*, 83(10):1915–1917, 2003.

[42] H. Y. Ryu, M. Notomi, and Y. H. Lee. High-quality-factor and small-mode-volume hexapole modes in photonic-crystal-slab nanocavities. *Appl. Phys. Lett.*, 83(21):4294–4296, 2003.

[43] Y. Akahane, T. Asano, B.-S. Song, and S. Noda. High-Q photonic nanocavity in a two-dimensional photonic crystal. *Nature*, 425(6961):944–947, 2003.

[44] K. Srinivasan and O. Painter. Momentum space design of high-Q photonic crystal optical cavities. *Opt. Express*, 10(15):670–684, 2002.

[45] S. G. Johnson, P. R. Villeneuve, S. H. Fan, and J. D. Joannopoulos. Linear waveguides in photonic-crystal slabs. *Phys. Rev. B*, 62(12):8212–8222, 2000.

[46] S. Kuchinsky, D. C. Allan, N. F. Borrelli, and J.-C. Cotteverte. 3D localization in a channel waveguide in a photonic crystal with 2D periodicity. *Opt. Commun.*, 175(1–3):147–152, 2000.

[47] H. Gersen, T. J. Karle, R. J. P. Engelen, W. Bogaerts, J. P. Korterik, N. F. van Hulst, T. F. Krauss, and L. Kuipers. Real-space observation of ultraslow light in photonic crystal waveguides. *Phys. Rev. Lett.*, 94(7):073903, 2005.

[48] M. Soljačić and J. D. Joannopoulos. Enhancement of nonlinear effects using photonic crystals. *Nature Mater.*, 3(4):211–219, 2004.

[49] S. Hughes. Enhanced single-photon emission from quantum dots in photonic crystal waveguides and nanocavities. *Opt. Lett.*, 29(22):2659–2661, 2004.

[50] S. Hughes, L. Ramunno, J. F. Young, and J. E. Sipe. Extrinsic optical scattering loss in photonic crystal waveguides: Role of fabrication disorder and photon group velocity. *Phys. Rev. Lett.*, 94(3):033903, 2005.

[51] E. Kuramochi, M. Notomi, S. Mitsugi, A. Shinya, T. Tanabe, and T. Watanabe. Ultrahigh-Q photonic crystal nanocavities realized by the local width modulation of a line defect. *Appl. Phys. Lett.*, 88(4):041112, 2006.

[52] T. Tanabe, M. Notomi, E. Kuramochi, A. Shinya, and H. Taniyama. Trapping and delaying photons for one nanosecond in an ultrasmall high-Q photonic-crystal nanocavity. *Nature Photon.*, 1(1):49–52, 2007.

[53] S.-H. Kwon, T. Sünner, M. Kamp, and A. Forchel. Ultrahigh-Q photonic crystal cavity created by modulating air hole radius of a waveguide. *Opt. Express*, 16(7):4605–4614, 2008.

[54] S. Tomljenovic-Hanic, C. M. de Sterke, and M. J. Steel. Design of high-Q cavities in photonic crystal slab heterostructures by air-holes infiltration. *Opt. Express*, 14(25):12451–12456, 2006.

[55] C. L. C. Smith, D. K. C. Wu, M. W. Lee, C. Monat, S. Tomljenovic-Hanic, C. Grillet, B. J. Eggleton, D. Freeman, Y. Ruan, S. Madden, B. Luther-Davies, H. Giessen, and Y.-H. Lee. Microfluidic photonic crystal double heterostructures. *Appl. Phys. Lett.*, 91(12):121103, 2007.

[56] C. L. C. Smith, U. Bog, S. Tomljenovic-Hanic, M. W. Lee, D. K. C. Wu, L. O'Faolain, C. Monat, C. Grillet, T. F. Krauss, C. Karnutsch, R. C. McPhedran, and B. J. Eggleton. Reconfigurable microfluidic photonic crystal slab cavities. *Opt. Express*, 16(20):15887–15896, 2008.

[57] S. Tomljenovic-Hanic, M. J. Steel, C. M. de Sterke, and D. J. Moss. High-Q cavities in photosensitive photonic crystals. *Opt. Lett.*, 32(5):542–544, 2007.

[58] B.-S. Song, S. Noda, T. Asano, and Y. Akahane. Ultra-high-Q photonic double-heterostructure nanocavity. *Nature Mater.*, 4(3):207–210, 2005.

[59] B.-S. Song, S. Noda, and T. Asano. Photonic devices based on in-plane hetero photonic crystals. *Science*, 300(5625):1537, 2003.

[60] B.-S. Song, T. Asano, and S. Noda. Heterostructures in two-dimensional photonic-crystal slabs and their application to nanocavities. *J. Phys. D*, 40 (9):2629–2634, 2007.

[61] B.-S. Song, T. Asano, and S. Noda. Physical origin of the small modal volume of ultra-high-Q photonic double-heterostructure nanocavities. *New J. Phys.*, 8:209, 2006.

[62] A. Mock, L. Lu, and J. D. O'Brien. Spectral properties of photonic crystal double heterostructure resonant cavities. *Opt. Express*, 16(13):9391–9397, 2008.

[63] Y. Akahane, T. Asano, B.-S. Song, and S. Noda. Fine-tuned high-Q photonic-crystal nanocavity. *Opt. Express*, 13(4):1202–1214, 2005.

[64] S. Noda, K. Tomoda, N. Yamamoto, and A. Chutinan. Full three-dimensional photonic bandgap crystals at near-infrared wavelengths. *Science*, 289(5479): 604–606, 2000.

[65] K. Aoki, H. T. Miyazaki, H. Hirayama, K. Inoshita, T. Baba, K. Sakoda, N. Shinya, and Y. Aoyagi. Microassembly of semiconductor three-dimensional photonic crystals. *Nature Mater.*, 2(2):117–121, 2003.

[66] M. H. Qi, E. Lidorikis, P. T. Rakich, S. G. Johnson, J. D. Joannopoulos, E. P. Ippen, and H. I. Smith. A three-dimensional optical photonic crystal with designed point defects. *Nature*, 429(6991):538–542, 2004.

[67] S. G. Johnson, S. Fan, A. Mekis, and J. D. Joannopoulos. Multipole-cancellation mechanism for high-Q cavities in the absence of a complete photonic band gap. *Appl. Phys. Lett.*, 78(22):3388–3390, 2001.

[68] K. Srinivasan and O. Painter. Fourier space design of high-Q cavities in standard and compressed hexagonal lattice photonic crystals. *Opt. Express*, 11(6): 579–593, 2003.

[69] P. Lalanne, S. Mias, and J. P. Hugonin. Two physical mechanisms for boosting the quality factor to cavity volume ratio of photonic crystal microcavities. *Opt. Express*, 12(3):458–467, 2004.

[70] D. Englund, I. Fushman, and J. Vučković. General recipe for designing photonic crystal cavities. *Opt. Express*, 13(16):5961–5975, 2005.

[71] R. Coccioli, M. Boroditsky, K. W. Kim, Y. Rahmat-Samii, and E. Yablonovitch. Smallest possible electromagnetic mode volume in a dielectric cavity. *IEE Proc. Optoelectron.*, 145(6):391–397, 1998.

[72] S. Maier. Effective mode volume of nanoscale plasmon cavities. *Opt. Quant. Electron.*, 38(1–3):257–267, 2006.

[73] J. Bravo-Abad, A. Rodriguez, P. Bermel, S. G. Johnson, J. D. Joannopoulos, and Marin Soljačić. Enhanced nonlinear optics in photonic-crystal microcavities. *Opt. Express*, 15(24):16161–16176, 2007.

[74] K. J. Vahala. Optical microcavities. *Nature*, 424(6950):839–846, 2003.

[75] M. O. Scully and M. S. Zubairy. *Quantum optics*. Cambridge University Press, 1997.

[76] R. J. Glauber and M. Lewenstein. Quantum optics of dielectric media. *Phys. Rev. A*, 43(1):467–491, 1991.

[77] E. T. Jaynes and F. W. Cummings. Comparison of quantum and semiclassical radiation theories with application to the beam maser. *Proc. IEEE*, 51(1): 89–109, 1963.

[78] K. Vahala. *Optical microcavities*. World Scientific Publishing, 2004.

[79] V. Weisskopf and E. Wigner. Berechnung der natürlichen Linienbreite auf Grund der Diracschen Lichttheorie. *Z. Phys. A*, 63:54–73, 1930.

[80] P. A. M. Dirac. The quantum theory of emission and absorption of radiation. *Proc. Roy. Soc. Lond. A*, 114(767):243–265, 1927.

[81] M. Boroditsky, R. Vrijen, T. F. Krauss, R. Coccioli, R. Bhat, and E. Yablonovitch. Spontaneous emission extraction and Purcell enhancement from thin-film 2-D photonic crystals. *J. Lightwave Technol.*, 17(11):2096–2112, 1999.

[82] E. M. Purcell. Spontaneous emission probabilities at radio frequencies. *Phys. Rev.*, 69:681, 1946.

[83] R. J. Thompson, G. Rempe, and H. J. Kimble. Observation of normal-mode splitting for an atom in an optical cavity. *Phys. Rev. Lett.*, 68(8):1132–1135, 1992.

[84] L. C. Andreani, G. Panzarini, and J. M. Gérard. Strong-coupling regime for quantum boxes in pillar microcavities: Theory. *Phys. Rev. B*, 60(19):13276–13279, 1999.

[85] A. Beveratos, R. Brouri, T. Gacoin, A. Villing, J.-P. Poizat, and P. Grangier. Single photon quantum cryptography. *Phys. Rev. Lett.*, 89(18):187901, 2002.

[86] E. Waks, K. Inoue, C. Santori, D. Fattal, J. Vučković, G. S. Solomon, and Y. Yamamoto. Secure communication: Quantum cryptography with a photon turnstile. *Nature*, 420(6917):762, 2002.

[87] D. Bouwmeester, J. W. Pan, K. Mattle, M. Eibl, H. Weinfurter, and A. Zeilinger. Experimental quantum teleportation. *Nature*, 390(6660):575–579, 1997.

[88] C. Santori, D. Fattal, J. Vučković, G. S. Solomon, and Y. Yamamoto. Indistinguishable photons from a single-photon device. *Nature*, 419(6907):594–597, 2002.

[89] W.-H. Chang, W.-Y. Chen, H.-S. Chang, T.-P. Hsieh, J.-I. Chyi, and T.-M. Hsu. Efficient single-photon sources based on low-density quantum dots in photonic-crystal nanocavities. *Phys. Rev. Lett.*, 96(11):117401, 2006.

[90] D. Englund, A. Faraon, B. Zhang, Y. Yamamoto, and J. Vučković. Generation and transfer of single photons on a photonic crystal chip. *Opt. Express*, 15(9): 5550–5558, 2007.

[91] D. Press, S. Götzinger, S. Reitzenstein, C. Hofmann, A. Löffler, M. Kamp, A. Forchel, and Y. Yamamoto. Photon antibunching from a single quantum-dot-microcavity system in the strong coupling regime. *Phys. Rev. Lett.*, 98 (11):117402, 2007.

[92] G. Björk, A. Karlsson, and Y. Yamamoto. Definition of a laser threshold. *Phys. Rev. A*, 50(2):1675–1680, 1994.

[93] M. Lončar, T. Yoshie, A. Scherer, P. Gogna, and Y. M. Qiu. Low-threshold photonic crystal laser. *Appl. Phys. Lett.*, 81(15):2680–2682, 2002.

[94] S. Strauf, K. Hennessy, M. T. Rakher, Y. S. Choi, A. Badolato, L. C. Andreani, E. L. Hu, P. M. Petroff, and D. Bouwmeester. Self-tuned quantum dot gain in photonic crystal lasers. *Phys. Rev. Lett.*, 96(12):127404, 2006.

[95] M. Nomura, S. Iwamoto, N. Kumagai, and Y. Arakawa. Ultra-low threshold photonic crystal nanocavity laser. *Physica E*, 40(6):1800–1803, 2008.

[96] C. Monroe. Quantum information processing with atoms and photons. *Nature*, 416(6877):238–246, 2002.

[97] L.-M. Duan and H. J. Kimble. Scalable photonic quantum computation through cavity-assisted interactions. *Phys. Rev. Lett.*, 92(12):127902, 2004.

[98] G. Nogues, A. Rauschenbeutel, S. Osnaghi, M. Brune, J. M. Raimond, and S. Haroche. Seeing a single photon without destroying it. *Nature*, 400(6741): 239–242, 1999.

[99] K. M. Birnbaum, A. Boca, R. Miller, A. D. Boozer, T. E. Northup, and H. J. Kimble. Photon blockade in an optical cavity with one trapped atom. *Nature*, 436(7047):87–90, 2005.

[100] D. Englund, A. Faraon, I. Fushman, N. Stoltz, P. Petroff, and J. Vučković. Controlling cavity reflectivity with a single quantum dot. *Nature*, 450(7171): 857–861, 2007.

[101] I. Fushman, D. Englund, A. Faraon, N. Stoltz, P. Petroff, and J. Vučković. Controlled phase shifts with a single quantum dot. *Science*, 320(5877):769–772, 2008.

[102] M. Modreanu, N. Tomozeiu, P. Cosmin, and M. Gartner. Optical properties of LPCVD silicon oxynitride. *Thin Solid Films*, 337(1–2):82–84, 1999.

[103] J. Kouba. *Investigation of silicon nitride based two-dimensional photonic crystals for the visible spectral range.* PhD thesis, Technische Universität Berlin, 2008.

[104] S. V. Deshpande, E. Gulari, S. W. Brown, and S. C. Rand. Optical properties of silicon nitride films deposited by hot filament chemical vapor deposition. *J. Appl. Phys.*, 77(12):6534–6541, 1995.

[105] S. G. Johnson and J. D. Joannopoulos. Block-iterative frequency-domain methods for Maxwell's equations in a planewave basis. *Opt. Express*, 8(3): 173–190, 2001.

[106] K. Yee. Numerical solution of initial boundary value problems involving Maxwell's equations in isotropic media. *IEEE Trans. Antennas Propagat.*, 44(3):302–307, 1966.

[107] O. Hess, C. Hermann, and A. Klaedtke. Finite-difference time-domain simulations of photonic crystal defect structures. *Phys. Status Solidi A*, 197(3): 605–619, 2003.

[108] A. F. Koenderink, M. Kafesaki, C. M. Soukoulis, and V. Sandoghdar. Spontaneous emission rates of dipoles in photonic crystal membranes. *J. Opt. Soc. Am. B*, 23(6):1196–1206, 2006.

[109] A. R. A. Chalcraft, S. Lam, D. O'Brien, T. F. Krauss, M. Sahin, D. Szymanski, D. Sanvitto, R. Oulton, M. S. Skolnick, A. M. Fox, D. M. Whittaker, H. Y. Liu, and M. Hopkinson. Mode structure of the L3 photonic crystal cavity. *Appl. Phys. Lett.*, 90(24):241117, 2007.

[110] Y. Ruan, M.-K. Kim, Y.-H. Lee, B. Luther-Davies, and A. Rode. Fabrication of high-Q chalcogenide photonic crystal resonators by e-beam lithography. *Appl. Phys. Lett.*, 90(7):071102, 2007.

[111] A. M. Adawi, A. R. A. Chalcraft, D. M. Whittaker, and D. G. Lidzey. Refractive index dependence of L3 photonic crystal nano-cavities. *Opt. Express*, 15 (22):14299–14305, 2007.

[112] Y. Tanaka, T. Asano, Y. Akahane, B.-S. Song, and S. Noda. Theoretical investigation of a two-dimensional photonic crystal slab with truncated cone air holes. *Appl. Phys. Lett.*, 82(11):1661–1663, 2003.

[113] M.-K. Kim, J.-K. Yang, Y.-H. Lee, and I.-K. Hwang. Influence of etching slope on two-dimensional photonic crystal slab resonators. *J. Korean Phys. Soc.*, 50 (4):1027–1031, 2007.

[114] T. Asano, B.-S. Song, and S. Noda. Analysis of the experimental Q factors ($\sim$ 1 million) of photonic crystal nanocavities. *Opt. Express*, 14(5):1996–2002, 2006.

[115] P. Strasser, F. Robin, C. F. Carlström, R. Wüest, R. Kappeler, and H. Jäckel. Sidewall roughness measurement inside photonic crystal holes by atomic force microscopy. *Nanotechnol.*, 18(40):405703, 2007.

[116] S. H. Kim, G. H. Kim, S. K. Kim, H. G. Park, Y. H. Lee, and S. B. Kim. Characteristics of a stick waveguide resonator in a two-dimensional photonic crystal slab. *J. Appl. Phys.*, 95(2):411–416, 2004.

[117] W. C. Stumpf, M. Fujita, M. Yamaguchi, T. Asano, and S. Noda. Light-emission properties of quantum dots embedded in a photonic double-heterostructure nanocavity. *Appl. Phys. Lett.*, 90(23):231101, 2007.

[118] H. Hagino, Y. Takahashi, Y. Tanaka, T. Asano, and S. Noda. Effects of fluctuation in air hole radii and positions on optical characteristics in photonic crystal heterostructure nanocavities. *Phys. Rev. B*, 79(8):085112, 2009.

[119] I. Bayn and J. Salzman. Ultra high-Q photonic crystal nanocavity design: The effect of a low-ε slab material. *Opt. Express*, 16(7):4972–4980, 2008.

[120] H.-G. Park, C. J. Barrelet, Y. Wu, B. Tian, F. Qian, and C. M. Lieber. A wavelength-selective photonic-crystal waveguide coupled to a nanowire light source. *Nature Photon.*, 2(10):622–626, 2008.

[121] F. de Angelis, M. Patrini, G. Das, I. Maksymov, M. Galli, L. Businaro, L. C. Andreani, and E. di Fabrizio. A hybrid plasmonic-photonic nanodevice for label-free detection of a few molecules. *Nano Lett.*, 8(8):2321–2327, 2008.

[122] M. W. McCutcheon and M. Lončar. Design of a silicon nitride photonic crystal nanocavity with a quality factor of one million for coupling to a diamond nanocrystal. *Opt. Express*, 16(23):19136–19145, 2008.

[123] S. Tomljenovic-Hanic, M. J. Steel, C. M de Sterke, and J. Salzman. Diamond based photonic crystal microcavities. *Opt. Express*, 14(8):3556–3562, 2006.

[124] C. Kreuzer, J. Riedrich-Möller, E. Neu, and C. Becher. Design of photonic crystal microcavities in diamond films. *Opt. Express*, 16(3):1632–1644, 2008.

[125] C. F. Wang, Y.-S. Choi, J. C. Lee, E. L. Hu, J. Yang, and J. E. Butler. Observation of whispering gallery modes in nanocrystalline diamond microdisks. *Appl. Phys. Lett.*, 90(8):081110, 2007.

[126] C. F. Wang, R. Hanson, D. D. Awschalom, E. L. Hu, T. Feygelson, J. Yang, and J. E. Butler. Fabrication and characterization of two-dimensional photonic crystal microcavities in nanocrystalline diamond. *Appl. Phys. Lett.*, 91(20): 201112, 2007.

[127] K. Rivoire, A. Faraon, and J. Vučković. Gallium phosphide photonic crystal nanocavities in the visible. *Appl. Phys. Lett.*, 93(6):063103, 2008.

[128] D. F. Nelson and E. H. Turner. Electro-optic and piezoelectric coefficients and refractive index of gallium phosphide. *J. Appl. Phys.*, 39(7):3337–3343, 1968.

[129] K. Rivoire, A. Kinkhabwala, F. Hatami, W. T. Masselink, Y. Avlasevich, K. Müllen, W. E. Moerner, and J. Vučković. Lithographic positioning of fluorescent molecules on high-Q photonic crystal cavities. *Appl. Phys. Lett.*, 95(12):123113, 2009.

[130] A. M. Zaitsev. *Optical properties of diamond.* Springer, 2001.

[131] A. Gruber, A. Dräbenstedt, C. Tietz, L. Fleury, J. Wrachtrup, and C. von Borczyskowski. Scanning confocal optical microscopy and magnetic resonance on single defect centers. *Science*, 276(5321):2012–2014, 1997.

[132] J. Wrachtrup and F. Jelezko. Processing quantum information in diamond. *J. Phys.: Condens. Matter*, 18(21):S807–S824, 2006.

[133] Y. Mita. Change of absorption spectra in type-Ib diamond with heavy neutron irradiation. *Phys. Rev. B*, 53(17):11360–11364, 1996.

[134] A. Lenef, S. W. Brown, D. A. Redman, S. C. Rand, J . Shigley, and E. Fritsch. Electronic structure of the N-V center in diamond: Experiments. *Phys. Rev. B*, 53(20):13427–13440, 1996.

[135] A. Lenef and S. C. Rand. Electronic structure of the N-V center in diamond: Theory. *Phys. Rev. B*, 53(20):13441–13455, 1996.

[136] N. B. Manson, J. P. Harrison, and M. J. Sellars. Nitrogen-vacancy center in diamond: Model of the electronic structure and associated dynamics. *Phys. Rev. B*, 74(10):104303, 2006.

[137] A. Gali, M. Fyta, and E. Kaxiras. Ab initio supercell calculations on nitrogen-vacancy center in diamond: Electronic structure and hyperfine tensors. *Phys. Rev. B*, 77(15):155206, 2008.

[138] F. M. Hossain, M. W. Doherty, H. F. Wilson, and L. C. L. Hollenberg. Ab initio electronic and optical properties of the N-V-center in diamond. *Phys. Rev. Lett.*, 101(22):226403, 2008.

[139] P. Tamarat, N. B. Manson, J. P. Harrison, R. L. McMurtrie, A. Nizovtsev, C. Santori, R. G. Beausoleil, P. Neumann, T. Gaebel, F. Jelezko, P. Hemmer, and J. Wrachtrup. Spin-flip and spin-conserving optical transitions of the nitrogen-vacancy centre in diamond. *New J. Phys.*, 10:045004, 2008.

[140] P. Neumann, R. Kolesov, V. Jacques, J. Beck, J. Tisler, A. Batalov, L. Rogers, N. B. Manson, G. Balasubramanian, F. Jelezko, and J. Wrachtrup. Excited-state spectroscopy of single NV defects in diamond using optically detected magnetic resonance. *New J. Phys.*, 11:013017, 2009.

[141] J. Loubser and J. A. van Wyk. Electron-spin resonance in study of diamond. *Rep. Prog. Phys.*, 41(8):1201–1248, 1978.

[142] N. R. S. Reddy, N. B. Manson, and E. R. Krausz. Two-laser spectral hole burning in a colour centre in diamond. *J. Lumin.*, 38(1–6):46–47, 1987.

[143] G. Davies and M. F. Hamer. Optical studies of 1.945 eV vibronic band in diamond. *Proc. Roy. Soc. Lond. A*, 348(1653):285–298, 1976.

[144] A. T. Collins, M. F. Thomaz, and M. I. B. Jorge. Luminescence decay time of the 1.945 eV centre in type Ib diamond. *J. Phys. C*, 16(11):2177–2181, 1983.

[145] A. Dräbenstedt, L. Fleury, C. Tietz, F. Jelezko, S. Kilin, A. Nizovtzev, and J. Wrachtrup. Low-temperature microscopy and spectroscopy on single defect centers in diamond. *Phys. Rev. B*, 60(16):11503–11508, 1999.

[146] C. Kurtsiefer, S. Mayer, P. Zarda, and H. Weinfurter. Stable solid-state source of single photons. *Phys. Rev. Lett.*, 85(2):290–293, 2000.

[147] F. Jelezko and J. Wrachtrup. Read-out of single spins by optical spectroscopy. *J. Phys.: Condens. Matter*, 16(30):R1089–R1104, 2004.

[148] J. Harrison, M. J. Sellars, and N. B. Manson. Optical spin polarisation of the N-V centre in diamond. *J. Lumin.*, 107(1–4):245–248, 2004.

[149] C. Santori, D. Fattal, S. M. Spillane, M. Fiorentino, R. G. Beausoleil, A. D. Greentree, P. Olivero, M. Draganski, J. R. Rabeau, P. Reichart, B. C. Gibson, S. Rubanov, D. N. Jamieson, and S. Prawer. Coherent population trapping in diamond N-V centers at zero magnetic field. *Opt. Express*, 14(17):7986–7994, 2006.

[150] G. Balasubramanian, P. Neumann, D. Twitchen, M. Markham, R. Kolesov, N. Mizuochi, J. Isoya, J. Achard, J. Beck, J. Tissler, V. Jacques, P. R. Hemmer, F. Jelezko, and J. Wratchtrup. Ultralong spin coherence time in isotopically engineered diamond. *Nature Mater.*, 8(5):383–387, 2009.

[151] F. Jelezko, I. Popa, A. Gruber, C. Tietz, J. Wrachtrup, A. Nizovtsev, and S. Kilin. Single spin states in a defect center resolved by optical spectroscopy. *Appl. Phys. Lett.*, 81(12):2160–2162, 2002.

[152] F. Jelezko, T. Gaebel, I. Popa, A. Gruber, and J. Wrachtrup. Observation of coherent oscillations in a single electron spin. *Phys. Rev. Lett.*, 92(7):076401, 2004.

[153] T. Gaebel, M. Domhan, I. Popa, C. Wittmann, P. Neumann, F. Jelezko, J. R. Rabeau, N. Stavrias, A. D . Greentree, S. Prawer, J. Meijer, J. Twamley, P. R. Hemmer, and J. Wrachtrup. Room-temperature coherent coupling of single spins in diamond. *Nature Phys.*, 2(6):408–413, 2006.

[154] L. Childress, M. V. Gurudev Dutt, J. M. Taylor, A. S. Zibrov, F. Jelezko, J. Wrachtrup, P. R. Hemmer, and M. D. Lukin. Coherent dynamics of coupled electron and nuclear spin qubits in diamond. *Science*, 314(5797):281–285, 2006.

[155] M. V. Gurudev Dutt, L. Childress, L. Jiang, E. Togan, J. Maze, F. Jelezko, A. S. Zibrov, P. R. Hemmer, and M. D. Lukin. Quantum register based on individual electronic and nuclear spin qubits in diamond. *Science*, 316(5829): 1312–1316, 2007.

[156] P. Neumann, N. Mizuochi, F. Rempp, P. Hemmer, H. Watanabe, S. Yamasaki, V. Jacques, T. Gaebel, F. Jelezko, and J. Wrachtrup. Multipartite entanglement among single spins in diamond. *Science*, 320(5881):1326–1329, 2008.

[157] F. Jelezko, C. Tietz, A. Gruber, I. Popa, A. Nizovtsev, S. Kilin, and J. Wrachtrup. Spectroscopy of single N-V centers in diamond. *Single Mol.*, 2 (4):255–260, 2001.

[158] H. J. Kimble, M. Dagenais, and L. Mandel. Photon antibunching in resonance fluorescence. *Phys. Rev. Lett.*, 39(11):691–695, 1977.

[159] F. de Martini, G. di Giuseppe, and M. Marrocco. Single-mode generation of quantum photon states by excited single molecules in a microcavity trap. *Phys. Rev. Lett.*, 76(6):900–903, 1996.

[160] B. Lounis and W. E. Moerner. Single photons on demand from a single molecule at room temperature. *Nature*, 407(6803):491–493, 2000.

[161] P. Michler, A. Kiraz, C. Becher, W. V. Schoenfeld, P. M. Petroff, L. D. Zhang, E. Hu, and A. Imamoğlu. A quantum dot single-photon turnstile device. *Science*, 290(5500):2282–2285, 2000.

[162] C. Santori, M. Pelton, G. Solomon, Y. Dale, and E. Yamamoto. Triggered single photons from a quantum dot. *Phys. Rev. Lett.*, 86(8):1502–1505, 2001.

[163] P. Michler, A. Imamoğlu, M. D. Mason, P. J. Carson, G. F. Strouse, and S. K. Buratto. Quantum correlation among photons from a single quantum dot at room temperature. *Nature*, 406(6799):968–970, 2000.

[164] R. Brouri, A. Beveratos, J. P. Poizat, and P. Grangier. Photon antibunching in the fluorescence of individual color centers in diamond. *Opt. Lett.*, 25(17): 1294–1296, 2000.

[165] R. Alléaume, F. Treussart, G. Messin, Y. Dumeige, J. F. Roch, A. Beveratos, R. Brouri-Tualle, J. P. Poizat, and P. Grangier. Experimental open-air quantum key distribution with a single-photon source. *New J. Phys.*, 6:92, 2004.

[166] A. Beveratos, S. Kühn, R. Brouri, T. Gacoin, J. P. Poizat, and P. Grangier. Room temperature stable single-photon source. *Eur. Phys. J. D*, 18(2):191–196, 2002.

[167] T. Gaebel, I. Popa, A. Gruber, M. Domhan, F . Jelezko, and J. Wrachtrup. Stable single-photon source in the near infrared. *New J. Phys.*, 6:98, 2004.

[168] E. Wu, J. R. Rabeau, G. Roger, F. Treussart, H. Zeng, P. Grangier, S. Prawer, and J.-F. Roch. Room temperature triggered single-photon source in the near infrared. *New J. Phys.*, 9:434, 2007.

[169] C. L. Wang, C. Kurtsiefer, H. Weinfurter, and B. Burchard. Single photon emission from SiV centres in diamond produced by ion implantation. *J. Phys. B*, 39(1):37–41, 2006.

[170] N. B. Manson and J. P. Harrison. Photo-ionization of the nitrogen-vacancy center in diamond. *Diamond Relat. Mater.*, 14(10):1705–1710, 2005.

[171] T. Gaebel, M. Domhan, C. Wittmann, I. Popa, F. Jelezko, J. Rabeau, A. Greentree, S. Prawer, E. Trajkov, P. R. Hemmer, and J. Wrachtrup. Photochromism in single nitrogen-vacancy defect in diamond. *Appl. Phys. B*, 82 (2):243–246, 2006.

[172] R. Hanbury Brown and R. Q. Twiss. Correlation between photons in two coherent beams of light. *Nature*, 177:27–29, 1956.

[173] J. Bernard, L. Fleury, H. Talon, and M. Orrit. Photon bunching in the fluorescence from single molecules: A probe for intersystem crossing. *J. Chem. Phys.*, 98(2):850–859, 1993.

[174] A. Beveratos, R. Brouri, T. Gacoin, J. P. Poizat, and P. Grangier. Nonclassical radiation from diamond nanocrystals. *Phys. Rev. A*, 64(6):061802, 2001.

[175] Y. Shen, T. M. Sweeney, and H. Wang. Zero-phonon linewidth of single nitrogen vacancy centers in diamond nanocrystals. *Phys. Rev. B*, 77(3):033201, 2008.

[176] J. R. Rabeau, A. Stacey, A. Rabeau, S. Prawer, F. Jelezko, I. Mirza, and J. Wrachtrup. Single nitrogen vacancy centers in chemical vapor deposited diamond nanocrystals. *Nano Lett.*, 7(11):3433–3437, 2007.

[177] P. Tamarat, T. Gaebel, J. R. Rabeau, M. Khan, A. D. Greentree, H. Wilson, L. C. L. Hollenberg, S. Prawer, P. Hemmer, F. Jelezko, and J. Wrachtrup. Stark shift control of single optical centers in diamond. *Phys. Rev. Lett.*, 97 (8):083002, 2006.

[178] A. Batalov, C. Zierl, T. Gaebel, P. Neumann, I.-Y. Chan, G. Balasubramanian, P. R. Hemmer, F. Jelezko, and J. Wrachtrup. Temporal coherence of photons emitted by single nitrogen-vacancy defect centers in diamond using optical Rabi-oscillations. *Phys. Rev. Lett.*, 100(7):077401, 2008.

[179] M. Faraday. The Bakerian lecture: Experimental relations of gold (and other metals) to light. *Phil. Trans. Roy. Soc. Lond.*, 147:145–181, 1857.

[180] S. A. Maier. *Plasmonics: Fundamentals and applications.* Springer, 2007.

[181] S. A. Kalele, N. R. Tiwari, S. W. Gosavi, and S. K. Kulkarni. Plasmon-assisted photonics at the nanoscale. *J. Nanophoton.*, 1:012501, 2007.

[182] L. Novotny and B. Hecht. *Principles of nano-optics.* Cambridge University Press, 2006.

[183] P. Drude. Zur Elektronentheorie der Metalle. *Ann. Phys.*, 306(3):566–613, 1900.

[184] S. M. Nie and S. R. Emery. Probing single molecules and single nanoparticles by surface-enhanced Raman scattering. *Science*, 275(5303):1102–1106, 1997.

[185] K. Kneipp, Y. Wang, H. Kneipp, L. T. Perelman, I. Itzkan, R. Dasari, and M. S. Feld. Single molecule detection using surface-enhanced Raman scattering (SERS). *Phys. Rev. Lett.*, 78(9):1667–1670, 1997.

[186] J. N. Farahani, D. W. Pohl, H.-J. Eisler, and B. Hecht. Single quantum dot coupled to a scanning optical antenna: A tunable superemitter. *Phys. Rev. Lett.*, 95(1):017402, 2005.

[187] P. Anger, P. Bharadwaj, and L. Novotny. Enhancement and quenching of single-molecule fluorescence. *Phys. Rev. Lett.*, 96(11):113002, 2006.

[188] S. Kühn, U. Håkanson, L. Rogobete, and V. Sandoghdar. Enhancement of single-molecule fluorescence using a gold nanoparticle as an optical nanoantenna. *Phys. Rev. Lett.*, 97(1):017402, 2006.

[189] J. N. Anker, W. P. Hall, O. Lyandres, N. C. Shah, J. Zhao, and R. P. van Duyne. Biosensing with plasmonic nanosensors. *Nature Mater.*, 7(6):442–453, 2008.

[190] S. Link and M. A. El-Sayed. Spectral properties and relaxation dynamics of surface plasmon electronic oscillations in gold and silver nanodots and nanorods. *J. Phys. Chem. B*, 103(40):8410–8426, 1999.

[191] K. L. Kelly, E. Coronado, L. L. Zhao, and G.C. Schatz. The optical properties of metal nanoparticles: The influence of size, shape, and dielectric environment. *J. Phys. Chem. B*, 107(3):668–677, 2003.

[192] M. Meier and A. Wokaun. Enhanced fields on large metal particles: Dynamic depolarization. *Opt. Lett.*, 8(11):581–583, 1983.

[193] E. Hao and G. C. Schatz. Electromagnetic fields around silver nanoparticles and dimers. *J. Chem. Phys.*, 120(1):357–366, 2004.

[194] C. Sönnichsen, T. Franzl, T. Wilk, G. von Plessen, J. Feldmann, O. Wilson, and P. Mulvaney. Drastic reduction of plasmon damping in gold nanorods. *Phys. Rev. Lett.*, 88(7):077402, 2002.

[195] W. Rechberger, A. Hohenau, A. Leitner, J. R. Krenn, B. Lamprecht, and F. R. Aussenegg. Optical properties of two interacting gold nanoparticles. *Opt. Commun.*, 220(1–3):137–141, 2003.

[196] K. H. Su, Q. H. Wei, X. Zhang, J. J. Mock, D. R. Smith, and S. Schultz. Interparticle coupling effects on plasmon resonances of nanogold particles. *Nano Lett.*, 3(8):1087–1090, 2003.

[197] P. K. Jain, W. Huang, and M. A. El-Sayed. On the universal scaling behavior of the distance decay of plasmon coupling in metal nanoparticle pairs: A plasmon ruler equation. *Nano Lett.*, 7(7):2080–2088, 2007.

[198] T. Atay, J. H. Song, and A. V. Nurmikko. Strongly interacting plasmon nanoparticle pairs: From dipole-dipole interaction to conductively coupled regime. *Nano Lett.*, 4(9):1627–1631, 2004.

[199] P. Mühlschlegel, H.-J. Eisler, O. J. F. Martin, B. Hecht, and D. W. Pohl. Resonant optical antennas. *Science*, 308(5728):1607–1609, 2005.

[200] E. Dulkeith, A. C. Morteani, T. Niedereichholz, T. A. Klar, J. Feldmann, S. A. Levi, F. C. J. M. van Veggel, D. N. Reinhoudt, M. Möller, and D. I. Gittins. Fluorescence quenching of dye molecules near gold nanoparticles: Radiative and nonradiative effects. *Phys. Rev. Lett.*, 89(20):203002, 2002.

[201] P. Bharadwaj and L. Novotny. Spectral dependence of single molecule fluorescence enhancement. *Opt. Express*, 15(21):14266–14274, 2007.

[202] R. Carminati, J. J. Greffet, C. Henkel, and J. M. Vigoureux. Radiative and non-radiative decay of a single molecule close to a metallic nanoparticle. *Opt. Commun.*, 261(2):368–375, 2006.

[203] F. Tam, G. P. Goodrich, B. R. Johnson, and N. J. Halas. Plasmonic enhancement of molecular fluorescence. *Nano Lett.*, 7(2):496–501, 2007.

[204] Y. Chen, K. Munechika, and D. S. Ginger. Dependence of fluorescence intensity on the spectral overlap between fluorophores and plasmon resonant single silver nanoparticles. *Nano Lett.*, 7(3):690–696, 2007.

[205] T. Härtling, P. Reichenbach, and L. M. Eng. Near-field coupling of a single fluorescent molecule and a spherical gold nanoparticle. *Opt. Express*, 15(20): 12806–12817, 2007.

[206] L. Rogobete, F. Kaminski, M. Agio, and V. Sandoghdar. Design of plasmonic nanoantennae for enhancing spontaneous emission. *Opt. Lett.*, 32(12):1623–1625, 2007.

[207] T. H. Taminiau, F. D. Stefani, F. B. Segerink, and N. F. van Hulst. Optical antennas direct single-molecule emission. *Nature Photon.*, 2(4):234–237, 2008.

[208] T. H. Taminiau, F. D. Stefani, and N. F. van Hulst. Single emitters coupled to plasmonic nano-antennas: Angular emission and collection efficiency. *New J. Phys.*, 10:105005, 2008.

[209] D. M. Eigler and E. K. Schweizer. Positioning single atoms with a scanning tunneling microscope. *Nature*, 344(6266):524–526, 1990.

[210] T. Junno, K. Deppert, L. Montelius, and L. Samuelson. Controlled manipulation of nanoparticles with an atomic force microscope. *Appl. Phys. Lett.*, 66 (26):3627–3629, 1995.

[211] L. Tong, T. Zhu, and Z. Liu. Atomic force microscope manipulation of gold nanoparticles for controlled Raman enhancement. *Appl. Phys. Lett.*, 92(2): 023109, 2008.

[212] J. Merlein, M. Kahl, A. Zuschlag, A. Sell, A. Halm, J. Boneberg, P. Leiderer, A. Leitenstorfer, and R. Bratschitsch. Nanomechanical control of an optical antenna. *Nature Photon.*, 2(4):230–233, 2008.

[213] A. Bek, R. Jansen, M. Ringler, S. Mayilo, T. A. Klar, and J. Feldmann. Fluorescence enhancement in hot spots of AFM-designed gold nanoparticle sandwiches. *Nano Lett.*, 8(2):485–490, 2008.

[214] G. Binnig, C. F. Quate, and C. Gerber. Atomic force microscope. *Phys. Rev. Lett.*, 56(9):930–933, 1986.

[215] J. E. Jones. On the determination of molecular fields. II. From the equation of state of a gas. *Proc. Roy. Soc. Lond. A*, 106(738):463–477, 1924.

[216] Y. Wang, Y. Zhang, B. Li, J. Lü, and J. Hu. Capturing and depositing one nanoobject at a time: Single particle dip-pen nanolithography. *Appl. Phys. Lett.*, 90(13):133102, 2007.

[217] K. Salaita, Y. Wang, and C. A. Mirkin. Applications of dip-pen nanolithography. *Nature Nanotechnol.*, 2(3):145–155, 2007.

[218] R. D. Piner, J. Zhu, F. Xu, S. Hong, and C. A. Mirkin. "Dip-pen" nanolithography. *Science*, 283(5402):661–663, 1999.

[219] M. S. Anderson. Nearfield surface enhanced spectroscopy using targeted nanoparticle deposition. *Appl. Phys. Lett.*, 92(12):123101, 2008.

[220] K. Hennessy, A. Badolato, P. M. Petroff, and E. Hu. Positioning photonic crystal cavities to single InAs quantum dots. *Photon. Nanostruct. Fund. Appl.*, 2:65–72, 2004.

[221] F. P. Laussy, E. del Valle, and C. Tejedor. Strong coupling of quantum dots in microcavities. *Phys. Rev. Lett.*, 101(8):083601, 2008.

[222] A. Imamoğlu, S. Fält, J. Dreiser, G. Fernandez, M. Atatüre, K. Hennessy, A. Badolato, and D. Gerace. Coupling quantum dot spins to a photonic crystal nanocavity. *J. Appl. Phys.*, 101(8):081602, 2007.

[223] T. Sünner, C. Schneider, M. Strauss, A. Huggenberger, D. Wiener, S. Höfling, M. Kamp, and A. Forchel. Scalable fabrication of optical resonators with embedded site-controlled quantum dots. *Opt. Lett.*, 33(15):1759–1761, 2008.

[224] B. A. Fairchild, P. Olivero, S. Rubanov, A. D. Greentree, F. WaIdermann, R. A. Taylor, I. Walmsley, J. M. Smith, S. Huntington, B. C. Gibson, D. N. Jamieson, and S. Prawer. Fabrication of ultrathin single-crystal diamond membranes. *Adv. Mater.*, 20(24):4793–4798, 2008.

[225] Y.-S. Park, A. K. Cook, and H. Wang. Cavity QED with diamond nanocrystals and silica microspheres. *Nano Lett.*, 6(9):2075–2079, 2006.

[226] P. E. Barclay, C. Santori, K.-M. Fu, R. G. Beausoleil, and O. Painter. Coherent interference effects in a nano-assembled diamond NV center cavity-QED system. *Opt. Express*, 17(10):8081–8097, 2009.

[227] A. F. Koenderink, M. Kafesaki, B. C. Buchler, and V. Sandoghdar. Controlling the resonance of a photonic crystal microcavity by a near-field probe. *Phys. Rev. Lett.*, 95(15):153904, 2005.

[228] S. Mujumdar, A. F. Koenderink, T. Sünner, B. C. Buchler, M. Kamp, A. Forchel, and V. Sandoghdar. Near-field imaging and frequency tuning of a high-Q photonic crystal membrane microcavity. *Opt. Express*, 15(25): 17214–17220, 2007.

[229] M.-K. Seo, H.-G. Park, J.-K. Yang, J.-Y. Kim, S.-H. Kim, and Y.-H. Lee. Controlled sub-nanometer tuning of photonic crystal resonator by carbonaceous nano-dots. *Opt. Express*, 16(13):9829–9837, 2008.

[230] D. E. Chang, A. S. Sørensen, P. R. Hemmer, and M. D. Lukin. Quantum optics with surface plasmons. *Phys. Rev. Lett.*, 97(5):053002, 2006.

[231] Y. Gong and J. Vučković. Design of plasmon cavities for solid-state cavity quantum electrodynamics applications. *Appl. Phys. Lett.*, 90(3):033113, 2007.

[232] H. Ditlbacher, A. Hohenau, D. Wagner, U. Kreibig, M. Rogers, F. Hofer, F. R. Aussenegg, and J. R. Krenn. Silver nanowires as surface plasmon resonators. *Phys. Rev. Lett.*, 95(25):257403, 2005.

[233] H. T. Miyazaki and Y. Kurokawa. Squeezing visible light waves into a 3-nm-thick and 55-nm-long plasmon cavity. *Phys. Rev. Lett.*, 96(9):097401, 2006.

[234] J.-C. Weeber, A. Bouhelier, G. Colas des Francs, L. Markey, and A. Dereux. Submicrometer in-plane integrated surface plasmon cavities. *Nano Lett.*, 7(5): 1352–1359, 2007.

[235] M. T. Hill, Y.-S. Oei, B. Smalbrugge, Y. Zhu, T. de Vries, P. J. van Veldhoven, F. W. M. van Otten, T. J. Eijkemans, J. P. Turkiewicz, Huug de Waardt, E. J. Geluk, S.-H. Kwon, Y.-H. Lee, R. Nötzel, and M. K. Smit. Lasing in metallic-coated nanocavities. *Nature Photon.*, 1(10):589–594, 2007.

[236] M. Allione, V. V. Temnov, Y. Fedutik, U. Woggon, and M. V. Artemyev. Surface plasmon mediated interference phenomena in low-Q silver nanowire cavities. *Nano Lett.*, 8(1):31–35, 2008.

[237] B. Min, E. Ostby, V. Sorger, E. Ulin-Avila, L. Yang, X. Zhang, and K. Vahala. High-Q surface-plasmon-polariton whispering-gallery microcavity. *Nature*, 457 (7228):455–459, 2009.

[238] P. Pinotsi and A. Imamoğlu. Single photon absorption by a single quantum emitter. *Phys. Rev. Lett.*, 100:093603, 2008.

[239] U. Fano. Effects of configuration interaction on intensities and phase shifts. *Phys. Rev.*, 124(6):1866–1878, 1961.

[240] E. Dulkeith, T. Niedereichholz, T. A. Klar, J. Feldmann, G. von Plessen, D. I. Gittins, K. S. Mayya, and F. Caruso. Plasmon emission in photoexcited gold nanoparticles. *Phys. Rev. B*, 70(20):205424, 2004.

[241] J. Zhang, Y. Fu, M. H. Chowdhury, and J. R. Lakowicz. Metal-enhanced single-molecule fluorescence on silver particle monomer and dimer: Coupling effect between metal particles. *Nano Lett.*, 7(7):2101–2107, 2007.

[242] O. L. Muskens, V. Giannini, J. A. Sánchez-Gil, and J. Gómez Rivas. Strong enhancement of the radiative decay rate of emitters by single plasmonic nanoantennas. *Nano Lett.*, 7(9):2871–2875, 2007.

[243] R. M. Bakker, H.-K. Yuan, Z. Liu, V. P. Drachev, A. V. Kildishev, V. M. Shalaev, R. H. Pedersen, S. Gresillon, and A. Boltasseva. Enhanced localized fluorescence in plasmonic nanoantennae. *Appl. Phys. Lett.*, 92(4):043101, 2008.

[244] R. J. Epstein, F. M. Mendoza, Y. K. Kato, and D. D. Awschalom. Anisotropic interactions of a single spin and dark-spin spectroscopy in diamond. *Nature Phys.*, 1(2):94–98, 2005.

[245] J. Enderlein. Dependence of the optical saturation of fluorescence on rotational diffusion. *Chem. Phys. Lett.*, 410(4–6):452–456, 2005.

[246] S. Hughes. Modified spontaneous emission and qubit entanglement from dipole-coupled quantum dots in a photonic crystal nanocavity. *Phys. Rev. Lett.*, 94(22):227402, 2005.

[247] S. Hughes. Coupled-cavity QED using planar photonic crystals. *Phys. Rev. Lett.*, 98(8):083603, 2007.

[248] T. van der Sar, E. C. Heeres, G. M. Dmochowski, G. de Lange, L. Robledo, T. H. Oosterkamp, and R. Hanson. Nanopositioning of a diamond nanocrystal containing a single nitrogen-vacancy defect center. *Appl. Phys. Lett.*, 94(17): 173104, 2009.

[249] E. Ampem-Lassen, D. A. Simpson, B. C. Gibson, S. Trpkovski, F. M. Hossain, S. T. Huntington, K. Ganesan, L. C. L. Hollenberg, and S. Prawer. Nano-manipulation of diamond-based single photon sources. *Opt. Express*, 17(14): 11287–11293, 2009.

[250] K.-M. Fu, C. Santori, P. E. Barclay, I. Aharonovich, S. Prawer, N. Meyer, A. M. Holm, and R. G. Beausoleil. Coupling of nitrogen-vacancy centers in diamond to a GaP waveguide. *Appl. Phys. Lett.*, 93(23):234107, 2008.

[251] P. E. Barclay, K.-M. Fu, C. Santori, and R. G. Beausoleil. Hybrid photonic crystal cavity and waveguide for coupling to diamond NV-centers. *Opt. Express*, 17(12):9588–9601, 2009.

[252] M. Larsson, K. Nima Dinyari, and H. Wang. Composite optical microcavity of diamond nanopillar and silica microsphere. *Nano Lett.*, 9(4):1447–1450, 2009.

[253] P. E. Barclay, K.-M. Fu, C. Santori, and R. G. Beausoleil. Chip-based microcavities coupled to nitrogen-vacancy centers in single crystal diamond. *Appl. Phys. Lett.*, 95(19):191115, 2009.

[254] I. Aharonovich, S. Castelletto, D. A. Simpson, A. Stacey, J. McCallum, A. D. Greentree, and S. Prawer. Two-level ultrabright single photon emission from diamond nanocrystals. *Nano Lett.*, 9(9):3191–3195, 2009.

[255] E. Chow, A. Grot, L. W. Mirkarimi, M. Sigalas, and G. Girolami. Ultracompact biochemical sensor built with two-dimensional photonic crystal microcavity. *Opt. Lett.*, 29(10):1093–1095, 2004.

[256] M. Lee and P. M. Fauchet. Two-dimensional silicon photonic crystal based biosensing platform for protein detection. *Opt. Express*, 15(8):4530–4535, 2007.

[257] D. F. Dorfner, T. Hürlimann, T. Zabel, L. H. Frandsen, G. Abstreiter, and J. J. Finley. Silicon photonic crystal nanostructures for refractive index sensing. *Appl. Phys. Lett.*, 93(18):181103, 2008.

[258] S. Mandal and D. Erickson. Nanoscale optofluidic sensor arrays. *Opt. Express*, 16(3):1623–1631, 2008.

[259] J. Topol'ančik, P. Bhattacharya, J. Sabarinathan, and P. C. Yu. Fluid detection with photonic crystal-based multichannel waveguides. *Appl. Phys. Lett.*, 82(8):1143–1145, 2003.

[260] N. Skivesen, A. Têtu, M. Kristensen, J. Kjems, L. H. Frandsen, and P. I. Borel. Photonic-crystal waveguide biosensor. *Opt. Express*, 15(6):3169–3176, 2007.

[261] M. Lončar, A. Scherer, and Y. M. Qiu. Photonic crystal laser sources for chemical detection. *Appl. Phys. Lett.*, 82(26):4648–4650, 2003.

[262] S.-H. Kim, J.-H. Choi, S.-K. Lee, S.-H. Kim, S.-M. Yang, Y.-H. Lee, C. Seassal, P. Regrency, and P. Viktorovitch. Optofluidic integration of a photonic crystal nanolaser. *Opt. Express*, 16(9):6515–6527, 2008.

[263] S. Kita, K. Nozaki, and T. Baba. Refractive index sensing utilizing a cw photonic crystal nanolaser and its array configuration. *Opt. Express*, 16(11): 8174–8180, 2008.

[264] A. Ashkin, J. M. Dziedzic, J. E. Bjorkholm, and S. Chu. Observation of a single-beam gradient force optical trap for dielectric particles. *Opt. Lett.*, 11 (5):288–290, 1986.

[265] D. G. Grier. A revolution in optical manipulation. *Nature*, 424(6950):810–816, 2003.

[266] M. Gu, J.-B. Haumonte, Y. Micheau, J. W. M. Chon, and X. Gan. Laser trapping and manipulation under focused evanescent wave illumination. *Appl. Phys. Lett.*, 84(21):4236–4238, 2004.

[267] M. Šiler, T. Čižmár, M. Šerý, and P. Zemánek. Optical forces generated by evanescent standing waves and their usage for sub-micron particle delivery. *Appl. Phys. B*, 84(1–2):157–165, 2006.

[268] P. C. Chaumet, A. Rahmani, and M. Nieto-Vesperinas. Optical trapping and manipulation of nano-objects with an apertureless probe. *Phys. Rev. Lett.*, 88 (12):123601, 2002.

[269] K. Okamoto and S. Kawata. Radiation force exerted on subwavelength particles near a nanoaperture. *Phys. Rev. Lett.*, 83(22):4534–4537, 1999.

[270] A. N. Grigorenko, N. W. Roberts, M. R. Dickinson, and Y. Zhang. Nanometric optical tweezers based on nanostructured substrates. *Nature Photon.*, 2(6): 365–370, 2008.

[271] J. Ng and C. T. Chan. Size-selective optical forces for microspheres using evanescent wave excitation of whispering gallery modes. *Appl. Phys. Lett.*, 92 (25):251109, 2008.

[272] S. Arnold, D. Keng, S. I. Shopova, S. Holler, W. Zurawsky, and F. Vollmer. Whispering gallery mode carousel – a photonic mechanism for enhanced nanoparticle detection in biosensing. *Opt. Express*, 17(8):6230–6238, 2009.

[273] O. Toader, S. John, and K. Busch. Optical trapping, field enhancement and laser cooling in photonic crystals. *Opt. Express*, 8(3):217–222, 2001.

[274] A. Rahmani and P. C. Chaumet. Optical trapping near a photonic crystal. *Opt. Express*, 14(13):6353–6358, 2006.

[275] J. C. Maxwell. *A treatise on electricity and magnetism, Vol. 2.* Macmillan & Co., 1873.

[276] M. Nieto-Vesperinas, P. C. Chaumet, and A. Rahmani. Near-field photonic forces. *Phil. Trans. Roy. Soc. Lond. A*, 362(1817):719–737, 2004.

[277] S. M. Barnett and R. Loudon. On the electromagnetic force on a dielectric medium. *J. Phys. B*, 39(15):S671–S684, 2006.

[278] P. C. Chaumet and M. Nieto-Vesperinas. Time-averaged total force on a dipolar sphere in an electromagnetic field. *Opt. Lett.*, 25(15):1065–1067, 2000.

[279] Y. Harada and T. Asakura. Radiation forces on a dielectric sphere in the Rayleigh scattering regime. *Opt. Commun.*, 124(5–6):529–541, 1996.

[280] J. P. Gordon. Radiation forces and momenta in dielectric media. *Phys. Rev. A*, 8(1):14–21, 1973.

[281] G. Mie. Beiträge zur Optik trüber Medien, speziell kolloidaler Metallösungen. *Ann. Phys.*, 330(3):377–445, 1908.

[282] A. Ashkin. Forces of a single-beam gradient laser trap on a dielectric sphere in the ray optics regime. *Biophys. J.*, 61(2):569–582, 1992.

[283] A. Rohrbach and E. H. K. Stelzer. Optical trapping of dielectric particles in arbitrary fields. *J. Opt. Soc. Am. A*, 18(4):839–853, 2001.

[284] A. Ashkin. Acceleration and trapping of particles by radiation pressure. *Phys. Rev. Lett.*, 24(4):156–159, 1970.

[285] A. Ashkin and J. M. Dziedzic. Observation of radiation-pressure trapping of particles by alternating light beams. *Phys. Rev. Lett.*, 54(12):1245–1248, 1985.

[286] S. Kawata and T. Tani. Optically driven Mie particles in an evanescent field along a channeled waveguide. *Opt. Lett.*, 21(21):1768–1770, 1996.

[287] S. Gaugiran, S. Gétin, J. M. Fedeli, G. Colas, A. Fuchs, F. Chatelain, and J. Dérouard. Optical manipulation of microparticles and cells on silicon nitride waveguides. *Opt. Express*, 13(18):6956–6963, 2005.

[288] B. S. Schmidt, A. H. J. Yang, D. Erickson, and M. Lipson. Optofluidic trapping and transport on solid core waveguides within a microfluidic device. *Opt. Express*, 15(22):14322–14334, 2007.

[289] K. Grujic, O. G. Hellesø, J. P. Hole, and J. S. Wilkinson. Sorting of polystyrene microspheres using a Y-branched optical waveguide. *Opt. Express*, 13(1):1–7, 2005.

[290] S.-H. Kwon, T. Sünner, M. Kamp, and A. Forchel. Optimization of photonic crystal cavity for chemical sensing. *Opt. Express*, 16(16):11709–11717, 2008.

[291] A. Di Falco, L. O'Faolain, and T. F. Krauss. Chemical sensing in slotted photonic crystal heterostructure cavities. *Appl. Phys. Lett.*, 94(6):063503, 2009.

[292] A. H. J. Yang, S. D. Moore, B. S. Schmidt, M. Klug, M. Lipson, and D. Erickson. Optical manipulation of nanoparticles and biomolecules in sub-wavelength slot waveguides. *Nature*, 457(7225):71–75, 2009.

[293] A. H. J. Yang, T. Lerdsuchatawanich, and D. Erickson. Forces and transport velocities for a particle in a slot waveguide. *Nano Lett.*, 9(3):1182–1188, 2009.

[294] S. Lin, J. Hu, L. Kimerling, and K. Crozier. Design of nanoslotted photonic crystal waveguide cavities for single nanoparticle trapping and detection. *Opt. Lett.*, 34(21):3451–3453, 2009.

[295] J. Coelho Neto, U. Agero, R. T. Gazzinelli, and O. N. Mesquita. Measuring optical and mechanical properties of a living cell with defocusing microscopy. *Biophys. J.*, 91(3):1108–1115, 2006.

[296] M. L. Juan, Gordon R., Y. Pang, F. Eftekhari, and R. Quidant. Self-induced back-action optical trapping of dielectric nanoparticles. *Nature Phys.*, 5:915–919, 2009.

[297] S. Mandal, X. Serey, and D. Erickson. Nanomanipulation using silicon photonic crystal resonators. *Nano Lett.*, 10(1):99–104, 2010.

[298] T. R. Glass, S. Lackie, and T. Hirschfeld. Effect of numerical aperture on signal level in cylindrical waveguide evanescent fluorosensors. *Appl. Opt.*, 26 (11):2181–2187, 1987.

[299] H. P. Kao, N. Yang, and J. S. Schoeniger. Enhancement of evanescent fluorescence from fiber-optic sensors by thin-film sol-gel coatings. *J. Opt. Soc. Am. A*, 15(8):2163–2171, 1998.

[300] C. K. Carniglia, L. Mandel, and K. H. Drexhage. Absorption and emission of evanescent photons. *J. Opt. Soc. Am.*, 62(4):479–486, 1972.

[301] B. J. Eggleton, C. Kerbage, P. S. Westbrook, R. S. Windeler, and A. Hale. Microstructured optical fiber devices. *Opt. Express*, 9(13):698–713, 2001.

[302] T. M. Monro, W. Belardi, K. Furusawa, J. C. Baggett, N. G. R. Broderick, and D. J. Richardson. Sensing with microstructured optical fibres. *Meas. Sci. Technol.*, 12(7):854–858, 2001.

[303] R. F. Cregan, B. J. Mangan, J. C. Knight, T. A. Birks, P. S. J. Russell, P. J. Roberts, and D. C. Allan. Single-mode photonic band gap guidance of light in air. *Science*, 285(5433):1537–1539, 1999.

[304] J. B. Jensen, L. H. Pedersen, P. E. Høiby, L. B. Nielsen, T. P. Hansen, J. R. Folkenberg, J. Riishede, D. Noordegraaf, K. Nielsen, A. Carlsen, and A. Bjarklev. Photonic crystal fiber based evanescent-wave sensor for detection of biomolecules in aqueous solutions. *Opt. Lett.*, 29(17):1974–1976, 2004.

[305] J. B. Jensen, P. E. Høiby, G. Emiliyanov, O. Bang, L. H. Pedersen, and A. Bjarklev. Selective detection of antibodies in microstructured polymer optical fibers. *Opt. Express*, 13(15):5883–5889, 2005.

[306] L. Rindorf, P. E. Høiby, J. B. Jensen, L. H. Pedersen, O. Bang, and O. Geschke. Towards biochips using microstructured optical fiber sensors. *Anal. Bioanal. Chem.*, 385(8):1370–1375, 2006.

[307] L. Rindorf, J. B. Jensen, M. Dufva, L. H. Pedersen, P. E. Høiby, and O. Bang. Photonic crystal fiber long-period gratings for biochemical sensing. *Opt. Express*, 14(18):8224–8231, 2006.

[308] C. M. B. Cordeiro, M. A. R. Franco, G. Chesini, E. C. S. Barretto, R. Lwin, C. H. B. Cruz, and M. C. J. Large. Microstructured-core optical fibre for evanescent sensing applications. *Opt. Express*, 14(26):13056–13066, 2006.

[309] S. Yiou, P. Delaye, A. Rouvie, J. Chinaud, R. Frey, G. Roosen, P. Viale, S. Février, P. Roy, J. L. Auguste, and J. M. Blondy. Stimulated Raman scattering in an ethanol core microstructured optical fiber. *Opt. Express*, 13 (12):4786–4791, 2005.

[310] S. O. Konorov, A. M. Zheltikov, and M. Scalora. Photonic-crystal fiber as a multifunctional optical sensor and sample collector. *Opt. Express*, 13(9): 3454–3459, 2005.

[311] F. M. Cox, A. Argyros, and M. C. J. Large. Liquid-filled hollow core microstructured polymer optical fiber. *Opt. Express*, 14(9):4135–4140, 2006.

[312] A. W. Snyder and J. D. Love. *Optical waveguide theory.* Chapman & Hall, 1983.

[313] T. A. Birks, J. C. Knight, and P. S. J. Russell. Endlessly single-mode photonic crystal fiber. *Opt. Lett.*, 22(13):961–963, 1997.

[314] T. A. Birks, D. M. Bird, T. D. Hedley, J. M. Pottage, and P. S. J. Russell. Scaling laws and vector effects in bandgap-guiding fibres. *Opt. Express*, 12(1): 69–74, 2004.

[315] P. S. J. Russell. Photonic-crystal fibers. *J. Lightwave Technol.*, 24(12):4729–4749, 2006.

[316] J. C. Knight, T. A. Birks, P. S. J. Russell, and D. M. Atkin. All-silica single-mode optical fiber with photonic crystal cladding. *Opt. Lett.*, 21(19):1547–1549, 1996.

[317] J. M. Fini. Microstructure fibres for optical sensing in gases and liquids. *Meas. Sci. Technol.*, 15(6):1120–1128, 2004.

[318] J. C. Knight, T. A. Birks, R. F. Cregan, P. S. J. Russell, and J. P. de Sandro. Large mode area photonic crystal fibre. *Electron. Lett.*, 34(13):1347–1348, 1998.

[319] Y. L. Hoo, W. Jin, H. L. Ho, D. N. Wang, and R. S. Windeler. Evanescent-wave gas sensing using microstructure fiber. *Opt. Eng.*, 41(1):8–9, 2002.

[320] F. Benabid, J. C. Knight, G. Antonopoulos, and P. S. J. Russell. Stimulated Raman scattering in hydrogen-filled hollow-core photonic crystal fiber. *Science*, 298(5592):399–402, 2002.

[321] T. Ritari, J. Tuominen, H. Ludvigsen, J. C. Petersen, T. Sørensen, T. P. Hansen, and H. R. Simonsen. Gas sensing using air-guiding photonic bandgap fibers. *Opt. Express*, 12(17):4080–4087, 2004.

[322] F. Benabid, F. Couny, J. C. Knight, T. A. Birks, and P. S. J. Russell. Compact, stable and efficient all-fibre gas cells using hollow-core photonic crystal fibres. *Nature*, 434(7032):488–491, 2005.

[323] M. J. F. Digonnet, H. K. Kim, G. S. Kino, and S. Fan. Understanding air-core photonic-bandgap fibers: Analogy to conventional fibers. *J. Lightwave Technol.*, 23(12):4169–4177, 2005.

[324] K. Nielsen, D. Noordegraaf, T. Sørensen, A. Bjarklev, and T. P. Hansen. Selective filling of photonic crystal fibres. *J. Opt. A*, 7(8):L13–L20, 2005.

[325] L.-J. Yang, T.-J. Yao, and Y.-C. Tai. The marching velocity of the capillary meniscus in a microchannel. *J. Micromech. Microeng.*, 14(2):220–225, 2004.

[326] Y. Y. Huang, Y. Xu, and A. Yariv. Fabrication of functional microstructured optical fibers through a selective-filling technique. *Appl. Phys. Lett.*, 85(22): 5182–5184, 2004.

[327] L. Xiao, W. Jin, M. S. Demokan, H. L. Ho, Y. L. Hoo, and C. L. Zhao. Fabrication of selective injection microstructured optical fibers with a conventional fusion splicer. *Opt. Express*, 13(22):9014–9022, 2005.

[328] P. Monk. *Finite element methods for Maxwell's equations*. Oxford University Press, 2003.

[329] H. P. Uranus and H. J. W. M. Hoekstra. Modelling of microstructured waveguides using a finite-element-based vectorial mode solver with transparent boundary conditions. *Opt. Express*, 12(12):2795–2809, 2004.

[330] H. P. Uranus, H. J. W. M. Hoekstra, and E. van Groesen. Galerkin finite element scheme with Bayliss-Gunzburger-Turkel-like boundary conditions for vectorial optical mode solver. *J. Nonlinear Opt. Phys. Mater.*, 13(2):175–194, 2004.

[331] Y. N. Zhu, H. Du, and R. Bise. Design of solid-core microstructured optical fiber with steering-wheel air cladding for optimal evanescent-field sensing. *Opt. Express*, 14(8):3541–3546, 2006.

[332] Y. Ruan, E. P. Schartner, H. Ebendorff-Heidepriem, P. Hoffmann, and T. M. Monro. Detection of quantum-dot labeled proteins using soft glass microstructured optical fibers. *Opt. Express*, 15(26):17819–17826, 2007.

[333] H. Yan, C. Gua, C. Yang, J. Liu, G. Jin, J. Zhang, L. Hou, and Y. Yao. Hollow core photonic crystal fiber surface-enhanced Raman probe. *Appl. Phys. Lett.*, 89(20):204101, 2006.

[334] S. Afshar, S. C. Warren-Smith, and T. M. Monro. Enhancement of fluorescence-based sensing using microstructured optical fibres. *Opt. Express*, 15(26):17891–17901, 2007.

[335] S. Afshar, Y. Ruan, S. C. Warren-Smith, and T. M. Monro. Enhanced fluorescence sensing using microstructured optical fibers: A comparison of forward and backward collection modes. *Opt. Lett.*, 33(13):1473–1475, 2008.

[336] T. G. Euser, J. S. Y. Chen, M. Scharrer, P. S. J. Russell, N. J. Farrer, and P. J. Sadler. Quantitative broadband chemical sensing in air-suspended solid-core fibers. *J. Appl. Phys.*, 103(10):103108, 2008.

[337] Y. Zhang, C. Shi, C. Gu, L. Seballos, and J. Z. Zhang. Liquid core photonic crystal fiber sensor based on surface enhanced Raman scattering. *Appl. Phys. Lett.*, 90(19):193504, 2007.

[338] F. M. Cox, A. Argyros, M. C. J. Large, and S. Kalluri. Surface enhanced Raman scattering in a hollow core microstructured optical fiber. *Opt. Express*, 15(21):13675–13681, 2007.

[339] H. Yan, J. Liu, C. Yang, G. Jin, C. Gu, and L. Hou. Novel index-guided photonic crystal fiber surface-enhanced Raman scattering probe. *Opt. Express*, 16(11):8300–8305, 2008.

[340] C. M. B. Cordeiro, E. M. dos Santos, C. H. B. Cruz, C. J. S. de Matos, and D. S. Ferreira. Lateral access to the holes of photonic crystal fibers – selective filling and sensing applications. *Opt. Express*, 14(18):8403–8412, 2006.

[341] C. M. B. Cordeiro, C. J. S. de Matos, E. M. dos Santos, A. Bozolan, J. S. K. Ong, T. Facincani, G. Chesini, A. R. Vaz, and C. H. B. Cruz. Towards practical liquid and gas sensing with photonic crystal fibres: Side access to the fibre microstructure and single-mode liquid-core fibre. *Meas. Sci. Technol.*, 18(10): 3075–3081, 2007.

[342] S. C. Warren-Smith, S. Afshar, and T. M. Monro. Theoretical study of liquid-immersed exposed-core microstructured optical fibers for sensing. *Opt. Express*, 16(12):9034–9045, 2008.

[343] S. C. Warren-Smith, H. Ebendorff-Heidepriem, T. C. Foo, R. Moore, C. Davis, and T. M. Monro. Exposed-core microstructured optical fibers for real-time fluorescence sensing. *Opt. Express*, 17(21):18533–18542, 2009.

[344] A. D. Greentree, P. Olivero, M. Draganski, E. Trajkov, J. R. Rabeau, P. Reichart, B. C. Gibson, S. Rubanov, S. T. Huntington, D. N. Jamieson, and S. Prawer. Critical components for diamond-based quantum coherent devices. *J. Phys.: Condens. Matter*, 18(21):S825–S842, 2006.

[345] C.-H. Su, A. D. Greentree, and L. C. L. Hollenberg. High-performance diamond-based single-photon sources for quantum communication. *Phys. Rev. A*, 80(5):052308, 2009.

[346] C.-H. Su, A. D. Greentree, and L. C. L. Hollenberg. Towards a picosecond transform-limited nitrogen-vacancy based single photon source. *Opt. Express*, 16(9):6240–6250, 2008.

[347] A. Young, C. Y. Hu, L. Marseglia, J. P. Harrison, J. L. O'Brien, and J. G. Rarity. Cavity enhanced spin measurement of the ground state spin of an NV center in diamond. *New J. Phys.*, 11:013007, 2009.

[348] S. Hughes and P. Yao. Theory of quantum light emission from a strongly-coupled single quantum dot photonic-crystal cavity system. *Opt. Express*, 17 (5):3322–3330, 2009.

[349] R. F. Oulton, V. J. Sorger, D. A. Genov, D. F. P. Pile, and X. Zhang. A hybrid plasmonic waveguide for subwavelength confinement and long-range propagation. *Nature Photon.*, 2(8):496–500, 2008.

[350] R. F. Oulton, V. J. Sorger, T. Zentgraf, R.-M. Ma, C. Gladden, L. Dai, G. Bartal, and X. Zhang. Plasmon lasers at deep subwavelength scale. *Nature*, 461 (7264):629–632, 2009.

[351] A. V. Akimov, A. Mukherjee, C. L. Yu, D. E. Chang, A. S. Zibrov, P. R. Hemmer, H. Park, and M. D. Lukin. Generation of single optical plasmons in metallic nanowires coupled to quantum dots. *Nature*, 450(7168):402–406, 2007.

[352] R. Kolesov, B. Grotz, G. Balasubramanian, R. J. Stöhr, A. A. L. Nicolet, P. R. Hemmer, F. Jelezko, and J. Wrachtrup. Wave-particle duality of single surface plasmon polaritons. *Nature Phys.*, 5(7):470–474, 2009.

[353] P. Biagioni, J. S. Huang, L. Duò, M. Finazzi, and B. Hecht. Cross resonant optical antenna. *Phys. Rev. Lett.*, 102(25):256801, 2009.

[354] F. Benabid, J. C. Knight, and P. S. J. Russell. Particle levitation and guidance in hollow-core photonic crystal fiber. *Opt. Express*, 10(21):1195–1203, 2002.

[355] S. Mandal and D. Erickson. Optofluidic transport in liquid core waveguiding structures. *Appl. Phys. Lett.*, 90(18):184103, 2007.

[356] T. G. Euser, M. K. Garbos, J. S. Y. Chen, and P. S. J. Russell. Precise balancing of viscous and radiation forces on a particle in liquid-filled photonic bandgap fiber. *Opt. Lett.*, 34(23):3674–3676, 2009.

[357] J. J. Peterson and T. D. Krauss. Fluorescence spectroscopy of single lead sulfide quantum dots. *Nano Lett.*, 6(3):510–514, 2006.

[358] P. B. Johnson and R. W. Christy. Optical constants of the noble metals. *Phys. Rev. B*, 6(12):4370–4379, 1972.

[359] B. Nikoobakht and M. A. El-Sayed. Preparation and growth mechanism of gold nanorods (NRs) using seed-mediated growth method. *Chem. Mat.*, 15: 1957–1962, 2003.

List of Own Publications

The following articles (listed in reverse chronological order) have been published by the author. Those marked by an asterisk arose from work which was not part of this thesis.

Book chapters

Barth *et al.* 2010a M. Barth, H. Bartelt, and O. Benson. *Handbook of optofluidics*, chapter Fluid-filled optical fibers. Taylor & Francis, 2010 (in press).

Bartelt *et al.* 2008 H. Bartelt, J. Kirchhof, J. Kobelke, K. Schuster, A. Schwuchow, K. Mörl, U. Röpke, J. Leppert, H. Lehmann, S. Smolka, M. Barth, O. Benson, S. Taccheo, and C. D'Andrea. *Nanophotonic materials*, chapter Preparation and application of functionalized photonic crystal fibers, pages 291–311. Wiley-VCH, 2008.

Peer-reviewed journals

Barth *et al.* 2010b M. Barth, S. Schietinger, S. Fischer, J. Becker, C. Sönnichsen, N. Nüsse, B. Löchel, T. Aichele, and O. Benson. A nanoassembled plasmonic-photonic hybrid cavity for tailored light-matter coupling. *Nano Lett.*, 2010 (in press).

Barth *et al.* 2010c M. Barth, S. Schietinger, T. Schröder, T. Aichele, and O. Benson. Controlled coupling of NV defect centers to plasmonic and photonic nanostructures. *J. Lumin.*, 2010 (in press).

Schietinger *et al.* 2009 S. Schietinger, M. Barth, T. Aichele, and O. Benson. Plasmon-enhanced single photon emission from a nanoassembled metal-diamond hybrid structure at room temperature. *Nano Lett.*, 9:1694–1698, 2009.

Barth *et al.* 2009a M. Barth, N. Nüsse, B. Löchel, and O. Benson. Controlled coupling of a single-diamond nanocrystal to a photonic crystal cavity. *Opt. Lett.*, 34(7):1108–1110, 2009.

Barth *et al.* 2009b M. Barth, J. Stingl, J. Kouba, N. Nüsse, B. Löchel, and O. Benson. A hybrid approach towards nanophotonic devices with enhanced functionality. *Phys. Status Solidi B*, 246(2):298–301, 2009.

Barth *et al.* 2008a M. Barth, N. Nüsse, J. Stingl, B. Löchel, and O. Benson. Emission properties of high-Q silicon nitride photonic crystal heterostructure cavities. *Appl. Phys. Lett.*, 93(2):021112, 2008.

Barth *et al.* 2007a M. Barth, J. Kouba, J. Stingl, B. Löchel, and O. Benson. Modification of visible spontaneous emission with silicon nitride photonic crystal nanocavities. *Opt. Express*, 15(25):17231–17240, 2007.

Bartelt *et al.* 2007 H. Bartelt, J. Kirchhof, J. Kobelke, K. Schuster, A. Schwuchow, K. Mörl, U. Röpke, J. Leppert, H. Lehmann, S. Smolka, M. Barth, O. Benson, S. Taccheo, and C. D'Andrea. Preparation and application of functionalized photonic crystal fibres. *Phys. Status Solidi A*, 204(11):3805–3821, 2007.

Smolka *et al.* 2007a S. Smolka, M. Barth, and O. Benson. Highly efficient fluorescence sensing with hollow core photonic crystal fibers. *Opt. Express*, 15(20):12783–12791, 2007.

Smolka *et al.* 2007b S. Smolka, M. Barth, and O. Benson. Selectively coated photonic crystal fiber for highly sensitive fluorescence detection. *Appl. Phys. Lett.*, 90(11):111101, 2007.

Barth *et al.* 2006a M. Barth and O. Benson. Manipulation of dielectric particles using photonic crystal cavities. *Appl. Phys. Lett.*, 89(25):253114, 2006.

*__Barth *et al.* 2006b__ M. Barth, R. Schuster, A. Gruber, and F. Cichos. Imaging single quantum dots in three-dimensional photonic crystals. *Phys. Rev. Lett.*, 96(24):243902, 2006.

*__Barth *et al.* 2005__ M. Barth, A. Gruber, and F. Cichos. Spectral and angular redistribution of photoluminescence near a photonic stop band. *Phys. Rev. B*, 72(8):085129, 2005.

*__Schuster *et al.* 2005__ R. Schuster, M. Barth, A. Gruber, and F. Cichos. Defocused wide field fluorescence imaging of single CdSe/ZnS quantum dots. *Chem. Phys. Lett.*, 413(4–6):280–283, 2005.

Conference Proceedings

Barth *et al.* 2010d M. Barth, M. Gregor, R. Henze, T. Schröder, N. Nüsse, B. Löchel, and O. Benson. Hybrid approaches towards single emitter coupling to optical microresonators. *Proc. SPIE*, 2010 (in press).

Barth *et al.* 2009c M. Barth, J. Stingl, N. Nüsse, B. Löchel, and O. Benson. Controlled coupling of nanoparticles to photonic crystal cavities. In *Proc. SPIE*, volume 7223, page 72230Y, 2009.

Nüsse *et al.* 2009 N. Nüsse, M. Barth, B. Löchel, and O. Benson. Fabrication and characterization of photonic crystal cavities in the visible. In *Proc. SPIE*, volume 7366, page 73661K, 2009.

Barth *et al.* 2008b M. Barth, J. Stingl, J. Kouba, B. Löchel, and O. Benson. Manipulation of quantum emitters on photonic crystal cavities. In *Conference on Lasers and Electro-Optics & Quantum Electronics and Laser Science Conference*, volume 1–9, pages 2942–2943, 2008.

Smolka *et al.* 2008 S. Smolka, M. Barth, and O. Benson. Highly efficient fluorescence sensing with hollow core photonic crystal fibers. In *Digest of the LEOS Summer Topical Meetings*, pages 181–182, 2008.

Barth *et al.* 2007b M. Barth, J. Kouba, J. Stingl, B. Löchel, and O. Benson. SiN photonic crystal cavities: Promising tools for the manipulation of light in the visible. In *Proc. SPIE*, volume 6645, page 664503, 2007.

Kouba *et al.* 2007 J. Kouba, S. Kiss, M. Barth, W. Eberhardt, and B. Löchel. Fabrication and optical characterization of Si_3N_4 2D-photonic crystals for applications in visible range. In *Proc. SPIE*, volume 6645, page 664505, 2007.

Smolka *et al.* 2007c S. Smolka, M. Barth, and O. Benson. Selectively infiltrated photonic crystal fibers for fluorescence sensing. In *Conference on Lasers and Electro-Optics & Quantum Electronics and Laser Science Conference*, volume 1–5, pages 1231–1232, 2007.

Barth *et al.* 2007c M. Barth and O. Benson. Manipulation of dielectric particles using photonic crystal cavities. In *Conference on Lasers and Electro-Optics & Quantum Electronics and Laser Science Conference*, volume 1–5, pages 1125–1126, 2007.

Barth *et al.* 2006c M. Barth and O. Benson. Interaction of photonic crystals with nanoscopic particles: Towards novel (bio-)sensing techniques. In *Proc. SPIE*, volume 6182, page 61821T, 2006.

List of Figures

List of Tables

Selbständigkeitserklärung

Hiermit erkläre ich, die vorliegende Arbeit selbständig und nur unter Verwendung der angegebenen Quellen und Hilfsmittel angefertigt zu haben. Ich habe mich anderweitig nicht um einen Doktorgrad beworben und besitze einen solchen auch nicht. Die dem Verfahren zugrunde liegende Promotionsordnung der Mathematisch-Naturwissenschaftlichen Fakultät I der Humboldt-Universität zu Berlin habe ich zur Kenntnis genommen.

Berlin, den 3. März 2010

Michael Barth